Discrete Supramolecular Stacks by Self-Assembly and Folding of Bis(merocyanine) Dyes

Dissertation zur Erlangung des
naturwissenschaftlichen Doktorgrades
der Julius-Maximilians-Universität Würzburg

vorgelegt von
Eva Kirchner
aus Wipfeld

Würzburg 2018

Eingereicht bei der Fakultät für Chemie und Pharmazie am:

11.01.2018

Gutachter der schriftlichen Arbeit:

1. Gutachter: Prof. Dr. Frank Würthner

2. Gutachter: Jun.-Prof. Dr. Ann-Christin Pöppler

Prüfer des öffentlichen Promotionskolloquiums:

1. Prüfer: Prof. Dr. Frank Würthner

2. Prüfer: Jun.-Prof. Dr. Ann-Christin Pöppler

3. Prüfer: Prof. Dr. Ingo Fischer

Datum des öffentlichen Promotionskolloquiums:

15.03.2018

Doktorurkunde ausgehändigt am:

_____

für meine Familie

LIST OF ABBREVIATIONS

Ac	acetyl
ADF	Amsterdam density functional
AFM	atomic force microscopy
AM1	Austin Model 1
Ar	aryl
ATOP	amino-thienyl dioxocyano-pyridine
BLA	bond length alternation
4,4'-bpe	*trans*-1,2-bis(4-pyridyl)ethylene
Bu	butyl
calcd.	calculated
CD	circular dichroism
COSY	homonuclear correlation spectroscopy
CPCM	conductor-like polarizable continuum model
2D	two-dimensional
DCM	dichloromethane
DCTB	*trans*-2-[3-(4-*tert*-butylphenyl)-2-methyl-2-propenylidene]-malononitrile
DFT	density functional theory
DLS	dynamic light scattering
DMF	*N*,*N'*-dimethylformamide
DMSO	dimethyl sulfoxide
DNA	deoxyribonucleic acid
DOSY	diffusion ordered spectroscopy
DPA	diphenylacetylene
DPB	diphenylbutadiyne
e.g.	for example (latin: exempli gratia)
ESI	electrospray ionization
Et	ethyl
FAB	fast atom bombardment
GPC	gel permeation chromatography
h	hour(s)
HBC	hexa-*peri*-hexabenzocoronene

HMBC	heteronuclear multiple bond coherence
HPLC	high performance liquid chromatography
HR	Huang-Rhys factor
HRMS	high-resolution mass spectrometry
HSQC	heteronuclear single quantum coherence
i.e.	that is (latin: id est)
ITC	isothermal titration calorimetry
min	minute(s)
MALDI	matrix-assisted laser desorption/ionization
MC	merocyanine
MCH	methylcyclohexane
Me	methyl
MM+	force field method
MMFF	Merck molecular force field
Mp	melting point
MS	mass spectrometry
NDI	naphthalene diimide
NMR	nuclear magnetic resonance
NOESY	nuclear Overhauser enhancement spectroscopy
ORTEP	oak ridge thermal ellipsoid plot
PBI	perylene bisimide
Ph	phenyl
Pr	propyl
PYBOX	2,6-bis(2-oxazolyl)pyridine
Ref.	reference
RNA	ribonucleic acid
ROESY	rotating-frame nuclear Overhauser enhancement spectroscopy
rpm	revolutions per minute
RT	room temperature
SAXS	small-angle X-ray scattering
SCC-DFTB	self-consistent-charge density functional based tight binding
SEM	scanning electron microscopy
SLS	static light scattering
STM	scanning tunnelling microscopy

TBAF	tetrabutylammonium fluoride
TDDFT	time-dependent density functional theory
TEM	transmission electron microscopy
TFA	trifluoroacetic acid
THF	tetrahydrofuran
TMS	trimethylsilyl
TOF	time of flight
UV	ultraviolet
vis	visible
Vol	volume
VPO	vapour pressure osmometry

TABLE OF CONTENT

Chapter 1

–

Introduction and Aim of This Thesis

Careful design and synthesis of large but finite-sized molecular materials are crucial for generating greater understanding in size-property relationships on a molecular level. Despite ongoing progress in synthetic techniques, access to discrete macromolecules including dendrimers,[1] ladder-type oligomers,[2] oligoamides,[3] or molecular nano-rings[4] is still limited by low yields of time-consuming multistep procedures and elaborate purification. Alternatively to this covalent synthetic entry, nature utilizes the supramolecular synthesis approach to realize extremely large size systems, like it is impressively demonstrated by the protein shell of viruses. The so-called capsids form by self-assembly of multiple protein subunits leading to a huge diversity of different structures with tailored functionalities such as the protection of the viral genome and the interaction with the host environment.[5] Also the light harvesting complex, which is a crucial component in the photosynthesis of purple bacteria, is self-assembled based on intermolecular forces between protein subunits.[6] Therefore, it is no surprise that supramolecular chemistry has developed to an own field of research with the aim of understanding intermolecular interactions between molecular building blocks to create complex artificial architectures with outstanding functionalities. Already in 1873 Johannes Diderik van der Waals discovered non-covalent forces between molecules for the first time[7] and in 1894 Hermann Emil Fischer postulated the lock-and-key principle based on his fundamental work on enzyme-substrate interactions.[8] The exploration of crown ethers and cryptands forming supramolecular complexes with ions or neutral molecules with high selectivity by Charles J. Pedersen,[9] Donald J. Cram[10] and Jean-Marie Lehn[11] is considered to be the breakthrough for the development of artificial molecular assemblies (Nobel Prize 1987) and paved the way towards highly functional systems. Thus, it was only a matter of time

before in 2016 the Nobel Prize went again to supramolecular chemists. Jean-Pierre Sauvage, Sir J. Fraser Stoddart and Bernard L. Feringa were awarded for the design and production of molecular machines[12] pointing out the tremendous progress in this field of research.

In the meanwhile, supramolecular architectures based on organic dyes have attracted considerable attention, since strong π-π-interactions between the conjugated molecules provide access to complex structures with unique optical and electronic properties.[13] The change in absorption behaviour upon self-assembly of chromophores has been observed for the first time by S. E. Sheppard[14] more than a century ago and in the 1960s the fundamental work of Davydov and Kasha provided a model that allows interpretation of optical properties of dye aggregates based on molecular exciton theory.[15] However, with the development of organic dyes as promising smart materials with applications in nanotechnology and in organic electronics and photovoltaics,[16] optimization of material properties on the molecular level becomes necessary to realize ideal device performance with advantageous absorption behaviour and consistent charge transport processes.[17] Thus, model systems are needed that enable detailed investigation of structure-property relationships of dye assemblies in solution. Most notably, such model systems demand highly ordered structures with finite and precisely defined number of interacting chromophore units and high aggregation constants.

For this purpose, the class of merocyanine (MC) dyes offers ideal molecular building blocks. Due to their donor-acceptor structure, these dyes exhibit large dipole moments and therefore are well known to self-assemble into discrete cofacially stacked antiparallel dimers in unpolar solvents driven by strong and directional dipole-dipole interactions, which allows facile prediction of the resulting aggregate structure.[18] Thereby, strong aggregation tendency and high degree of order facilitate structural elucidation for example by nuclear magnetic resonance (NMR) spectroscopy and narrow and intense absorption bands give the opportunity to monitor the self-assembly processes by UV/vis spectroscopy. However, sophisticated strategies are needed to realize supramolecular dye ensembles of desired size and structure. By connecting two chromophores with an appropriate spacer unit, during the last decade a huge variety of different structural aggregate motifs based on merocyanine dyes has been established in our group.[19] Hence, careful design of the linker moiety provides access to discrete stacks with up to four interacting aromatic subunits (**Bis(MC) 1** in Figure 1).[20]

Following up this groundwork, the aim of the first part of this thesis was to create even larger but still finite-sized merocyanine dye stacks by increasing the length of the spacer unit of bis(merocyanine) dyes (Figure 1). The aggregation behaviour of these bichromophoric molecules should be investigated by UV/vis absorption studies. Furthermore, the structures of

the dye stacks should be elucidated by detailed one- and two-dimensional NMR spectroscopy in order to gain insights into the structural arrangement of the chromophores within the stacks. The thereby developed series of discrete merocyanine dye stacks should be used as model system to perform detailed studies on optical properties of dye assemblies in dependency on the number of interacting chromophores, which will be discussed in terms of exciton theory involving quantum chemical calculations.

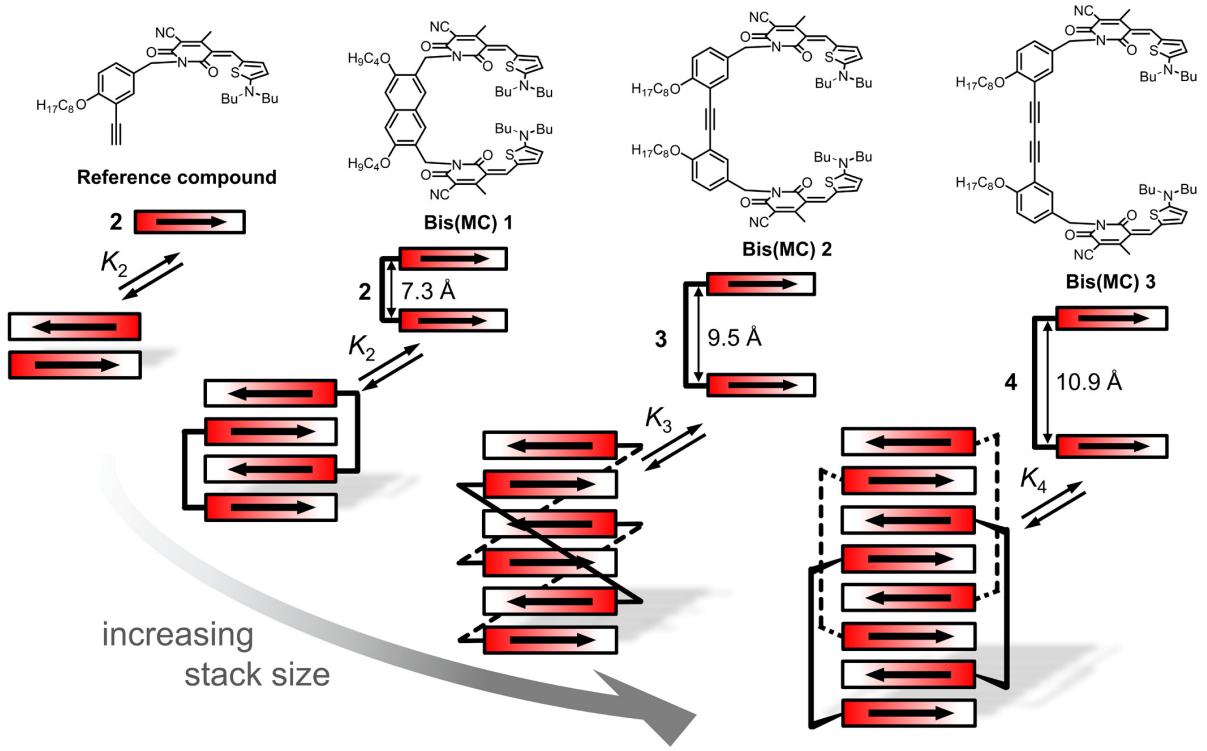

Figure 1 Chemical structures of reference merocyanine and of bis(merocyanine) dyes **Bis(MC) 1**,[20a] **Bis(MC) 2** and **Bis(MC) 3**, respectively. The self-assembly of the molecules into discrete dye stacks with defined number of interacting chromophores depending on the spacer length is illustrated schematically. Merocyanine units are represented by colored bars and their dipole moments are depicted as black arrows

In the second part of this work, the synthesis of bis(merocyanine) foldamers will be described bearing two merocyanine chromophores attached in *ortho*- and *meta*-positon to a diphenylacetylene (DPA) linker. From previous work it is known that this linker favours an intramolecular pleated conformation of the molecule in unpolar solvents with antiparallel stacked dye units.[19h] By connecting two merocyanines with either equal or different conjugation length to the DPA backbone, discrete homo- and hetero-chromophoric dimer models should be accessible (Figure 2) allowing investigation of absorption properties of dimer stacks with systematic variation of the excited state energy difference between the interacting chromophores. Folding of the dyes should be investigated by solvent-dependent UV/vis

absorption studies. Furthermore, density functional theory (DFT) calculations as well as quantum chemical analysis should give fundamental insights into coupling between chromophores in homo- and hetero-aggregates.

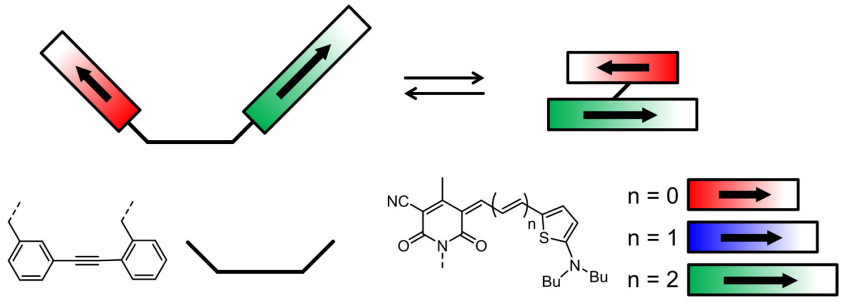

Figure 2 Schematic representation of the folding process of a bis(merocyanine) dye containing variable combinations of two of the three merocyanine units with different conjugation length.

Chapter 2 gives a brief overview about common analytical techniques for structural characterization of supramolecular aggregates. Furthermore, different approaches are introduced to realize finite-sized and highly ordered π-stacks with well-defined number of stacked aromatic moieties. These methods are illustrated based on representative literature examples whose structural characterization is discussed.

Chapter 3 presents the development of a series of bis(merocyanine) dyes that show self-assembly into discrete supramolecular aggregates with well-defined number of stacked chromophores depending on the length of the linker moiety. Following the description of the synthesis of the dyes and elucidation of the aggregate structure, optical properties of the stacks are interpreted by means of exciton theory and are related to the number of stacked chromophores.

Chapter 4 describes synthesis and folding studies of homo- and hetero-bis(merocyanine) dyes. The so formed series of merocyanine dimer stacks constitute a model system that is used to rationalize absorption properties of dimer aggregates with variable energy difference between the adjacent chromophores.

Chapter 5 and **Chapter 6** summarize the results of this thesis in English and German.

In **Chapter 7**, the experimental part of this work is documented. The synthetic procedures and characterization of literature unknown compounds are described as well as the used materials and methods.

Chapter 2

—

Literature Survey on Finite-Sized Supramolecular π-Stacks: Strategies for Engineering and Structural Characterization

2.1 Introduction

Controlling the self-assembly of aromatic molecules has developed as the key to create sophisticated new materials for various applications since the coupling of chromophores leads to outstanding electronic and photophysical properties that are not inherent in the respective monomeric chromophores. Already in 1936, the pioneering work of Jelley and Scheibe provided fundamental understanding of dye-dye interactions with concomitant "aggregation-induced emission" and exciton migration phenomena.[21] Amongst others, to date a huge variety of artificial supramolecular architectures based on π-π-stacking has been published.[13a, 22] However, supramolecular self-assembly driven by π-π-interactions usually results in one-dimensional H-type aggregates of infinite size that often show a broad distribution of lengths and low degree of order. Especially for proper structural characterization and for the performance of basic studies, *e.g.* on charge transport phenomena, model systems with highly ordered structures are essential. Hence, sophisticated strategies are needed to control the extent of supramolecular assemblies. Indeed, some examples are known where molecular terminator were used as chain stopper to prevent further stacking at the end of one-dimensional aggregates.[23] However, this strategy still does not lead to distinct monodisperse systems of predictable size.

Following a brief introduction into common analytical techniques for the characterization of supramolecular aggregates, this chapter will give an overview of the different approaches in the literature to realize finite-sized and highly ordered π-stacks with well-defined numbers of stacked aromatic moieties. The methods will be illustrated based on representative examples, whose structural characterization will be discussed. As outlined in Figure 3, a classification into extrinsic (blue panel) and intrinsic (green panels) entries can be conducted.

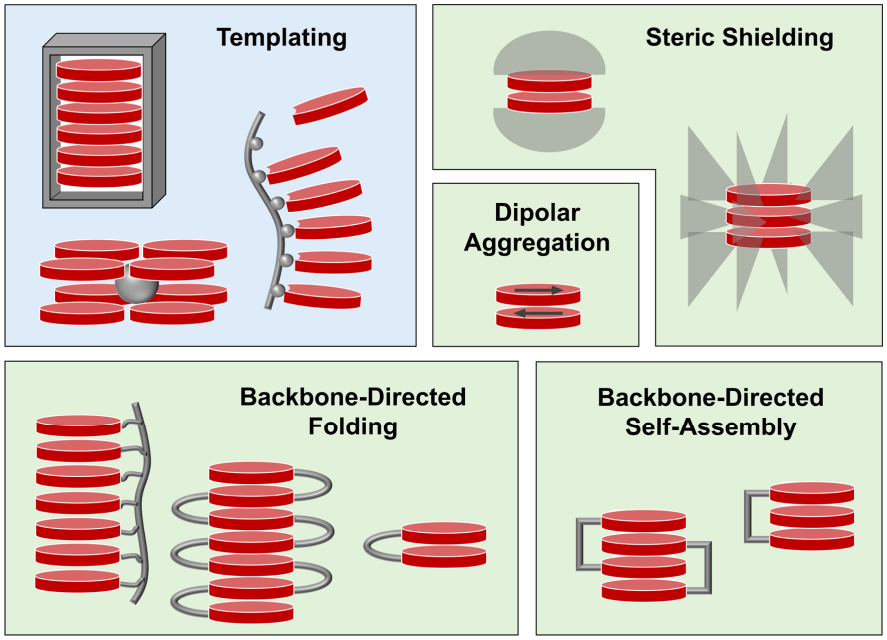

Figure 3 Overview of different extrinsic (blue panel) and intrinsic (green panels) methods to create finite-sized highly ordered supramolecular π-stacks of aromatic molecules (red discs).

On the one hand, external factors as for example the use of specific templates can guide π-π-stacking. On the other hand, supramolecular aggregation can be controlled intrinsically by programming the structural information in the molecular building blocks themselves. Thus, repulsive interactions between sterically demanding side chains provide a convenient point of contact to create finite-sized π-stacks. Introduction of additional highly directional supramolecular forces like dipole-dipole interactions seems to be a reasonable strategy, as well. Furthermore, creation of discrete aggregates by folding-induced intramolecular stacking of aromatic moieties directed by a flexible backbone will be reviewed in this chapter. In contrast, systems in which the aromatic elements are covalently connected in a rigid conformation enforcing π-contact without any degree of flexibility like given in cyclophanes[24] or the cofacially bound perylene bisimides (PBIs)[25] are not included here, although these compounds constitute important model systems for studies on charge and energy transfer processes.

2.2 Overview of Analytical Techniques for the Characterization of Supramolecular Aggregates

To adequately characterize the structure of supramolecular π-stacked aggregates, a broad repertory of different instrumental techniques is available.[26] Due to the reversibility of non-covalent interactions, supramolecular aggregates in solution can be considered as dynamic materials with advantageous self-healing properties.[27] The equilibrium between aggregated and non-aggregated species strongly depends on parameters like concentration, temperature and solvent polarity and therefore, defines the scope of suitable characterization techniques (Figure 4).

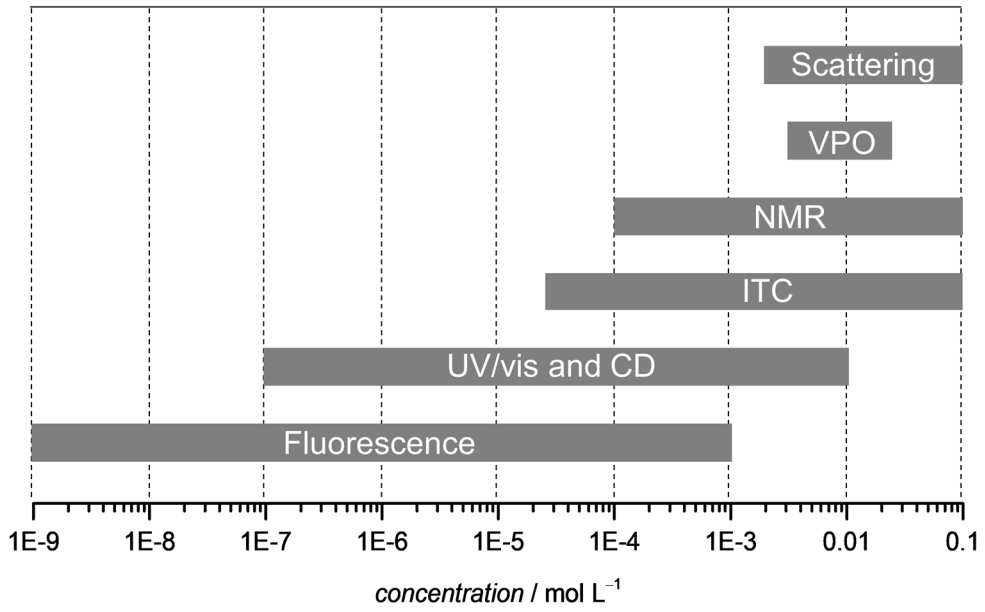

Figure 4 Analytical methods in solution and their operable concentration range.[26a]

UV/vis and fluorescence spectroscopy can be applied through a relatively broad concentration range.[28] Thus, especially concentration-dependent studies are commonly performed to investigate structural and thermodynamic properties of dye aggregates, since the photophysical properties of dye molecules are known to change upon interaction between chromophores in an aggregate. By fitting the experimental data with appropriate aggregation models,[22c, 29] information about binding constants, aggregation mechanism and aggregate size can be obtained.

The use of circularly polarized light in circular dichroism (CD) absorption studies gives information on the helicity in chiral molecules or aggregates and therefore, this spectroscopic technique is commonly applied to elucidate the secondary structure of biological molecules.[30]

Another analytical method to gain access to thermodynamic parameters of aggregation processes such as binding affinity, enthalpy changes and binding stoichiometry, is the isothermal titration calorimetry (ITC). It also allows determining the Gibbs energy changes and entropy changes upon aggregation or disassembly. The applicable concentration range for running ITC experiments is in general relatively broad but depends on the system under investigation. Thus, the concentration should be high enough to observe a heat effect that can be measured decently (≥10 μcal).[31]

A technique that requires significantly higher concentrations and therefore often fails due to limited solubility of the supramolecular systems is nuclear magnetic resonance (NMR) spectroscopy.[28, 32] Furthermore, this analytical method can only be applied to highly ordered aggregate systems, otherwise dynamic effects complicate analysis due to pronounced signal broadening. Nevertheless, NMR spectroscopy is a powerful tool to gain detailed information about the nature of molecular interactions for example by analysing chemical shifts of proton resonances caused by a modified chemical environment of the protons upon aggregation induced by solvent-polarity, temperature or concentration changes. The nuclear Overhauser effect (NOE) allows identification of close spatial proximity between protons by through space correlation in two-dimensional rotating-frame Overhauser enhancement spectroscopy (ROESY) or nuclear Overhauser enhancement spectroscopy (NOESY) experiments and therefore, gives insight into the exact structural arrangement in aggregates.[33] Moreover, the hydrodynamic radius of a species in solution can be obtained according to the Stokes-Einstein equation based on the diffusion coefficient from diffusion ordered spectroscopy (DOSY) experiments.[34] However, it has to be noted that the original Stokes-Einstein equation holds true under the assumption of spherical particles and therefore, results for rod-shaped and other non-spherical aggregates might be inaccurate.

Further commonly used analytical techniques that provide information about the size and structure of supramolecular aggregates in solution are light scattering (static (SLS) and dynamic (DLS) light scattering)[35] and vapour pressure osmometry (VPO).[36] Both methods require high aggregate concentrations ($>10^{-3}$ M) and thus, sample preparation plays an important role to attain reliable results. Whereas VPO is highly sensitive towards low molecular mass components such as residual monomers or solvent impurities, in light scattering experiments even trace amounts of contaminants like dust particles cause intense scattering signals leading to defective results. To determine the size of kinetically stable aggregates in solution, size exclusion chromatography can be applied as well. However, using an appropriate standard for referencing is crucial.[37]

Recent progress in the field of gas-phase experiments and especially the development of soft ionization techniques such as matrix-assisted laser desorption/ionization (MALDI), electrospray ionization (ESI) and fast atom bombardment (FAB) has made mass spectrometry to an important technique, not only for the determination of the molecular weight of supramolecular assemblies, but also to investigate non-covalent forces involved in the binding process.[38] Thereby, environment-free conditions in the gas phase imply the advantage to in turn draw conclusions on the effect of solvation on the aggregation behaviour and furthermore lead to high comparability with theoretical calculations. Nevertheless, results from mass spectrometric experiments should be interpreted with caution, since unspecific binding often appears in the gas phase.

A wide range of different scanning probe microscopy techniques like atomic force microscopy (AFM), scanning tunnelling microscopy (STM), scanning electron microscopy (SEM) and many others enable to investigate supramolecular π-stacks on a surface.[39] Depending on the method, the resolution of these imaging methods ranges up to the visualization of single molecules and therefore, besides estimation of the aggregate size distribution, structural information like for instance the helical pitch and handedness in case of chiral columnar stacks might be accessible.[40] One drawback of the microscopic techniques is the interaction of the aggregates with the surface that might influence the aggregation behaviour.

The ultimate tool to elucidate the exact structure of supramolecular architectures in the solid state is X-ray crystallography.[41] However, in many cases the aggregate species are not prone to crystallize. Especially, the growth of single-crystals suitable for X-ray diffraction based on molecular building blocks equipped with long alkyl chains in order to provide sufficient solubility in solution is challenging. Besides, in many cases inclusion of solvent molecules within the solid state packing is a problem, since evaporation of the solvent during the measurement may lead to destruction of the crystal. Furthermore, it has to be noted that the solid state structure does not necessarily coincide with the structure of the supramolecular aggregate formed in solution. Thus, an X-ray crystal structure does not replace the solution based analytical techniques discussed above.

2.3 Template-Controlled Supramolecular Self-Assembly

According to the definition of D. H. Busch, "a chemical template organizes an assembly of atoms, with respect to one or more geometric loci, in order to achieve a particular linking of atoms."[42] Initially, this definition was related to the field of synthetic chemistry, where it has been demonstrated extensively that the formation of complex molecules like for example macrocycles,[4a, 43] catenanes[44] or molecular knots[45] can be controlled regio- and stereoselectively *via* non-covalent interactions to metal ions or by electrostatic and hydrogen bonding templating agents.[46] But also in supramolecular chemistry the templating effect has developed to a powerful tool to extrinsically affect the structure of self-assembled architectures.[47] Inspiration is taken from biological systems like the light-harvesting (LH) apparatus found in the photosystems of purple bacteria (Figure 5).[6] The complex structures contain light absorbing bacteriochlorophyll *a* and carotenoid dyes that are embedded non-covalently into circularly arranged polypeptide subunits. In this way the hydrophobic proteins template the precise structural arrangement of a well-defined number of chromophores within an extremely large but finite-sized supramolecular assembly. Taking nature as a model, strategies have been elaborated during the last decade that enable exact control over the size of supramolecular π-stacks by specific templates.

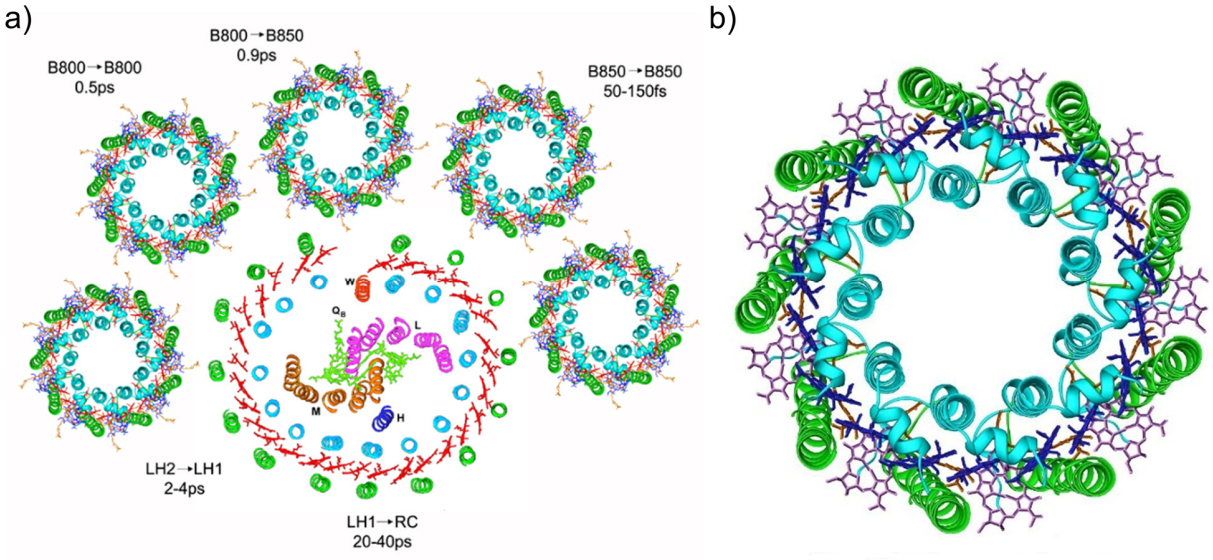

Figure 5 Schematic representation of a) the photosystem of purple bacteria and b) the light harvesting complex (LH2).[6e] Adapted with permission from Ref. [6e]. Copyright 2006 Cambridge University Press.

2.3.1 Chain-Templated Self-Assembly

Polymer chains capable of binding molecular subunits *via* supramolecular recognition sites represent appropriate templating agents to control the self-assembly of aromatic molecules in π-stacked aggregates. Thereby, the number of recognition sites strictly defines the number of molecules in the stack and the distance between the recognition sites in the strand is of crucial importance in order to enable efficient π-π-stacking between the docked molecular subunits. The probably most prominent model of a natural template, the DNA (deoxyribonucleic acid), motivates this approach. Carrying the genetic information of living organisms, during replication of the genome, the DNA strand itself acts as a template for the formation of a new strand by complementary base pairing through hydrogen bonding.[48] Another amazing example of templating in natural systems is demonstrated by the self-assembled structure of the Tobacco Mosaic Virus.[49] Exactly 2130 protein subunits are organized along a finite-sized helical RNA (ribonucleic acid) backbone and thus, the dimension of the very basic rod-like architecture is specified by the templating strand.

Following this examples, the groups of Schenning and Meijer presented an artificial DNA species, in which a supramolecular stack of aromatic molecules is formed through hydrogen bonding to a single strand of oligothymine DNA *via* a complementary diamino triazine unit (Figure 6).[50] It was shown that the aggregate size is defined by the number of nucleotides in the DNA template (**1**) and therefore, discrete stacks of 40 naphthalene (**2**) or oligo(*p*-phenylene)vinylene (**3**) moieties could be realized. The right-handed helical alignment of the chromophores within the stack has been proven by concentration-dependent UV/vis and CD spectroscopy and the mass of the supramolecular aggregate was determined by ESI mass spectrometry.

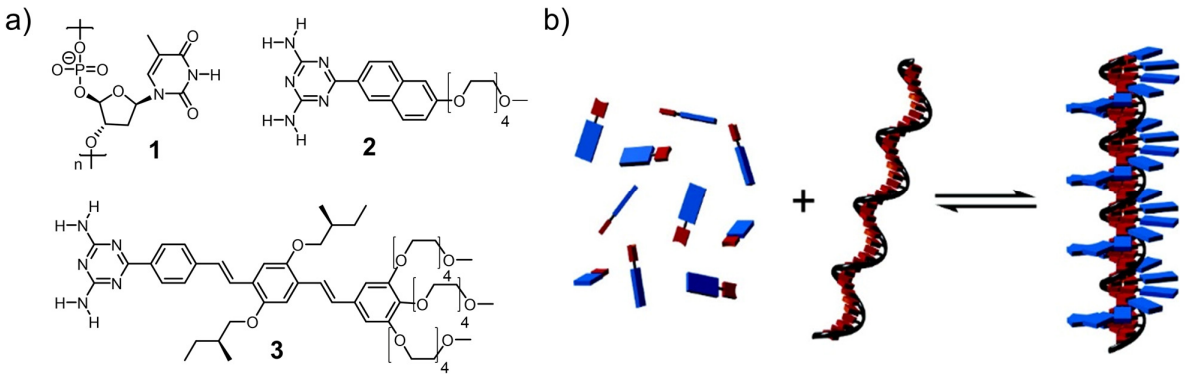

Figure 6 a) Chemical structures of **1**, **2** and **3** and b) schematic illustration of supramolecular stacking of naphthalene (**2**) and oligo(*p*-phenylene)vinylene (**3**) chromophores templated by hydrogen bonding to a single strand of oligothymine DNA (**1**).[50] Adapted with permission from Ref. [50]. Copyright 2007 American Chemical Society.

In contrast to the naturally occurring DNA template, the Sada group used a synthetic templating strand of oligomeric secondary dialkylammonium cations to control aggregation of aromatic molecules in ladder-type supramolecular structures (Figure 7).[51] Two 2,6-bis(2-oxazolyl)pyridine (PYBOX) ligands that are well-known receptors for secondary dialkylammonium cations have been attached on opposite sides to a porphyrin core. This enables the formation of one-dimensional H-stacked arrays of the dyes by complexation of the PYBOX units with two template chains *via* hydrogen bonding. Consequently, the number of recognition sites in the oligomer strands determines the number of steps in the ladder and thus, discrete porphyrin dimer and trimer stacks could be realized. Polymeric supramolecular ladders up to an averaged number of 130 stacked aromatic molecules were achieved by increasing the number of repeating units in the secondary dialkylammonium chain.[52] The binding process was deduced from UV/vis and CD spectral changes of the bis(PYBOX) ligand (**4**) upon addition of poly(trimethylene iminium) (**5**). However, a precise structural characterization of these large architectures is not provided and the averaged dimensions were only estimated by AFM measurements.

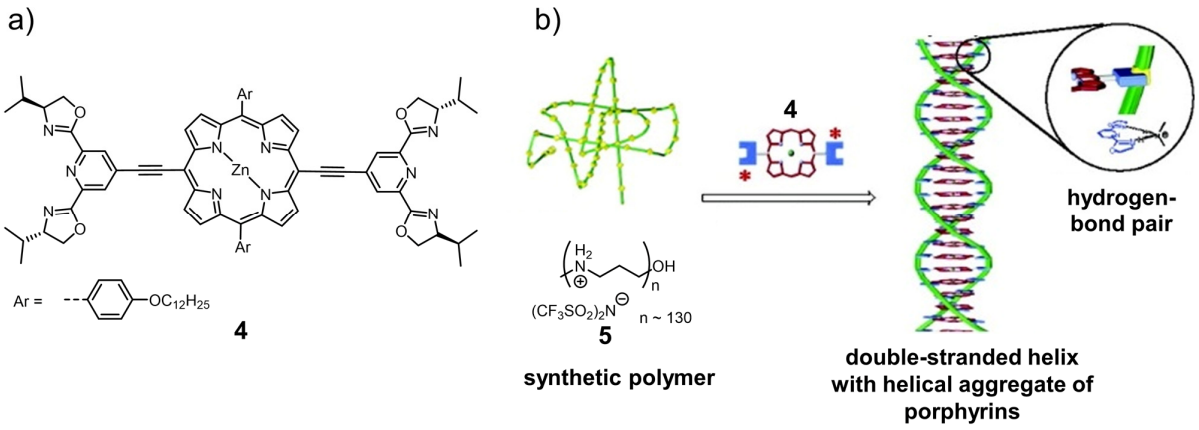

Figure 7 a) Chemical structure of a porphyrin equipped with two PYBOX ligands (**4**) and b) schematic representation of the formation of a double-stranded helix with a discrete helical stack of porphyrins by complementary hydrogen bonding between the N-atoms of the PYBOX receptors and the complementary protons of the templating oligomeric *sec*-dialkylammonium cations (**5**).[52] Adapted with permission from Ref. [52]. Copyright 2007 American Chemical Society.

Similar ladder-type assemblies based on hydrogen bonding interactions were reported by MacGillivray and coworkers.[53] They observed discrete double, triple and quadruple stacks of *trans*-1,2-bis(4-pyridyl)ethylene (4,4`-bpe, **6**) in the solid state by cocrystallization with indolocarbazole (IC, **7**) depending on the molar ratio of the two components (Figure 8). Single-crystal X-ray analysis revealed aromatic stacking of the 4,4`-bpe moieties in a cofacial manner induced by hydrogen bonding between the N−H groups of the indolocarbazole rails and the N

atoms of 4,4`-bpe. Unfortunately, this system could not be transferred to solution and is limited to a stack size of four molecules due to the restricted number of receptor sites of the indolocarbazole template.

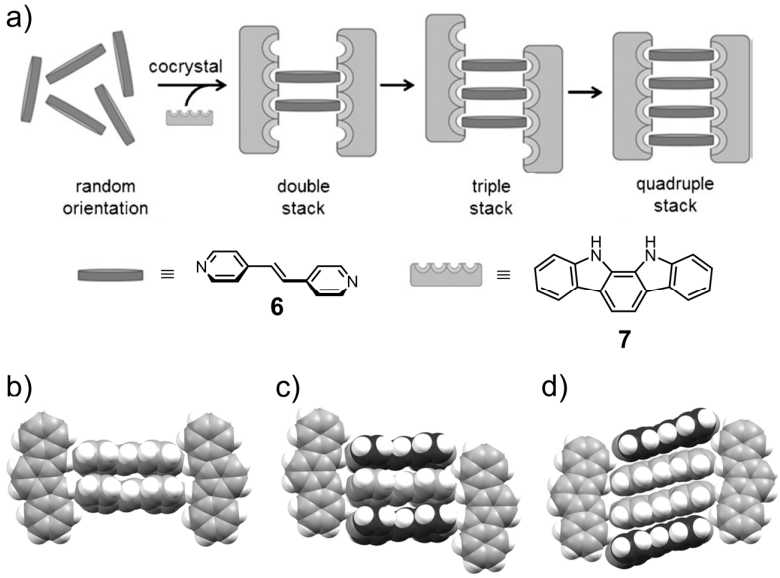

Figure 8 a) Schematic representation of the formation of discrete stacks of 4,4`-bpe (**6**) by cocrystallization with indolocarbazole (**7**) and space-filling model of the single-crystal X-ray structure of b) double, c) triple and d) quadruple stacks.[53] Adapted with permission from Ref. [53]. Copyright 2013 John Wiley and Sons.

As depicted in Figure 9, the group of Stoddart utilized the unique templating effect of dumbbell-shaped oligomer strands to create remarkably well-defined π-stacks within oligorotaxanes.[54] [24]Crown-8 rings containing aromatic residues were self-assembled around a defined number of $–CH_2–NH_2^+–CH_2–$ recognition sites along the rod section of the dumbbells by a clipping approach in a one-pot, multicomponent synthesis. Efficient π-π-stacking interactions between the aromatic residues of adjacent rings is guaranteed by a constant distances of 3.5 Å between the recognition sites provided by trismethylene bridges. Moreover, 3,5-dimethoxy phenyl groups at both ends of the oligomer strand serve as stoppers resulting in mechanically interlocked structures with discrete stacks of up to 19 crown ethers. ^{1}H NMR spectroscopy provides unambiguous evidence for these accurately defined systems and the existence of multiple π-π-interactions between the aromatic residues of the crown ethers was verified by high-field shifts of the respective aromatic protons.

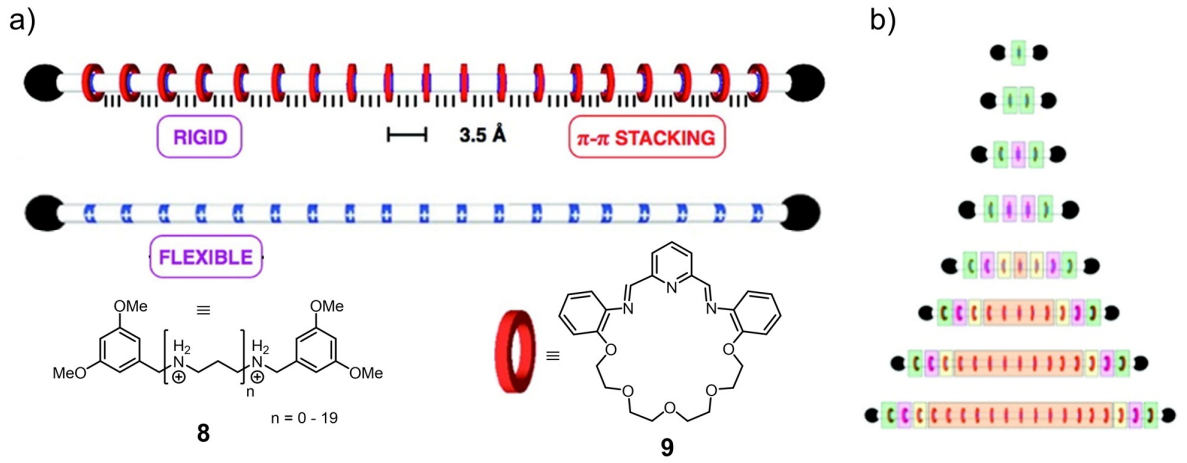

Figure 9 a) Principle of assembling π-stacks with well-defined numbers of interacting aromatic moieties by creating dumbbell-shaped oligorotaxanes with a distinct number of recognition sites for [24]crown-8 rings and b) series of oligorotaxanes with discrete stacks of up to 19 aromatic residues of the crown ethers.[54b] Adapted with permission from Ref. [54b]. Copyright 2012 American Chemical Society.

2.3.2 Metal Ion-Templated Self-Assembly

The concept of using metal ions as templates to precisely control the size of π-stacks in solution is amply demonstrated by a vast number of studies on the self-assembly of guanosine mononucleoside (G) derivatives.[55] In aqueous as well as in organic media these molecules organize into tetrameric structures *via* hydrogen bonding between four guanine bases (Figure 10).[56] The so-formed G-quartets exhibit a planar cyclic structure with four carbonyl oxygens pointing into the central cavity forming a well-organized pocket for the coordination of cations by ion-dipole interactions, which stabilizes the tetrads. Generally, in the absence of metal ions organization into ribbon-like structures is observed.[56b, 57] Furthermore, metal ions were found to promote the self-assembly of the pre-formed G-quartets into discrete columnar π-stacks of well-defined size, the so-called G-quadruplexes.[58] Depending on the ratio of metal ions to guanosine monomers, aggregation into ordered octameric, dodecameric and hexadecameric structures can be achieved, as proven by ^{1}H NMR titration experiments in organic solvents by the group of Rivera.[59] A ratio below 1:8 preferably results in the stacking of two G-quartets into C_4-symmetric sandwich-type octameric aggregates, whereas larger stacks like the hexadecamer are formed at a ratio > 1:8. However, to achieve the elusive dodecamer intermediate, additional intrinsic parameters like the sterical demand of side chains have to be adjusted to find the ideal balance between attractive and repulsive non-covalent interactions.[59b]

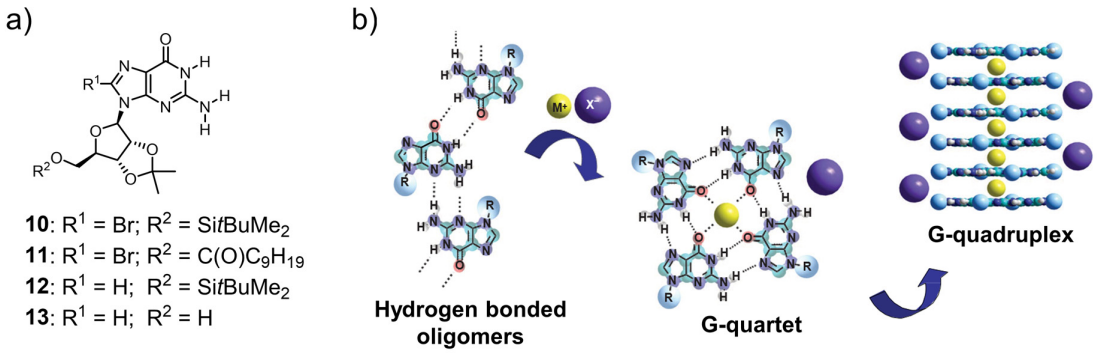

Figure 10 a) Chemical structure of guanosine derivatives **10**-**13** and b) organization into tetrameric structures (G-quartets) driven by coordination to a metal ion template. The G-quartets further self-assemble into discrete columnar stacks depending on the amount of metal ions.[60] Adapted with permission from Ref. [60]. Copyright 2009 Nature Publishing Group.

Furthermore, the choice of the appropriate metal ion constitutes an efficient tool to control the G-quartet self-assembly since it turned out that the ionic radius and the strength of the cation-carbonyl interactions play a central role for the stability of the complexes.[61] Discrete octameric structures preferably form in the presence of monovalent (Na^+, K^+, Rb^+, NH_4^+) and divalent cations (Sr^{2+}, Ba^{2+}, Pb^{2+}),[55a] whereas trivalent lanthanide metal ions (La^{3+}, Tb^{3+}, Dy^{3+}, Tm^{3+}) support stacking into tripledecker-like G-dodecamers incorporating only one metal ion in the central G-quartet. The most selective formation of dodecamers was observed for La^{3+} as its ionic radius seems to be ideal for the cavity of the complex structure.[61a] Even a metallo-responsive conversion of the hexadecameric to an octameric G-quadruplex could be achieved with high specificity upon replacing the potassium template by strontium ions.[62]

The influence of the counter ion on the structure and stability of the G-quadruplex has been addressed in detail by Meijer[60] and Davis.[63] Meijer could show that the formation of discrete stacks of G-quartets is strongly related to the dissociation energy of the ion pair, which represents the thermodynamically unfavourable process in the self-assembly equilibrium. Whereas the cation is satisfactory complexed in the centre of the G-quartet, the anion remains at the periphery destabilizing the assembly. It has been shown that the formation of larger complexes is favoured in solvents that can efficiently solvate the anion. Thus, the nature of the anion itself and carefully adjusting its stabilization by the solvent environment provides selective access to G-quadruplexes comprising two, three, four or six G-quartet subunits.[60, 64] Furthermore, the use of carefully designed organic anions that interact with functional groups at the periphery of the G-quadruplexes *via* hydrogen bonding can even stabilize one specific complex species. By applying this approach the group of Davis generated discrete hexadecameric aggregates of guanosine derivatives, where two octameric subunits are held

together by four picrate anions (**14**).[63] Thus, the counter anion acts as a clip by forming hydrogen bonds to the amino protons of the two inner G-quartets as it was proven by single-crystal X-ray analysis (Figure 11).

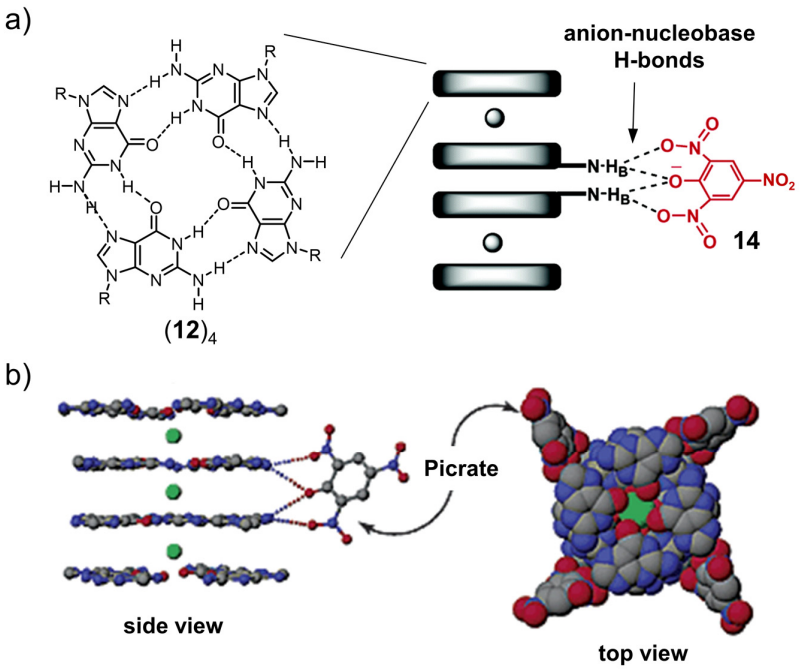

Figure 11 a) Schematic representation and b) X-ray crystal structure in side view (left) and top view (right) of a discrete hexadecameric G-quadruplex (**12**)$_4$ showing anion-nucleobase hydrogen bonding between four picrate anions (**14**) and the amino protons of the two inner G-quartets.[63] Adapted with permission from Ref. [63]. Copyright 2003 American Chemical Society.

2.3.3 Coordination Cages as Supramolecular Templates

Coordination cages formed upon self-assembly of metal complexes and organic pillar ligands constitute fascinating architectures with great functionality.[65] Their well-defined cavities can act as receptors for highly specific molecular recognition and thus have high potential for application as molecular flasks for chemical reactions,[66] transport containers for drug molecules,[67] sensors[68] or for stabilization of reactive species in an isolated space.[69] Furthermore, the concept of coordination cages appears to be a promising opportunity to investigate discrete aromatic stacks in solution since the box-shaped hosts are capable of accommodating self-assembled arrays of multiple aromatic guests. Thereby, the cavity dimension, which is determined by the length of the used pillars, limits the number of stacked planar molecules allowing precise control over the size of the stack.

In 2003 the Fujita group reported the first prismatic coordination cage formed by self-assembly of two panel-like triazine ligands **16** that are connected with three pyrazine linkers **17** *via* end-capped Pt(II) ions (Figure 12).[70] The interplanar distance provided by the length of the pillars allows intercalation of one aromatic guest such as coronene (**18**) with close π-π-contact to the panels of the cage (Figure 12a). By replacing the bidentate pyrazine pillar **17** by a slightly longer bipyridine linker the cavity size increases, enabling incorporation of two aromatic molecules (Figure 12b) and therefore discrete dimer stacks of coronenes, perylenes and porphyrins could be realized.[71]

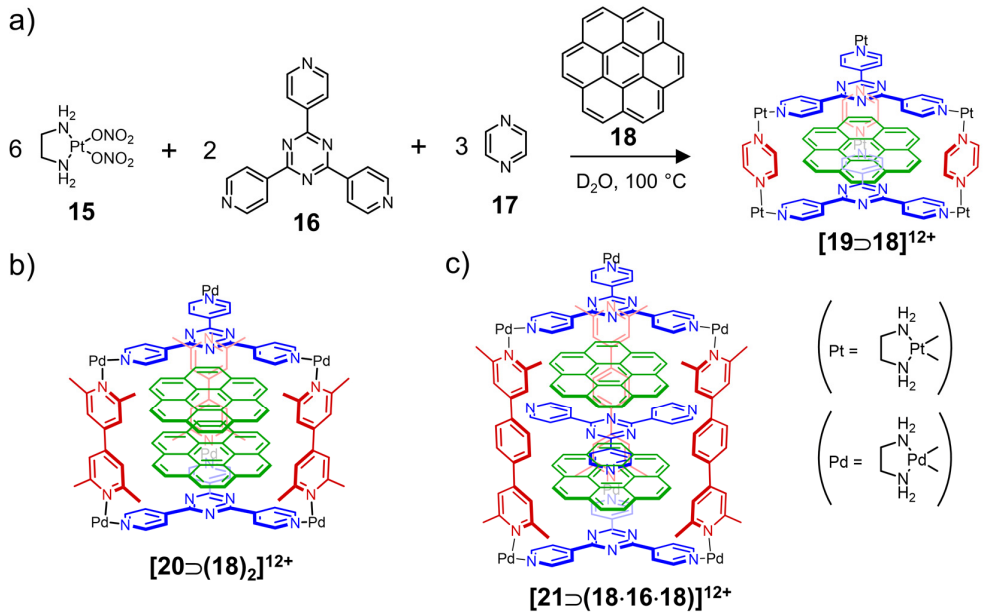

Figure 12 a) Schematic illustration of the supramolecular synthesis of prismatic coordination cage **19** hosting one coronene (**18**) guest molecule. Chemical structures of b) cage **20** accommodating two π-stacked coronene molecules and c) cage **21** with a discrete hetero-chromophoric A-D-A-D-A stack of coronene and triazine **16** units.[71a] Adapted with permission from Ref. [71a]. Copyright 2005 John Wiley and Sons.

However, this approach is limited to aromatic guests of well-defined size and shape, since the three pillared linkers do not only confine the longitudinal but also the transverse dimension of the stack, which unfortunately complicates introduction of functional residues. Furthermore, it has been shown that inclusion of exclusively electron rich aromatic guests is restricted to a stack size of two, which is attributed to unfavourable electrostatic repulsion.[71a, b] Thus, box-shaped assembly **21**, whose cavity is capable of hosting three stacked aromatic compounds templates the formation of a hetero-stack with one molecule of uncoordinated triazine **16** sandwiched between the planes of two coronene or porphyrin guests (Figure 12c). The efficient assembly was attributed to strong donor-acceptor (D-A) charge transfer interactions between the electron rich coronenes and the electron poor Pd(II)-coordinated and unbound triazine panels leading to a discrete A-D-A-D-A system. Consequently, the use of carefully designed

coordination cages allows assembly of discrete hetero-chromophoric arrays as well, which has been proven by further examples.[72] Recently, Chi and coworkers reported on an iridium-cornered prismatic cage, where the encapsulation of coronene and naphthalenediimide (NDI) guest molecules could be monitored successively by UV/vis and NMR spectroscopy illustrating a feasible approach to selectively create any stack composition of multiple different aromatic molecules.[73]

The so far largest discrete π-stack of equal chromophores templated by the cavity of a box-shaped coordination cage has been achieved by the Fujita group.[74] By preparing a comprehensive series of prism-like cages with organic pillars of different length (Figure 13) they have demonstrated precise control over the stacking number up to an assembly consisting of five polarized aromatic pyrene-4,5-dione molecules. The supramolecular systems enabled studies on the role of dipole-dipole interactions on the stacking and the preferential orientation of the dipolar molecules. Hence, an antiparallel orientation in even numbered stacks has been confirmed that causes extinction of the net dipole moment. In comparison, in the odd numbered stacks the molecules do not show an alternating orientation but rather exhibit a certain degree of rotational displacement with respect to each other resulting in an overall dipole moment of zero as well.[74a]

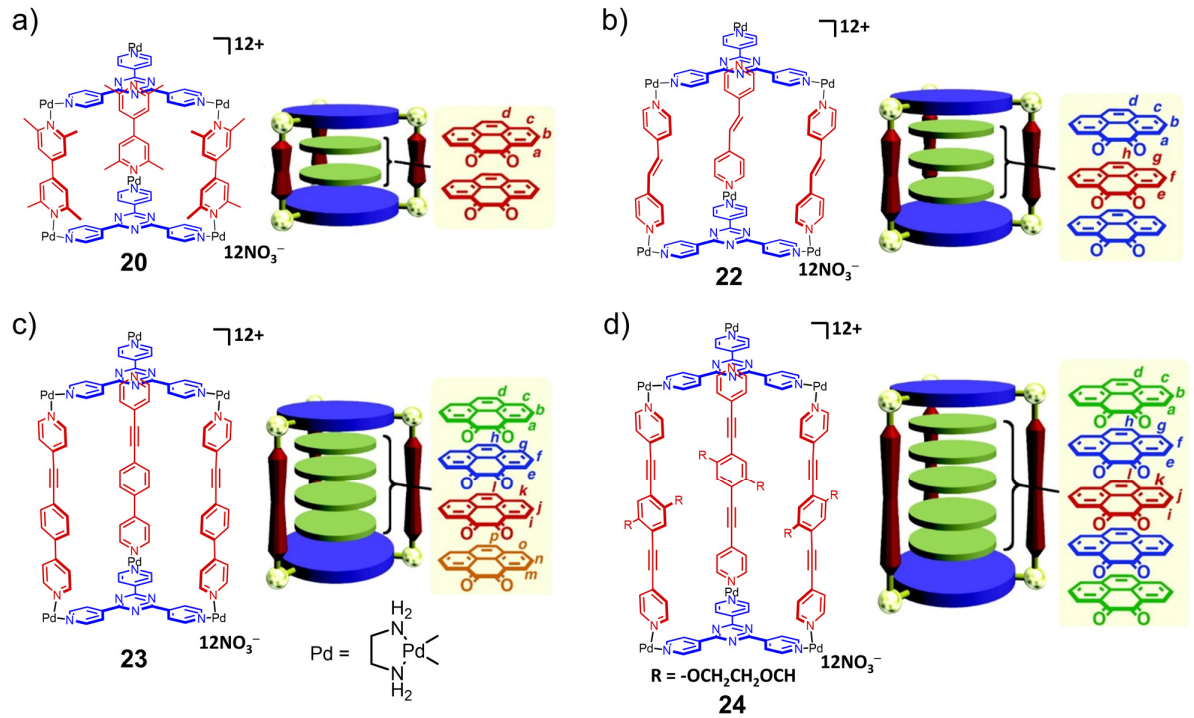

Figure 13 Chemical structures of a series of prism-like coordination cages **20**, **22**, **23** and **24** with organic pillars of different length. The templated π-stacking of a) two, b) three, c) four and d) five polarized aromatic pyrene-4,5-dione molecules insight the cage cavities is represented schematically.[74a] Adapted with permission from Ref. [74a]. Copyright 2010 American Chemical Society.

Moreover, the metal coordinated panel-like linkers do not only terminate the assemblies, but can also be part of the stacks if two coordination cages mechanically interpenetrate each other. Figure 14 illustrates the principle of discrete π-π-stacking of different aromatic units within catenanes. The self-assembly is templated by aromatic guests that occupy the three cavities in the three-dimensionally interlocked structure. By this method, remarkably large, discrete hetero-chromophoric π-stacks were generated consisting of seven to nine chromophores according to the length of the used pillars.[75]

Isolated stacks of up to nine alternating pyrene and NDI molecules were obtained in a similar way by π-π-stacking between two NDI-based metallarectangles that host three pyrene guests.[76] Two additional pyrenes were found to stack at the periphery of the assembly in the solid state. In contrast to the catenanes described above, in this examples no interpenetration between the two rectangles takes place leading to more dynamic structures.

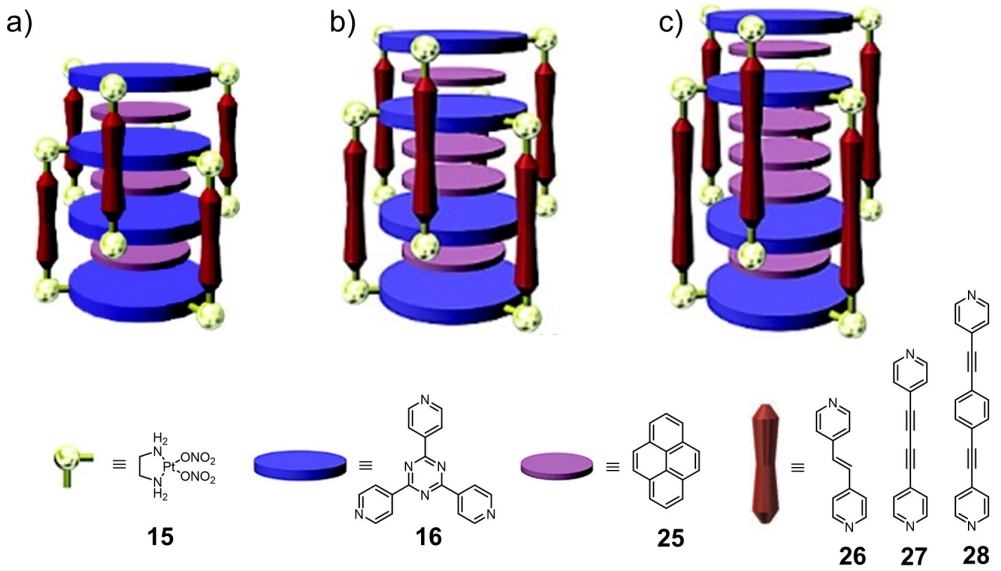

Figure 14 Design and schematic representation of discrete hetero-chromophoric a) heptameric, b) octameric and c) nonameric π-stacks within two mechanically interpenetrated coordination cages bearing organic pillars of different length.[75] Adapted with permission from Ref. [75]. Copyright 2008 American Chemical Society.

In general, afore presented self-assembled coordination cages containing discrete stacks of aromatic molecules inside their cavity were structurally characterized by NMR spectroscopy. Figure 15 shows the well-resolved ^{1}H NMR spectrum of **24** as an example. The integral ratio between the signals of cage protons (highlighted by blue circles) and those of pyrene-4,5-dione units amounts to 1:5 and three sets of pyrene proton signals were found with an integral ratio of 2:2:1. In combination with further 2D NMR experiments, these results give strong evidence for the predicted aggregate structure. Moreover, most of the cages show strong propensity to

crystallize giving the unique opportunity to elucidate the exact structural arrangement of chromophores within the stack by single-crystal X-ray analysis.

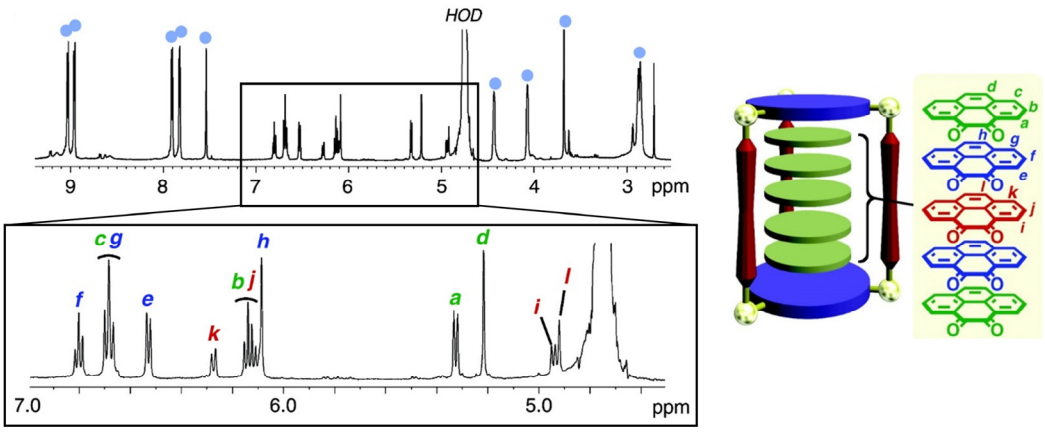

Figure 15 ^{1}H NMR spectrum of **24** accommodating a stack of five pyrene-4,5-dione guest molecules in D_2O and schematic representation of the complex with the assignment of pyrene protons (letters). Signals of cage protons are highlighted by blue circles.[74a] Adapted with permission from Ref. [74a]. Copyright 2010 American Chemical Society.

2.4 Self-Assembly with Sterically Limited Stack Growth

Programming the self-assembly of molecules by their intrinsic structural properties like the bulkiness of substituents at the periphery of the aromatic core constitutes a feasible approach to achieve discrete, finite-sized supramolecular π-stacks. In general, introduction of sterically demanding side-chains leads to a shielding of the π-surfaces and consequently, to suppression of π-π-interactions between molecules due to steric repulsion. Thus, in order to yield a desired supramolecular species of well-defined number of stacked aromatic units, a delicate balance between strongly attractive π-π-interactions and repulsive forces has to be found. In this regard, not only the bulkiness of the attached residues, but also their flexibility and their distance to the aromatic core is a crucial parameter as demonstrated by a series of hexa-*peri*-hexabenzocoronenes (HBCs) that are peripherally substituted by different residues (Figure 16).[77] The large polycyclic aromatic hydrocarbon core of these disc-shaped compounds usually causes self-assembly into infinite one-dimensional columnar aggregates due to strong π-π-interactions. It was shown that introduction of flexible dodecyl side chains in **29a** does not affect the high aggregation tendency. On the contrary, using rigid, dimensionally stable polyphenylene dendrons (**29b**) as peripheral substituents interrupts the stacking to a certain degree, leading to an equilibrium between monomers and discrete dimer

species in 1,1,2,2-tetrachloroethane solution. Further, HBC **29c** exhibiting bulky dendron arms in closer proximity to the aromatic core, does not show any aggregation behaviour, impressively demonstrating the difficult tightrope walk between attractive and repulsive interactions.[77]

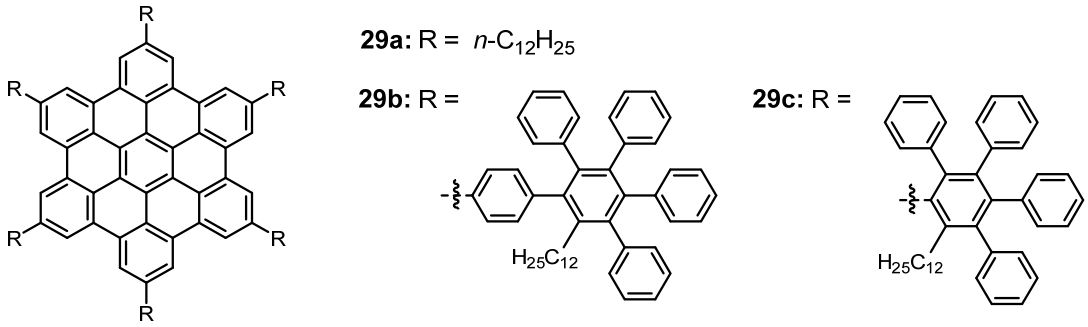

Figure 16 Chemical structure of differently peripherally substituted hexabenzocoronenes **29a-c**.[77]

Introduction of carefully designed bulky substituents can also control the stacking of disc-shaped aromatic macrocycles.[78] In the solid state, isolated hexamer stacks were observed for Pt_4 Schiff base macrocycles equipped with peripheral tris(4-*tert*-butylphenyl)methyl residues (**30a**), whereas extension of the side groups in **30b** increases the steric demand and therefore, affords tetrameric aggregates (Figure 17).[78b]

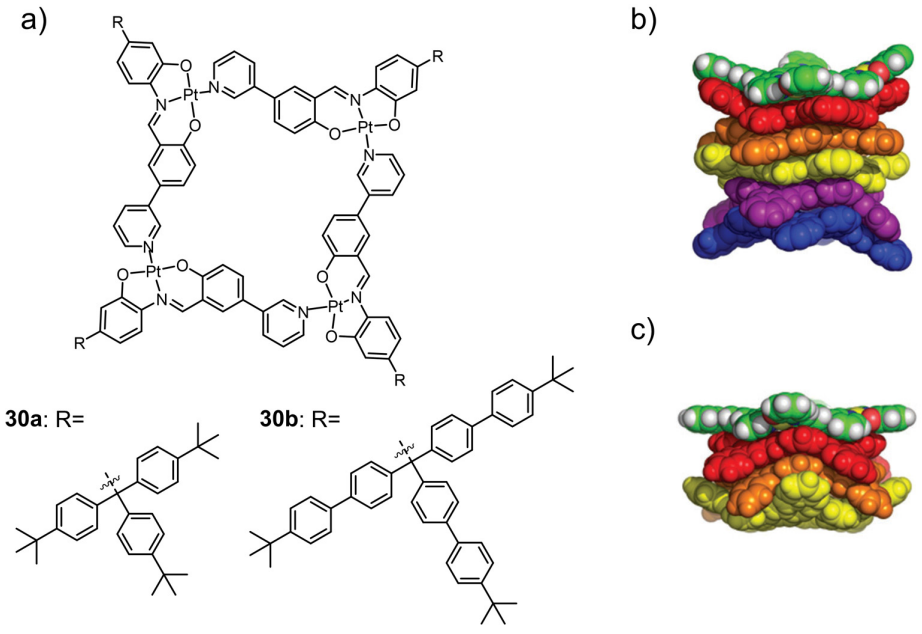

Figure 17 a) Chemical structure of disc-shaped Pt_4 macrocycles **30a** und **30b** with sterically demanding peripheral residues and solid state structure of a discrete b) hexameric stack of **30a** and c) tetrameric stack of **30b** in side view omitting peripheral side chains.[78b] Adapted with permission from Ref. [78b]. Copyright 2012 John Wiley and Sons.

On the contrary, in chloroform solution it was proven by dynamic and static light scattering, variable concentration NMR spectroscopy and transmission electron microscopy experiments that self-assembly of **30a** stops already at discrete dimeric assemblies.[78a] Discrete stacks of the macrocycles larger than dimers could not be detected in solution, which is attributed to rotational motions of the bulky triarylmethyl substituents leading to a high sterical demand.

An exceptionally well-defined finite-sized aggregate in solution based on butadiyne-linked zinc porphyrins (**31**) was reported by the groups of Anderson and Claridge.[79] The assembly consists of exactly three parallel offset strands with face-to-face stacked porphyrins (Figure 18). Careful adjustment of the porphyrin-porphyrin distance in the molecular thread allows effective interdigitation of the bulky aryl side groups, while van der Waals contact between the porphyrins is maximized, strongly favouring the formation of trimer aggregates as pointed out by UV/vis absorption measurements. Thus, the number of stacked molecules is strictly controlled by the need of the substituents to intertwine, as well as by the space between the tethered porphyrin units. Furthermore, the highly defined structure of this assembly and its slow exchange with the monomer species allowed detailed structural characterization by NMR spectroscopy in solution.

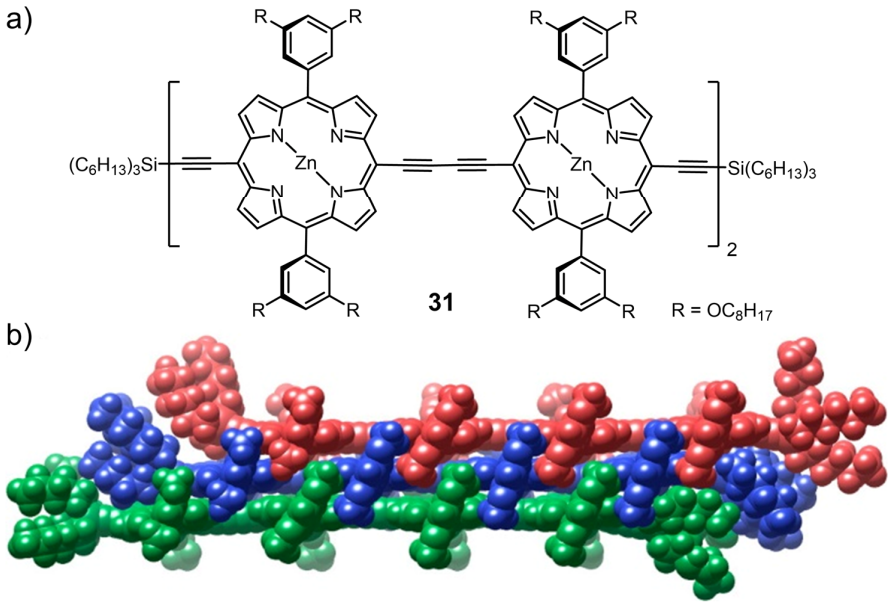

Figure 18 a) Chemical structure of butadiyne-linked zinc porphyrin strand **31** and b) triple-strand aggregate structure of **31** illustrated by a calculated molecular model. Octyl residues were replaced by methoxy groups.[79] Adapted with permission from Ref. [79]. Copyright 2013 American Chemical Society.

In contrast to the ^{1}H NMR spectrum of the monomer (Figure 19a), the aggregate spectrum (Figure 19b) shows a larger number of sharp resonances. The assignment of *β*-pyrrolic (Ha-Hh, red), *para*-aryl (Hi and Hj, blue) and *ortho*-aryl (Hk-Hn, green) protons of the three

different porphyrin strands (A-C) within the assembly was achieved by extensive 2D NMR ^{1}H-^{13}C HSQC (heteronuclear single quantum coherence), ^{1}H-^{29}Si HMBC (heteronuclear multiple bond coherence) and COSY (homonuclear correlation spectroscopy) data analysis. The different chemical shifts of the proton signals in the aggregate spectrum with respect to the ones of the monomer spectrum could be attributed to ring current shielding of some of the protons in the stack and interactions obtained by NOESY measurements as indicated by black double arrows (Figure 19c) are consistent with the proposed aggregate structure. Moreover, the size of the supramolecular species estimated from DOSY studies is in good agreement with an aggregate consisting of two to four strands and finally, small-angle X-ray scattering (SAXS) experiments corroborate the trimeric aggregate structure.

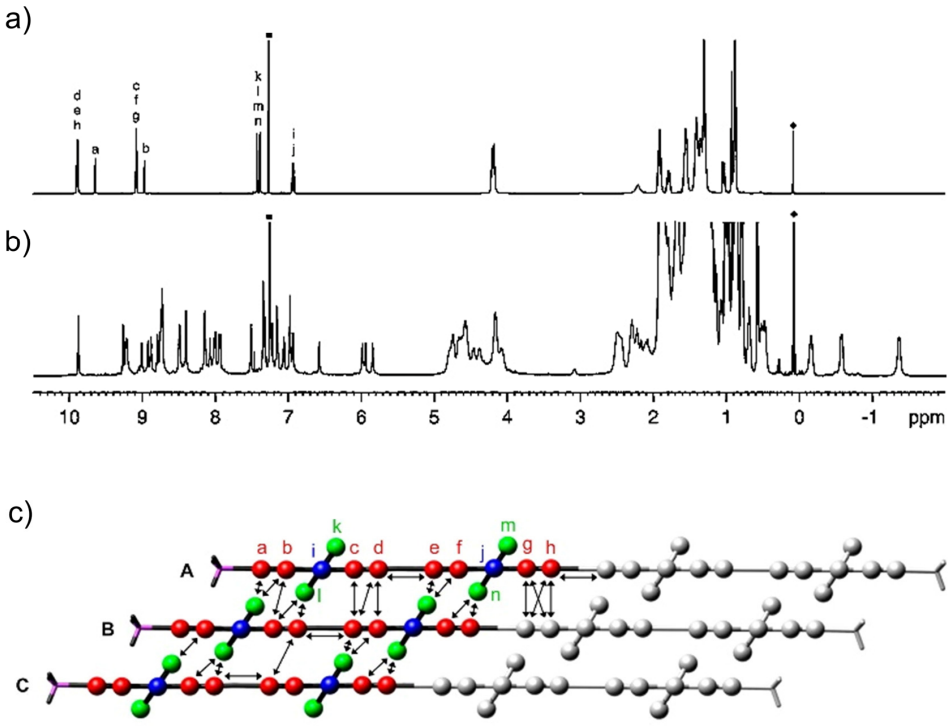

Figure 19 ^{1}H NMR (500 MHz, 298 K) spectra of a) monomeric **31** in $CDCl_3$ with the addition of 1% pyridine-d_5 and b) of the aggregate in $CDCl_3$. c) Structural model of the trimer of **31** with color coding of *β*-pyrrolic (Ha-Hh, red), *para*-aryl (Hi and Hj, blue) and *ortho*-aryl (Hk-Hn, green) protons of three different porphyrin strands A, B and C. Black double arrows indicate NOE interactions obtained by NOESY experiments.[79] Adapted with permission from Ref. [79]. Copyright 2013 American Chemical Society.

Whereas for the previous stacks the number of stacked molecules is not obvious, preferential dimerization is more straightforward to control. Thus, the group of Würthner could realize defined dimer assemblies of PBI dyes by shielding one side of the aromatic core by sterically demanding residues.[80] The unsymmetrical PBI **32** depicted in Figure 20a is equipped with one rigid and one flexible substituent in the imide positions. Here the bulky 2,5-di-*tert*-

butylphenyl group cannot rotate around the C–N bond due to the sterically demanding *tert*-butyl group that shields one side of the perylene plane, whereas the other side is unblocked. The benzyl residue at the second imide position can easily rotate and bend away to enable close contact between the free π-surfaces in a dimer. Out of three possible dimer conformations, only the one exhibiting largest π-π-overlap between the perylene cores is formed as proven by two-dimensional ROESY NMR studies. Further stacking into extended one-dimensional aggregates is blocked by the bulky groups that occupy the exterior π-surfaces of the dimer.[80a] A similar strategy has been utilized by the group of Matile to realize discrete dimers based on NDI dyes.[81] Another efficient way to block one side of the aromatic plane in order to allow exclusively dimerization is to introduce a bridging unit. Chiral macrocyclic PBIs **33a**,**b** (Figure 20b) strapped by oligoethylene glycol chains at the bay positions of the perylene core form homo-chiral dimers enabling fundamental studies on self-recognition and self-discrimination of chiral π-surfaces.[80b, c]

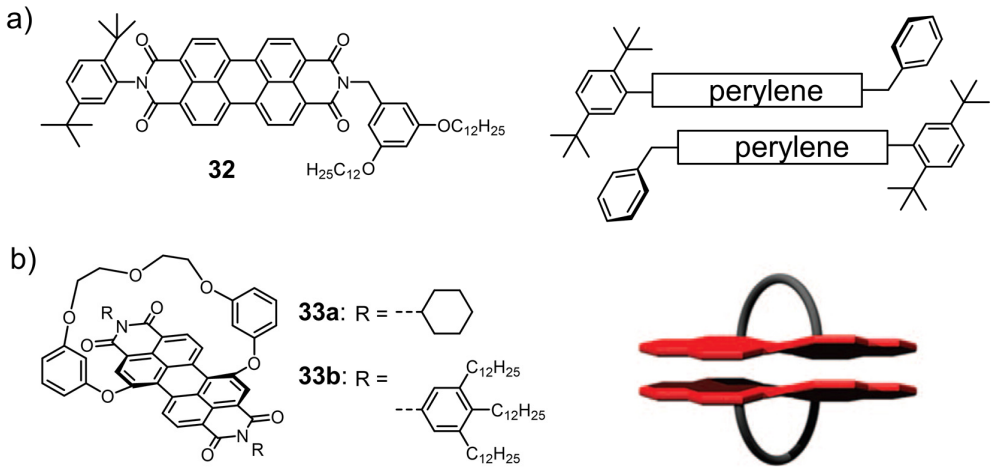

Figure 20 Chemical structures (left) of PBI a) **32** and b) **33a**,**b** and schematic illustration of the discrete dimer aggregates (right).[80a, b] Adapted with permission from Ref. [80a, b]. Copyright 2012 and 2010 John Wiley and Sons.

These examples illustrate that the strategy of controlling the supramolecular stacking of aromatic molecules by the introduction of sterically demanding side chains is so far limited to the formation of rather small stacks. Discrete dimer aggregates can be realized by attaching bulky substituents to the aromatic core shielding one side of the π-surface or by completely blocking it through an oligoethylene glycol loop. However, increasing the number of stacked molecules seems to be more difficult since the ideal balance between attractive π-π-interaction and steric repulsion must be figured out. If the steric demand is too low, extended one-dimensional assemblies are formed, whereas bulky groups being too rigid or too close to the

aromatic core inhibit aggregation at all. Thus, the so far largest discrete π-stack realized by this approach in solution is just a trimer species.

2.5 Self-Assembly of Discrete Dimers Through Dipolar Aggregation

A very simple but nonetheless smart approach to encode the final structure of the self-assembled supramolecular architecture by the properties of the molecular building blocks themselves is to utilize aromatic compounds with large ground state dipole moments. Self-assembly of such chromophores is dominated by strong and highly directional dipole-dipole interactions with only minor contribution from dispersion forces. Thus, in unpolar solvents, the formation of discrete, tightly bound dimers with antiparallel aligned dipole moments is observed. Due to the antiparallel arrangement, the dipole moments of the individual chromophores are totally compensated resulting in an unpolar discrete dimer structure that lacks significant driving force for further stack growth. Hence, the high directionality of dipole-dipole interactions allows accurate prediction of the size and geometry of supramolecular assemblies.

In 2000, the Würthner group for the first time described dimerization of dipolar merocyanine dyes as an opportunity to construct discrete supramolecular motifs with interesting optical and electronic properties.[18b, d] Figure 21 schematically illustrates the aggregation motif of merocyanine dye **34**. The highly dipolar character of this special class of dyes originates from the general structure consisting of a hetero-cyclic donor and an acceptor moiety bridged by a polymethine chain. In this way, push-pull chromophores with dipole moments μ_g larger than 20 D can be realized.[18c, 82]

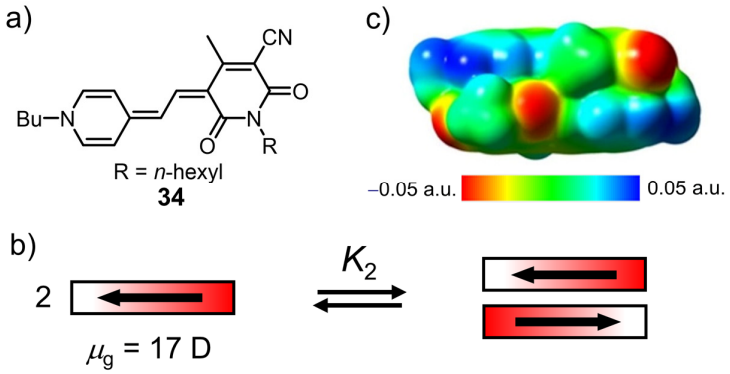

Figure 21 a) Chemical structure of dipolar merocyanine dye **34** and b) self-assembly process into antiparallel dimer aggregates. c) The electrostatic potential map of the dimer complex is depicted as well.[18a, d] Adapted with permission from Ref. [18a]. Copyright 2016 American Chemical Society.

The self-assembly behaviour of the dyes can easily be monitored by concentration-dependent UV/vis absorption studies in unpolar solvents due to their sharp and intense cyanine-like absorption band in the visible region that can be rationalized by a pronounced intramolecular charge-transfer. In Figure 22a the aggregation study of dye **34** in 1,4-dioxane is depicted as an example. At high dilution (c = 1 x 10^{-6} M) the typical monomer band of this class of dyes is observed with an absorption maximum at 569 nm and a weak shoulder at lower wavelength representing the vibronic progressions. As indicated by the black arrows, upon increasing the concentration the intensity of the monomer band drops down, while a new band at lower wavelengths (λ_{max} = 492 nm) appears concomitantly. According to Kasha's exciton theory,[15c, 83] this hypsochromic shift of the absorption can be explained by a splitting of the excited state into a higher and a lower lying exciton state upon coupling of transition dipole moments of the chromophores in the dimer. In an H-type dimer with perfectly antiparallel aligned transition dipole moments, only transition to the higher exciton state is allowed with a high oscillator strength of the respective absorption band.

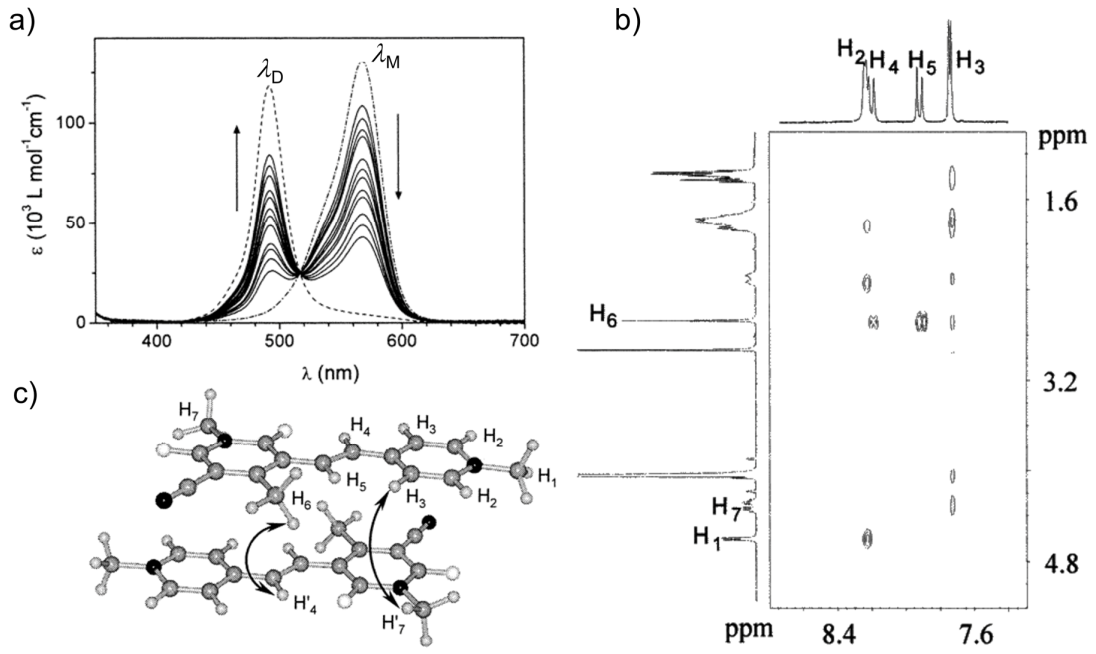

Figure 22 a) Concentration-dependent UV/vis absorption spectra (3 x 10^{-5} – 1 x 10^{-6} M at 298 K) of merocyanine dye **34** in 1,4-dioxane. Spectra of the monomer (M) and dimer (D) depicted in dotted lines were calculated according to the dimerization model.[22c] The arrows indicate spectral changes upon increasing concentration. b) Selected area of the ROESY NMR spectrum of **34** in 1,4-dioxane-d_8 at 300 K (c = 5 x 10^{-3} M) and c) illustration of close spatial proximity between protons in the dimer (indicated by black double arrows) on the basis of a geometry-optimized (AM1) structural dimer model as evidenced by ROESY cross-peaks.[18d] Adapted with permission from Ref. [18d]. Copyright 2002 American Chemical Society.

In contrast, the transition to the lower exciton state is forbidden due to the out-of-phase coupling of the transition dipole moments of the individual chromophores. Thus, the absorption band is shifted to higher energy compared to the monomer absorption band. Furthermore, a well-defined isosbestic point corroborates the existence of a thermodynamic equilibrium between two distinct species, *i.e.* the monomer and the dimer. This monomer-dimer equilibrium was confirmed by successfully fitting the experimental UV/vis data with a dimerization model.

NMR spectroscopy represents a useful characterization method to elucidate the exact structural arrangement of the chromophores in a merocyanine dimer, since aggregate formation appears at a concentration regime suitable for this spectroscopic technique. Besides, strong binding forces and the unique directionality of the dipole-dipole interactions are highly beneficial to achieve a slow exchange between monomer and dimer on the NMR time scale yielding well-resolved spectra with sharp signals. Cross-peaks between proton signals of $H_4^{'}$ and H_6 and between H_3 and $H_7^{'}$ in ROESY experiments in 1,4-dioxane-d_8 (Figure 22b) revealed close spatial proximity between these protons, which can definitely be attributed to intermolecular through space coupling since these cross-signals are not observed in $CDCl_3$, a solvent of intermediate polarity that shifts the equilibrium towards the monomeric species. Thus, two-dimensional NMR spectroscopy provides strong evidence for a centrosymmetric dimer structure with antiparallel orientation of the chromophores, which is in good agreement with the AM1 geometry-optimized model (Figure 22c). Finally, single-crystal X-ray analysis showed a densely packed dimer synthon in the solid state with an interplanar distance of 3.5 Å, whose structure perfectly coincides with the spectroscopic results. Dimerization in unpolar solvents has been observed for a broad variety of different merocyanine dyes and systematic aggregation studies provided a fundamental understanding in the relationship between molecular structure and aggregation behaviour.[18d] As expected, with increasing dipole moment and length of the π-conjugated system the dimerization constant K_2 increases, whereas it decreases upon introduction of bulky substituents to the aromatic core. Moreover, a bent shape of the chromophore reduces efficient π-π-overlap in the dimeric structure leading to decreased binding strength.

To date, a great library of merocyanine dyes has been established providing building blocks to generate finite-sized supramolecular structures with tailored properties. Although the strategy to create finite-sized assemblies by dipolar aggregation appears to be limited to dimer aggregates for simple merocyanines, construction of larger but still finite supramolecular

motifs is feasible by covalent linking of chromophores, as it will be discussed in the following section.

2.6 Backbone-Directed Folding of Covalently Linked Chromophores

The backbone-directed intramolecular stacking of aromatic moieties into discrete finite-sized π-stacks constitutes a combined covalent and supramolecular approach. Chromophores can be covalently tethered by a flexible scaffold leading to a preorganization, which enables efficient π-π-stacking by intramolecular folding even in dilute solution. Hence, control over the number of stacked units is determined by the beforehand synthesized molecular backbone. Despite high synthetic costs, this foldamer approach provides access to functional supramolecular architectures with highly defined structure and size similar to natural proteins.[48a, 84] Initially, the term "foldamer" was introduced by the scientific community working on synthetic biomimetic polymers.[85] But also in supramolecular chemistry with focus on dye aggregates, folding of molecules containing aromatic subunits connected by a linker moiety became a common approach to create discrete bi- and multichromophoric arrays. The first intramolecular interaction between two tethered π-conjugated systems was probably observed in the 1960s.[86] Hirayama performed fluorescence studies on a series of diphenylalkanes with different length of the aliphatic tether unit.[86b] Excimer emission due to intramolecular interactions between the phenyl rings in cyclohexane solution was only found in those systems, in which the phenyl groups are linked by a chain of three methylene groups. Similar results have been reported by Klöpffer, who observed excimer emission in 1,3-biscarbazolylpropane leading to the so-called "n = 3 rule".[87] This rule means that the linker requires a length of exactly three sp^3 carbons to ensure a parallel sandwich-type geometry with efficient π-overlap between the chromophores. The statement was confirmed by intramolecular excimer formation of many aromatic systems like naphthalenes, anthracenes and carbazoles.[88] One example of a bis(pyrene) is depicted in Figure 23.[89]

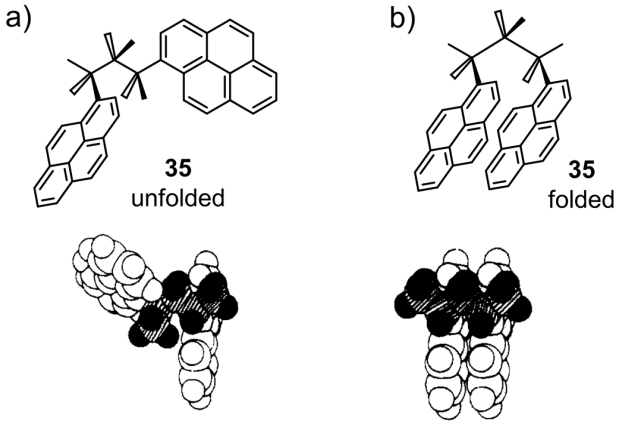

Figure 23 Chemical structure (top) and space filling model (bottom) of *meso*-2,4-diarylpentane (**35**) in a) unfolded and b) folded conformation.[89] Adapted with permission from Ref. [89]. Copyright 1987 American Chemical Society.

The substantial impact of the tether unit on the formation of discrete dimer stacks of merocyanine dyes upon intramolecular folding has intensively been studied by the group of Würthner.[18a, 19g, 90] A broad series of bis(merocyanine) dyes (**36a-h**) bearing two amino-thienyl dioxocyano-pyridine (ATOP) chromophores tethered by different spacer units (Figure 24a) was synthesized and the folding behaviour was analysed by solvent-dependent UV/vis spectroscopy.[19g]

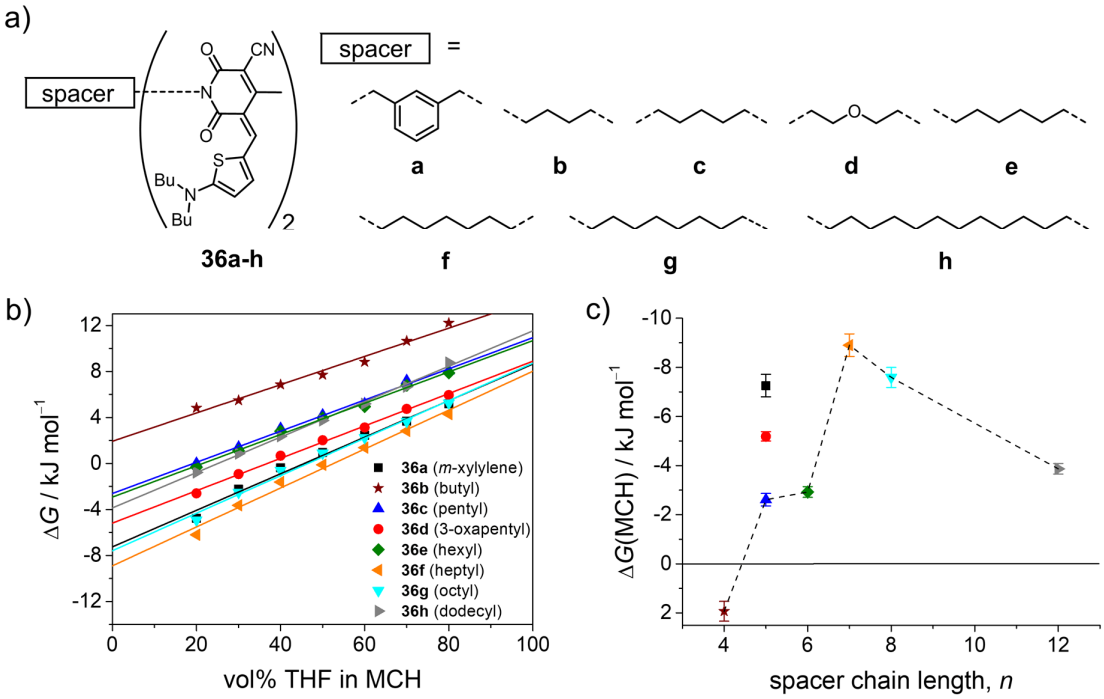

Figure 24 a) Chemical structure of bis(merocyanine) foldamers **36a-h** bearing different spacer units. b) Plot of the free energy changes ΔG of the folding process of dyes **36a-h** as a function of solvent composition (tetrahydrofuran (THF)/methylcyclohexane (MCH)) and c) plot of calculated ΔG in pure MCH as a function of the number of linking carbon atoms.[19g] Adapted with permission from Ref. [19g]. Copyright 2015 John Wiley and Sons.

Comparison of the free energy changes Δ*G* of these dyes upon folding revealed a more complex situation as suggested by the previous example of bis(pyrenes). Thus, the folding tendency of bis(merocyanine) dyes, in which the two dipolar chromophores are connected by alkyl chains, considerably increases with increasing chain length from C4 to C7 (Figure 24b,c) and for tether units larger than C7, the folding tendency drops only slightly. These results could be rationalized by the quantification of the rotational displacement angle between the chromophores in the folded state, where the most favoured antiparallel alignment was only enabled by spacer lengths of ≥ C7. Further increase of the chain length leads however, to reduced preorganization, resulting in a decreased association strength. In contrast, the C4 spacer is too short to allow significant interaction between the chromophores in an intramolecular folded conformation and therefore, the molecule stays in an open conformation. Thus, it can be concluded that the C3 chain provides only the ideal linker length to realize discrete tightly stacked chromophores by the foldamer approach when dispersion forces prevail. For dipolar chromophores like merocyanine dyes, whose preferred antiparallel orientation in a dimer stack interferes with such a backfolding with parallel dipole orientation, significantly longer tether units are needed. Studies on similar merocyanine dyes tethered by alkyl chains of variable length reported by the group of Whitten coincide with these observations.[91]

To address the influence of the nature of the tether unit on the folding behaviour of bis(merocyanine) dyes, Δ*G* values of compounds **36a**,**c** and **d** comprising different spacer units with five linking atoms were compared. Amongst these systems, compound (**36a**) bearing a *meta*-xylylene spacer showed the highest folding tendency, which is attributed to the better preorganization due to the reduced number of freely rotatable bonds in the C5-linker. Since the number of freely rotatable bonds in **36c** and **36d** is equal, the higher folding tendency of **36d** must originate from the higher flexibility of the 3-oxapentyl chain compared to the all-*trans* preferring pentyl linker. The geometry-optimized structure of bis(merocyanine) **36a** and the ROESY cross-peaks between corresponding protons of different chromophores in the folded state clearly demonstrate that the dyes are not perfectly antiparallel aligned (Figure 25c).[90] This rotational displacement of 34° leads to incomplete annihilation of the dipole moments of the individual chromophores, which may contribute to the driving force towards further intermolecular aggregation of the folded species into extended H-stacks with a strongly hypsochromic shifted absorption band. The extended aggregates could be employed in bulk hetero-junction solar cells affording a significant improvement of photocurrent generation.[90]

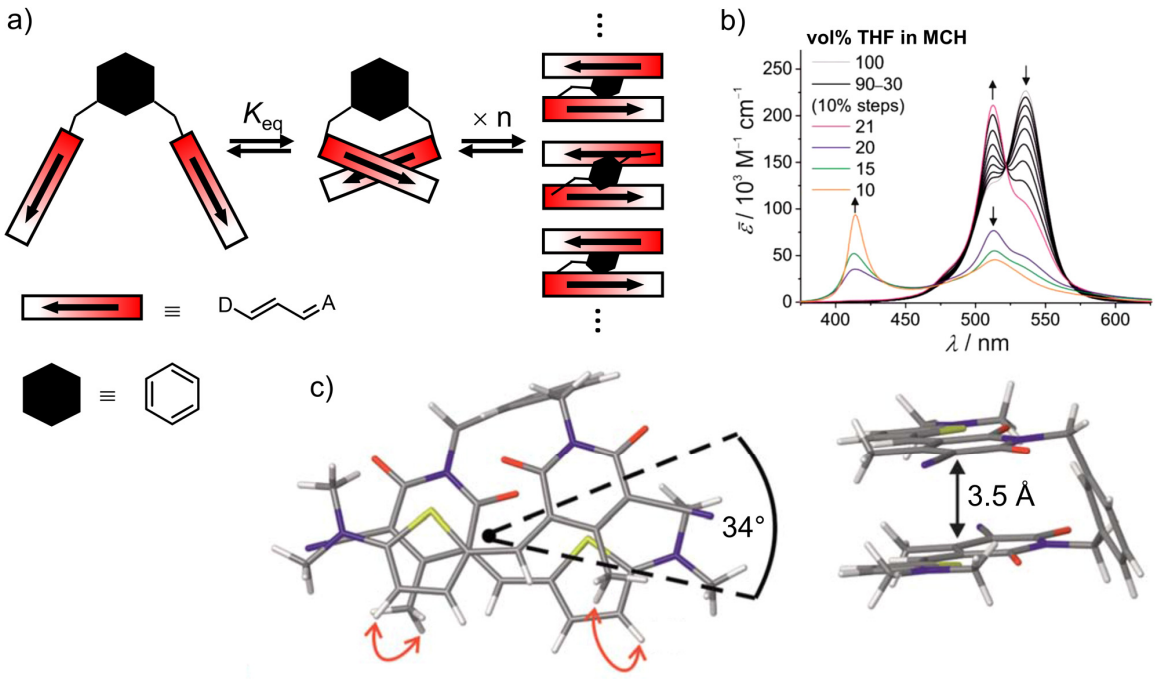

Figure 25 a) Schematic representation of the folding process of bis(merocyanine) dye **36a** and subsequent supramolecular polymerization into extended H-type aggregates. b) Solvent-dependent UV/vis absorption spectra of **36a** in different THF/MCH mixtures at 5 x 10^{-6} M. Arrows indicate spectral changes upon decreasing solvent polarity. c) Geometry-optimized structure of folded **36a** in top view (left) and side view (right). Butyl residues are replaced by methyl groups and the red double arrows indicate close spatial proximity between protons according to cross-peaks observed by ROESY experiments.[90] Adapted from Ref. [90] with permission from The Royal Society of Chemistry. Copyright 2013 The Royal Society of Chemistry.

In contrast to the flexible linker shown above, a rather rigid calix[4]arene spacer unit was used to link two PBI dyes in order to generate discrete PBI-dimer stacks upon intramolecular folding (Figure 26).[92] Indeed, the bichromophoric molecule (**37**) shows an equilibrium between an open conformation without any interaction between the PBI units and a conformation in which the dyes adopt a π-stacked sandwich-type orientation. UV/vis absorption measurements in solvents of different polarity revealed the dependence of this equilibrium on solvent polarity. Hence, in polar solvents the spectra show characteristic absorption bands of independent chromophores in the open conformation, whereas spectral features in unpolar solvents are indicative of pronounced interactions between the aromatic systems suggesting a folded state. ^{1}H NMR studies give additional evidence for the folding behaviour since the doublets corresponding to the Ar-CH_2-Ar protons of the calix[4]arene unit broaden significantly in unpolar solvents indicating molecular motion on the NMR timescale. The so-formed discrete PBI dimer stack constitutes a model system to quantitatively study excited state properties and decay behaviour of two π-stacked PBI chromophores.

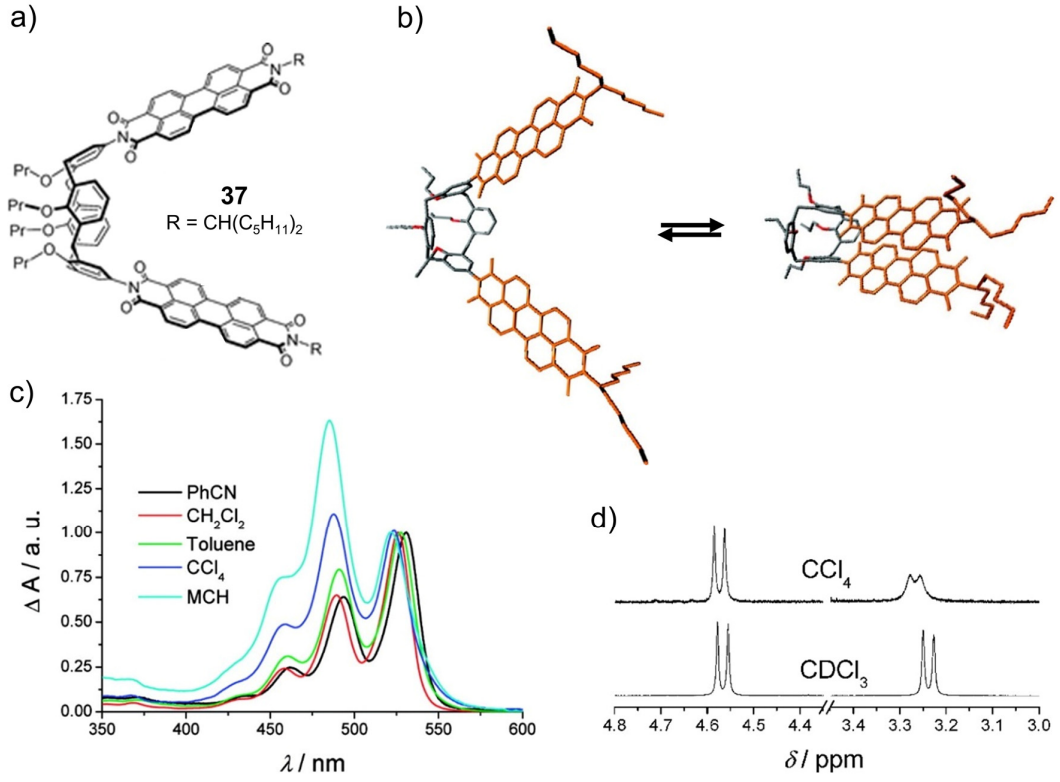

Figure 26 a) Chemical structure of bis(PBI) **37** bearing a calix[4]arene spacer unit and b) illustration of the equilibrium between open and pinched cone conformation with π-π-interactions between the PBI units based on a force-field calculated molecular model. c) Normalized UV/vis absorption spectra of **37** in different solvents at room temperature and d) relevant sections of 600 MHz ^{1}H NMR spectra of **37** in CCl_4 (top) and $CDCl_3$ (bottom) at room temperature showing resonances of the Ar-CH_2-Ar protons.[92] Adapted with permission from Ref. [92]. Copyright 2008 American Chemical Society.

In order to create discrete stacks of more than two aromatic units by applying the foldamer approach, two structural motifs are possible. Either the chromophores have to be aligned by a flexible linker like pearls on a chain or the linker has to offer possibilities to anchor multiple chromophores in a way that enables intramolecular interactions between the π-systems (Figure 3) as it is nicely demonstrated by single stranded RNA and DNA.

The former approach is adequately demonstrated by Janssen and coworkers.[93] They prepared linear oligomers (**38**, Figure 27) containing alternating segments of up to four PBI chromophores and flexible polybutylene glycol chains. In this system, the covalent linkage brings the dye units in close proximity resulting in a folding of the polymer into cofacially stacked chromophores driven by π-π-interactions in *ortho*-dichlorobenzene as evident from the hypsochromically shifted absorption maximum. As expected, the length of the linker chain plays an important role with regard to the strength of the intramolecular interactions. Thus, folding tendency increases with decreasing chain length due to the better preorganization of the chromophores.

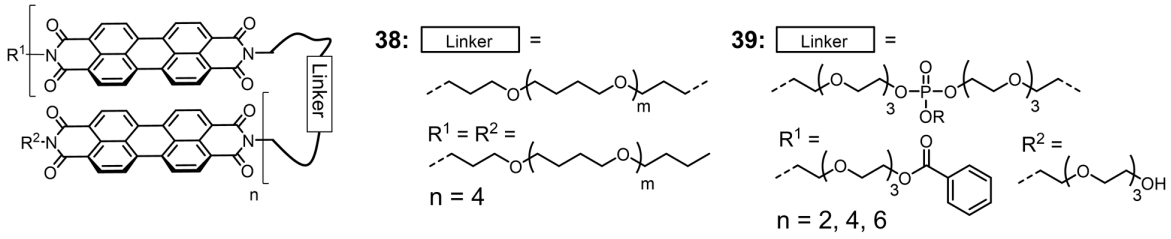

Figure 27 Chemical structure of PBI foldamers **38** and **39**.[93]

A structurally related system has been reported by the group of Li (**39**, Figure 27).[94] The linear oligomers consist of a distinct number of up to six PBI chromophores connected by flexible ethylene glycol chains that enable intramolecular folding into well-defined discrete π-stacks. The proposed H-type stacked geometry of the chromophores in the folded state was deduced from the hypsochromic shift of the absorption maximum and by the pronounced upfield shift of the perylene proton resonances of the oligomer in the ^{1}H NMR spectrum compared to those of the single reference chromophore.

Polymers comprising conjugated oligomers of bis(2-ethylhexyl)-*p*-phenylene vinylene tethered by flexible *n*-decyl or tetraethylene glycol chains demonstrate that by increasing the size of the adjacent chromophores, enhanced π-π-interactions strengthen the folding tendency and result in higher structural order in the intramolecular pleated conformation.[95]

Although a multitude of aromatic oligoamides of the Huc group form amazingly well-defined folded structures through intramolecular hydrogen bonding and π-π-stacking,[3, 85b, 96] these discrete helical structures cannot be considered as classical π-stacks and therefore will not be reviewed here. However, the group is also working on artificial *β*-sheet foldamers and these systems indeed exhibit discrete stacks of up to five linear aromatic segments (**40**, Figure 28). Rigid 4,6-dinitro-1,3-phenylenediamine turn units, *i.e.* again five atom connections, were used to tether dibutoxy- and dimethoxy-terephthalamides. The sheet-like folding based on π-π-stacking in organic solvents was evidenced by a series of NMR experiments (HSQC, HMBC, ROESY). Furthermore, the folded structure of **40** could be verified by single-crystal X-ray analysis.[97]

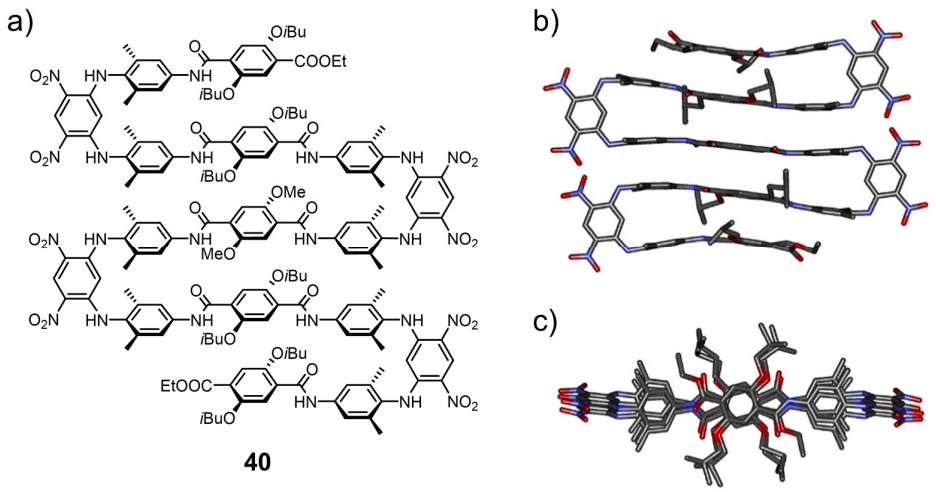

Figure 28 a) Chemical structure of aromatic *β*-sheet foldamer **40** and b) side and c) top view of the crystal structure of **40**. Hydrogen atoms and solvent molecules were omitted.[97a] Adapted with permission from Ref. [97a]. Copyright 2014 American Chemical Society.

The foldamer approach was also utilized to create discrete hetero-chromophoric stacks of up to six alternating electron-rich and electron-deficient aromatic units. Already in 1995 Iverson and coworkers reported on 1,5-dialkoxynaphthalene and 1,4,5,8-naphthalenetetracarboxylic diimide (NDI) containing synthetic oligomers (Figure 29).[98] To ensure distinct tendency of folding into pleated donor-acceptor structures with parallel stacked chromophores, *L*-aspartic acid has been figured out as ideal tether unit based on a X-ray structure of NDI-dialkoxynaphthalene co-crystals. Spectroscopic evidence for an intramolecularly folded structure in aqueous solution was deduced from a broad charge-transfer band in the UV/vis absorption spectrum that is independent of concentration. Finally, the structure of the folded species was elucidated in detail by NMR spectroscopy. The change of chemical shifts of the diimide hydrogen signals is in accordance with a modified electronic environment upon stacking of the aromatic groups and the diastereotopic character of the backbone methylene protons displays restricted rotation on the NMR timescale. Additionally, close spatial proximity between protons of adjacent chromophores was detected by ROESY experiments.

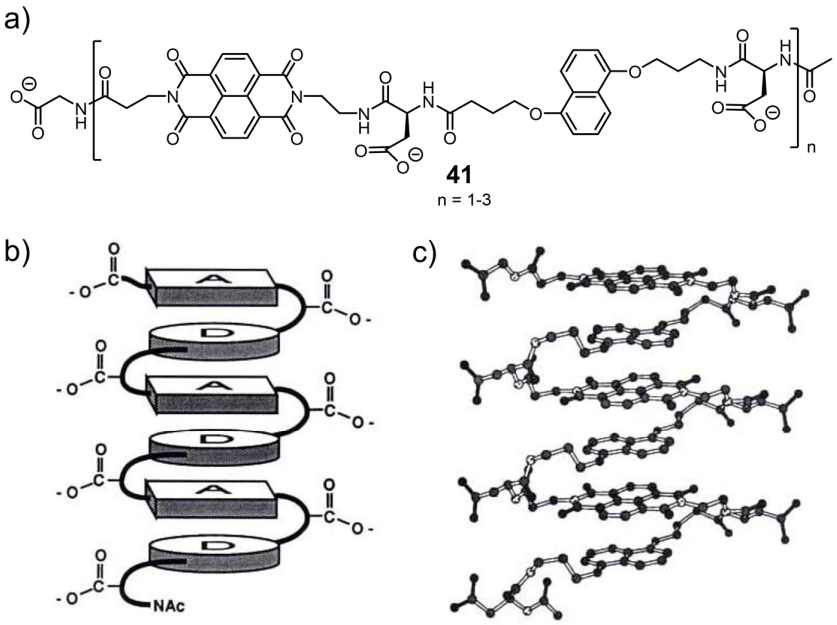

Figure 29 a) Chemical structure of oligomer **41** containing alternating 1,5-dialkoxynaphthalene and 1,4,5,8-naphthalenetetracarboxylic diimide units and folded conformation of **41** represented b) schematically and c) according to a calculated structural model.[98] Adapted with permission from Ref. [98]. Copyright 1995 Nature Publishing Group.

To increase the propensity of folding, Ramakrishnan and Ghosh introduced an additional supramolecular binding motif to the backbone of a similar donor-acceptor system that assists the formation of intramolecular pleated structures upon addition of metal ions (Figure 30).[99]

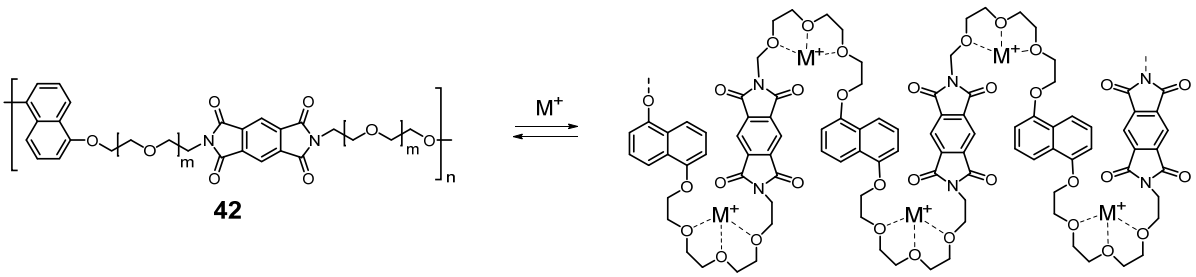

Figure 30 Chemical structure and folding process of oligomer **42** upon addition of metal ions (M^+).[99a]

Hence, discrete and highly stable stacks of up to ten alternating electron-rich and electron-poor aromatic units became accessible in chloroform solution as proven by UV/vis and NMR studies.

The second approach pointed out in Figure 3 to create discrete stacks with well-defined number of aromatic moieties by anchoring to a backbone is illustrated by the prominent example of single stranded RNA and DNA. In these natural structures, the sugar-phosphate backbone preorganizes the attached nucleobases and folds upon π-π-stacking interactions between the aromatic cores. Thus, the scaffold accomplishes perfect balance between flexibility on the one

hand to enable folding and rigidity on the other hand to preorganize the π-systems, allowing strong intramolecular interactions. This general structural motif from nature has been copied to create synthetic dye stacks as summarized in Figure 31.

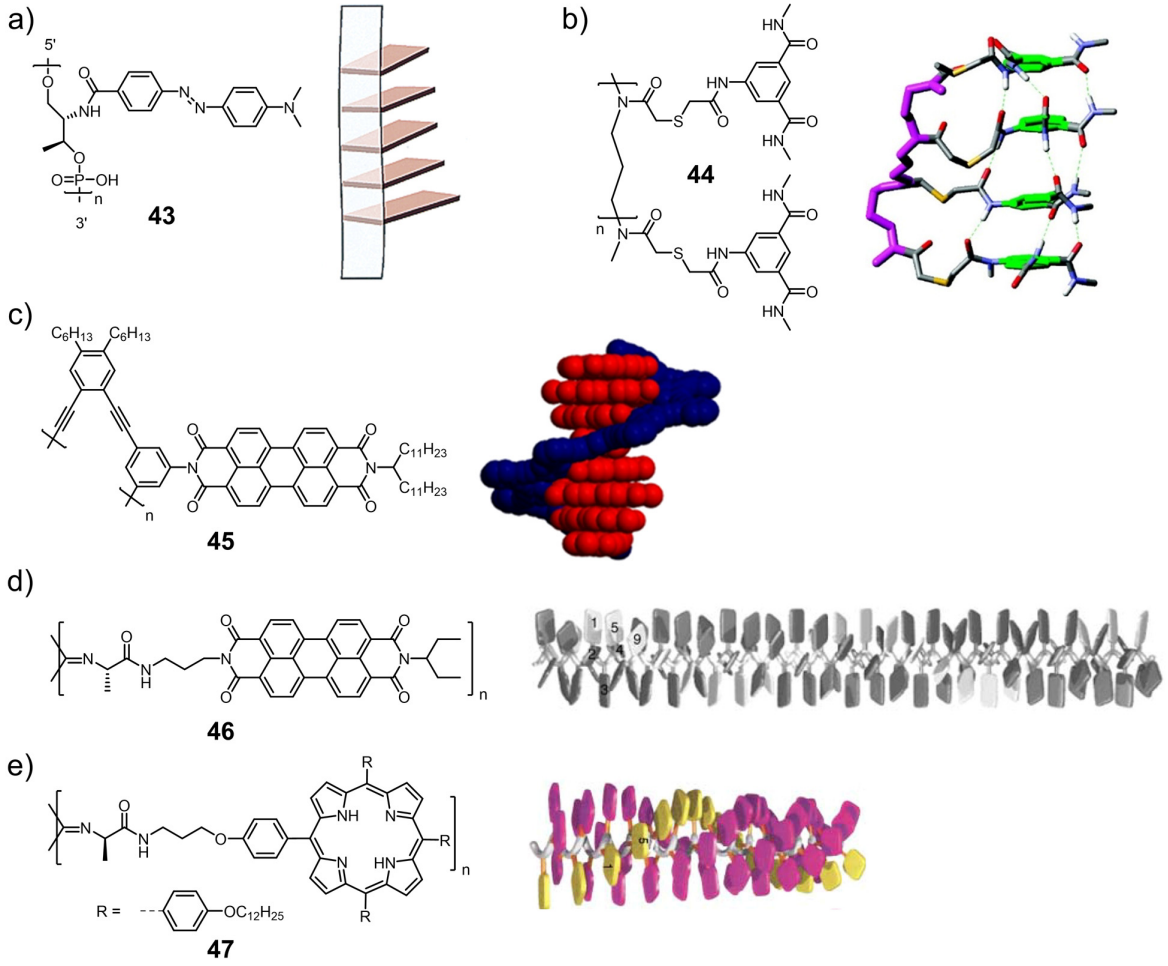

Figure 31 Chemical structure (left) and folded structure (right) of a) methyl red (**43**),[100] b) benzenetricarboxamide (**44**),[101] c,d) PBI chromophore (**45**, **46**)[102] and e) porphyrin (**47**)[103] containing oligomeric backbones illustrated by calculated structural models (b,c) or by schematic drawings (a,d,e). Adapted with permission from Ref. [100-103]. Copyright 2003/2004 John Wiley and Sons. Copyright 2011 The Royal Society of Chemistry. Copyright 2003/2011 American Chemical Society.

In contrast to the template approach discussed in section 2.3.1, the aromatic units are covalently attached to a linear backbone providing control over the number of stacked chromophores. In this way, methyl red aggregates with predetermined number of stacked chromophores were realized by Asanuma and coworkers (Figure 31a).[100] Therefore, one to six methyl red units were sequentially introduced into a DNA strand by incorporating the respective phosphoramidite monomer in the DNA synthesis. The UV/vis spectra of various DNA conjugates show pronounced hypsochromically shifted and narrowed absorption bands

providing evidence of an H-type stacked arrangement of the dye moieties. Similar systems with multiple chromophores embedded within oligonucleotide sequences were realized by Wagenknecht and Häner.[104]

Discrete stacks of four disc-shaped benzenetricarboxamides (Figure 31b) were prepared by attaching the aromatic units to a preformed flexible oligoamine chain consisting of $–NH(CH_2)_3–$ sequences.[101] Intramolecular hydrogen bonding between the stacked moieties in chloroform solution was identified by ^1H NMR spectroscopy and the predicted folded conformation was studied by computational modelling. Furthermore, the existence of intermolecularly aggregated species could be excluded by vapour pressure osmometry and introduction of chiral side groups enabled probing of the folded conformation consisting of helically arranged benzenetricarboximide units by CD spectroscopy.

The foldamer concept has also been applied to create finite-sized stacks of PBI dyes as well (Figure 31c).[102a] Besides of smaller discrete systems bearing two or three PBIs[105] also polydisperse systems with about eight chromophores attached to a rigid foldable diphenylene ethynylene backbone were investigated. They all showed intramolecular folding driven by π-π-interactions between the PBI units in unpolar solvents, as proven by UV/vis absorption and fluorescence emission studies. Hence, the rigid scaffold enforces a highly ordered staircase-like folded geometry with a well-defined π-stack of PBI chromophores. Although the synthetic pathway including co-polymerization by Sonogashira cross-coupling of the functionalized PBI units with 1,2-diethynyl-4,5-dihexylbenzene yielded the large target molecule with a sharp size distribution as indicated by the very small index of polydispersity, the synthetic costs are tremendous.

In contrast, synthetic route towards well-defined extremely long arrays of PBIs (Figure 31d) or porphyrins (Figure 31e) anchored to a polyisocyanide scaffold is more straightforward.[102b, 103, 106] The resulting polymer strands exhibit an overall length of 87 nm and presumably consist of four columns of approximately 200 face-to-face stacked chromophores running parallel to the rigid polymer backbone. H-type coupling interactions between aromatic units in the polymer were revealed by the blue-shifted band in the UV/vis absorption spectra compared to the absorption of the respective monomeric dye. However, preparation of the PBI or perylene polymer fibres by polymerization of monoisocyanopeptide functionalized chromophores leads to polydisperse structures, whose average molecular weight and length can only be estimated from AFM images and light scattering techniques. Consequently, this example constitutes a rather inappropriate system to create discrete stacks with accurately defined number of chromophores.

2.7 Backbone-Directed Intermolecular Self-Assembly of Tweezer-Type Molecules and Triple π-Stacks by the Encapsulation of Aromatic Guests

As the name suggests, a molecular tweezer, also called clip or cleft, consists of two aromatic pincers that are connected by a rigid tether unit. The spacer keeps the aromatic sidewalls at a distinct interplanar distance inhibiting intramolecular self-association as in the examples of the previous section and instead providing an open cavity for binding aromatic guests by dispersion or donor-acceptor interactions. Thus, encapsulation of aromatic molecules between the parallel pincers in a sandwich-type manner provides access to discrete π-stacks of three aromatic moieties. Already in 1978, Chen and Whitlock described the first molecular tweezer in a pioneering study in the field of supramolecular chemistry (Figure 32).[107]

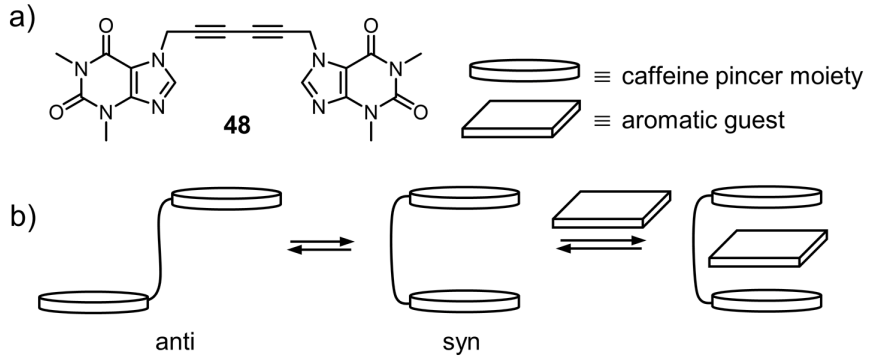

Figure 32 a) Chemical structure of the first molecular tweezer **48** and b) schematic representation of the complexation process of aromatic molecules between the caffeine planes of **48** in the syn conformation.[107] Adapted with permission from Ref. [107]. Copyright 1978 American Chemical Society.

Two caffeine chromophores were tethered by a diyne spacer unit that establishes an ideal interplanar distance of around 7 Å in the syn conformation to bind a huge variety of small aromatic guest molecules between the pincer planes *via* strong π-π-interactions at short van der Waals distance. To show one more example of this special type of host-guest-complexation, Figure 33 depicts the Zimmerman tweezer **49**, which was prepared by attaching two acridine chromophores to a dibenz[*c*,*h*]acridine linker.[108] The rigid backbone enforces a syn cofacial orientation of the aromatic planes at 7 Å interplanar distance and therefore, provides ideal preorganization for high affinity towards 2,4,7-trinitrofluorene (**50**) in organic solvents driven by donor-acceptor interactions. Evidence for the strong binding behaviour was found by considerable shifts of proton resonances in NMR titration experiments and analysis of the experimental data by nonlinear least-square curve-fitting method verified association constants up to 700 M^{-1} in chloroform.

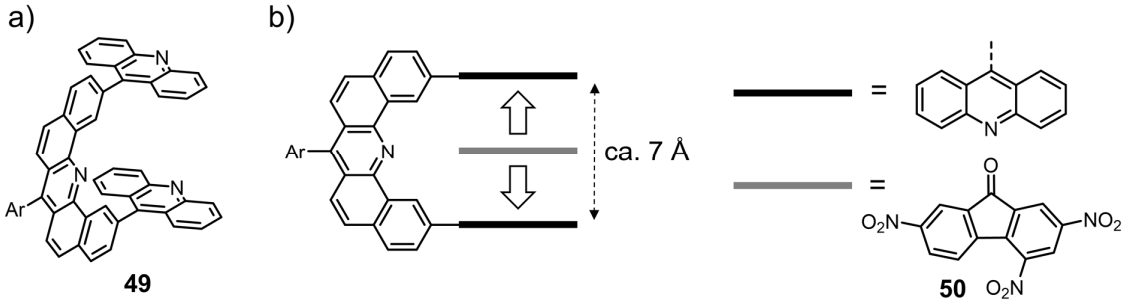

Figure 33 a) Chemical structure of tweezer **49** consisting of two acridine chromophores attached to a rigid dibenz[*c,h*]acridine backbone and b) schematic illustration of its complex with 2,4,7-trinitrofluorene (**50**).[108] Adapted with permission from Ref. [108]. Copyright 1989 American Chemical Society.

Based on this general structural motif, a huge number of tweezer-type architectures containing different aromatic pincer moieties and rigid or flexible spacers were developed and their behaviour of binding aromatic guest molecules was investigated.[109] Moreover, molecular tweezers bearing rigid scaffolds and a suitable distance between the planes of adjacent chromophores can undergo strong intermolecular self-recognition forming interdigitated dimers through mutual π-π-interactions. This approach represents a viable strategy to realize discrete π-stacks composed of four aromatic units. Hence, it is quite astonishing that until today only few examples of self-associating tweezer molecules are reported in the literature.

One of the first tweezer-type molecules showing self-assembly in solution is the glycoluril based system depicted in Figure 34a.[110] The glycoluril scaffold, which was introduced by Nolte *et al*.,[111] provides a U-shaped cavity, whose size can be varied by attaching different aromatic side walls. Besides the ability to encapsulate aromatic guests like phenols, dihydroxybenzene or dihydroxynaphthalene, Isaacs *et al*. observed the formation of self-associated dimers of the clip-shaped molecule **51** in chloroform solution (Figure 34c).[110] The high kinetic and thermodynamic stability of the dimeric aggregates can be attributed to the combination of hydrogen bonding and π-π-interactions between four aromatic rings, as indicated by ^{1}H NMR aggregation studies. Clear evidence for the dimer structure was deduced from X-ray crystal analysis showing interlocked glycoluril tweezer dimers (Figure 34b).

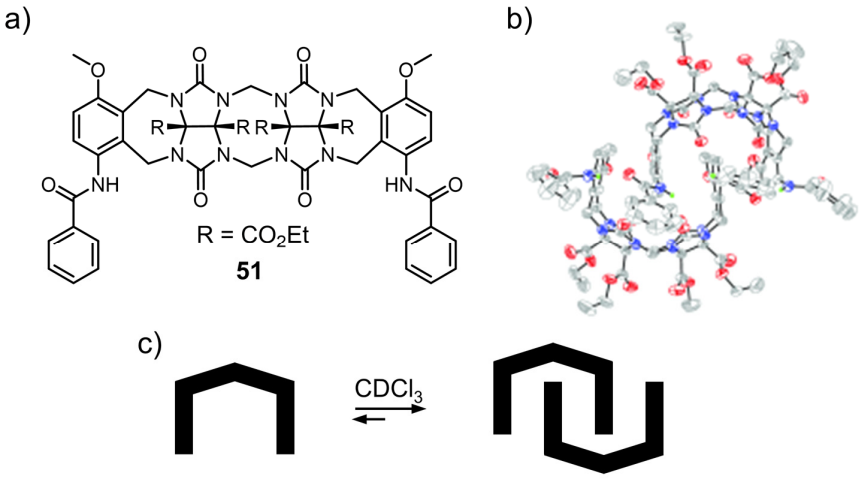

Figure 34 a) Chemical structure of glycoluril based tweezer **51** and b) ORTEP (oak ridge thermal ellipsoid plot) drawing of the single-crystal X-ray structure of **51** showing the interdigitated dimer. Solvent molecules and hydrogen atoms have been omitted for clarity. c) Schematic representation of the self-assembly process of **51** into bimolecular complexes in $CDCl_3$ solution.[110a] Adapted with permission from Ref. [110a]. Copyright 2002 John Wiley and Sons.

The self-assembly of bis(merocyanine) tweezers in solution reported by the Würthner group[20] constitutes another example for the formation of discrete supramolecular stacks supported by a backbone. In 2009 it has been described for the first time that by attaching two dipolar merocyanine chromophores to a 2,7-naphthalenedimethylene or 4,4'-dimethylenediphenyl-methane backbone tightly bound quadruple π-stacks are created from tweezer-type molecules (Figure 35a).[20b]

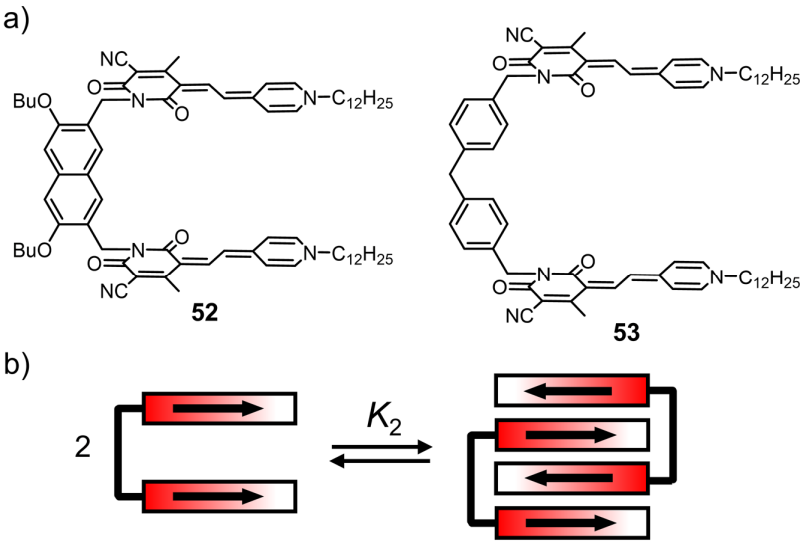

Figure 35 a) Chemical structure of 2,7-naphthalenedimethylene (**52**, left) and 4,4'-dimethylene-diphenylmethane (**53**, right) spacer bearing bis(merocyanine) tweezers and b) schematic representation of the self-assembly process of **52** and **53** into bimolecular complexes with a stack of four antiparallel chromophores.[20b]

In chloroform solution, these molecular tweezers are in thermodynamic equilibrium with a sandwich-type bimolecular complex exhibiting a discrete stack of four antiparallel aligned chromophores (Figure 35b). The former spacer bears a rigid scaffold leading to a distance of around 7 Å between the planes of the two connected chromophores, which is twice the ideal van der Waals distance found in the crystal structures of π-stacked molecules. Therefore, the merocyanine chromophores are ideally preorganized to self-assemble driven by strong dipole-dipole interactions into tightly packed aggregates with high binding constants of $> 10^9$ M^{-1} in chloroform as determined by concentration-dependent UV/vis absorption studies.

In contrast, the 4,4'-dimethylenediphenylmethane spacer is more flexible due to a larger number of rotational degrees of freedom and furthermore shows a larger interplanar distance of around 9 Å, which is reflected by a considerably decreased association constant (2 x 10^6 M^{-1} in chloroform). A comparison of the dimerization constants K_2 of both systems clearly points out the crucial aspect of the choice of the right spacer length and flexibility. In addition to aggregation studies by UV/vis absorption measurements, MALDI-TOF mass spectrometry provided further evidence for a dimerization of bis(merocyanines) **52** and **53**. Besides the peak corresponding to the single-charged monomer, also the mass peak of the single-charged dimer was detected. The exact structure of the dimer aggregate was investigated by detailed NMR spectroscopy studies (Figure 36).

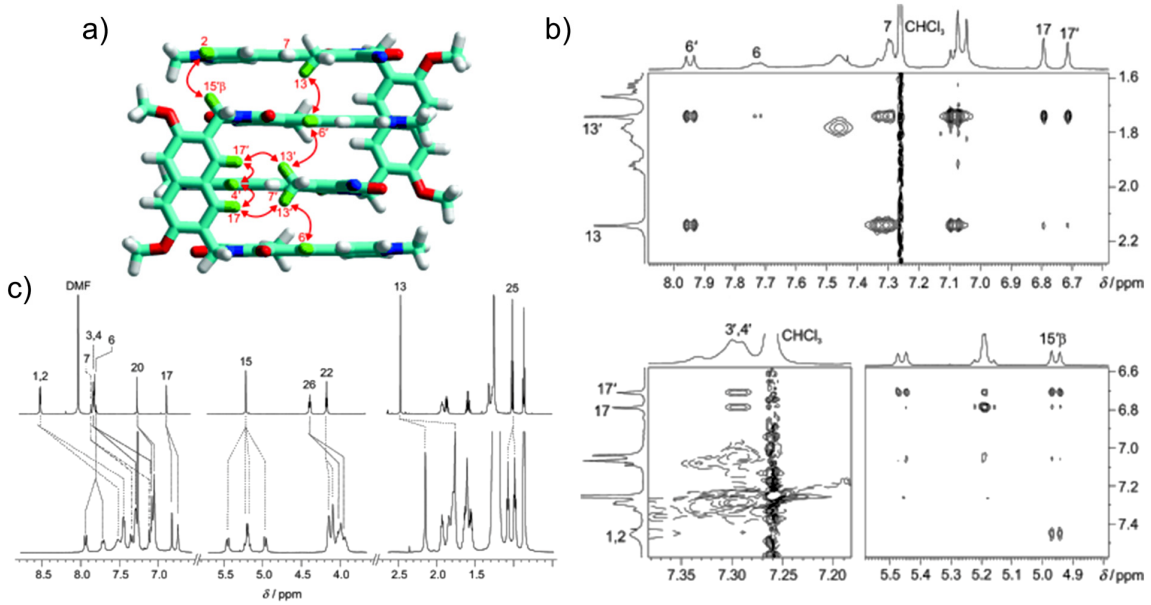

Figure 36 a) Structural model of bis(merocyanine) **52** dimer with the assignment of protons. Red double arrows indicate close spatial proximity between protons based on cross-peaks found in b) relevant sections of 2D ROESY experiments of **52** in $CDCl_3$ at 274 K (c = 1 x 10^{-2} M). c) Selected areas of 600 MHz ^{1}H NMR (293 K) spectrum of **52** monomer (top, DMF-d_7, c = 3 x 10^{-3} M) and dimer (bottom, $CDCl_3$, c = 1 x 10^{-2} M).[20b] Adapted with permission from Ref. [20b]. Copyright 2009 John Wiley and Sons.

Whereas in polar DMF-d_7, a solvent that favours the monomeric form, one single set of proton resonances was observed for the symmetric molecule, the ^{1}H NMR spectrum of the dimer solution in $CDCl_3$ shows a more complex pattern. Assignment of the signals by COSY, HSQC and HMBC measurements revealed two sets of signals according to the loss of chemical equivalence of the protons in the centrosymmetric dimer complex. Remarkable upfield shifts of most of the proton resonances can be explained by a shielding of these protons in the aggregate structure. Moreover, intermolecular close spatial proximity between protons has been detected by through space coupling in ROESY experiments. Thus, cross-peaks were found between the spacer protons 17/17' and the ones of the inner chromophore (4'/13'), which is in good agreement with the geometry-optimized (MM+) structural model depicted in Figure 36a. Recently, the same 2,7-naphthalenedimethylene spacer unit has been used to create a tweezer-type molecule based on another class of merocyanine dyes (**54**, Figure 37a).[20a]

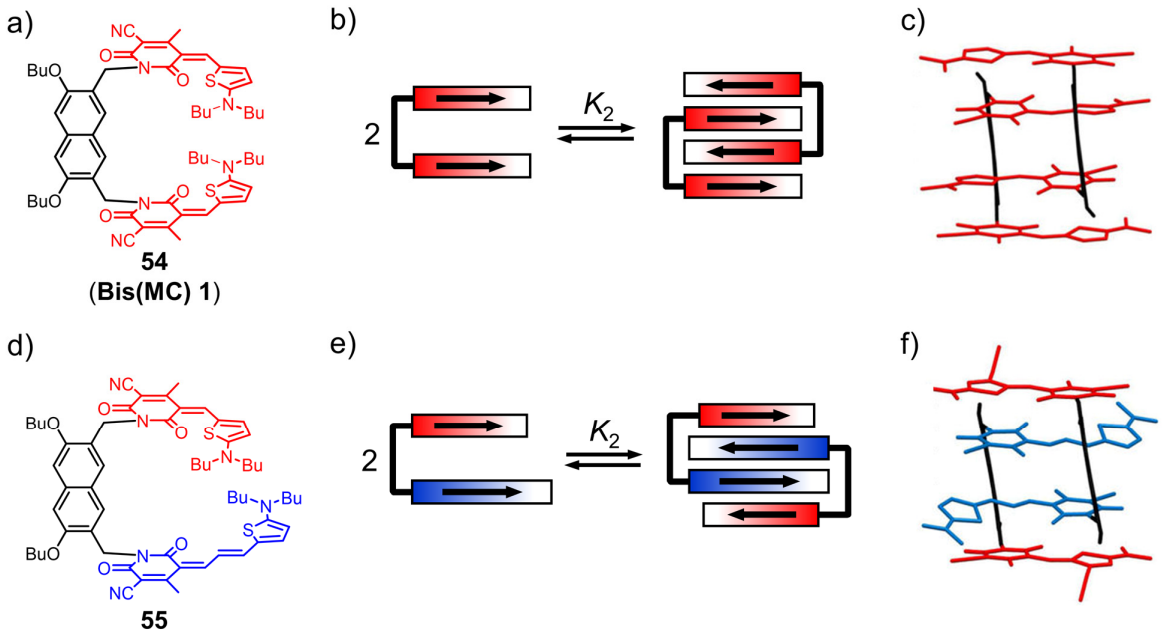

Figure 37 a,d) Chemical structure of bis(merocyanine) dyes **54** (**Bis(MC) 1**) and **55** and b,e) schematic illustration of the dimerization process of **54** and **55** into bimolecular complexes. Solvent molecules and hydrogen atoms in the single-crystal structure of c) **54** and f) **55** are omitted and butyl residues are replaced by methyl groups.[20a] Adapted with permission from Ref. [20a]. Copyright 2016 Nature Publishing Group.

Like compounds **52** and **53**, bis(merocyanine) **54** undergoes self-assembly into centrosymmetric bimolecular aggregates, as investigated by UV/vis and NMR experiments in unpolar solvents. Furthermore, the aggregate structure could even be proven by single-crystal X-ray analysis revealing a tightly packed dimer with a discrete stack of four antiparallel chromophores (Figure 37c). This structural concept was further developed by attaching two merocyanine chromophores of different length to the rigid spacer unit (**55**, Figure 37d).[20a] The

self-association behaviour of the so formed hetero-bis(merocyanine) compound causes unique spectral changes in the UV/vis, which could be interpreted in terms of molecular exciton theory. Both, detailed NMR studies and the solid state structure obtained by single-crystal X-ray analysis (Figure 37f) revealed interaction of the tweezer-type molecules in a dimeric aggregate with a stack of four antiparallel chromophores with the two shorter dyes positioned at the exterior of the stack. By using *para*-xylylene as linker moiety to connect the same merocyanine chromophores, the resulting tweezer-type molecule shows self-assembly into bimolecular complexes similar to the ones depicted in Figure 37a-c. This compatibility with different spacer units demonstrates the broad practicability of the tweezer approach.[19g]

Another spacer unit that provides an interplanar distance of ~7 Å is the chiral (1*R*,2*R*)-1,2-diaminocylohexane in combination with two (+)-usnic acid moieties as pincers.[112] This system represents a tweezer-type molecule (**56**, Figure 38a) that is able to bind one 2,4,7-trinitrofluorenone guest molecule by π-π-stacking interactions in a charge-transfer complex. However, the X-ray crystal structure of **56** (Figure 38b) shows that two of the molecules self-associate in the solid state resulting in a dimer assembly with aromatic interactions and the concentration-dependence of chemical shifts in ^{1}H NMR studies points out to the formation of a similar species in chloroform solution.

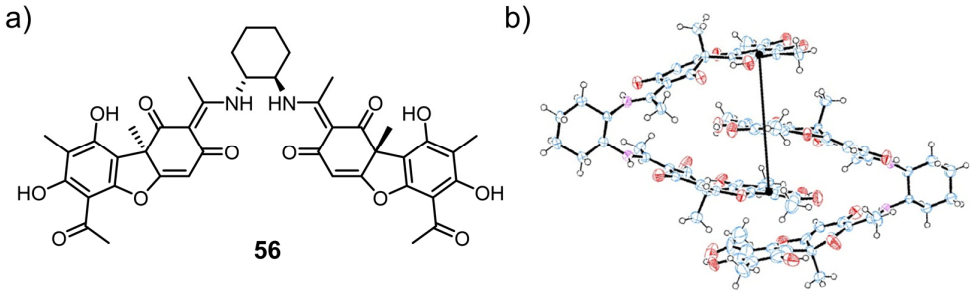

Figure 38 a) Chemical structure of tweezer **56** bearing two (+)-usnic acid moieties and b) ORTEP drawing of the X-ray crystal structure of **56**.[112] Adapted with permission from Ref. [112]. Copyright 2009 American Chemical Society.

The group of Colquhoun described the self-assembly of a pyrene-based imido-tweezer as "Roman Handshake"[113] since the dimeric structure reminds of the type of handshake which was common in the ancient Rome (Figure 39). Attaching a NDI residue to the amino-functionalized bis(pyrene) molecule yielded the self-complementary tweezer **57**, which shows dimerization into discrete trichromophoric donor-acceptor-donor double stacks with high binding constant in chloroform/trifluoroacetic acid (TFA) solution. The high self-association constant (10^4 M^{-1} in chloroform/TFA 9:1) obtained by concentration-dependent UV/vis studies can be attributed to multiple supramolecular interactions such as complementary π-π-

stacking and hydrogen bonding. The unique aggregate structure was characterized by ^{1}H NMR spectroscopy and could finally be verified by single-crystal X-ray analysis revealing two discrete, adjacent stacks of a NDI core sandwiched between two pyrene planes.

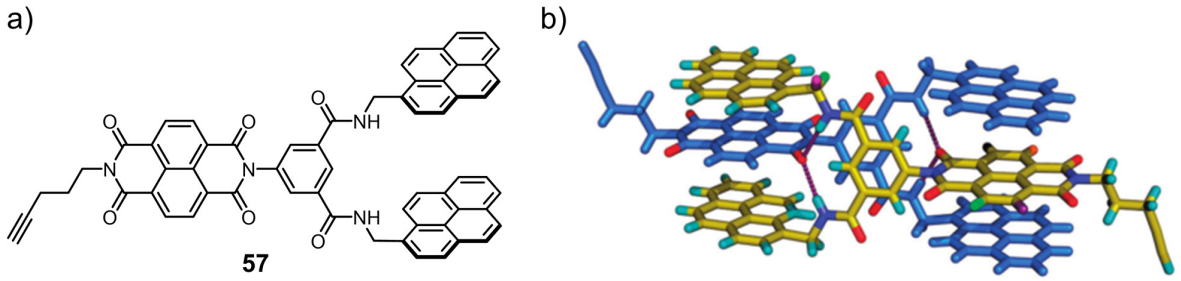

Figure 39 a) Chemical structure of pyrene-based imido-tweezer **57** and b) single-crystal X-ray structure of **57** showing the dimeric structure of **57** also referred to as "Roman Handshake".[113] Adapted from Ref. [113] with permission from The Royal Society of Chemistry. Copyright 2013 The Royal Society of Chemistry.

As a last example, a self-complementary tweezer based on dynamic switching devices will be introduced. This special class of tweezer has been developed by Lehn and Barboiu allowing precise control over the self-assembly pathway.[114] They demonstrated that tweezer-like self-recognition can be triggered by external stimuli such as metal ions or light. Through binding of a metal ion, molecular systems containing terpyridine moieties perform a conformational switch from a W-shaped to a tweezer-like U-shaped form, initiating self-assembly into complementary duplex compounds involving discrete stacking of four attached π-systems (Figure 40).

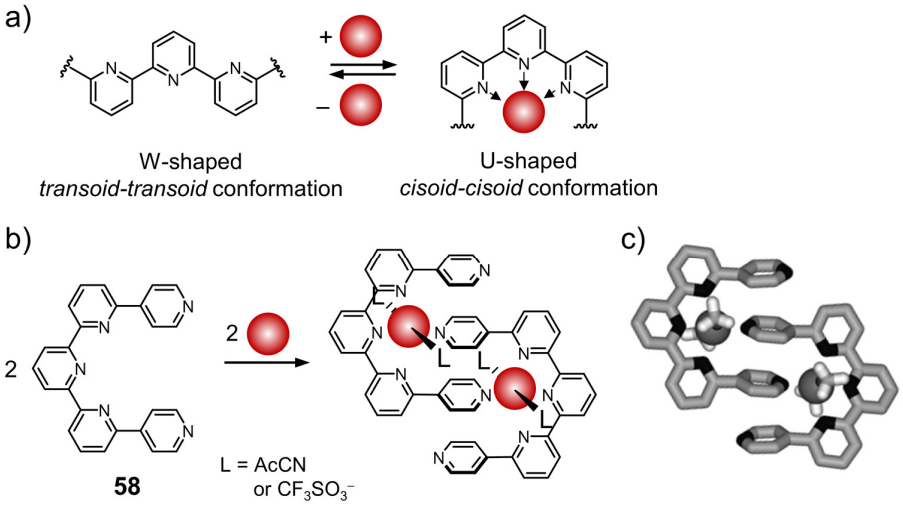

Figure 40 a) Interconversion of a terpyridine backbone between the W-shaped *transoid-transoid* and the U-shaped *cisoid-cisoid* conformation upon binding/release of a metal cation (red sphere). b) Schematic representation of the dimerization of **58** induced by the coordination of metal ions and c) crystal structure of the bimolecular complex including two cobalt ions (grey spheres).[114a] Adapted with permission from Ref. [114a]. Copyright 2004 John Wiley and Sons.

2.8 Conclusion

Discrete highly ordered supramolecular π-stacks in solution constitute ideal model systems to deduce characteristic properties of solid state materials arising from tightly packed aromatic molecules. Hence, engineering finite-sized aggregates by limiting the growth of one-dimensional π-stacks is a crucial issue. In this chapter, different strategies reported in the literature to create discrete supramolecular stacks of aromatic molecules have been reviewed. Besides template-directed aggregation into finite-sized architectures, intramolecular folding of covalently tethered chromophores seems to be a viable approach to generate π-stacks with a well-defined number of stacked aromatic moieties. However, this strategy usually involves considerable synthetic effort. In contrast, including additional highly directional supramolecular forces such as dipole-dipole interactions represents a promising approach to realize larger discrete dye aggregates of predictable size, in particular if such dipolar chromophores are incorporated into tweezer type molecular building blocks.

Furthermore, on the basis of some representative examples, structural elucidation of the aggregate species by analytical techniques has been discussed. It can be concluded that in most cases, it is not sufficient to apply only one specific characterization method but instead a combination of results from different experiments is required to elucidate the exact aggregate structure. Here, techniques like UV/vis and NMR spectroscopy together with mass spectrometry are most commonly utilized whilst X-ray crystallography is more the exception despite this method can most credibly provide insight into the structure of supramolecular assemblies.

Chapter 3

–

Intermolecular Self-Assembly of Bis(merocyanine) Dyes into Discrete Merocyanine π-Stacks

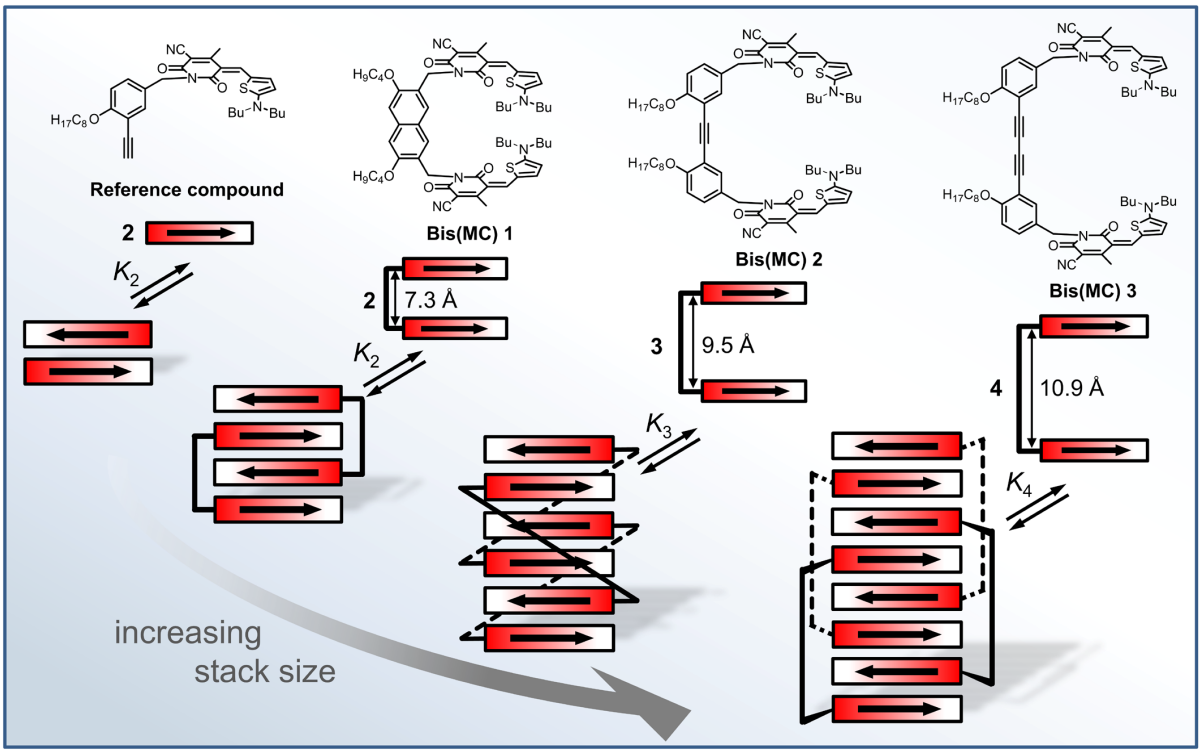

3.1 Introduction

The non-covalent synthesis approach constitutes a promising entry to create complex artificial systems with new functionalities.[115] Thereby, careful design of the molecular building blocks plays a crucial role to achieve the desired aggregate structure. Furthermore, fundamental knowledge about structure-property relationships is essential for the development of smart materials and to improve material properties on the molecular level. Hence, well-defined highly ordered model systems are needed that enable studies on aggregate properties depending on their size and structure. Although supramolecular strategies have been developed to create discrete π-stack architectures with a well-defined number of stacking chromophores (see Chapter 2), for the vast majority of artificial assemblies π-π-interactions lead to extended stacks of undefined size due to the presence of two π-faces with equal or at least similar binding affinity.[22c, 116] Since the aim of the present work is to realize finite-sized assemblies, the great challenge is to limit the growth of π-stacking. Furthermore, highly defined structures are essential to enable sound standing structural characterization by commonly accessible methods, in particular NMR spectroscopic techniques.

For this reason, merocyanine dyes (MC) were chosen as supramolecular building blocks. These highly polar dyes self-assemble into centrosymmetric dimer π-stacks (Figure 41a) by dipole-dipole interaction. This particular interaction affords high binding constants (K_2) of larger than 10^6 M^{-1} in unpolar solvents for the first face-to-face self-assembly and orders of magnitude smaller ones for the second π-face.[18b, d] As dipolar interactions of merocyanines are very strong and directional, well-defined supramolecular structures should be achievable by proper design of merocyanine building blocks. Indeed, bis(merocyanine) tweezer **Bis(MC) 1** bearing a rigid naphthalenedimethylene spacer self-assembles into discrete bimolecular complexes containing four π-stacked merocyanine units[19g, 20b] (Figure 41b) and unambiguous evidence for this tetrachromophoric π-stack has been provided recently by single-crystal X-ray analysis.[20a] However, larger finite dye stacks self-assembled by dipolar interactions are to-date unprecedented. To establish a series of discrete and well-defined large stacks of merocyanine chromophores properly designed bis(merocyanines) **Bis(MC) 2** and **Bis(MC) 3** will be introduced in this Chapter. Their self-assembly into tri- and tetramolecular complexes (Figure 41c,d) was investigated by concentration-dependent UV/vis spectroscopic studies and particular emphasis was put on the structure determination of the largest stack comprising eight chromophores. It could be proven by different NMR techniques, high-resolution mass spectrometry and atomic force microscopy that the size of the supramolecular structure is

indeed limited to eight chromophores. Finally, the series of merocyanine dye stacks consisting of two, four, six and eight chromophores represents a unique model system that enables in-depth analysis of optical properties of exciton-coupled chromophores in dependence on the number of stacking units.

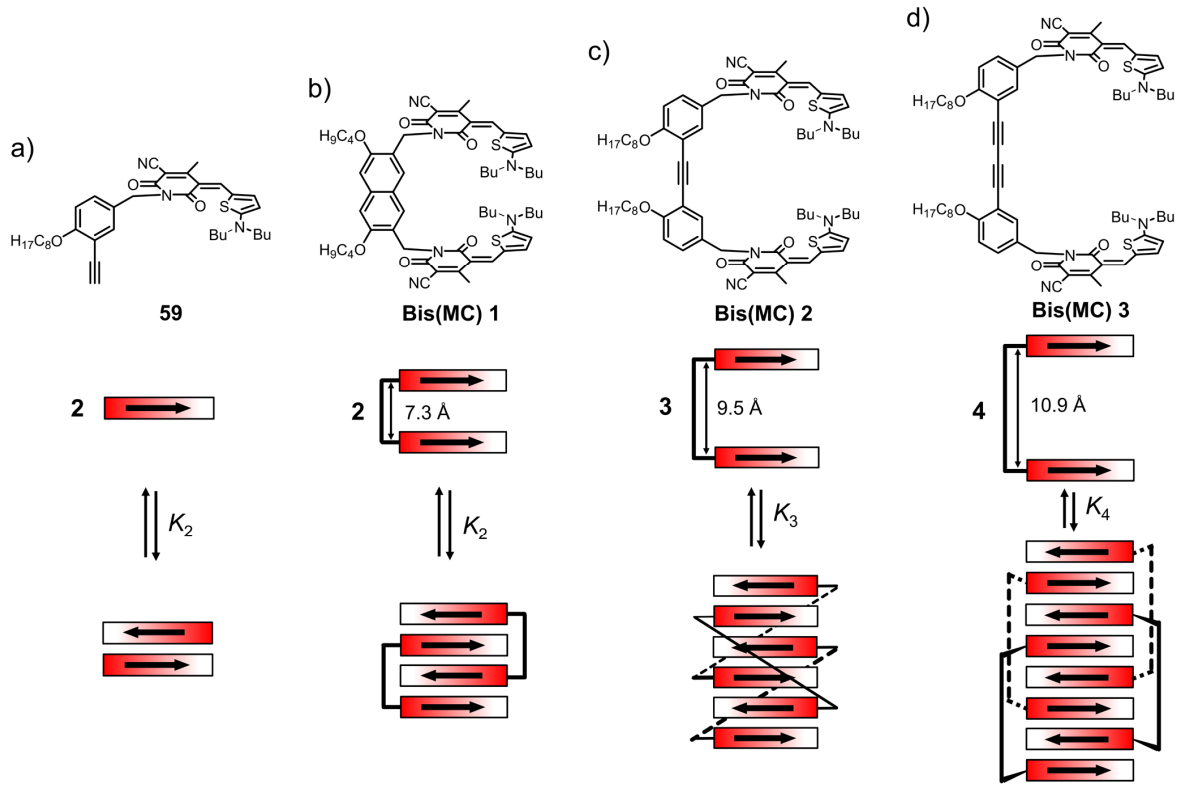

Figure 41 Chemical structures and schematic representation of the self-assembly process of a) reference dye **59** into antiparallel dimers, b) the dimerization of **Bis(MC) 1** into π-stacks of four merocyanine chromophores, c) the trimerization of **Bis(MC) 2** into π-stacks of six chromophores and d) the tetramerization of **Bis(MC) 3** into π-stacks of eight chromophores. Merocyanine units are illustrated as colored bars and their dipole moments are depicted as black arrows.

3.2 Results and Discussion[1]

3.2.1 Molecular Design

The strategy for the design of molecular building blocks, which self-assemble into well-defined, finite-sized π-stacks requires careful selection of the length and rigidity of the spacer units that define the interplanar distance between two merocyanine chromophores in a

[1] Computational calculations were performed by Dr. David Bialas and AFM measurements by Dr. Vladimir Stepanenko. Aggregation models were implemented into a global fitting algorithm by Dr. Franziska Fennel.

bichromophoric system. Recently, it has been demonstrated that the naphthalenedimethylene spacer (**Bis(MC) 1**, Figure 41b), which provides a distance of 7.3 Å between the chromophores, enables bimolecular complex formation leading to tetrachromophoric π-stacks of merocyanine dyes.[20] Hence, to increase the number of stacking chromophores, spacer moieties with considerably larger distance are required to imbed more than one merocyanine unit between the π-faces of tethered chromophores. Based on molecular modeling studies, a rigid diphenylacetylene (DPA) backbone was employed that provides a distance of 9.5 Å (**Bis(MC) 2**, Figure 41c), which should be ideal for the incorporation of two chromophores within a hexachromophoric stack. Furthermore, to realize supramolecular self-assembly into tetramolecular aggregates consisting of eight merocyanine units, **Bis(MC) 3** was chosen (Figure 41d) containing a diphenylbutadiyne (DPB) backbone that features an interplanar distance of 10.9 Å. To ensure adequate solubility in unpolar solvents, long alkyl chains are introduced to the DPA and DPB backbones, respectively.

3.2.2 Synthesis

The synthesis of **Bis(MC) 1**[2] was reported previously,[20a] whereas **Bis(MC) 2** and **Bis(MC) 3** were prepared by newly developed synthetic routes. **Bis(MC) 2** was synthesized by Knoevenagel condensation of literature known thiophene aldehyde **66a**[118] and a DPA spacer bearing bis(pyridone), which was built up in six steps starting from commercially available 3-bromo-4-hydroxybenzonitrile (**60**) (Scheme 1). In the first step, etherification of **60** with octyl bromide in DMF gave the corresponding aryl ether **61** in almost quantitative yield. Subsequent Sonogashira coupling with trimethylsilyl acetylene under palladium catalysis, followed by deprotection of the silyl group with tetrabutylammonium fluoride in tetrahydrofuran (THF), afforded phenylacetylene derivative **63**. The symmetric dicyano spacer **64** was obtained in good yield (72%) by Sonogashira cross-coupling reaction of **63** with aryl bromide **61** under palladium catalysis in the presence of copper iodide in THF. Therefore, a solution of the acetylene functionalized compound **63** in THF was added dropwise to a mixture of the other starting materials under the exclusion of oxygen in order to avoid the formation of the homocoupling side product. Reduction of **64** with lithium aluminum hydride afforded the corresponding bis(amine), which was subsequently reacted without further purification with methyl cyanoacetate to obtain bis(cyanoacetamide) **65**.

[2] **Bis(MC) 1** was synthesized by Dr. André Zitzler-Kunkel.[117]

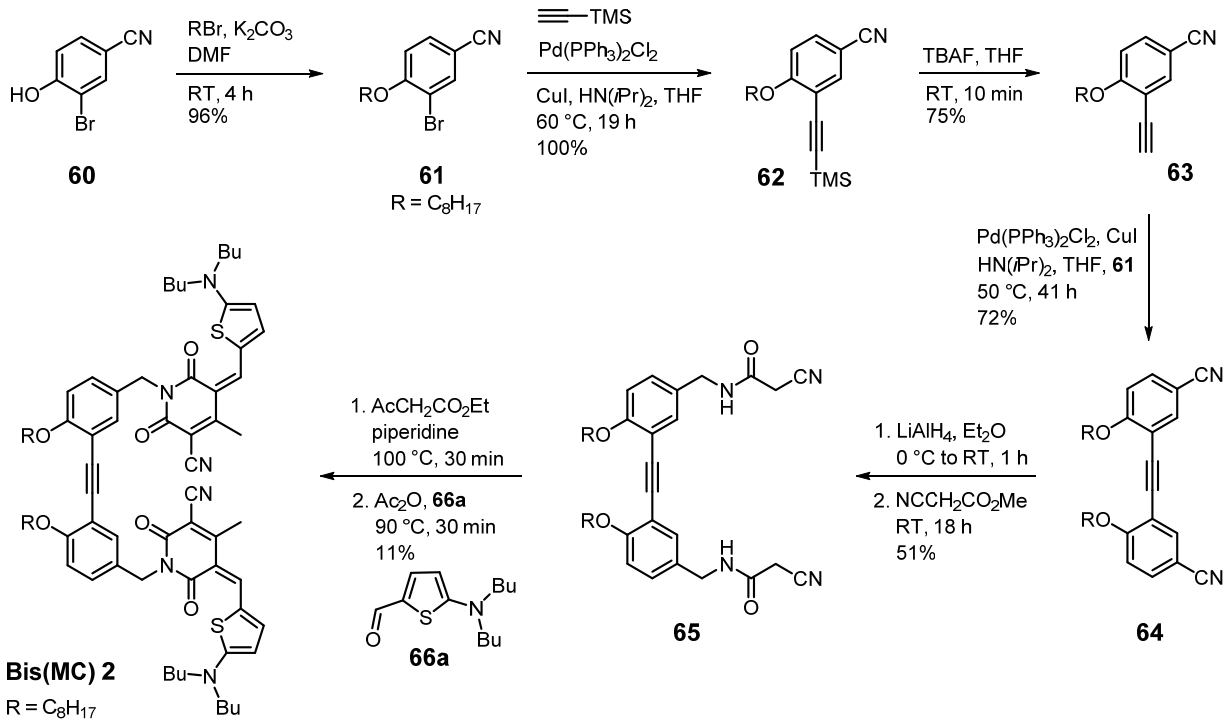

Scheme 1 Synthetic route to **Bis(MC) 2**.

By reacting **65** with ethyl acetoacetate in piperidine, the bis(hydroxypyridone) intermediate was synthesized and finally subjected to a Knoevenagel condensation reaction with aminothiophene aldehyde **66a**, which was prepared according to the literature,[118] to afford the target compound **Bis(MC) 2**. The crude product was purified by column chromatography to give **Bis(MC) 2** after precipitation from DCM/*n*-hexane solution as a purple solid in 11% yield. All compounds of this synthetic route were fully characterized by common analytical techniques (for details, see the Experimental Section).

Bis(MC) 3 was synthesized according to the route depicted in Scheme 2 starting with compound **63**, whose preparation is described in Scheme 1. Reduction of **63** with lithium aluminum hydride afforded the corresponding amine, which was subsequently reacted without further purification with methyl cyanoacetate to obtain cyanoacetamide **67** in adequate purity after column chromatography. The hydroxypyridone intermediate was synthesized by reacting **67** with ethyl acetoacetate in piperidine and subjected to a Knoevenagel condensation reaction with aminothiophene aldehyde **66a** in acetic anhydride to afford the merocyanine reference dye **59** in 40% yield over two steps. Finally, the target compound **Bis(MC) 3** was synthesized *via* Glaser coupling of reference merocyanine **59** under palladium catalysis in the presence of copper iodide in THF. Purification of the crude product was performed by column chromatography on silica gel and the purple solid was collected by filtration after precipitation

from DCM/*n*-hexane solution in a yield of 56%. **Bis(MC) 3** as well as the precursor molecules **67** and **59** were completely characterized (for details, see the Experimental Section).

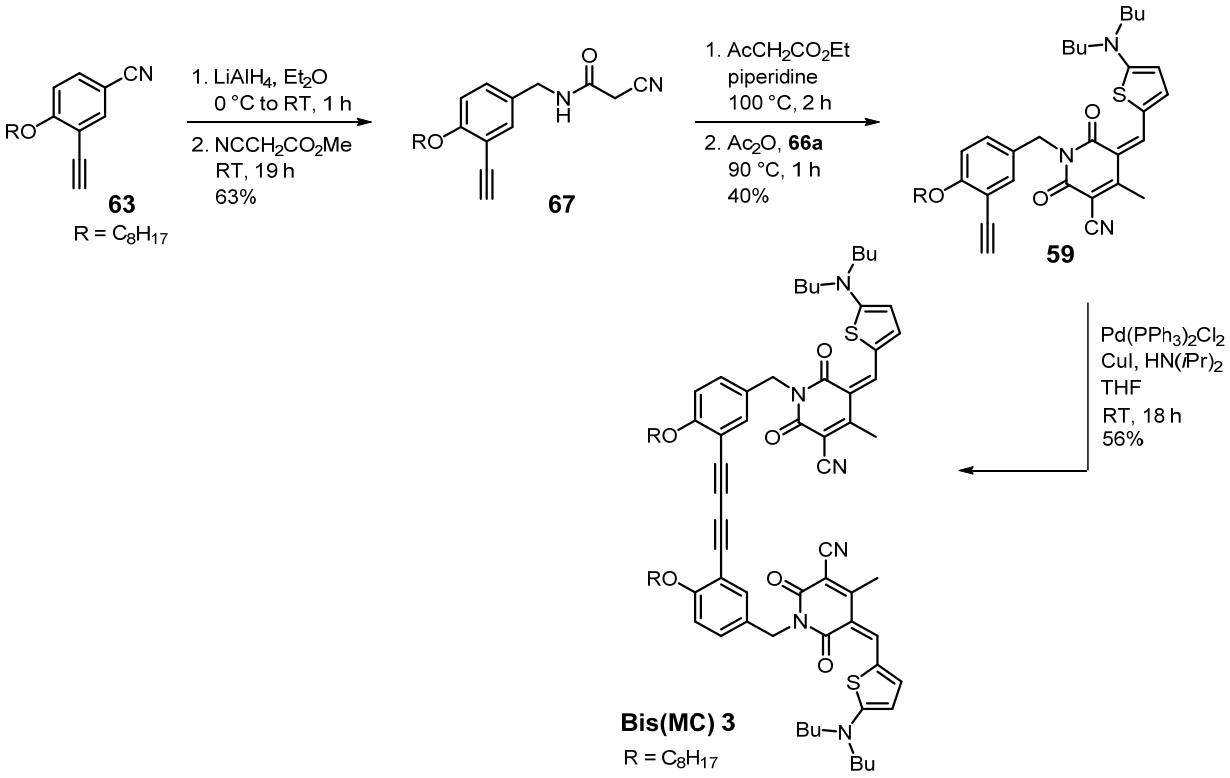

Scheme 2 Synthetic route to **Bis(MC) 3**.

3.2.3 UV/vis Spectroscopy

The aggregation behaviour of **Bis(MC) 1**, **Bis(MC) 2** and **Bis(MC) 3**, in comparison with the monochromophoric reference compound **59**, was studied by concentration-dependent UV/vis spectroscopy. The spectra of all dyes are displayed in Figure 42. For the aggregation studies of **59** as well as for **Bis(MC) 2** and **Bis(MC) 3**, a mixture of less polar THF and unpolar methylcyclohexane (MCH) in a ratio of 17.5 : 82.5 was chosen as the polarity of this solvent composition is properly suited to cover most of the transition from the monomeric (at low concentrations) to the aggregated species (at high concentrations) within the accessible concentration range of UV/vis measurements. Experiments with **Bis(MC) 1** were performed in pure THF as this solvent allows to cover the transition from monomer to dimer compared to studies in THF/MCH mixtures, in which complete aggregation is observed also for moderate concentrations.[20a]

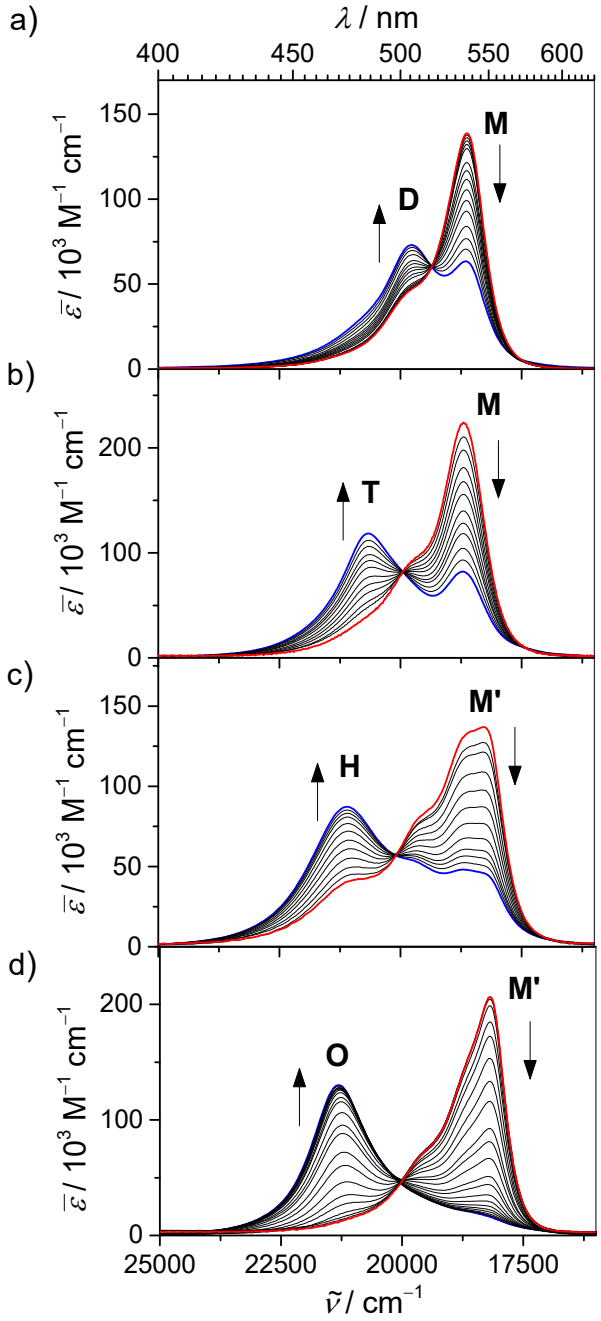

Figure 42 Concentration-dependent UV/vis spectra of a) monochromophoric reference dye **59** in THF/MCH 17.5 : 82.5 (c = 4.2 x 10^{-4} M – 2.7 x 10^{-6} M), b) **Bis(MC) 1** (c = 8.1 x 10^{-4} M – 5.6 x 10^{-7} M) in THF, c) **Bis(MC) 2** (c = 2.3 x 10^{-6} M – 1.2 x 10^{-7} M) in THF/MCH 17.5 : 82.5 and d) **Bis(MC) 3** (c = 2.8 x 10^{-4} M – 8.0 x 10^{-8} M) in THF/MCH 17.5 : 82.5 at 295 K starting at high concentration (blue line) and successively diluting the solution (black lines). The spectrum at lowest concentration is depicted in red line. Black arrows indicate the decrease in the intensity of the monomer band and the appearance of the aggregate band upon increasing concentration.

At the lowest concentrations applied, reference dye **59** and bichromophoric dye **Bis(MC) 1** exhibit the typical monomer absorption band for this merocyanine chromophore[18c] with a maximum at 537 nm (Figure 42a,b; denoted as M). Notably, the monomer absorption band of

Bis(MC) 2 and **Bis(MC) 3** is bathochromically shifted to 550 nm (denoted as M', Figure 42c,d) which is attributed to weak intramolecular J-type exciton coupling between the two adjacent chromophore units.[21a, c, 91, 119] With increasing concentration, the intensity of the monomer band of all four dyes decreases with concomitant appearance of a hypsochromically shifted absorption band (denoted as D, T, H and O) which is a clear indication for the formation of cofacially stacked aggregates with H-type exciton coupling.[15b, c] For each of these dyes, one well-defined isosbestic point exists over the whole concentration range, implying the presence of a thermodynamic equilibrium between two defined species that are obviously the respective monomer and the corresponding H-type aggregate. It has to be noted that for the study of **Bis(MC) 2**, the concentration range was limited to a range, where a clear isosbestic point was observed (c = 2.3 x 10^{-6} M – 1.2 x 10^{-7} M). At higher concentrations, the absorption band is further hypsochromically shifted with a loss of the isosbestic point indicating the formation of another aggregate species that is presumably an extended dye stack (see the Appendix, Figure A3).

The hypsochromic shift of the aggregate bands of these dyes in the concentration-dependent spectra provides the first evidence for a spacer-encoded aggregate size. Thus, the monochromophoric reference dye **59** shows a blue shift of the absorption of 32 nm ($\Delta\tilde{\nu}$ = 1180 cm^{-1}) between the monomer and the dimer band. Based on earlier work, this spectral change can be attributed to the coupling of transition dipole moments in a centrosymmetric dimer.[18d] In comparison, **Bis(MC) 1** with a rigid spacer providing a distance of 7.3 Å, which is known to direct the self-association of the bichromophoric merocyanine tweezer into centrosymmetric dimers with four stacked chromophores,[20] shows a stronger hypsochromic shift of 52 nm ($\Delta\tilde{\nu}$ = 2000 cm^{-1}). Finally, **Bis(MC) 2** and **Bis(MC) 3** with larger spacers of 9.5 Å and 10.9 Å exhibit the most prominent blue shifts of 64 nm ($\Delta\tilde{\nu}$ = 2520 cm^{-1}) and 67 nm ($\Delta\tilde{\nu}$ = 2660 cm^{-1}), neglecting the intramolecular J-type coupling of the folded monomers. The optical properties of the monomer and aggregate species of the herein investigated compounds are summarized in Table 1.

The concentration-dependent UV/vis spectral data of reference dye **59** and **Bis(MC) 1** could be successfully fitted to the dimerization model[18d, 22c] by a global fit analysis yielding the calculated absorption spectra of the respective monomers and the bimolecular complexes (Figure 43a,b). These results are in good agreement with the self-assembly behaviour of the dyes reported in the literature.[18b, 20a] The UV/vis data of **Bis(MC) 2** and **Bis(MC) 3** could be properly fitted by the trimerization and tetramerization model (Figure 43c,d). Details on the aggregation models are given in the Appendix.

Table 1 Experimental absorption maxima λ_{max} and the corresponding transition energies E_{max} of the monomer (M) and aggregate (A) species of reference dye **59**, **Bis(MC) 1**, **Bis(MC) 2** and **Bis(MC) 3** as well as the energy difference $\Delta\tilde{\nu}$ between the monomer and aggregate absorption maximum, respectively. The monomer absorption maximum of **Bis(MC) 2** and **Bis(MC) 3** is denoted as M' due to a bathochromic shift arising from weak intramolecular interactions between the adjacent chromophores.

	59[a]	**Bis(MC) 1**[b]	**Bis(MC) 2**[a]	**Bis(MC) 3**[a]
$\lambda_{max,M(M')}$ / nm	537	537	(550)	(550)
$E_{max,M(M')}$ / cm^{-1}	18600	18600	(18200)	(18200)
$\lambda_{max,A}$ / nm	505	485	473	470
$E_{max,A}$ / cm^{-1}	19800	20600	21100	21300
$\Delta\tilde{\nu}$ / cm^{-1}	1180	2000	2520*	2660*

[a]In THF/MCH 17.5 : 82.5. [b]In THF. *Calculated by the difference between $E_{max,A}$ and $E_{max,M}$.

Apparently, the trimeric aggregate of **Bis(MC) 2** with a stack of six chromophores and a tetrameric assembly of **Bis(MC) 3** comprising a π-stack of eight chromophore units are formed. These findings are further corroborated by the increased hypsochromic shift of the aggregate absorption band that points out to the formation of stacks larger than the tetrachromophoric stack.[15b, c] The estimated dimerization constant for reference dye **59** in THF/MCH 17.5 : 82.5 is $K_2 = 5.0 \times 10^3$ M^{-1}. In contrast, **Bis(MC) 1** has an exceptionally strong tendency to aggregate such that the monomeric form was not observed in the THF/MCH 17.5 : 82.5 solvent mixture even at the lowest concentration of 4.0×10^{-7} M. Therefore, one can estimate that the aggregation constant[3] in the solvent mixture is $> 2.5 \times 10^6$ M^{-1}. In order to monitor the aggregation of **Bis(MC) 1**, pure THF was used, where the aggregation tendency is reduced. The dimerization constant of **Bis(MC) 1**[3] in THF is $K_2 = 1.0 \times 10^5$ M^{-1}. In case of **Bis(MC) 2** and **Bis(MC) 3**, the aggregation study was performed in THF/MCH 17.5 : 82.5 mixture. Accordingly, the trimerization constant[3] of **Bis(MC) 2** is $K_3 = 2.3 \times 10^6$ M^{-1} and the tetramerization constant[3] of **Bis(MC) 3** is $K_4 = 9.0 \times 10^5$ M^{-1}.

In conclusion, the lowest aggregation constant was observed for reference compound **59**. In contrast, the aggregation constants of the bis(merocyanine) dyes are at least two order of magnitudes higher, which can be attributed to the effect of the preorganization by the tether unit and the multiple interactions within the larger π-stacks. Thus, with increasing length and

[3] Defined as the binding constant per binding site (for details, see the Appendix).

flexibility of the spacer moiety from **Bis(MC) 1** to **Bis(MC) 3**, a reduction of the aggregation constant is observed.

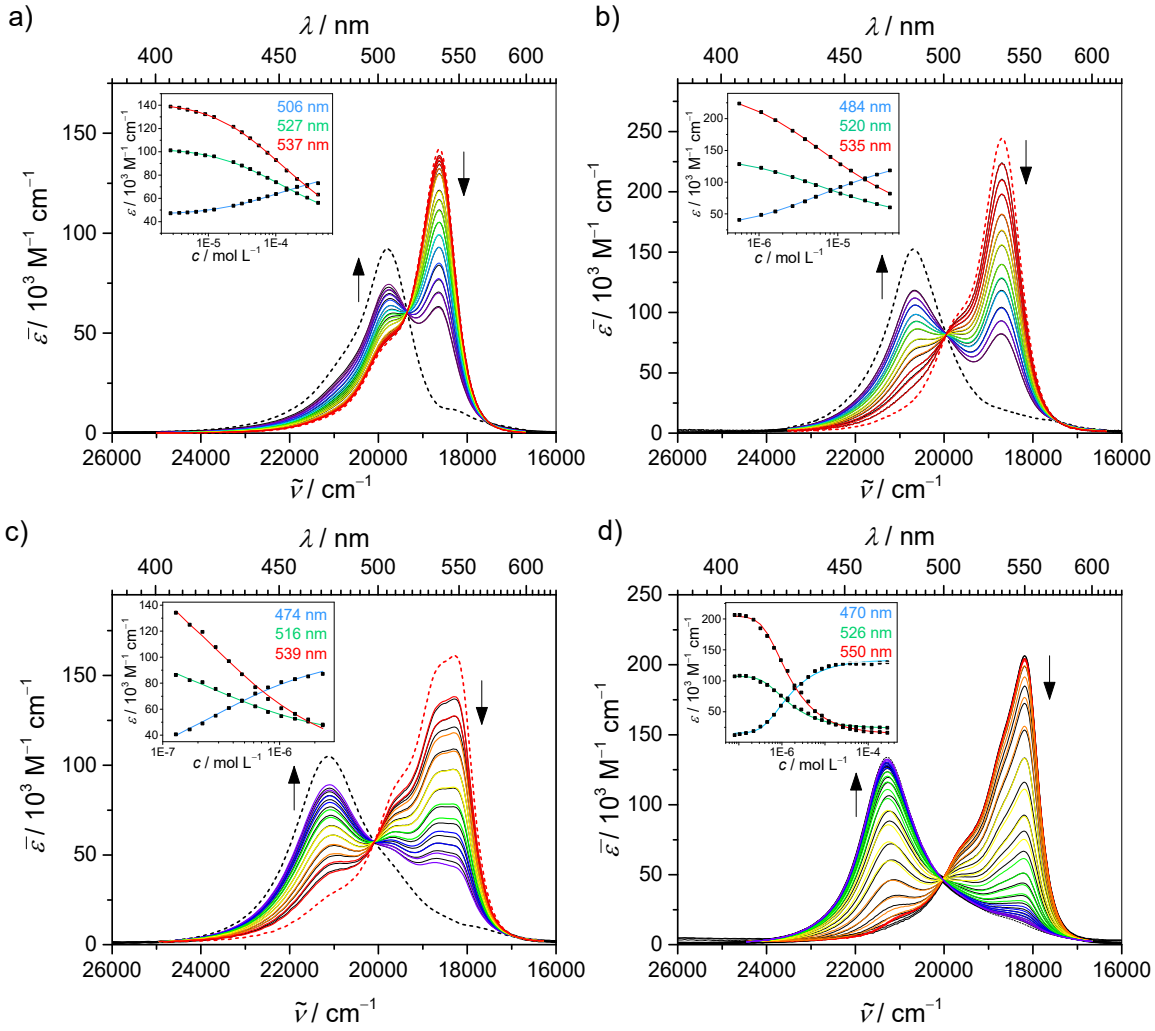

Figure 43 Concentration-dependent UV/vis spectra of a) monochromophoric reference dye **59** in THF/MCH 17.5 : 82.5 (c = 4.2 x 10^{-4} M – 2.7 x 10^{-6} M), b) **Bis(MC) 1** (c = 8.1 x 10^{-4} M – 5.6 x 10^{-7} M) in THF, c) **Bis(MC) 2** (c = 2.3 x 10^{-6} M – 1.2 x 10^{-7} M) in THF/MCH 17.5 : 82.5 and d) **Bis(MC) 3** (c = 2.8 x 10^{-4} M – 8.0 x 10^{-8} M) in THF/MCH 17.5 : 82.5 at 295 K (black lines). Colored lines represent the spectra obtained by global fit analysis according to the dimerization model (a, b), trimerization model (c) and tetramerization model (d). Dashed lines correspond to the calculated spectra of monomer (red) and the respective aggregate (black). Black arrows indicate the decrease in the intensity of the monomer band and the appearance of the aggregate band upon increasing concentration. The insets show the analysis of the concentration-dependent extinction data at various wavelengths according to the respective model.

3.2.4 Mass Spectrometry and Atomic Force Microscopy

Further information on the size of the aggregates was acquired by mass spectrometry (MS). The matrix assisted laser desorption/ionization (MALDI) mass spectrum of **Bis(MC) 1** (Figure A4) revealed a main peak (*m/z* 1038.49), which can be assigned to the singly charged monomer cation, and a peak at *m/z* 2077.81 that clearly corresponds to the singly charged dimer cation of this dye. MS investigation of **Bis(MC) 2** and **Bis(MC) 3** aggregate required a more soft ionization technique due to lower binding strength of the larger complexes. Therefore, the electrospray ionization (ESI) technique was applied to a solution of **Bis(MC) 2** and **Bis(MC) 3** in chloroform/methanol (3:1) mixture (Figure 44).

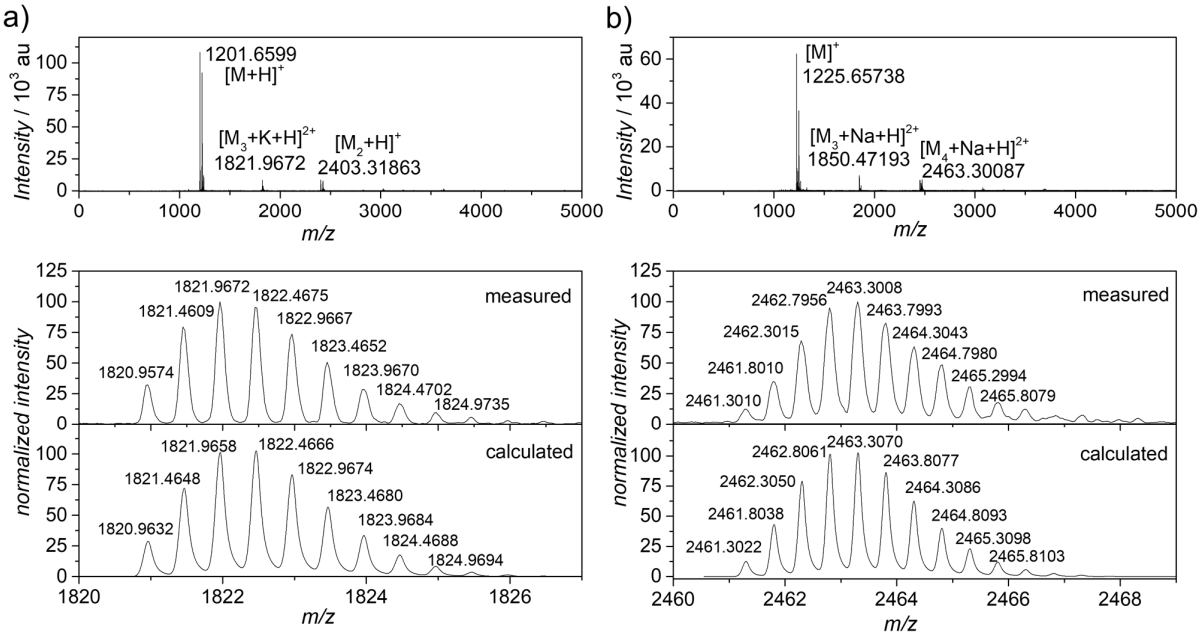

Figure 44 Entire spectrum (top) and relevant section (bottom) of calculated and experimentally observed ESI-TOF mass spectra (positive ion mode) from a solution of a) **Bis(MC) 2** and b) **Bis(MC) 3** in chloroform/methanol 3:1 mixture (c = 4 x 10^{-5} M). The solution of **Bis(MC) 3** was stored at –20 °C for four hours before measurement.

In the ESI MS spectrum of **Bis(MC) 3**, a double charged tetramer species was detected along with the monomeric and partially fragmented species like the dimer and trimer complex, whereas the one of **Bis(MC) 2** shows the mass of the double charged trimer as the largest detectable species. The observed isotope patterns and their peak distance perfectly match the calculated natural abundances and thus, strongly corroborate the existence of discrete trimeric aggregates of **Bis(MC) 2** and tetrameric aggregates of **Bis(MC) 3** in solution.

Further evidence on the dimensions of the bis(merocyanine) dye aggregates was obtained by atomic force microscopy (AFM) measurements on thin films prepared by spin-coating solutions of **Bis(MC) 1-3** in $CHCl_3$ on *Mica*. AFM height images of all three bis(merocyanine)

dyes (Figure 45) show films consisting of spherical nanoparticles. The obtained diameters roughly fit to the dimensions of **Bis(MC) 1** dimer, **Bis(MC) 2** trimer and **Bis(MC) 3** tetramer aggregates, thus ruling out the formation of extended polymeric fibers.

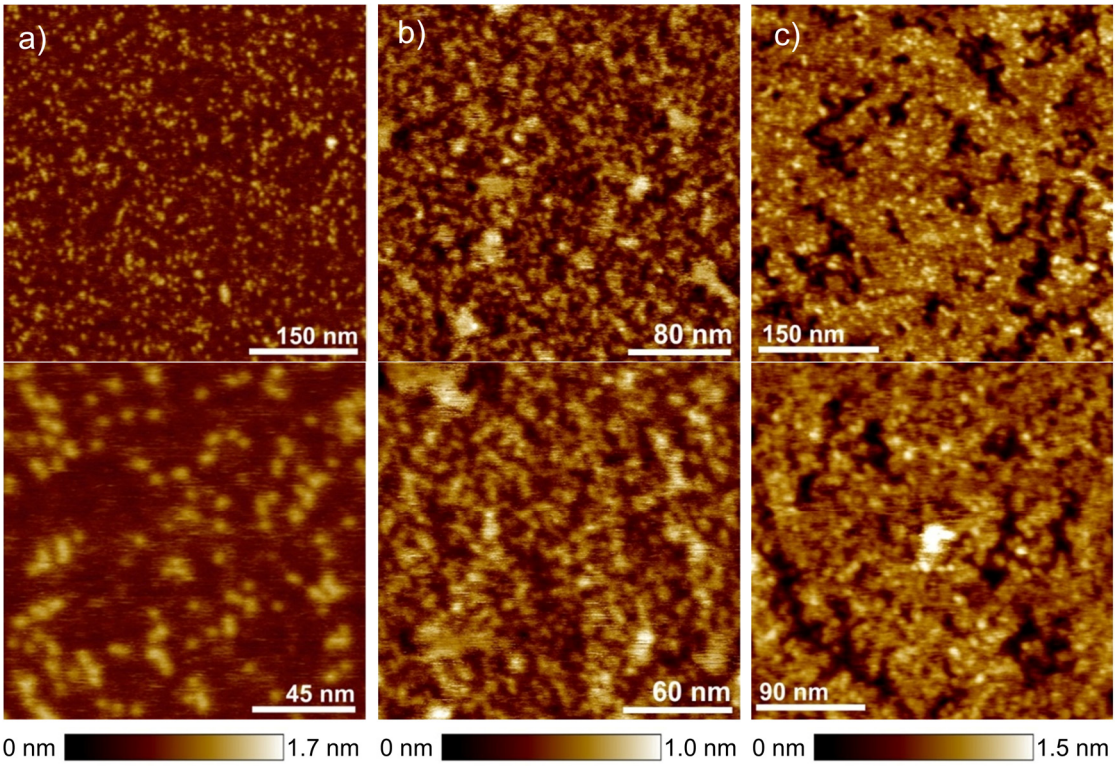

Figure 45 AFM images of thin films of a) **Bis(MC) 1**, b) **Bis(MC) 2** and c) **Bis(MC) 3** prepared by spin-coating from a solution of the respective dye in chloroform on *Mica* (c = 1 x 10^{-5} M, 4000 rpm) showing layers composed of small spherical nanoparticles with an average diameter of 3.9 ± 0.3 nm (**Bis(MC) 1**), 3.9 ± 0.5 nm (**Bis(MC) 2**) and 3.4 ± 0.5 nm (**Bis(MC) 3**). Particles of a second layer appear brighter.

3.2.5 Structural Characterization of Bis(MC) 3 Aggregate by NMR Spectroscopy

For an in-depth structure determination of the **Bis(MC) 3** aggregate, representing the largest dye stack within the series of merocyanine aggregates, NMR spectroscopic investigations were performed in toluene-d_8 at different temperatures as UV/vis absorption studies of this dye in the low polarity solvent revealed a temperature-dependent transformation from the monomer to the aggregate (see the Appendix, Figure A1). Structural characterization of the **Bis(MC) 1** dimer by detailed NMR studies was reported previously,[20a] whereas the **Bis(MC) 2** trimer could not be characterized by this analytical technique since the formation of extended aggregates at high concentration or at low temperature leads to a significant broadening of the

proton resonances and thus, prevents detection of the discrete trimer species (for details, see the Appendix Figure A2, Figure A3 and Figure A5).

Indeed, upon successively decreasing the temperature from 374 K to 254 K in steps of 10 K, the ^{1}H NMR spectrum of **Bis(MC) 3** in toluene-d_8 (c = 1 x 10^{-3} M) shows significant changes (Figure 46). At 374 K, the spectrum is characterized by one set of sharp signals that can be reliably assigned to the respective monomer protons (highlighted with color code in Figure 47) of this C_{2v} symmetric molecule with two chemically equivalent halves by 2D COSY, ROESY, HSQC and HMBC NMR techniques (Appendix, Figure A7 and Table A2).

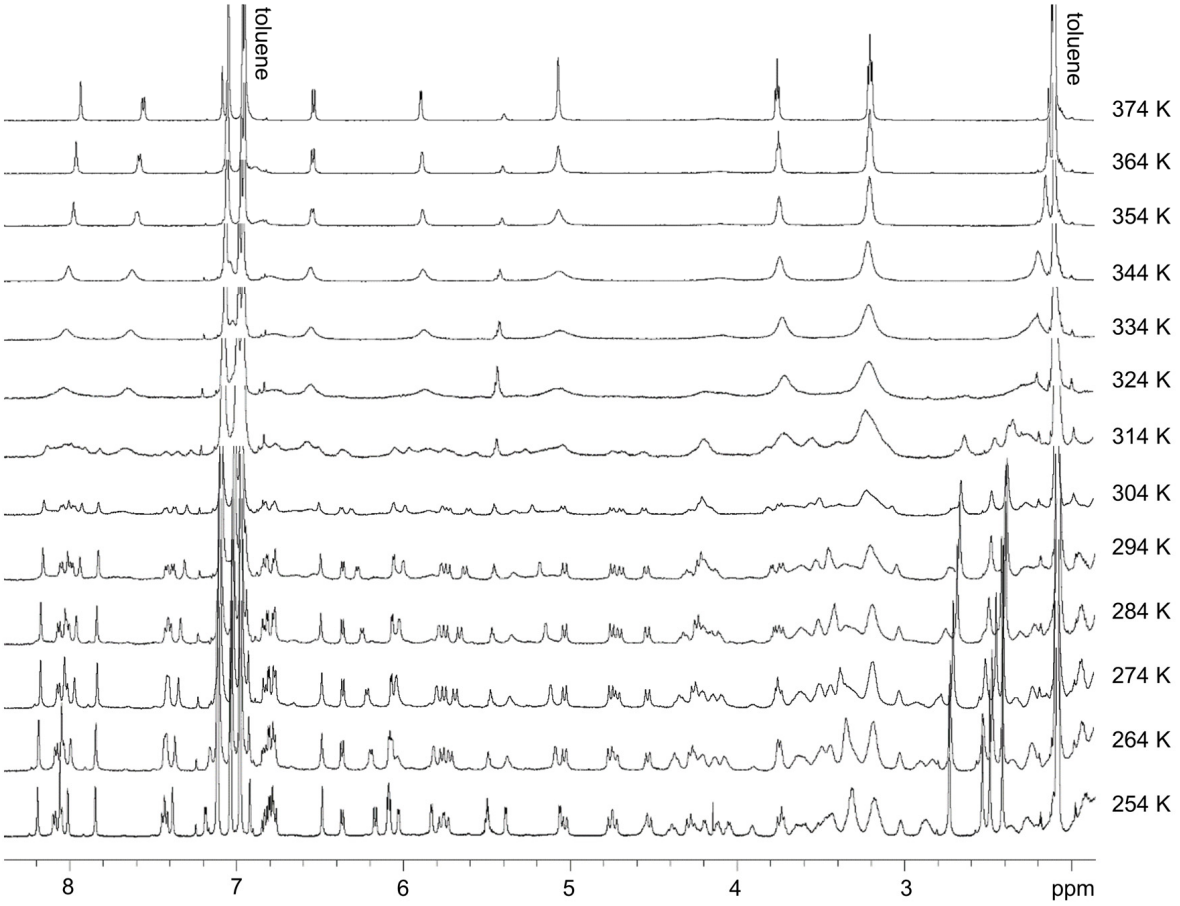

Figure 46 Selected area of temperature-dependent ^{1}H NMR (600 MHz) spectra of **Bis(MC) 3** in toluene-d_8 at c = 1 x 10^{-3} M starting at 374 K (top) and successively decreasing the temperature in steps of 10 K to 254 K (bottom).

Upon decreasing temperature, the signals considerably broaden until a coalescence temperature (~ 324 K) is reached, where almost no signal pattern is observed. By further cooling down, a multitude of sharp signals appears giving a complex spectrum at 254 K. However, the resonances are remarkably well-resolved and disperse over a wide range of chemical shift, facilitating proper analysis of the spectrum and signal assignment. On the basis of the signal integrals, multiplicities and coupling constants as well as 2D COSY experiments (Figure 48a),

exactly four sets of signals could be identified that are assignable to the spacer and chromophore protons of **Bis(MC) 3** (Figure 47, for the detailed assignment, see Appendix Table A2) with four different chemical environments. For the spacer methylene protons of **Bis(MC) 3** (highlighted in purple), for which a singlet is observed in the monomer spectrum (Figure 47c), four sets of two doublets with a coupling constant of around 14 Hz are observed in the aggregate spectrum (Figure 47d) due to their diastereotopic character in the rigidified aggregate structure.

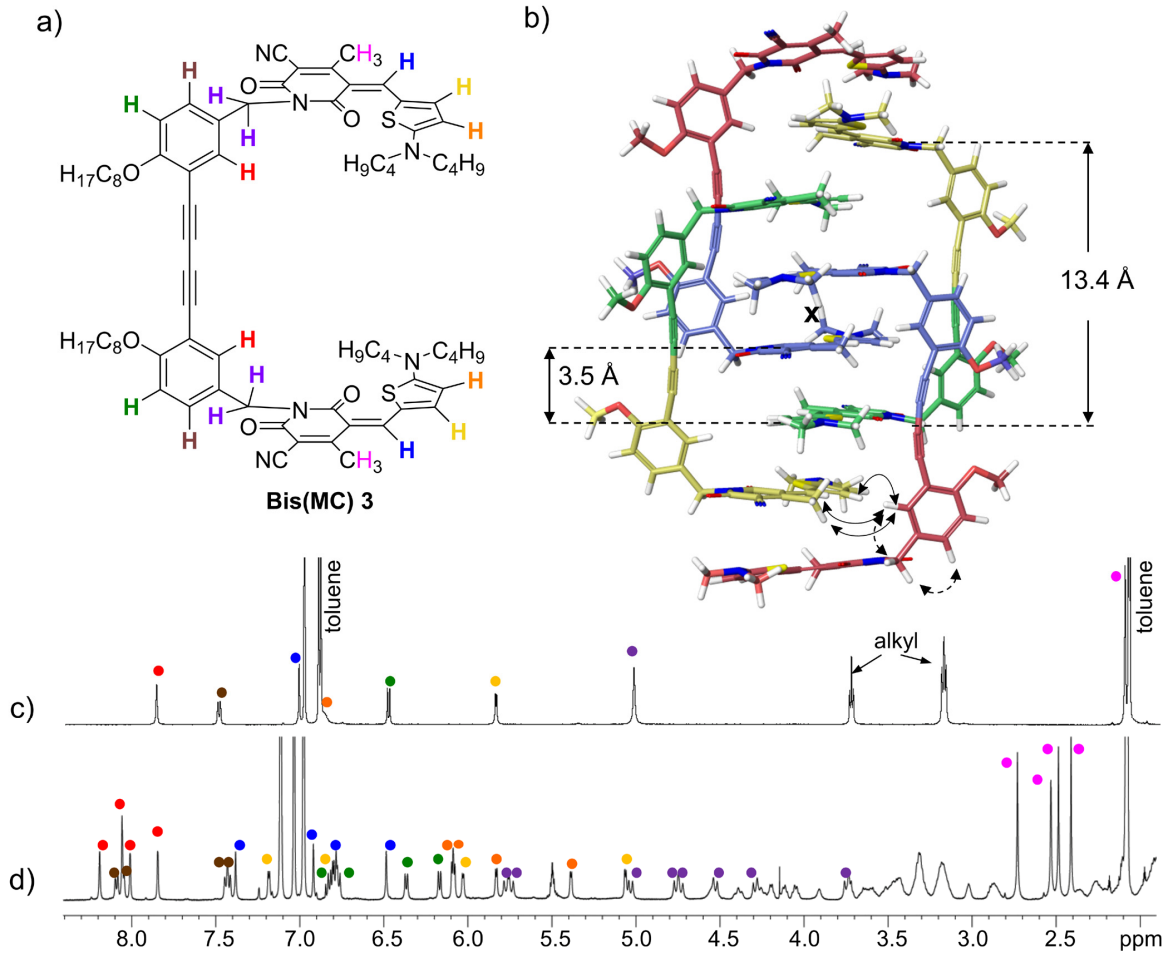

Figure 47 a) Chemical structure of **Bis(MC) 3** with the significant protons highlighted in color. b) Energy-minimized structure of the tetramer aggregate obtained by force field calculations (*Maestro Macro Model*, MMFF, $CHCl_3$, constrained dihedral angles within the chromophores; alkyl chains are replaced by methyl groups). The inversion center of the aggregate is indicated with a cross, and the curved arrows indicate the close proximity of protons in the stack. Relevant section of ^{1}H NMR (600 MHz) c) monomer (at 374 K) and d) aggregate spectrum (at 254 K) of **Bis(MC) 3** in toluene-d_8 (c = 1 x 10^{-3} M) with the assignment of the significant proton signals.

All these results of the ^{1}H NMR study corroborate a centrosymmetric tetramer structure comprising a stack of eight merocyanine chromophores as illustrated by the energy-minimized model in Figure 47b. The centrosymmetric character of the aggregate structure leads to four

pairs of chemically equivalent halves of monomers that are highlighted by different colors. Consequently, the structural model is in good agreement with the four sets of signals observed in ^{1}H NMR spectrum of the aggregate.

To gain more insight into the molecular arrangement in the tetramer aggregate of **Bis(MC) 3**, 2D ROESY experiments were performed (Figure 48).

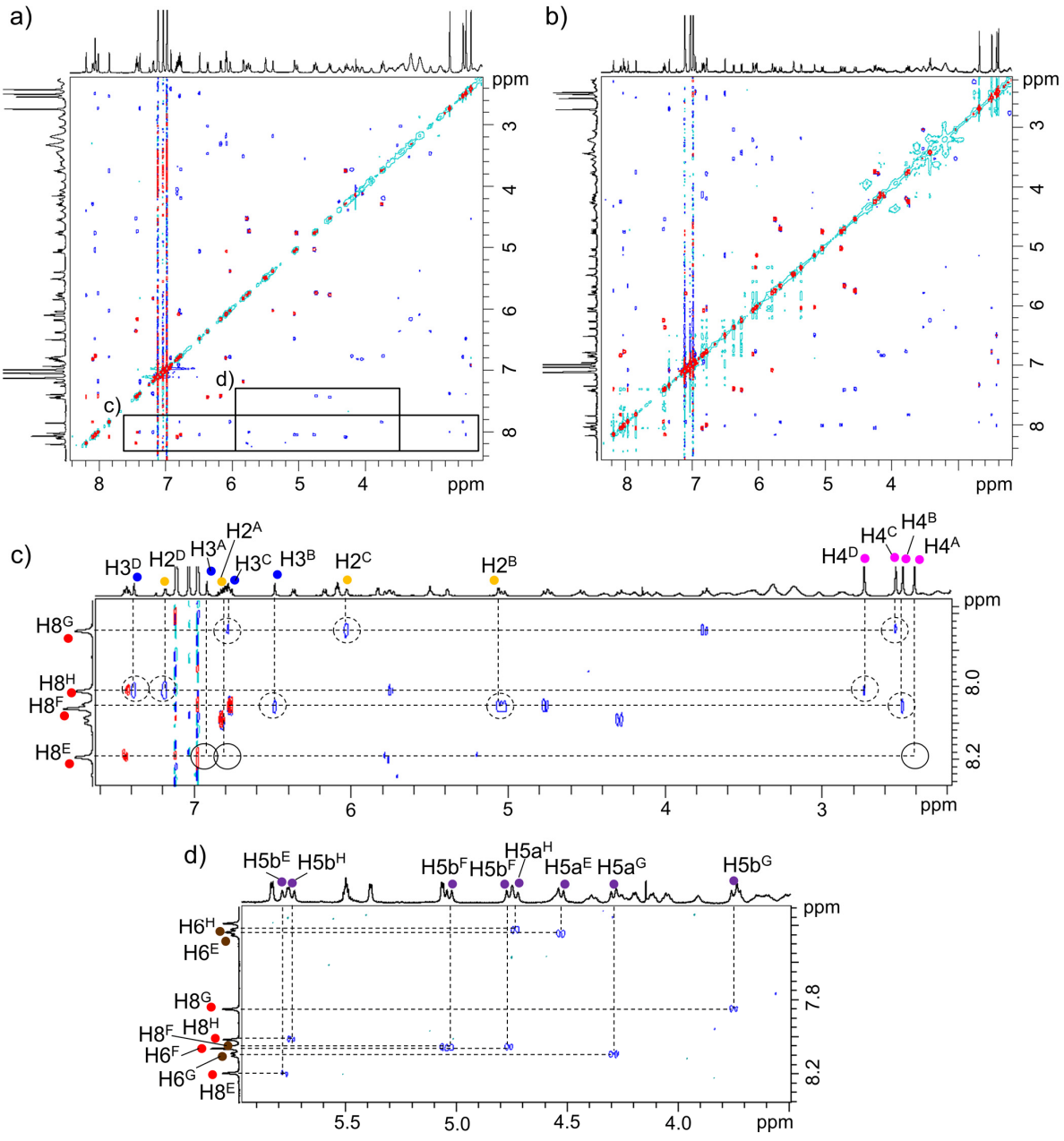

Figure 48 2D COSY (red signals) and ROESY (blue and cyan signals) NMR (600 MHz, c = 1 x 10^{-3} M) spectra of **Bis(MC) 3** in toluene-d_8 at a) 254 K and b) 284 K and c,d) significant regions of 2D COSY and ROESY NMR spectra of **Bis(MC) 3** in toluene-d_8 at 254 K with the assignment of the important proton signals.

The existence of cross-peaks between three sets of chromophore resonances with one of the red labelled signals of the spacer protons (Figure 48c) strongly suggests close spatial proximity of these protons (exemplified for one chromophore as solid black double arrows in Figure 47b; for details, see Figure A9), which is in agreement with the aggregate structural model. On the other hand, for one set of chromophore resonances no intermolecular cross-peaks were found at all, clearly providing an indication that this merocyanine unit must be located at the end of the octachromophoric stack. No intermolecular cross-peaks were found between proton resonances of different chromophores, which is in accordance with the assumption of antiparallel aligned chromophores in the stack. Furthermore, ROESY cross-peaks were observed between signals of the methylene protons (highlighted in purple, Figure 48d) and the respective spacer phenyl protons (highlighted in red and brown). One of the methylene protons shows close spatial proximity to the phenyl proton (highlighted in brown), while the other methylene proton is next to the red colored phenyl proton (dotted double arrows in Figure 47b). Thus, the conformation of the methylene group is clearly defined. Remarkably, under the conditions applied for the NMR experiments (c = 1 x 10^{-3} M, 254 K) no exchange signals were observed in the ROESY spectrum that would have appeared with a negative sign. This finding reveals that no exchange between the halves of individual molecules in the stack takes place within the time scale of the mixing time of the ROESY measurements (200 ms). Only at higher temperature (284 K) negative cross-peaks between signals of identically colored protons appear, revealing a dynamic exchange on the NMR time scale (cyan cross-peaks, Figure 48b). Additional, strong evidence for the proposed tetrameric aggregate structure of **Bis(MC) 3** is provided by DOSY NMR (Figure 49b). These experiments yielded a diffusion coefficient of D = 1.33 x 10^{-10} m^2 s^{-1} and a hydrodynamic radius of r = 13.0 Å was calculated by the Stokes-Einstein equation, which is in accordance with the dimensions of the tetramer structural model (Figure 49a) and thus, rules out the formation of larger aggregates. For adequate referencing, a DOSY NMR spectrum of **Bis(MC) 1** dimer, whose hydrodynamic radius is known from the crystal structure, has been measured under identical conditions (see the Appendix Figure A10). As expected, the diffusion coefficient of **Bis(MC) 1** dimer (D = 2.98 x 10^{-10} m^2 s^{-1}) is higher compared to the one of **Bis(MC) 3** tetramer.

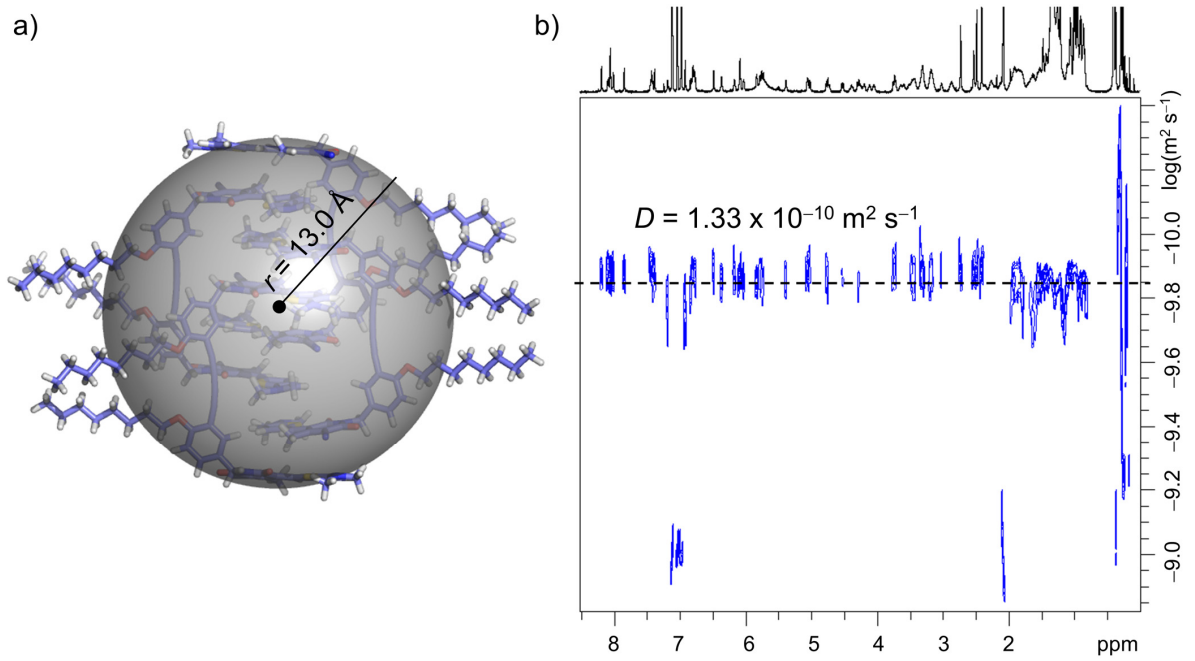

Figure 49 a) Illustration of the hydrodynamic diameter as obtained from the Stokes-Einstein equation based on DOSY NMR spectroscopy included as transparent grey sphere in the MMFF-minimized (*Maestro Macro Model*) aggregate model of **Bis(MC) 3**. b) 2D plot of DOSY NMR (600 MHz, 254 K) spectrum of **Bis(MC) 3** in toluene-d_8 (c = 1 x 10^{-3} M).

3.2.6 Quantum Chemical Calculations for Bis(MC) 3 Aggregate

Self-consistent-charge density functional based tight binding calculations (SCC-DFTB, parameter set mio-1-1, for details, see the Appendix) were performed for **Bis(MC) 3** aggregate involving structural information from NMR spectroscopic studies yielding the geometry-optimized aggregate structure of **Bis(MC) 3** (Figure 50). The calculated model shows a discrete centrosymmetric aggregate species comprising a stack of eight tightly packed chromophores with antiparallel orientation. The four DPB backbones are arranged around the columnar stack. Furthermore, the model demonstrates the high flexibility of the DPB spacer units that results in a bending of the backbones within the tetrameric aggregate. Thus, the interplanar distance between the two chromophores of each individual tweezer-type molecule is enlarged to around 13.4 Å and the merocyanine units can adopt a distance of around 3.5 Å within the stack, which is in the range of the ideal van der Waals distance.[120]

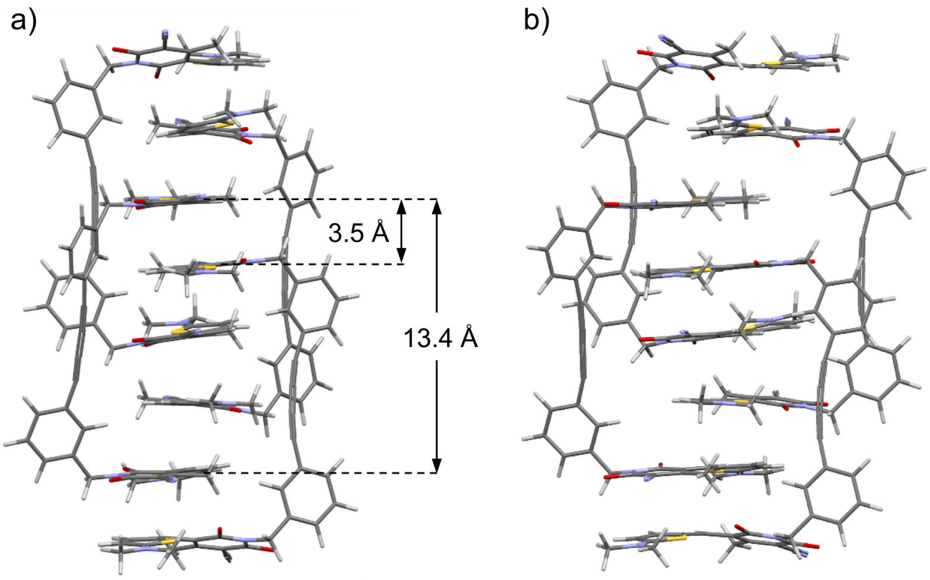

Figure 50 a,b) Side views of the SCC-DFTB (parameter set mio-1-1) geometry-optimized tetramer aggregate of **Bis(MC) 3**. Butyl chains are replaced by methyl groups and alkoxy residues by hydrogen atoms.

In order to rationalize the absorption properties of the herein investigated dye stacks in more detail, time-dependent density functional theory (TDDFT, ωB97[121]/def2-SVP[122], for details, see the Appendix) calculations were carried out on the geometry-optimized aggregate structure of **Bis(MC) 3**. Figure 51 shows the simulated absorption spectrum of **Bis(MC) 3** aggregate in comparison to the experimental one. Accordingly, the shape of the calculated spectrum is in good accordance with the experimental spectrum. For the stack consisting of eight chromophores, eight non-degenerated excited states are observed. The oscillator strength *f* (Appendix, Table A3) is largest for the highest excited state leading to a strongly allowed transition and therefore to an intense absorption band of the aggregate at higher energy compared to the monomer absorption. On the contrary, transitions to the lower excited states are either entirely forbidden ($f = 0$) or only partially allowed as evident from a low oscillator strength giving rise to weak absorption at lower energy. Hence, the good agreement between calculated and experimental spectra gives further evidence that **Bis(MC) 3** indeed self-assembles into tetramers with a stack of eight chromophores.

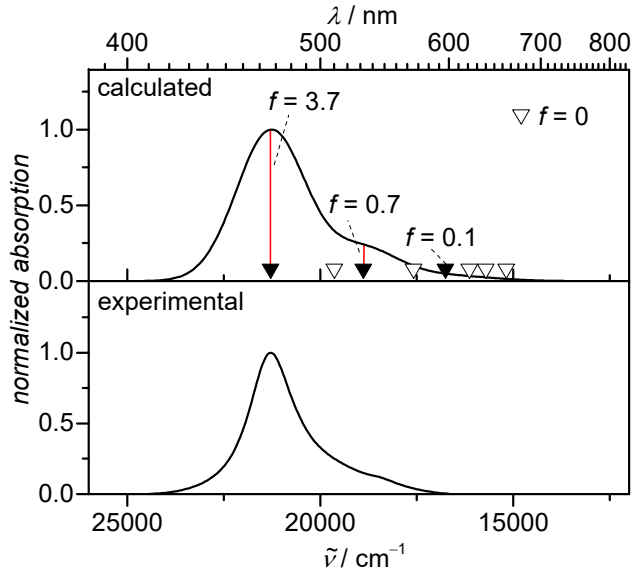

Figure 51 Simulated (top, calculated by TDDFT (ωB97[121]/def2-SVP[122])) and experimental (bottom, in THF/MCH mixture 17.5 : 82.5; calculated according to the tetramerization model) UV/vis absorption spectrum of the octachromophoric stack of **Bis(MC) 3** aggregate. The calculated absorption spectrum was shifted by 0.62 eV towards lower energies. A half-width at half maximum of 0.13 eV was used for the simulation of the spectrum.

3.2.7 Theoretical Investigations

The established series of merocyanine dye stacks enables systematic analysis of optical properties of the aggregates depending on the number of stacked chromophores.[4] According to Kasha,[15b, c] spectral changes upon dye aggregation can be attributed to exciton coupling between the transition dipole moments of the chromophores and therefore, it is reasonable to interpret the absorption properties of the merocyanine π-stacks in terms of exciton theory and to assume that the excited states of the dye stacks represent exciton states. Figure 52a shows the exciton state diagram of perfect H-aggregates with $N = 2, 4, 6, 8$ merocyanine chromophores. Coupling of N parallel aligned identical transition dipole moments μ_{eg} leads to a splitting of the excited state into N non-degenerated exciton states S_1^j ($j = 1, 2, \ldots N$). The energy of the exciton states E_j can be calculated from the eigenvalues of the corresponding Hamiltonian matrix (for details, see the Appendix Table A4 and previous work[20a]) by assuming a coupling energy $J = 1700$ cm^{-1} between next neighbours as it was found for these

[4] It is well known that H-type aggregates are in general nonfluorescent.[15c, 123] Thus, fluorescence properties of the merocyanine stacks are not considered in this thesis.

type of dyes by using atomic transition charges obtained from Mulliken population analysis of the transition densities (see also Chapter 4).[20a, 124]

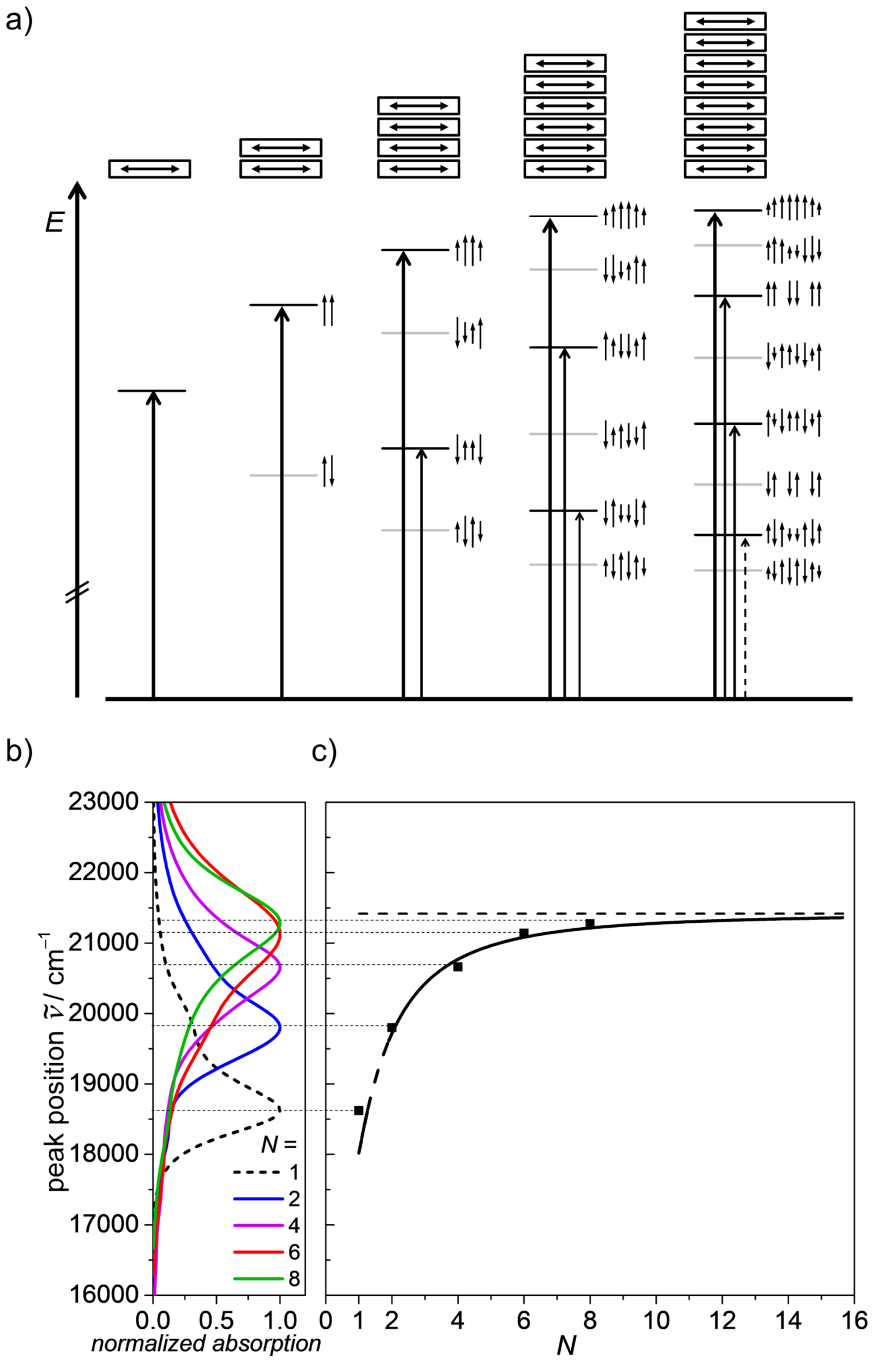

Figure 52 a) Energy level diagram of calculated exciton states based on exciton theory[15b, c] demonstrating allowed electronic transitions (long arrows) for monomers and H-stacks composed of $N = 2, 4, 6, 8$ interacting chromophores in the case of perfectly coplanar transition dipole moments represented as double arrows. b) Calculated absorption spectra of monomer (dotted black line) and dimeric stack (blue line) of the reference dye **59**, tetrachromophoric stack of **Bis(MC) 1** (purple line), hexachromophoric stack of **Bis(MC) 2** (red line) and octachromophoric stack of **Bis(MC) 3** (green line) in THF/MCH mixture (17.5 : 82.5) according to the respective aggregate model. c) Fit (black line) of the peak positions corresponding to the highest exciton state of the respective aggregates as a function of the number of stacked chromophores *N*.

For the highest exciton state of the respective dye stacks, all transition dipole moments couple in-phase as indicated by the small arrows in Figure 52a pointing in the same direction. The resulting value for the overall transition dipole moment is high since it is defined as the linear combination of the transition dipole moments of the individual chromophores. Thereby, the corresponding coefficients describe the contribution of the individual chromophores to the exciton states and are reflected by the length of the respective arrows. Hence, transition to the highest exciton state is strongly allowed, which is expressed by an intense absorption band at higher energy compared to the monomer absorption. In contrast, transition to the lower exciton state is forbidden in case of a bichromophoric stack, since the out-of-phase coupling leads to an annihilation of the overall transition dipole moment. Indeed, transition to S_1^1 and S_1^3 in the tetrachromophoric stack, S_1^1, S_1^3 and S_1^5 in the hexachromophoric stack and S_1^1, S_1^3, S_1^5 and S_1^7 in the octachromophoric stack are also forbidden due to the same reason. However, some of the lower exciton states are partially allowed (S_1^2 of the stack with $N = 4$ chromophores; S_1^2 and S_1^4 of the stack with $N = 6$ chromophores; S_1^2, S_1^4 and S_1^6 of the stack with $N = 8$ chromophores), due to the incomplete annihilation, as can be seen by the coefficients in Table A5–Table A8 in the Appendix. Consequently, contributions from the low energy exciton states are expected to appear in the absorption spectrum. The absorption of the stacks of reference compound **59**, **Bis(MC) 1**, **Bis(MC) 2** and **Bis(MC) 3** are displayed in Figure 52b. It becomes clear that the peak of the absorption shifts to the blue with increasing stack size from reference compound **59** to **Bis(MC) 3**. This blueshift is associated to the highest exciton state that gains energy with increasing aggregate size and exhibits the largest oscillator strength. With increasing stack size, a smooth shoulder of the absorption is observed at lower wavelengths, which is caused by partially allowed transitions to lower exciton states.

The energy of the highest exciton state for a stack consisting of N coupled identical chromophores with the same molecular transition energy E_0 and next neighbour coupling J can be described by Equation 1:[125]

$$E_N = E_0 + 2J \cos\left(\frac{j\pi}{N+1}\right), \quad (1)$$

with the index of the wave vector j that is equal to N for the highest transition energy E_N. The experimental transition energies E_N are extracted from the absorption maximum in the THF/MCH solvent mixture (Figure 42 and Table 1) of the individual stacks and are displayed in dependency of the chromophore number N in Figure 52c. The experimental data for $N = 2, 4, 6, 8$ were fitted by Equation 1 assuming the theoretically determined coupling of 1700 cm^{-1}.[20a, 124] The best fit is obtained for $E_0 = 18020$ cm^{-1} (black curve in Figure 52c).

This transition energy of 18020 cm^{-1} differs from the experimental one (18620 cm^{-1}), as van der Waals lowering and polarization effects are neglected in this model. However, comparing the fit of Equation 1 with the experimental data reveals that the absorption spectra of the stack series can be rationalized based on exciton theory. Furthermore, this theory predicts a plateau for large *N*, which is in accordance with the experimental data. It is noteworthy that the stack of eight chromophores with its peak position at $\lambda_{max,A}$ = 470 nm ($E_{max,A}$ = 21300 cm^{-1}) is already closely approaching the predicted value of $\lambda_{max,A}$ = 467 nm ($E_{max,A}$ = 21400 cm^{-1}) for an infinite π-stack.

3.3 Conclusion

In this chapter, a new strategy for the construction of large-sized, finite supramolecular π-stacks by self-assembly of bis(merocyanine) dyes has been introduced. Careful selection of the length of the spacer unit that defines the interplanar distance between the tethered chromophores directed the self-assembly of the respective bis(merocyanines) into centrosymmetric dimers, trimers and tetramers comprising large, structurally precise π-stacks of four, six or eight merocyanine chromophores with antiparallel orientation of the dipole moments. It could be demonstrated that the structure of such large supramolecular architectures can be adequately elucidated by commonly accessible analysis tools, in particular NMR techniques in combination with UV/vis measurements and mass spectrometry. Supported by TDDFT calculations, the absorption spectra of the herein investigated aggregates could be explained and a relationship between the absorption properties and the number of stacking chromophores could be established based on exciton theory. This work provides a viable approach to construct large supramolecular π-stacks of well-defined size and thus, for the first time a systematic analysis of the experimental absorption properties depending on the stack size could be achieved. Such model systems are useful to study the excited states of stacked aromatic entities and should inspire further theoretical investigations and time-resolved spectroscopy.

3.4 Appendix

Aggregation Models

Dimer:[18d] The equilibrium between monomer (M) and dimer (D) is given by M + M ⇌ D. The dimerization constant K_2 is given by

$$K_2 = \frac{c_D}{{c_M}^2} \tag{A1}$$

where c_M and c_D are the monomer and dimer concentration, respectively.

The molecular concentration of the solution is given by the sum of the concentration of the monomers and dimers:

$$c = c_M + 2c_D. \tag{A2}$$

Trimer: The equilibrium between monomer (M) and Trimer (T_3) is given by M + M + M ⇌ T_3. The next-neighbour trimerization constant K_3 that is defined as the binding constant per binding site is given by

$$K_3 = \sqrt{\frac{c_{T_3}}{{c_M}^3}} \tag{A3}$$

where c_M and c_{T_3} are the monomer and trimer concentration, respectively.

The molecular concentration of the solution is given by the sum of the concentration of the monomers and trimers:

$$c = c_M + 3c_{T_3}. \tag{A4}$$

Tetramer: The equilibrium between monomer (M) and Tetramer (T_4) is given by M + M + M + M ⇌ T_4. The next-neighbour tetramerization constant K_4 that is defined as the binding constant per binding site is given by

$$K_4 = \sqrt[3]{\frac{c_{T_4}}{{c_M}^4}} \tag{A5}$$

where c_M and c_{T_4} are the monomer and tetramer concentration, respectively.

The molecular concentration of the solution is given by the sum of the concentration of the monomers and tetramers:

$$c = c_M + 4c_{T_4}. \tag{A6}$$

These three different models were implemented into a global fitting algorithm according to a recent literature example[126] in order to fit the concentration-dependent extinction data of reference dye **59** and the **Bis(MC) 1**, **Bis(MC) 2** and **Bis(MC) 3**.

UV/vis Spectroscopic Studies

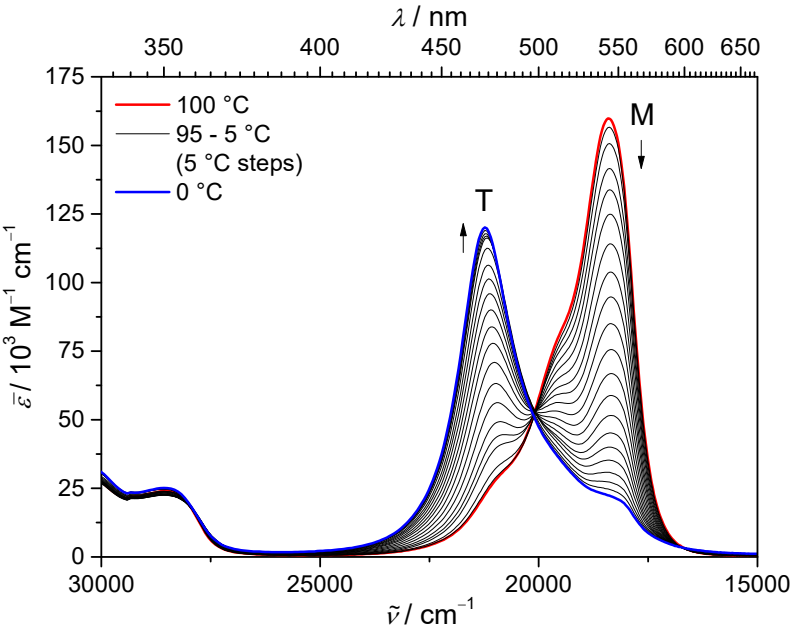

Figure A1 Density adjusted temperature-dependent (100 – 0 °C) UV/vis absorption spectra of **Bis(MC) 3** (c = 1 x 10^{-3} M) in toluene. The arrows indicate the decrease in the intensity of the monomer band (M, red line, $\lambda_{max,M}$ = 543 nm) and the appearance of the tetramer aggregate band (T, blue line, $\lambda_{max,T}$ = 471 nm) with decreasing temperature.

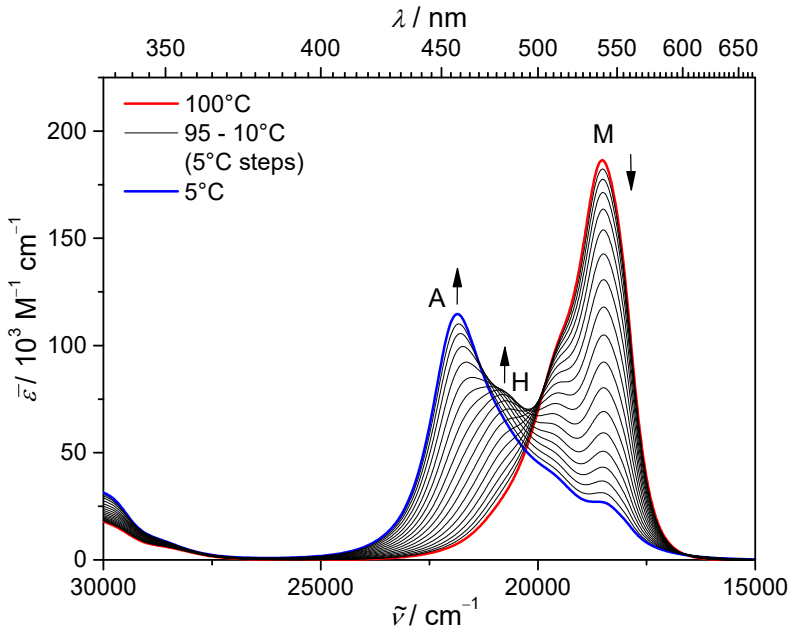

Figure A2 Density adjusted temperature-dependent (100 – 5 °C) UV/vis absorption spectra of **Bis(MC) 2** (c = 2 x 10^{-4} M) in toluene. The arrows indicate the decrease in the intensity of the monomer band (M, red line, $\lambda_{max,M}$ = 540 nm) and the appearance of the trimer aggregate band (H) and a further hypsochromically shifted aggregate band (A, blue line, $\lambda_{max,A}$ = 457 nm) with decreasing temperature.

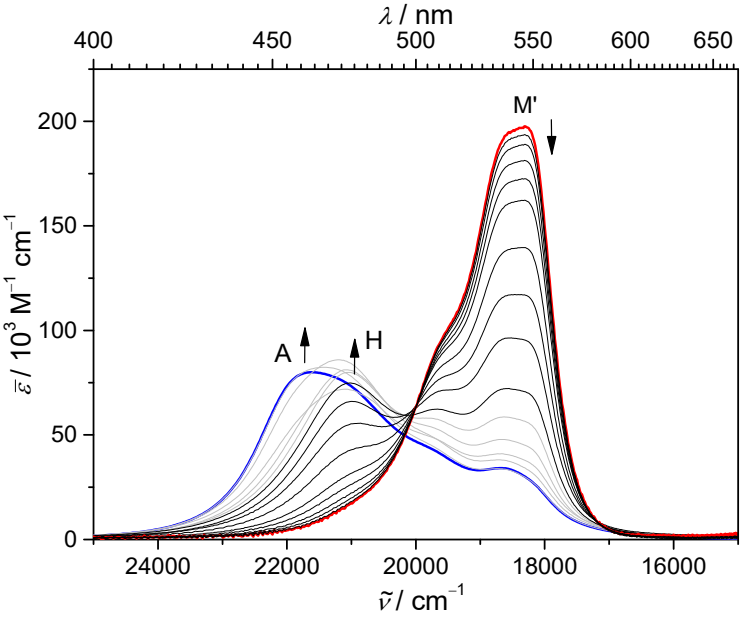

Figure A3 Concentration-dependent UV/vis spectra of **Bis(MC) 2** (c = 9.0 x 10^{-5} M – 3.9 x 10^{-8} M) in THF/MCH 25 : 75 at 295 K starting at high concentration (blue line) and successively diluting the solution (grey/black lines). The spectrum at lowest concentration is depicted in red line. Black arrows indicate the decrease in the intensity of the monomer band (M', $\lambda_{max,M'}$ = 548 nm) and the appearance of the trimer aggregate band (H, $\lambda_{max,H}$ = 474 nm) and a further hypsochromically shifted aggregate band (A, $\lambda_{max,A}$ = 460 nm) upon increasing concentration. Within the concentration range of c = 3.6 x 10^{-6} M – 3.9 x 10^{-8} M (black lines) one well-defined isosbestic point is observed, which gets lost at higher concentration (c = 9.0 x 10^{-5} M – 6.1 x 10^{-6} M, grey lines) due to the formation of an extended aggregate species.

Mass Spectrometry

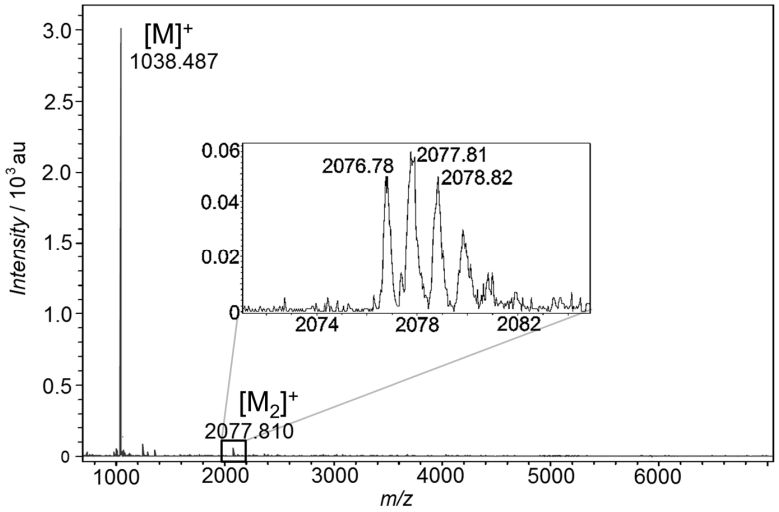

Figure A4 MALDI-TOF mass spectrum of **Bis(MC) 1** in positive-ion mode. The sample was prepared by solvent evaporation of a chloroform solution of **Bis(MC) 1** containing DCTB as a matrix. $[M]^+$ and $[M_2]^+$ denote the mass peaks corresponding to the singly charged monomer and dimer cation, respectively.

NMR Spectroscopic Studies

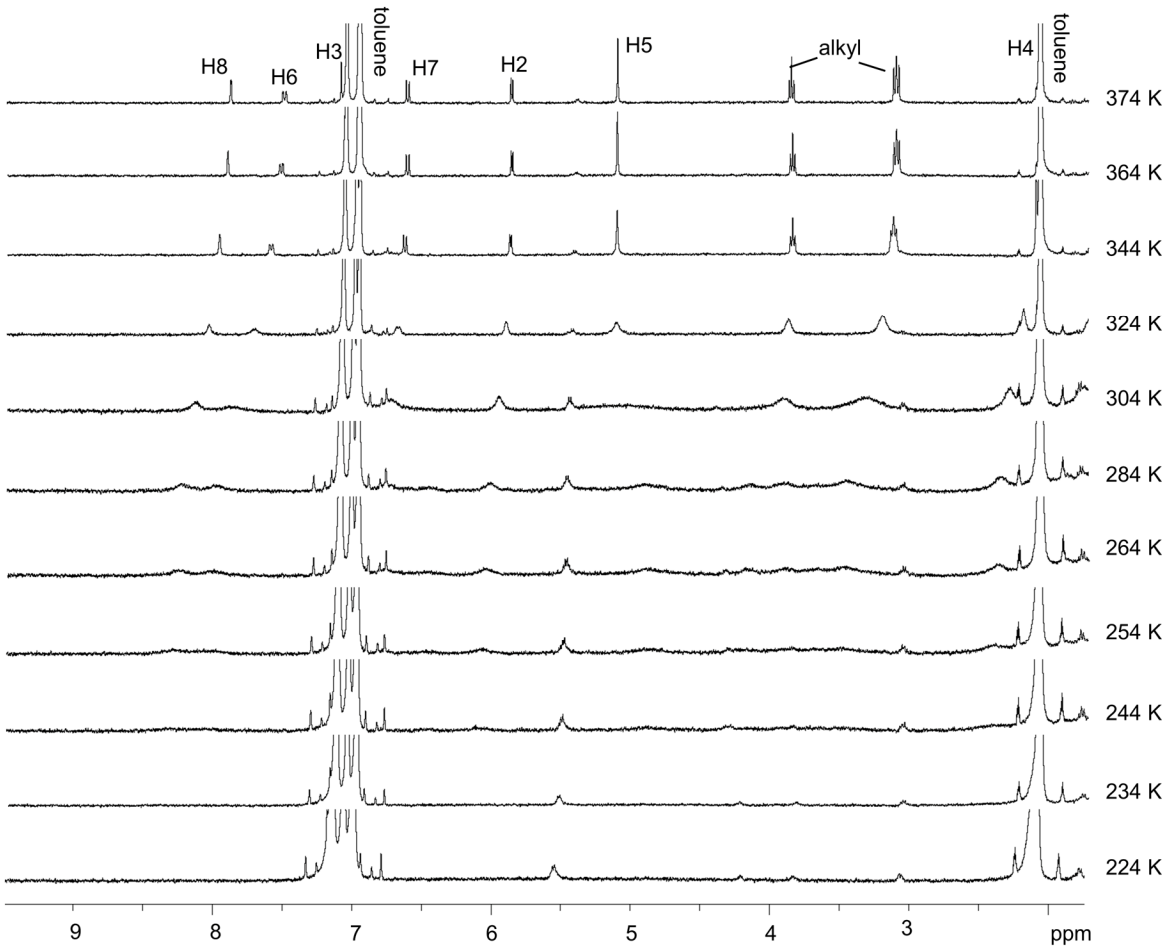

Figure A5 Selected area of temperature-dependent ^{1}H NMR (400 MHz) spectra of **Bis(MC) 2** in toluene-d_8 at $c = 2 \times 10^{-4}$ M starting at 374 K (top, with the assignment of the important proton signals) and successively decreasing the temperature to 224 K (bottom).

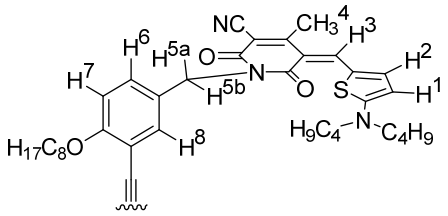

Figure A6 Half of the structure of **Bis(MC) 2** with the assignment of significant protons. Chemically equivalent parts of this symmetric molecule are omitted for clarity. The chromophore and backbone moieties of the molecule show one set of signals in the ^{1}H NMR monomer spectrum (400 MHz, toluene-d_8, 374 K).

Table A1 Summary of ^{1}H NMR data (400 MHz, toluene-d_8): chemical shifts δ (ppm) and coupling constants J (Hz), and assignment of significant chromophore (H1−H4) and backbone proton (H5–H8) signals of **Bis(MC) 2** monomer (at 374 K).

chromophore protons	**H1**	**H2**	**H3**	**H4**
	(overlapped with solvent signal	5.87 (d, ^{3}J = 5.0, 2H)	7.09 (s, 2H)	2.09 (overlapped with solvent signal)

backbone protons	**H5**	**H6**	**H7**	**H8**
	5.11 (s, 4H)	7.50 (dd, ^{3}J = 8.5, ^{4}J = 2.1, 2H)	6.62 (d, ^{3}J = 8.6, 2H)	7.88 (d, ^{4}J = 2.1, 2H)

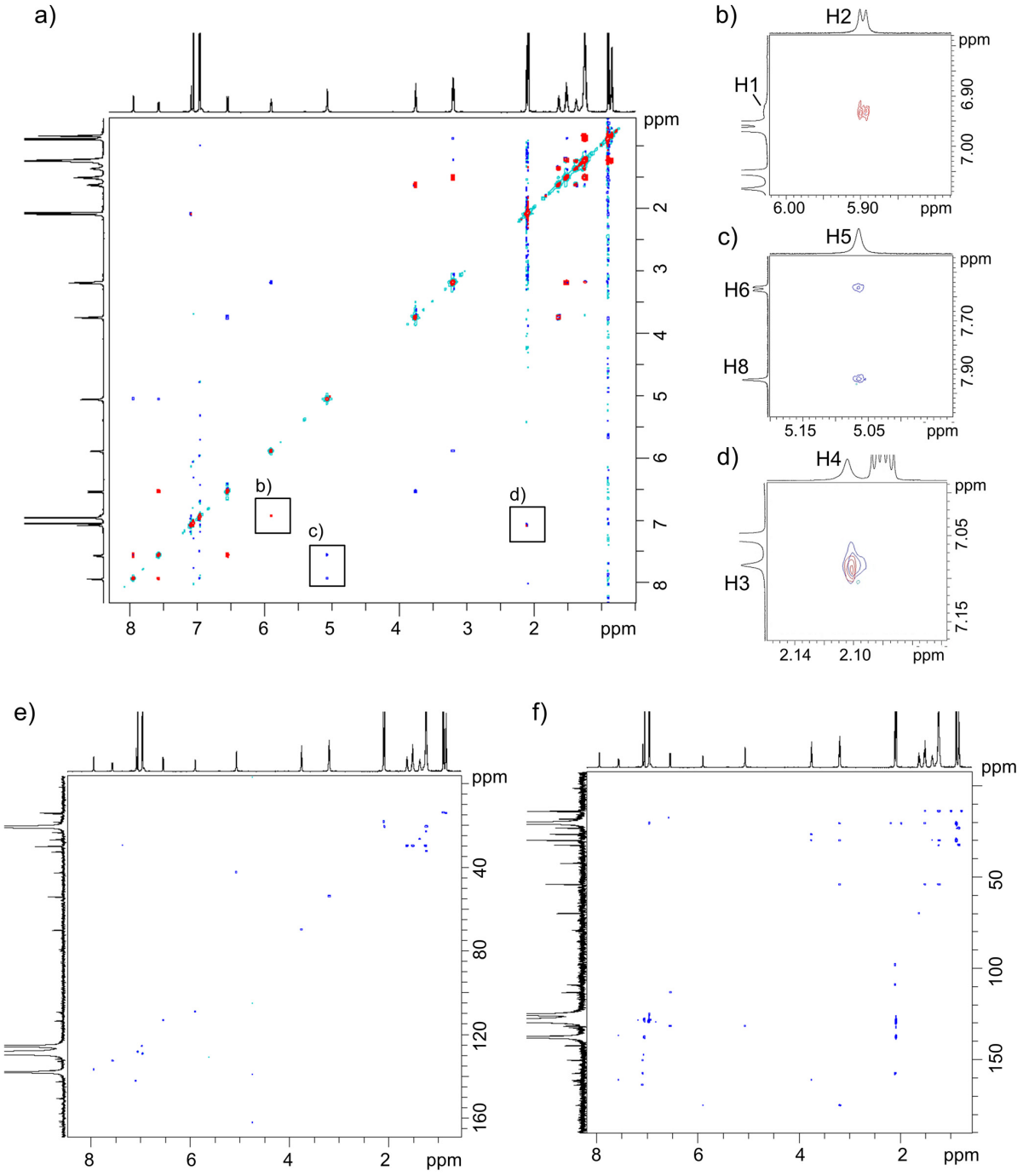

Figure A7 2D NMR (600 MHz) spectra of **Bis(MC) 3** in toluene-d_8 at 374 K (c = 1 x 10^{-3} M): a) Entire spectrum and b-d) selected regions of 2D COSY (red signals) and ROESY (blue signals) spectra; e) HSQC and f) HMBC spectra.

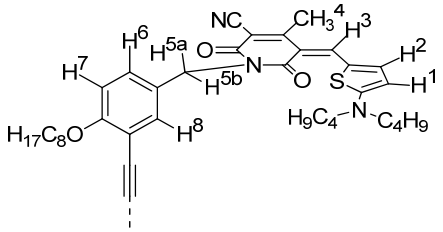

Figure A8 Half of the structure of **Bis(MC) 3** with the assignment of significant protons. Chemically equivalent parts of this symmetric molecule are omitted for clarity. The chromophore and backbone moieties of the molecule show one set of signals in the ^{1}H NMR monomer spectrum (600 MHz, toluene-d_8, 374 K) and four sets of signals (denoted as A–D for the chromophores and E–H for the backbones) in the ^{1}H NMR aggregate spectrum (600 MHz, toluene-d_8, 254 K).

Table A2 Summary of ^{1}H NMR data (600 MHz, toluene-d_8): chemical shifts δ (ppm) and coupling constants J (Hz), and assignment of significant chromophore (H1–H4) and backbone proton (H5–H8) signals of **Bis(MC) 3** monomer (at 374 K) and aggregate (at 254 K). The four sets of signals for the chromophore protons in the aggregate are denoted as A, B, C, D and for the aggregate backbone protons as E, F, G and H.

chromophore protons		**H1**	**H2**	**H3**	**H4**
monomer		6.93 (br, overlapped with solvent signal	5.89 (d, ^3J = 4.9, 2H)	7.08 (s, 2H)	2.10 (s, 6H)
aggregate	**A**	6.09 (d, ^3J = 5.1, 2H)	6.80 (d, ^3J = 5.0, 2H)	6.91 (s, 2H)	2.41 (s, 6H)
	B	6.08 (d, ^3J = 5.1, 2H)	5.06 (d, ^3J = 4.9, 2H)	6.48 (s, 2H)	2.48 (s, 6H)
	C	5.38 (d, ^3J = 4.6, 2H)	6.02 (d, ^3J = 4.6, 2H)	6.78 (s, 2H)	2.53 (s, 6H)
	D	5.83 (d, ^3J = 5.1, 2H)	7.18 (d, ^3J = 5.1, 2H)	7.38 (s, 2H)	2.72 (s, 6H)

backbone protons		**H5**		**H6**	**H7**	**H8**
		H5a	**H5b**			
monomer		5.06 (s, 4H)		7.56 (d, ^3J = 8.6, 2H)	6.53 (d, ^3J = 8.6, 2H)	7.94 (s, 2H)
aggregate	**E**	4.52 (d, ^3J = 13.9, 2H)	5.77 (d, ^3J = 13.9, 2H)	7.43 (d, ^3J = 8.5, 2H)	6.36 (d, ^3J = 8.5, 2H)	8.19 (s, 2H)
	F	4.76 (d, ^3J = 13.6, 2H)	5.03 (d, ^3J = 13.5, 2H)	8.05 (d, overlapped with H8^F)	6.76 (d, ^3J = 9.2, 2H)	8.05 (s, 2H)
	G	4.29 (d, ^3J = 14.2, 2H)	3.74 (d, ^3J = 14.3, 2H)	8.09 (d, ^3J = 8.9, 2H)	6.82 (d, ^3J = 8.9, 2H)	7.84 (s, 2H)
	H	4.73 (d, ^3J = 14.0, 2H)	5.74 (d, ^3J = 14.0, 2H)	7.42 (d, ^3J = 8.6, 2H)	6.16 (d, ^3J = 8.6, 2H)	8.00 (s, 2H)

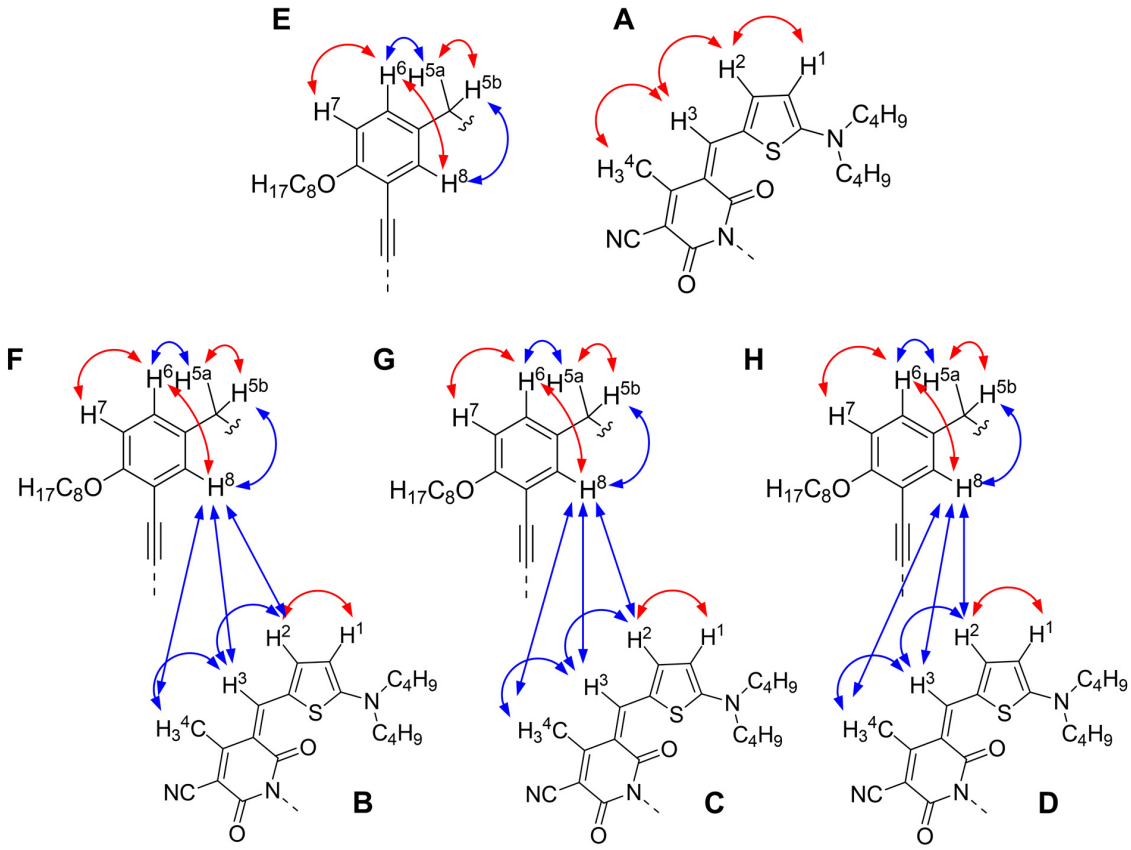

Figure A9 Visualization of intra- as well as intermolecular proton couplings observed in 2D COSY (red arrows) and ROESY (blue arrows) NMR (600 MHz) spectra of **Bis(MC) 3** in toluene-d_8 at 254 K (c = 1 x 10^{-3} M). A–D represent chromophores and E–H parts of the backbones with different chemical environments.

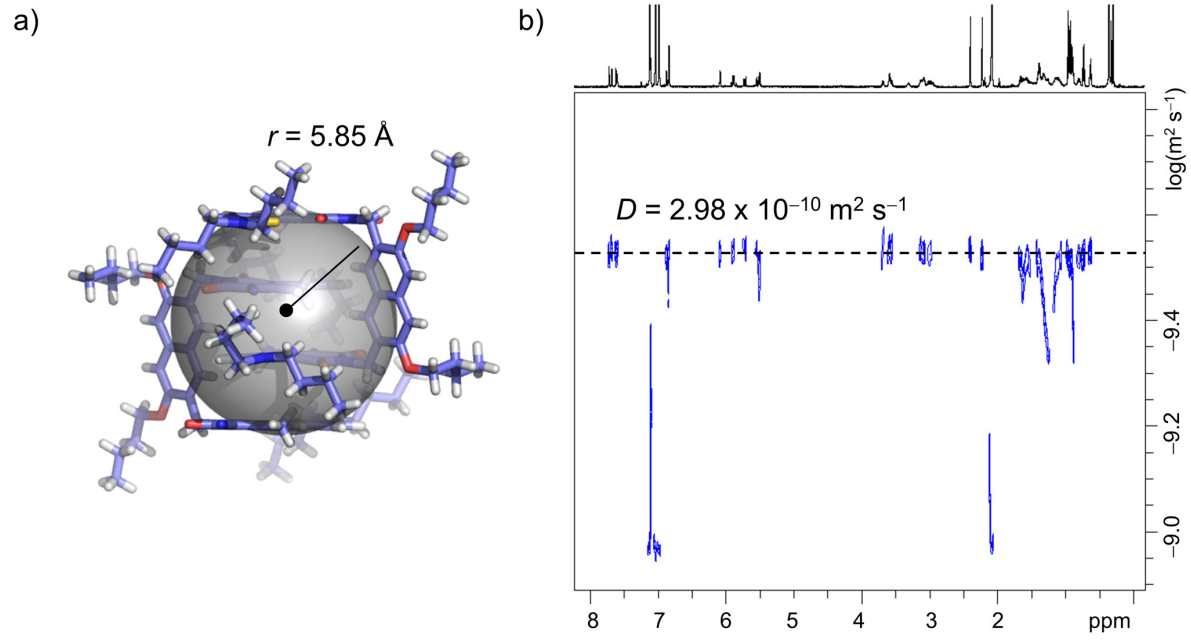

Figure A10 a) Illustration of hydrodynamic diameter as obtained from the Stokes-Einstein equation based on DOSY NMR spectroscopy included as transparent grey sphere in the dimeric unit of the crystal structure of **Bis(MC) 1**. b) 2D plot of DOSY NMR (600 MHz, 254 K) spectrum of **Bis(MC) 1** in toluene-d_8 (c = 1 x 10^{-3} M).

Computational Details

Geometry-optimization of **Bis(MC) 3** aggregate was performed by SCC-DFTB calculations using the parameter set mio-1-1 as implemented in the program ADF (Amsterdam density functional) package.[127] Butyl chains were replaced by methyl groups and alkoxy residues by hydrogen atoms.

TDDFT calculation (ωB97[121]/def2-SVP[122]) was performed on the geometry-optimized structure (DFTB). The UV/vis spectrum (Figure 51) was simulated with the help of the GaussView 5[128] visualization software package using the results obtained by TDDFT calculations. To reduce computational efforts, spacer units of the bis(merocyanine) molecules were omitted for the calculation. A half-width at half maximum of 0.13 eV was used for the simulation of the spectrum. In addition, the spectrum was shifted by 0.62 eV towards lower energies for better comparability with the experimental one.

Table A3 Exciton state energies E_j ($j = 1, 2, \ldots N$) and the corresponding oscillator strengths f of **Bis(MC) 3** aggregate obtained by TDDFT (ωB97[121]/def2-SVP[122]) calculations.

j	1	2	3	4	5	6	7	8
E_j / cm^{-1}	20200	20700	21100	21700	22600	23900	24600	26300
f	0.01	0.02	0.02	0.08	0.04	0.74	0.04	3.66

Theoretical Investigations

Table A4 Exciton state energies E_j ($j = 1, 2, \ldots N$) of the aggregate of reference dye **59** and of **Bis(MC) 1**, **Bis(MC) 2** and **Bis(MC) 3** calculated from the eigenvalues E_{Ej} of the corresponding Hamiltonian matrix.

	59	**Bis(MC) 1**[a]	**Bis(MC) 2**[a]	**Bis(MC) 2**[a]
E_1	16407 cm^{-1}	15646 cm^{-1}	15044 cm^{-1}	14989 cm^{-1}
E_2	19807 cm^{-1}	17098 cm^{-1}	15987 cm^{-1}	15565 cm^{-1}
E_3	-	19116 cm^{-1}	17350 cm^{-1}	16448 cm^{-1}
E_4	-	20568 cm^{-1}	18864 cm^{-1}	17531 cm^{-1}
E_5	-	-	20227 cm^{-1}	18683 cm^{-1}
E_6	-	-	21170 cm^{-1}	19766 cm^{-1}
E_7	-	-	-	20649 cm^{-1}
E_8	-	-	-	21225 cm^{-1}

[a]translated by E_{Ej} + 18107 cm^{-1} due to the definition of the zero level.

Table A5 Calculated coefficients *c* of the normed eigenvectors of the Hamiltonian matrix of the bichromophoric stack of reference dye **59**.

	c_1	c_2
E_{E1}	–0.7071	0.7071
E_{E2}	0.7071	0.7071

Table A6 Calculated coefficients *c* of the normed eigenvectors of the Hamiltonian matrix of the tetrachromophoric stack of **Bis(MC) 1**.

	c_1	c_2	c_3	c_4
E_{E1}	0.3717	–0.6015	0.6015	–0.3717
E_{E2}	–0.6015	0.3717	0.3717	–0.6015
E_{E3}	–0.6015	–0.3717	0.3717	0.6015
E_{E4}	0.3717	0.6015	0.6015	0.3717

Table A7 Calculated coefficients *c* of the normed eigenvectors of the Hamiltonian matrix of the hexachromophoric stack of **Bis(MC) 2**.

	c_1	c_2	c_3	c_4	c_5	c_6
E_{E1}	0.2319	–0.4179	0.5211	–0.5211	0.4179	–0.2319
E_{E2}	–0.1479	0.5211	–0.2319	–0.2319	0.5211	–0.4179
E_{E3}	–0.5211	0.2319	0.4179	–0.4179	–0.2319	0.5211
E_{E4}	0.5211	0.2319	–0.4179	–0.4179	0.2319	0.5211
E_{E5}	–0.4179	–0.5211	–0.2319	0.2319	0.5211	0.4179
E_{E6}	0.2319	0.4179	0.5211	0.5211	0.4179	0.2319

Table A8 Calculated coefficients *c* of the normed eigenvectors of the Hamiltonian matrix of the octachromophoric stack of **Bis(MC) 3**.

	c_1	c_2	c_3	c_4	c_5	c_6	c_7	c_8
E_{E1}	–0.1612	0.3030	–0.4082	0.4642	–0.4642	0.4082	–0.3030	0.1612
E_{E2}	0.3030	–0.4642	0.4082	–0.1612	–0.1612	0.4082	–0.4642	0.3030
E_{E3}	0.4082	–0.4082	0	0.4082	–0.4082	0	0.4082	–0.4082
E_{E4}	0.4642	–0.1612	–0.4082	0.3030	0.3030	–0.4082	–0.1612	0.4642
E_{E5}	0.4642	0.1612	–0.4082	–0.3030	0.3030	0.4082	–0.1612	–0.4642
E_{E6}	0.4082	0.4082	0	–0.4082	–0.4082	0	0.4082	0.4082
E_{E7}	–0.3030	–0.4642	–0.4082	–0.1612	0.1612	0.4082	0.4642	0.3030
E_{E8}	0.1612	0.3030	0.4082	0.4642	0.4642	0.4082	0.3030	0.1612

Chapter 4

—

Foldamers as Model Systems for the Elucidation of Optical Properties of Homo- and Hetero-Merocyanine π-Stacks

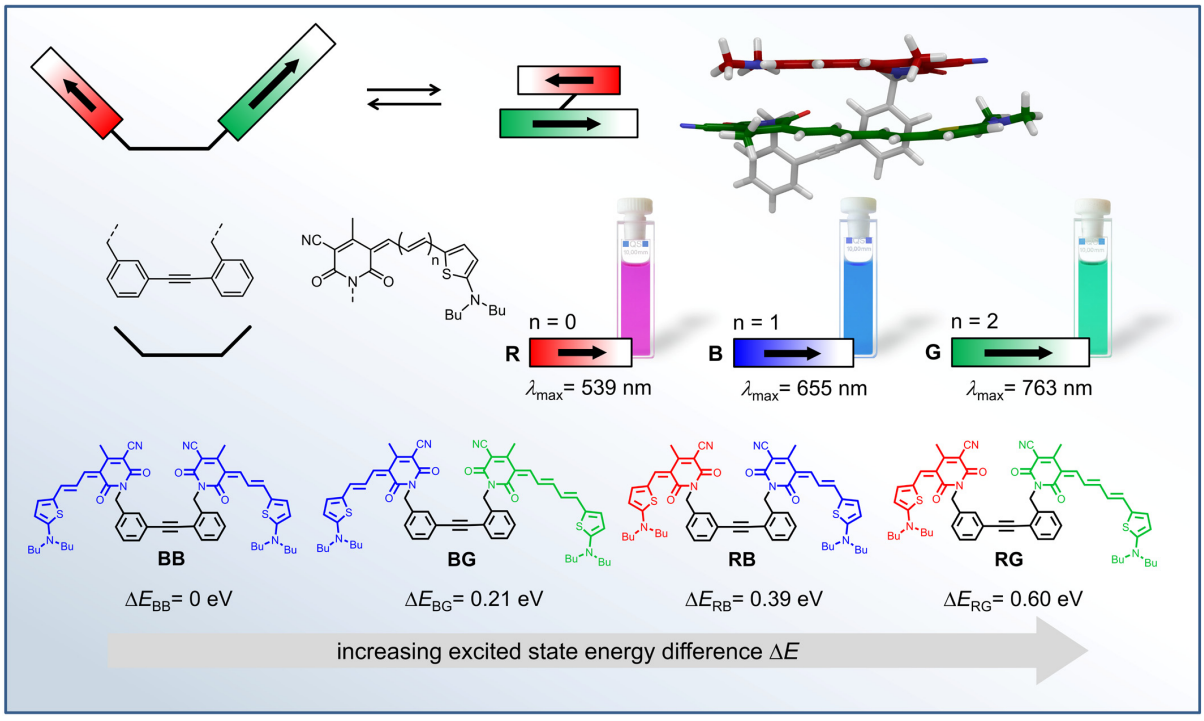

4.1 Introduction

The functional properties of dye aggregates strongly depend on their optical features, which are influenced by interchromophoric interactions.[13, 21b, c, 22c, 129] In this regard, exciton coupling between chromophores plays an important role as demonstrated by the pioneering work of Davydov[15a] and Kasha.[15c, 83] Meanwhile it has been amply demonstrated that exciton theory is applicable to aggregated π-systems of identical chromophores,[119, 130] but exciton coupling between different chromophores has only been investigated for few examples interpreted in controversial manners.[131] Recently, it was shown that structurally well-defined π-stacks of two equal merocyanine dyes are accessible in low polarity solvents by connecting two chromophores by a rigid diphenylacetylene spacer unit.[19h] The ideal preorganization of the dyes allows a folding into cofacially stacked dimers driven by dipole-dipole interaction with antiparallel orientation of the two chromophores. This homo-dimer clearly showed strong H-type coupling which could be explained based on molecular exciton theory. Hence, the same spacer unit was applied to tether two dipolar merocyanine chromophores of different conjugation length resulting in the formation of hetero-dimers.[19h] Interestingly, the absorption properties of these π-stacks differed significantly from the absorption properties of the constituent monomeric dyes, suggesting also a strong exciton coupling between the different types of chromophores. Inspired by these findings, this work systematically investigates the influence of exciton coupling on the absorption properties of highly defined hetero-dye aggregates with varying differences in the excited state energies ΔE of the adjacent chromophores. For this purpose hetero-bis(merocyanine) dyes **BG** (ΔE_{BG} = 0.21 eV), **RB**[19h] (ΔE_{RB} = 0.39 eV) and **RG** (ΔE_{RG} = 0.60 eV) containing variable combinations of two of the three merocyanine units **R** (red), **B** (blue) and **G** (green) with different conjugation length (Figure 53) were synthesized.

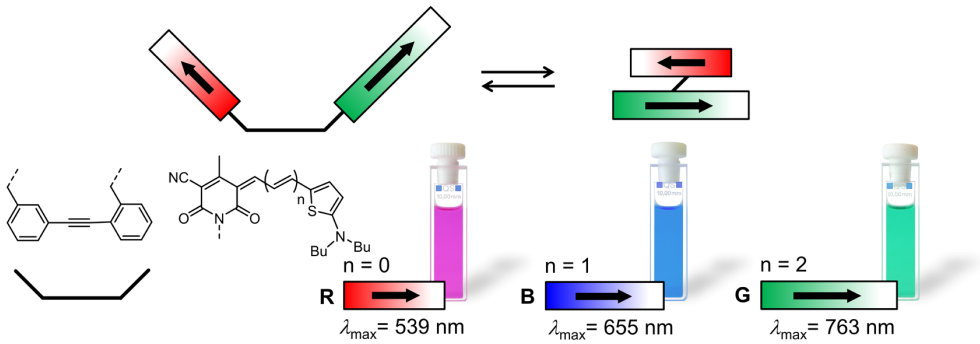

Figure 53 Schematic representation of the folding process of a bis(merocyanine) dye containing variable combinations of two of the three merocyanine units **R** (red), **B** (blue) and **G** (green) with different conjugation length.

The extension of the chromophore π-system affects the electronic properties leading to a red shift of the absorption maximum λ_{max}.[82, 132] Homo-bis(merocyanine) dyes **RR**,[19h] **BB** and **GG** are included in the studies for comparison and dyes **R**,[82] **B**[82] and **G** serve as monochromophoric references. The chemical structures of all bis(merocyanine) dyes and the reference merocyanines applied in this study are depicted in Figure 54.

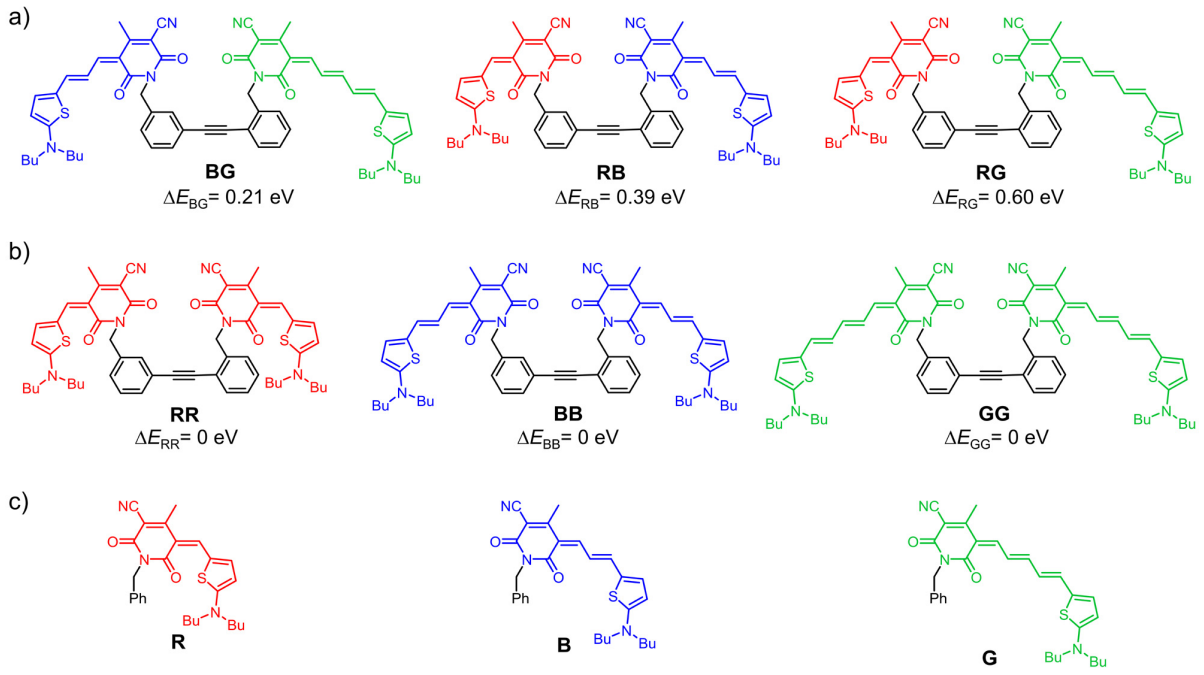

Figure 54 Chemical structures of a) hetero-bis(merocyanines) **BG**, **RB** and **RG**, b) homo-bis(merocyanines) **RR**, **BB** and **GG** and c) the monochromophoric reference dyes **R**, **B** and **G** employed in this work.

4.2 Results[5]

4.2.1 Synthesis

The synthesis of all hetero- and homo-bis(merocyanine) dyes applied in this study is described in Scheme 3. Whereas bis(merocyanines) **BG**, **RG**, **BB** and **GG** were newly synthesized, preparation of dyes **RR**[6] and **RB** has recently been reported.[19h] Compounds **BG** and **RG** comprising different types of chromophores were synthesized by Pd-catalyzed Sonogashira coupling reaction of the corresponding precursors **69a**,**b** and **71b** in 17%, and 15% yield,

[5] (Time-dependent) DFT calculations and the synthesis of bis(merocyanine) **RB** were performed by Dr. David Bialas. X-ray analysis was performed by Dr. David Schmidt.
[6] Whereas in Ref. [19h] bis(merocyanine) **RR** has been synthesized by Knoevenagel condensation of the respective merocyanine building blocks, in the present work it was prepared according to Scheme 3 by the synthetic route of homo-bis(merocyanine) dyes.[133]

respectively. The preparation of merocyanine precursors **69a**[19h] and **71a**[19h] has previously been reported and **69b** was synthesized in analogous manner by Knoevenagel condensation of hydroxy pyridone **68**[19h] with aminothiophene aldehyde **66b**.[82] The acetylene functionalized derivative **71b** was prepared in good yield (62%) by condensation of hydroxy pyridone **70**[19h] with aminothiophene aldehyde **66c**.

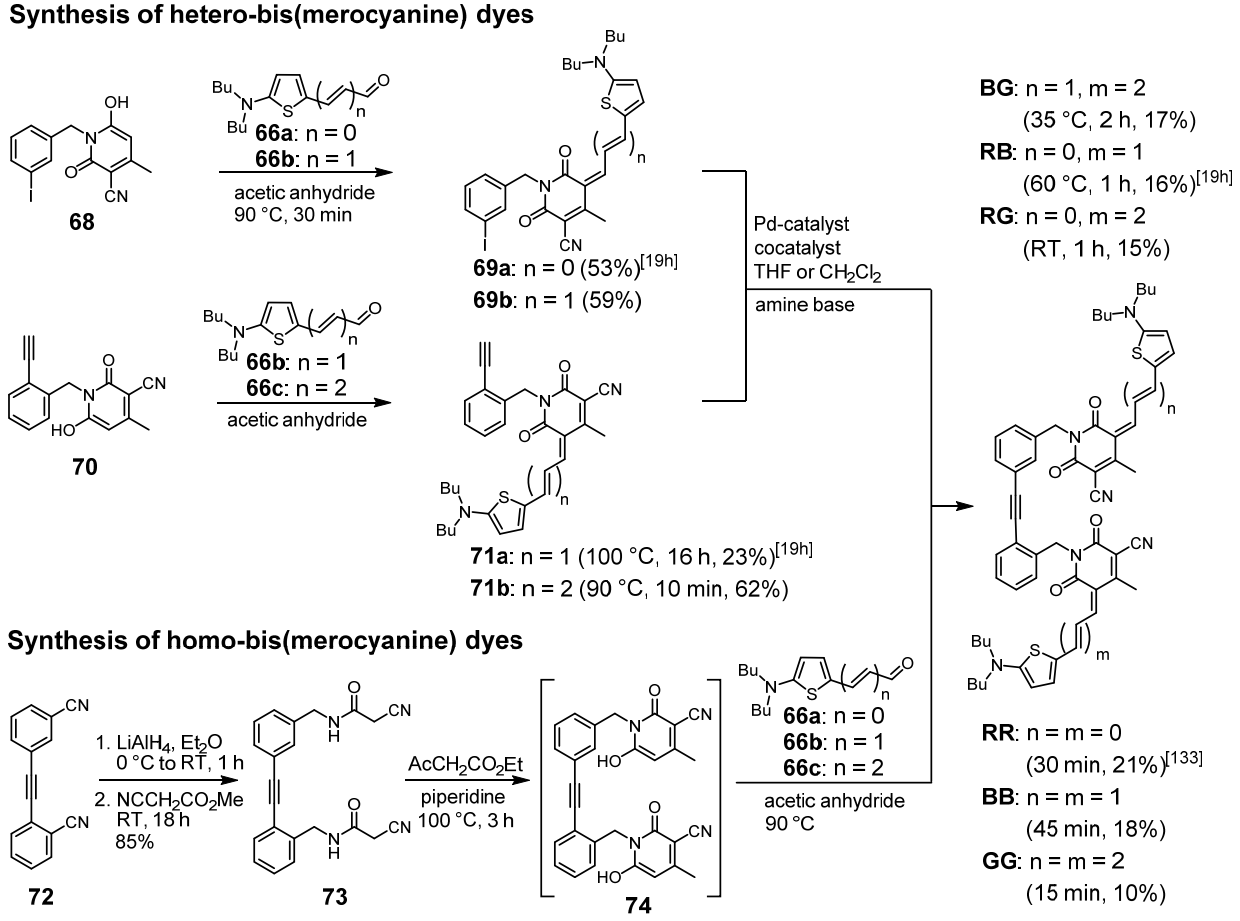

Scheme 3 Synthesis of hetero-bis(merocyanines) **BG**, **RB**[19h] and **RG** (top) and homo-bis(merocyanines) **RR**,[133] **BB** and **GG** (bottom).

Homo-bis(merocyanine) dyes **RR**,[133] **BB** and **GG** bearing the same chromophores were synthesized starting with the reduction of literature known bis(cyano) compound **72**[134] using lithium aluminum hydride in diethyl ether. The resulting bis(amine) was subsequently converted to bis(amide) **73** with methyl cyanoacetate under solvent-free conditions. Reacting **73** with ethyl acetoacetate in piperidine at 100 °C provided bis(hydroxypyridone) **74**,[133] which was then used without further purification for Knoevenagel condensation with the respective aminothiophene aldehyde **66a-c** affording the desired homo-bis(merocyanine) dyes in an overall yield of 21% (**RR**), 18% (**BB**) and 10% (**GG**). Employing this synthetic route, the

formation of Glaser coupling side products could be avoided which should complicate the separation of the desired products by column chromatography due to similar polarity.

The π-extended aminothiophene aldehyde **66c**[7] was prepared by Wittig olefination of literature known aminothiophene aldehyde **66b**[82] with (1,3-dioxolan-2-ylmethyl)tributylphosphonium bromide using sodium hydride as a base and subsequent cleavage of the acetal group with hydrochloric acid in almost quantitative yield (Scheme 4).

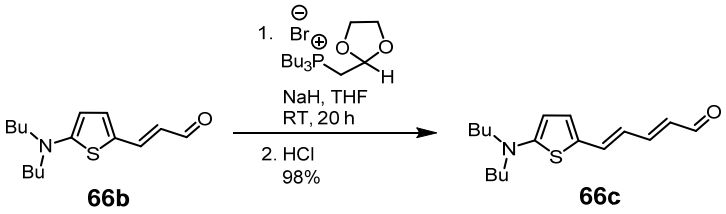

Scheme 4 Preparation of aminothiophene aldehyde **66c** by Wittig olefination.

Reference merocyanine **G** was synthesized by Knoevenagel condensation of literature known hydroxy pyridone **75**[82] with the π-extended aminothiophene aldehyde **66c** in acetic anhydride at 90 °C in a yield of 42% (Scheme 5).

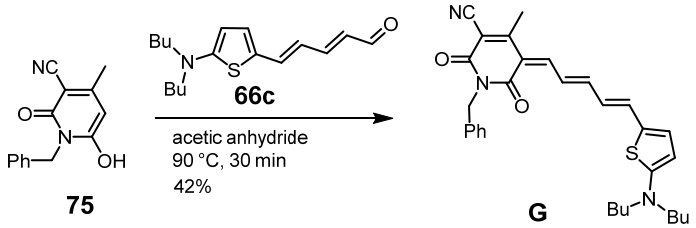

Scheme 5 Synthesis of reference merocyanine **G** by Knoevenagel condensation of hydroxy pyridone **75** with aminothiophene aldehyde **66c**.

All merocyanine dyes were purified by column chromatography on silica gel followed by precipitation from a DCM/*n*-hexane solution and subsequent filtration. For detailed synthetic procedures and full characterization of the new bis(merocyanine) dyes as well as of reference dye **G** and the precursors see the Experimental Section.

[7] The synthesis of aminothiophene aldehyde **66c** was performed by Lisa Gerbig.[135]

4.2.2 UV/vis Spectroscopy

The aggregation of merocyanine dyes is driven by dipole-dipole interactions and is therefore strongly influenced by the solvent polarity.[18a] Accordingly, strong interactions are given in low polarity solvents such as hexanes, tetrachloromethane or dioxane whereas only a weak driving force for the antiparallel stacking is observed in dipolar solvents such as dichloromethane, THF or DMF.[18b, d] Hence, the folding process of the investigated bis(merocyanine) dyes was analyzed by solvent-dependent UV/vis absorption spectroscopy starting in pure dichloromethane (DCM), a solvent of already considerable polarity (ε = 8.93), which is known to favour the unfolded conformation.[19g, h] Then, the volume ratio of the low polarity solvent 1,4-dioxane (ε = 2.25) was successively increased to shift the equilibrium towards the folded species. For a summary of the absorption maxima and the corresponding extinction coefficients of all bis(merocyanines) as well as of the reference dyes see the Appendix (Table A9). Solvatochromism effects can play a significant role for dipolar dyes like merocyanines[136] and thus, also reference dyes **R**, **B** and **G** were investigated by solvent-dependent UV/vis absorption studies (Figure 55). As expected, by increasing the conjugation length of the chromophores the absorption maximum in DCM solution is shifted towards longer wavelengths (Figure 55, thick dashed lines). Hence, the absorption band of reference dye **R** shows a maximum at 539 nm whilst the maximum of **B** is bathochromically shifted by 116 nm (λ_{max} = 655 nm) and that of reference **G** is shifted by another 108 nm towards longer wavelengths (λ_{max} = 763 nm). For **R** only a weak solvatochromism is observed upon increasing the amount of 1,4-dioxane (Figure 55a), while dye **B** (Figure 55b) and most pronounced dye **G** (Figure 55c) show considerable enhanced vibronic coupling in unpolar solvents with an increase of the 0−1 absorption band.[136-137] Since the absorption spectra in pure 1,4-dioxane are independent of concentration within the applied concentration range (see the Appendix, Figure A11), intermolecular aggregation of the reference dyes can be excluded and thus, the solvent-dependent spectral changes can definitely be ascribed to solvatochromism.[136] The origin of this solvatochromism includes a significant change of the dyes' π-scaffold, which is in a more polyene-like structure with bond length alternation in unpolar environment but polarized by more polar environment into the so-called cyanine limit with equal bond lengths along the polymethine chain.[138]

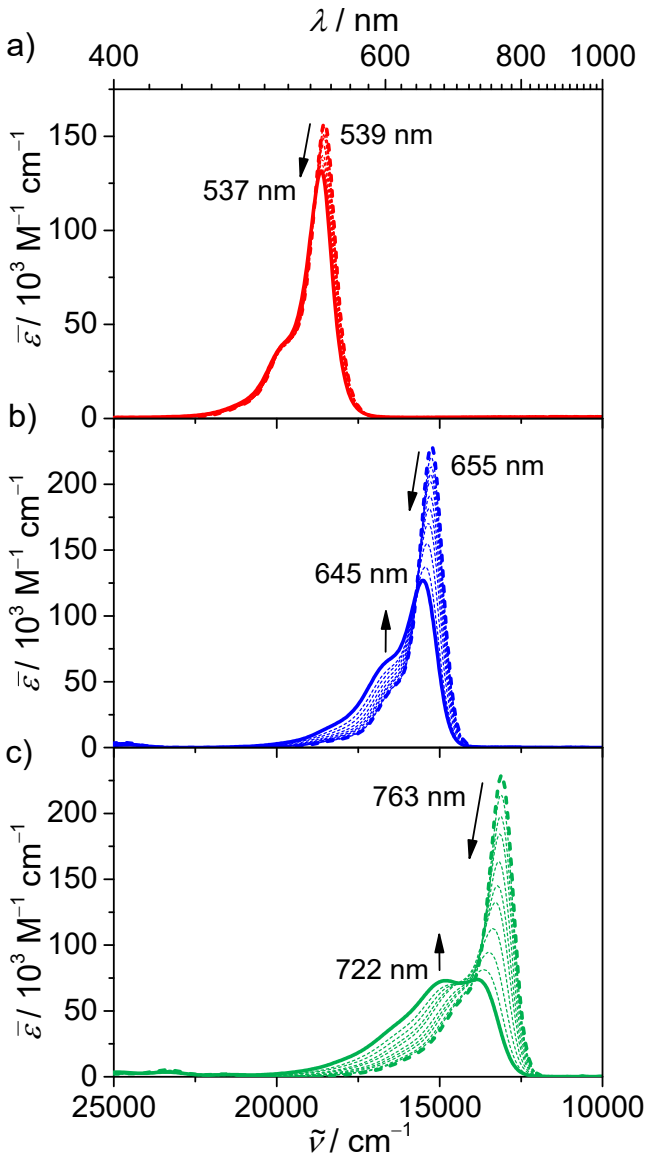

Figure 55 Solvent-dependent UV/vis absorption spectra of reference merocyanines a) **R**, b) **B** and c) **G** in DCM/1,4-dioxane mixtures (c = 4 x 10^{-6} M) starting in pure DCM (thick dashed line) and successively increasing the volume fraction of 1,4-dioxane in steps of 10 vol% (thin dotted lines) up to pure 1,4-dioxane (solid line) at 295 K. The arrows indicate the spectral changes upon increasing the volume fraction of 1,4-dioxane.

In Figure 56 the solvent-dependent UV/vis spectra of homo-bis(merocyanine) dyes **RR**, **BB**, and **GG** are shown. The spectra were recorded at a low concentration of 4 x 10^{-6} M at 295 K to avoid intermolecular aggregation, which was proven by UV/vis dilution studies in 1,4-dioxane (see the Appendix, Figure A12a-c).

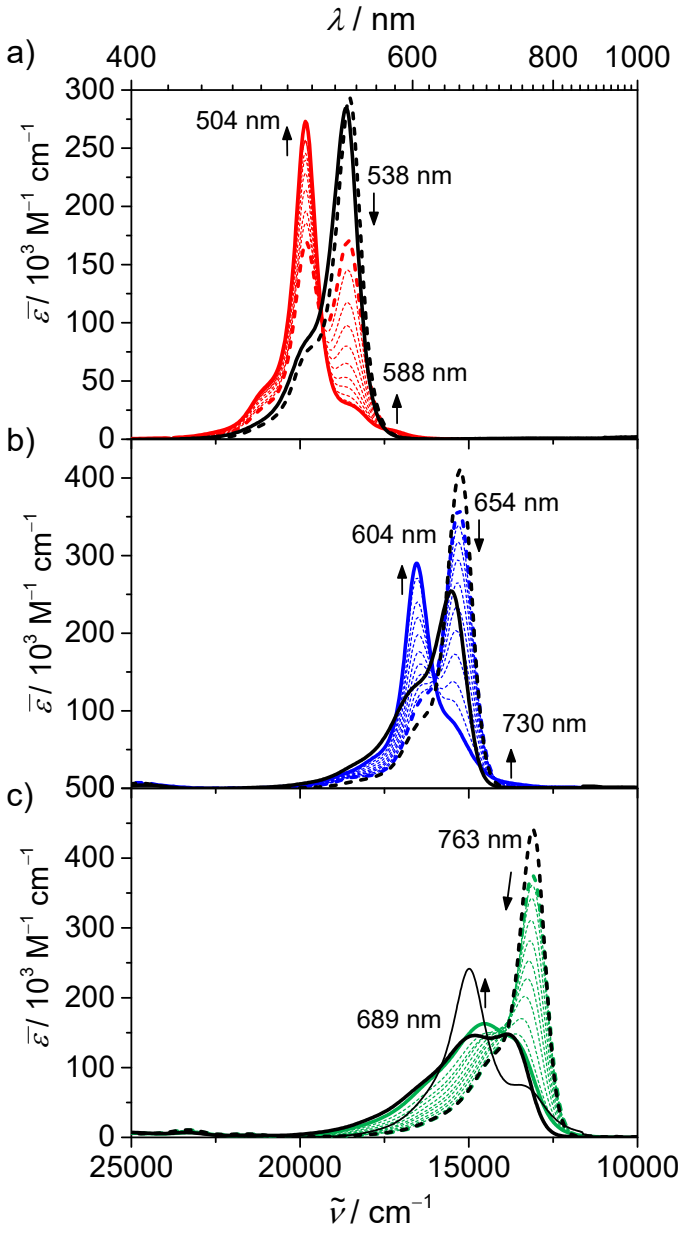

Figure 56 Solvent-dependent UV/vis absorption spectra of homo-bis(merocyanine) dyes a) **RR**, b) **BB** and c) **GG** in DCM/1,4-dioxane mixtures starting in pure DCM (thick dashed colored line) and successively increasing the volume fraction of 1,4-dioxane in steps of 10 vol% (thin dotted colored lines) up to pure 1,4-dioxane (solid colored line). Additionally, the linear combination of the respective reference spectra in DCM (dashed black line) and 1,4-dioxane (solid black line) are depicted. The calculated spectrum (according to the dimerization model, for details see the Appendix) of reference **G** dimer (**G**$_2$) in 1,4-dioxane is included in panel c) in thin black line as well. All spectra were recorded at a concentration of 4 x 10^{-6} M at 295 K. Arrows indicate the spectral changes upon increasing the volume fraction of 1,4-dioxane.

The UV/vis spectrum of bis(merocyanine) **BB** comprising two identical chromophores in DCM (Figure 56b, thick dashed blue line) shows one intense absorption band with a maximum at 654 nm and a weak shoulder at 612 nm corresponding to the vibronic progression of the main

absorption band. The position of the absorption maximum perfectly matches the one of reference dye **B** (dashed black line) indicating that in DCM no considerable interaction between the chromophores is present. Upon increasing the amount of 1,4-dioxane, the intensity of the absorption band at 654 nm decreases with a concomitant appearance of a hypsochromically shifted absorption band at 604 nm. Since these solvent-dependent spectral changes are not observed for reference dye **B** (solid black line), the hypsochromic shift of the absorption band for bis(merocyanine) **BB** can be attributed to an intramolecular H-type coupling between the chromophores upon folding. Furthermore, quasiisosbestic points indicate a thermodynamic equilibrium between two distinct species, *i.e.* the open and folded conformation of **BB**. The additional very weak absorption band at 730 nm in the spectrum of bis(merocyanine) **BB** can be ascribed to a slightly twisted alignment of the transition dipole moments in the H-type aggregate resulting in a weakly allowed transition to the lower exciton state (J-band).

As reported previously,[19h] the spectroscopic behaviour of bis(merocyanine) **RR** upon varying solvent polarity also points out to an intramolecular H-type coupling between the two adjacent chromophores: In pure 1,4-dioxane the absorption band of the H-type coupled merocyanine dimer is present (solid red line, Figure 56a), which is shifted by 34 nm towards smaller wavelength compared to the absorption band (539 nm) of the reference dye **R**. Even in the more polar solvent DCM, **RR** is not completely in the unfolded state as evident from the significant absorption band at 504 nm (thick dashed red line). Accordingly, the driving force for folding appears to be increased for the smaller **R** dye.

The solvent-dependent UV/vis absorption spectra of bis(merocyanine) **GG** (Figure 56c) reveal less clear signatures for a folding of the molecule into H-type coupled π-stacked chromophores. The most obvious spectral changes here resemble the ones observed already for reference monomer **G** indicating a change in the bond orders along the conjugated chain due to the change of the solvent polarity. The comparison of the absorption spectrum of **GG** in 1,4-dioxane (solid green line) with the spectrum of reference **G** dimer ($\mathbf{G_2}$, thin black line), which was calculated according to the dimerization model (for details, see the Appendix), shows that the absorption spectrum of bis(merocyanine) **GG** does not reflect the spectral signature of the double dye stack. However, since deviations between the spectrum of **G** (thick black line) and **GG** (solid green line) in 1,4-dioxane can be observed, a partial folding seems reasonable.

The solvent-dependent UV/vis spectra of hetero-bis(merocyanine) dyes **BG**, **RB**, and **RG** are depicted in Figure 57. To ensure that spectral changes upon changing solvent polarity are not

caused by intermolecular aggregation, also concentration-dependent UV/vis studies of hetero-bis(merocyanine) dyes were performed (see the Appendix, Figure A12d-f).

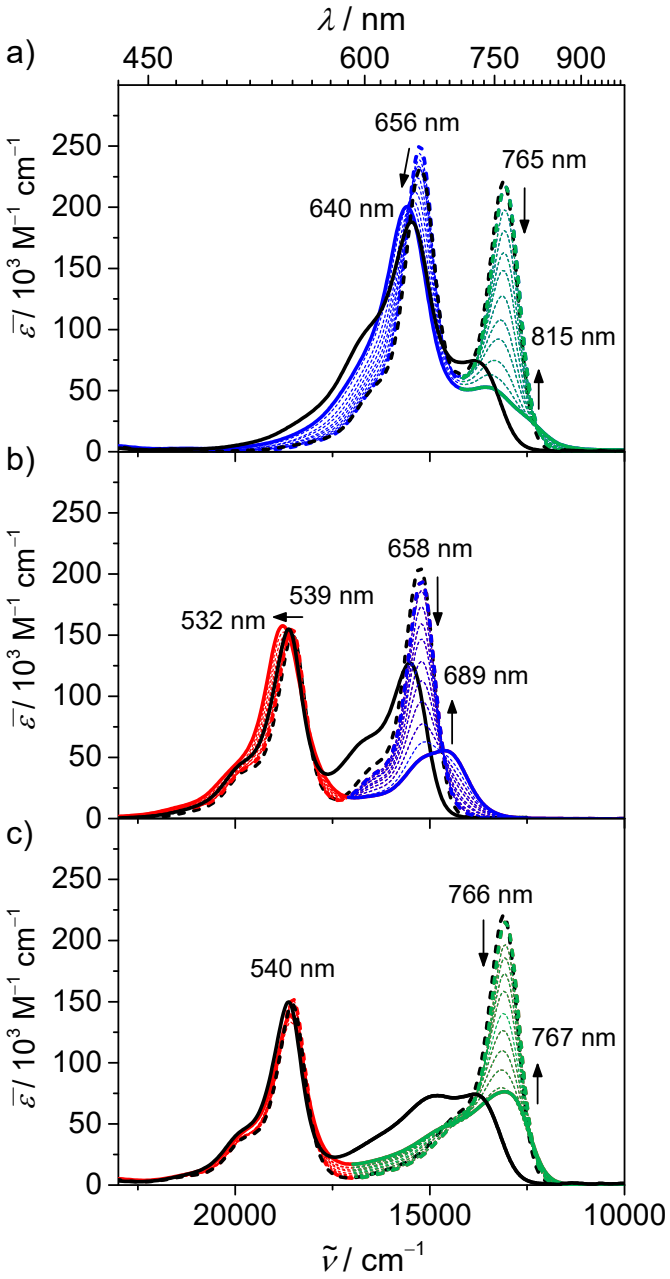

Figure 57 Solvent-dependent UV/vis absorption spectra of hetero-bis(merocyanine) dyes a) **BG**, b) **RB** and c) **RG** in different DCM/1,4-dioxane mixtures starting in pure DCM (thick dashed colored line) and successively increasing the volume fraction of 1,4-dioxane in steps of 10% (thin dotted colored lines) up to pure 1,4-dioxane (solid colored line). Additionally, the linear combination of the respective reference spectra in DCM (dashed black line) and 1,4-dioxane (solid black line) are depicted. All spectra were recorded at a concentration of 4 x 10^{-6} M at 295 K. Arrows indicate the spectral changes upon decreasing solvent polarity with increasing amounts of 1,4-dioxane.

The absorption spectra of the hetero-bis(merocyanine) dyes **BG**, **RB** and **RG** in pure DCM (thick dashed colored lines) are in excellent agreement with the linear combination of the spectra of the respective monomeric reference dyes (dashed black lines). Thus, an unfolded conformation without any coupling between the chromophore units seems reasonable in pure DCM. Upon increasing the amount of less polar 1,4-dioxane, the high energy absorption band of **BG** located at 656 nm decreases with a concomitant blue shift of 16 nm (Figure 57a, solid blue line). For the high energy band of bis(merocyanine) **RB** a blue shift of 7 nm is observed as well (Figure 57b, solid red line), while for **RG** almost no change in the absorption band at lower wavelength is present (Figure 57c, solid red line). Remarkably, for the low energy absorption bands of the hetero-bis(merocyanine) dyes it is not the spectral shift but the strong decrease of intensity, which manifests the dye-dye interaction upon folding. Hence, the low energy absorption band in 1,4-dioxane (solid colored lines) does not resemble the absorption band of the respective monomeric chromophore in the same solvent (solid black lines).

To interpret the solvent-dependent spectral changes in the long-wavelength region of the hetero-bis(merocyanine) dyes, solvatochromic effects must be considered. On the one hand, positive solvatochromism of the chromophores effects a blue shift and a decrease in intensity of the absorption band due to band broadening originating from increased vibronic coupling in unpolar solvents as observed in the solvent-dependent UV/vis studies of the reference dyes (Figure 55). On the other hand, folding of the bis(merocyanine) dyes creates a more polar environment of the chromophores due to close proximity to the dipolar counterpart in the dimer and thus, the absorption band should partially recover the sharp and intense cyanine type structure like in the polar solvent, which counteracts the solvatochromic effect. However, for all three hetero-bis(merocyanine) dyes at longer wavelengths no intense, cyanine like absorption bands are observed, but rather low intensity absorption bands are present that significantly differ from the absorption bands of the respective reference dyes. Hence, an electronic communication between the chromophores in the folded state is apparent which induces the spectral changes upon folding.

Interestingly, the intensity of the long-wavelength absorption in 1,4-dioxane is highest for bis(merocyanine) **RG** exhibiting the largest energy difference (ΔE_{RG} = 0.60 eV) between the individual chromophores within the series of hetero-bis(merocyanines). In contrast, the higher wavelength absorption band of **BG**, whose constituent chromophores have a small excited state energy difference (ΔE_{BG} = 0.21 eV), is significantly weaker. In addition, the absorption spectra of homo-bis(merocyanine) dyes **RR**, **BB** and **GG** with ΔE = 0 show only a very weak shoulder at longer wavelengths (Figure 56). Thus, it can be noticed that an increase of the energy

difference between the chromophores leads to an increase of the intensity of the low energy absorption band.

4.2.3 Quantum Chemical Investigations

To gain insight into the structural arrangements of the chromophores of the examined bis(merocyanine) dyes in the folded conformation, geometry-optimizations were carried out on the DFT level using the B97D3[139] functional including dispersion correction and def2-SVP[122] as basis set. The conductor-like polarizable continuum model (CPCM)[140] was employed to account for solvent effects using 1,4-dioxane as solvent (for details, see the Appendix). The geometry-optimized structures of all bis(merocyanine) dyes and the reference merocyanines are depicted in Figure 58. For all bis(merocyanine) dyes a π-stacked arrangement of the chromophores at short van der Waals distance (3.4–3.5 Å) is present with an antiparallel orientation of the chromophores. The interchromophoric distances are in good agreement with the van der Waals distances observed in the crystal structures of merocyanine dyes **R**,[82] **B**[82] and **G** (Appendix Figure A15). Notably, the ground state dipole moments of the two chromophores of homo-bis(merocyanine) dye **RR** (Figure 58d) show an almost perfect antiparallel orientation, leading to a very small overall dipole moment μ_g of 2.1 D. On the contrary, for **BB** an increased rotational displacement of 10° between the two chromophores is present resulting in a larger overall dipole moment of 3.8 D and for homo-bis(merocyanine) **GG** an even more pronounced angle of 13° and consequently a high value for the overall dipole moment of 7.2 D is observed. These findings suggest that the diphenylacetylene spacer unit properly guides the two short chromophores of **RR** into a tight π-stack with antiparallel orientation, whereas with increasing length of the chromophores a folded conformation becomes less favoured as evident from the results of the UV/vis absorption studies. For the hetero-bis(merocyanine) dyes larger ground state dipole moments of the dye stacks are present due to the different magnitudes of the ground state dipole moments of the individual chromophores. Thus, albeit the chromophores in **RB** are nearly perfectly antiparallel aligned, the stack exhibits an overall dipole moment of 5.7 D (Figure 58h). In the case of folded **BG** (Figure 58g) and **RG** (Figure 58i) even larger values of 6.4 D and 12.7 D are obtained, which can be attributed to the larger twist angles of 12° and 23°, respectively, as well as to the increased difference of the dipole moments of the individual chromophores in the case of **RG**.

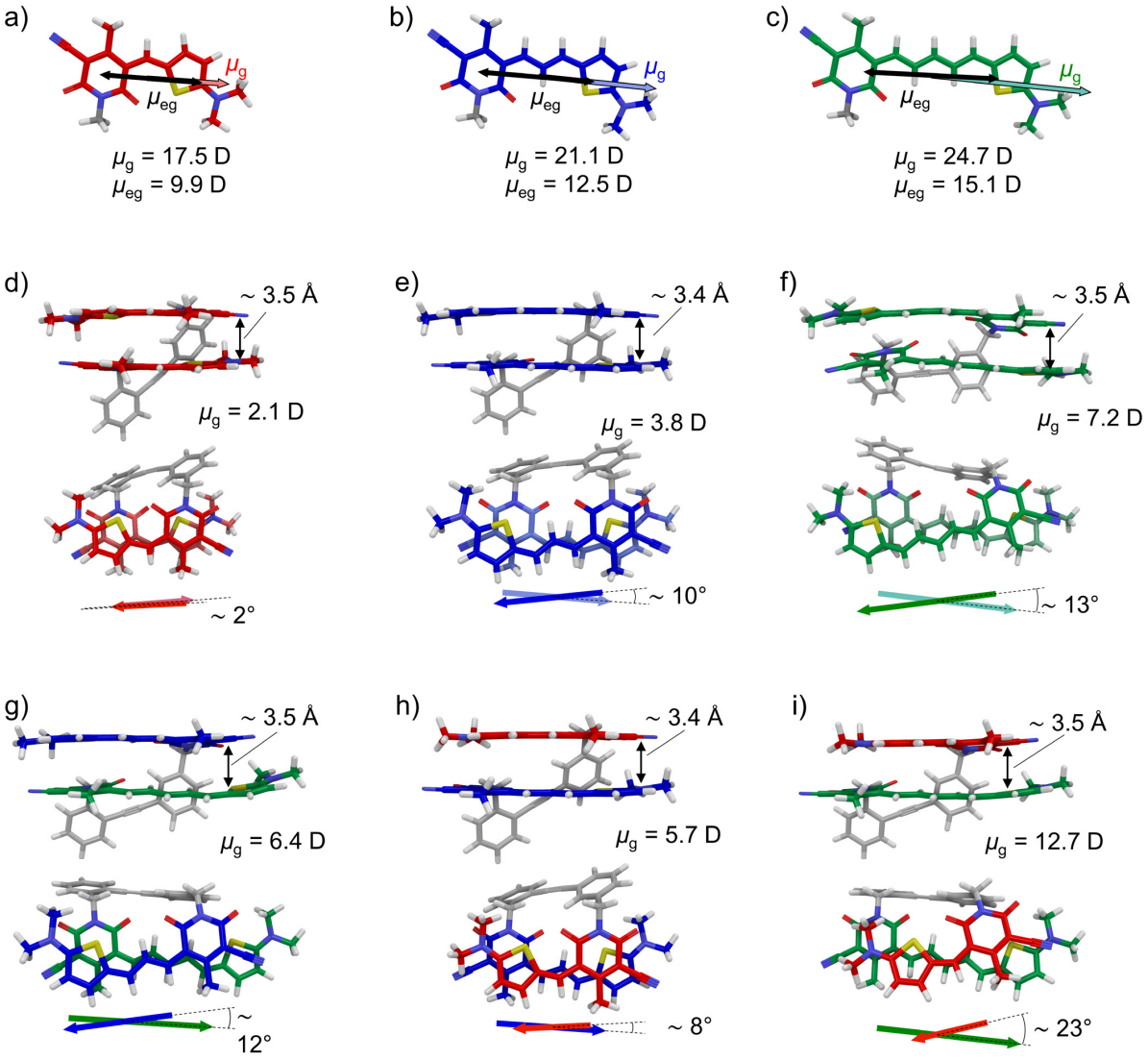

Figure 58 Geometry-optimized structures (B97D3[139]/def2-SVP[122]; butyl and benzyl groups were replaced by methyl groups) of reference merocyanines a) **R**, b) **B** and c) **G** and of homo-bis(merocyanine) dyes d) **RR**, e) **BB** and f) **GG** and hetero-bis(merocyanines) g) **BG**, h) **RB** and i) **RG** in side view (top) and top view (bottom). Bold colored arrows indicate the orientation of the ground state dipole moments μ_g of the chromophores and bold black double arrows denote the orientation of the transition dipole moments μ_{eg} of reference dyes **R**, **B** and **G**.

4.3 Discussion

To rationalize the different absorption behavior of **R**, **B** and **G** in solvent-dependent UV/vis studies,[8] the geometry-optimized structures (note that 1,4-dioxane was used as solvent for geometry-optimizations) were analyzed by calculating the bond length alternation (*BLA*) value, which describes the difference between the average length of the nominally single and double bonds along the polymethine bridge.[141] The *BLA* values obtained from bond length found in the crystal structures of **R**,[82] **B**[82] and **G** (Figure A15) are not suitable for this purpose since the values strongly depend on the arrangement of the chromophores in the crystal lattice. In addition, the Huang-Rhys factor (*HR*), which is directly proportional to the displacement *d* of the excited state energy potential surface resulting from different equilibrium geometries in the electronic ground and excited state of a molecule (Figure 59),[142] was determined from the experimental absorption spectra of the dyes in DCM and 1,4-dioxane (for details, see the Appendix). Another method to address the electronic properties of the ground and excited states of dipolar dyes is electro-optical absorption spectroscopy, which allows calculation of the resonance parameter c^2 from the experimentally obtained dipole difference $\Delta\mu$ and the transition dipole moment μ_{eg}.[143] Unfortunately, investigation of reference dye **G** by this technique was not successful, since the chromophore decomposed in the electric field. The *BLA* values as well as the Huang-Rhys factors are summarized in Table 2 and for a detailed list of all bond length within the polymethine bridge of geometry-optimized reference structures see Table A10 in the Appendix.

Table 2 Bond length alternation (*BLA*) value of reference merocyanines **R**, **B** and **G** in 1,4-dioxane. The Huang-Rhys factors (*HR*) of the dyes in DCM and 1,4-dioxane are summarized as well.

		R	**B**	**G**
BLA[a] / pm		0	1.00	1.40
HR[b]	DCM	0.29	0.22	0.29
	1,4-dioxane	0.31	0.52	1.01

[a]Calculated by the difference between the average length of the nominally single and double bonds along the polymethine bridge of the geometry-optimized (B97D3[139]/def2-SVP[122]) structures. [b]Determined from the experimental absorption spectra of the dyes in DCM and 1,4-dioxane (for details, see the Appendix).

[8] It is well known that H-type aggregates are in general nonfluorescent.[15c, 123] Thus, fluorescence properties of the merocyanine stacks are not considered in this thesis.

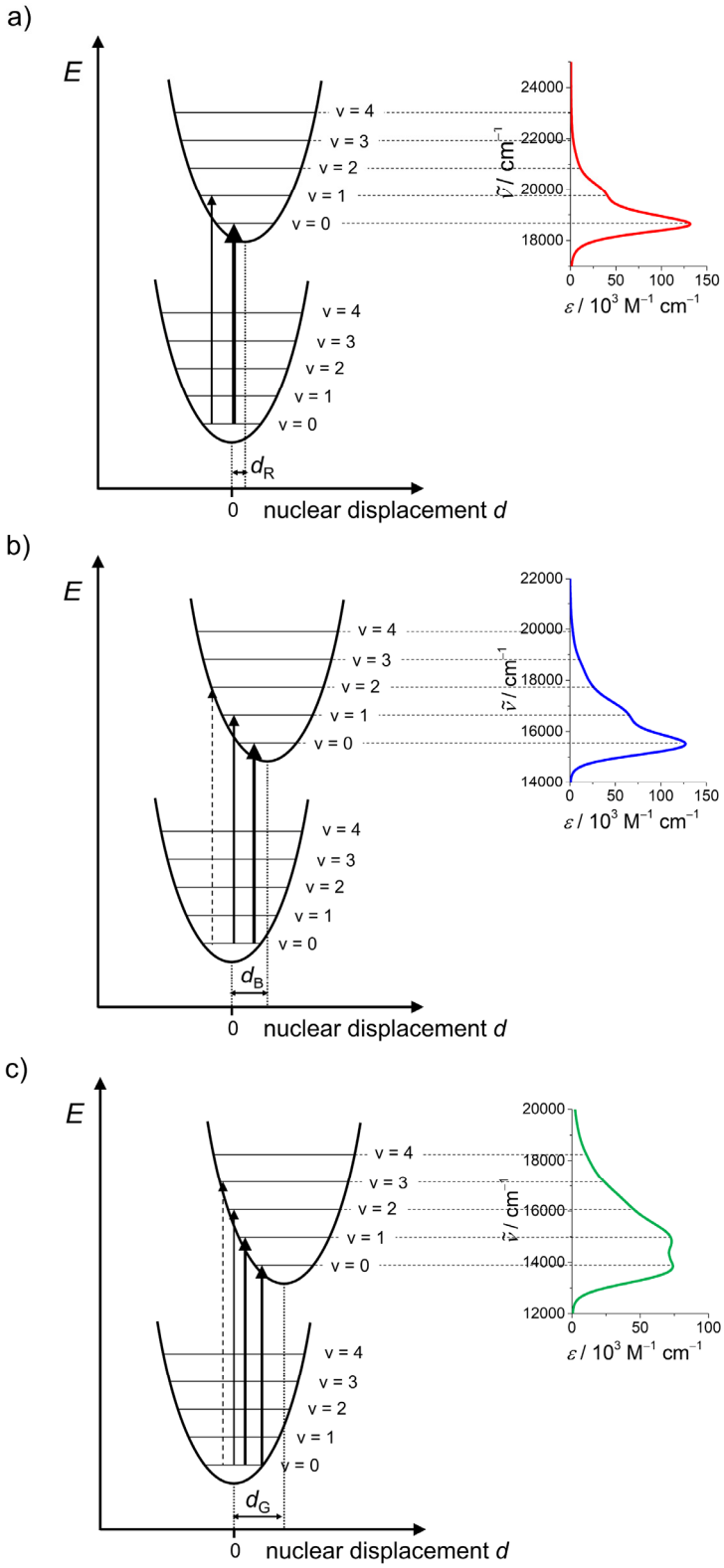

Figure 59 Schematic potential energy diagram (left) of electronic ground state and excited state of reference merocyanines a) **R**, b) **B** and c) **G** with multiple transitions in the absorption process indicated as vertical arrows giving rise to vibronic progression of the absorption band (right) of the dyes in 1,4-dioxane (c = 4 x 10^{-6} M) at 295 K. The line width of the arrows denotes the probability of the transitions according to the overlap integral of the vibronic wave functions of the respective vibrational energy levels and d denotes the displacement of the excited state energy potential surface.

As expected, reference dye **R** exhibits a ground state structure in 1,4-dioxane without any *BLA* along the methine bridge (BLA_R = 0 pm) pointing out to a highly conjugated π-system. This finding is in agreement with the intense and narrow absorption band of **R** in unpolar 1,4-dioxane, which is typical for merocyanine dyes in the cyanine limit (c^2 = 0.50)[136, 138a] and can be explained by negligible geometric changes upon excitation. Thus, for **R** a resonance parameter of c^2 = 0.47 was reported.[82] Accordingly, the Huang-Rhys factor of **R** changes only slightly (from 0.29 to 0.31) upon decreasing solvent polarity and the overlap integral between the vibronic wave functions of the v = 0 vibrational states in the two electronic surfaces is maximal (Figure 59a).

Whereas reference **B** exhibits a sharp cyanine-like absorption band in the more polar solvent DCM, the band is considerably broadened in the unpolar solvent 1,4-dioxane and shows a decreased ratio between the 0–0 and 0–1 absorption band (Figure 59b). The *BLA* value of **B** (BLA_B = 1.00 pm) in 1,4-dioxane is higher compared to the one of reference **R**. Hence, upon decreasing solvent polarity the ground state resonance structure of the chromophore is shifted towards a more polyene-like character as already reported for these type of chromophores.[136] Furthermore, the Huang-Rhys factor increases from 0.22 in DCM to 0.52 in 1,4-dioxane indicating a larger nuclear displacement between the ground and excited state, and consequently rationalizes the pronounced vibronic progression of the absorption band in 1,4-dioxane (Figure 59b).

An even stronger vibronic progression in the unpolar solvent 1,4-dioxane was found for dye **G** with an inversion of the band intensities of the 0–0 and 0–1 transition. For this dye, which exhibits the longest polymethine bridge amongst the reference compounds, the strongest increase of the Huang-Rhys factor was observed (from 0.29 in DCM to 1.01 in 1,4-dioxane) by decreasing solvent polarity. This reveals that the displacement between the electronic potential surfaces is largest for **G** (Figure 59c) and suggests a strong effect of the solvent polarity on the electronic structure of the chromophore. Moreover, the considerable influence of the environment polarity is reflected by the *BLA* of **G**. In an unpolar surrounding (1,4-dioxane), for reference **G** the largest *BLA* within the series of reference dyes of 1.40 pm was calculated. In addition, the *BLA* values for chromophore **G** in the folded structures of bis(merocyanine) dyes **RG**, **BG** and **GG** were determined. In these systems, the polarity of the environment of chromophore **G** increases through the close proximity to the second highly dipolar chromophore in the dimer stack. Within the series **R**, **B**, **G** the ground state dipole moment of the chromophores increases from 17.5 D (**R**) to 24.7 D (**G**) (Figure 58a-c) and thus, the polarity of the environment of **G** in the respective dimer stacks increases. Consequently, a

decrease of the *BLA* value is calculated for **G** (**RG**: 0.30 pm; **BG**: 0.23 pm; **GG**: −0.03 pm), demonstrating the strong influence of the neighbour dye on the structural properties of the long chromophore. Therefore, whilst with increasing length of the polymethine chain the ground state structure of the chromophore is increasingly shifted towards a more polyene-like structure in unpolar solvents resulting in pronounced vibronic progression, this trend is reversed in the folded arrangement by the dipolar neighbour chromophore. This result is in good agreement with the UV/vis aggregation study of reference **G** in 1,4-dioxane, which in the monomeric state exhibits a broad absorption band with pronounced vibronic progression, whereas upon dimerization a sharp and intense H-band is formed (Figure A13).

Time-dependent DFT (TDDFT) calculations were performed on the geometry-optimized structures employing the same solvent model as for the geometry-optimizations to investigate the excited state properties of the dye stacks. The long-range corrected ωB97 functional[121] was applied (for details, see the Appendix), which has already been used to adequately describe the excited state properties of double[19h] and quadruple[20a] merocyanine dye stacks with same or different chromophores. Figure 60a-f (top) shows the calculated spectra of the π-stacks of homo-bis(merocyanines) **RR**, **BB** and **GG** and hetero-bis(merocyanine) dyes **BG**, **RB** and **RG** in comparison to the experimental ones measured in 1,4-dioxane (bottom). Since **GG** is only partially folded in 1,4-dioxane, the spectrum of the reference **G** dimer (**G**$_2$) is used for the discussion. Notably, the experimental spectra are reasonably well reproduced by the simulated spectra. Accordingly, for all dye stacks, two non-degenerated excited states are obtained and the transition to the higher excited state is strongly allowed, which is reflected by a large oscillator strength *f*. In contrast, the lower excited state is forbidden ($f = 0$) in the case of the homo-bis(merocyanine) dyes. Therefore, the absorption spectrum of dimer stacks comprising identical chromophores is mainly characterized by only one intense absorption band (Figure 60a-c). The spectra of the hetero-chromophoric stacks show besides the intense absorption band at shorter wavelengths an additional band at longer wavelengths with considerably strong intensity (Figure 60d-f). Thus, transition to the lower excited state is partially allowed in the case of the hetero-chromophoric dye stacks. Remarkably, the intensity of the low energy band increases within the series **BG** ($f = 0.34$), **RB** ($f = 0.56$) and **RG** ($f = 1.15$).

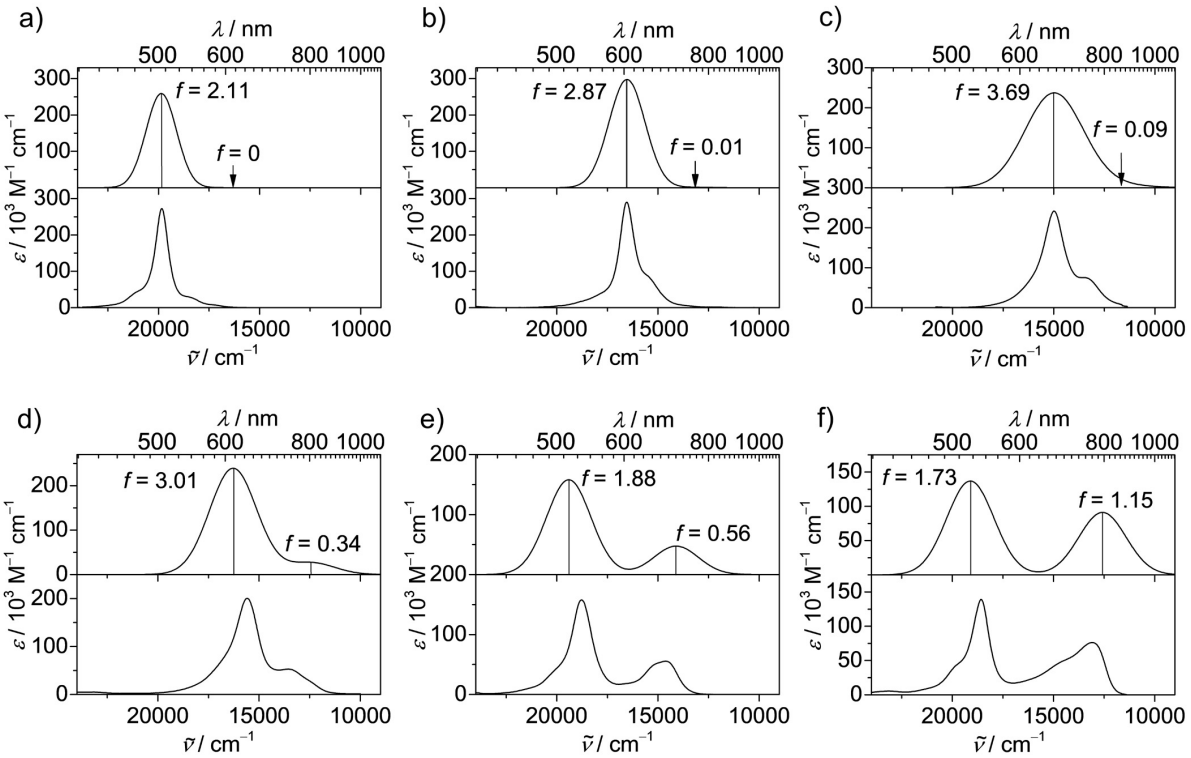

Figure 60 Simulated (calculated by TDDFT (ωB97[121]), top) and experimental (1,4-dioxane at 4 x 10^{-6} M; bottom) UV/vis absorption spectra of folded homo-bis(merocyanines) a) **RR**, b) **BB** and c) **GG** and hetero-bis(merocyanine) dyes d) **BG**, e) **RB** and f) **RG**. In panel c) the absorption spectrum of reference $\mathbf{G_2}$ is shown (for details, see the Appendix). The calculated absorption spectra were shifted towards lower energies for better comparability with the experimental spectra.

The transition densities of π-stacks of homo- and hetero-bis(merocyanine) dyes (Figure 61a-f) obtained by TDDFT calculations can be described by an in-phase/out-of-phase coupling of the transition densities of the individual chromophores for the higher/lower excited state. The in-phase and out-of-phase coupling is in accordance with the exciton theory by Kasha,[83] who described the exciton coupling in terms of an interaction between transition dipole moments. Hence, it is reasonable to assume that the excited states of the dye stacks represent exciton states. The transition density is equally distributed over both chromophores in the case of the homo-aggregates (Figure 61a-c), whereas it is more localized on the shorter/longer chromophore for the higher/lower excited state in the hetero-dye stacks (Figure 61d-f). Interestingly, the localization of the transition density on one of the chromophores in the hetero-dimer increases as the energy difference between the chromophores rises.

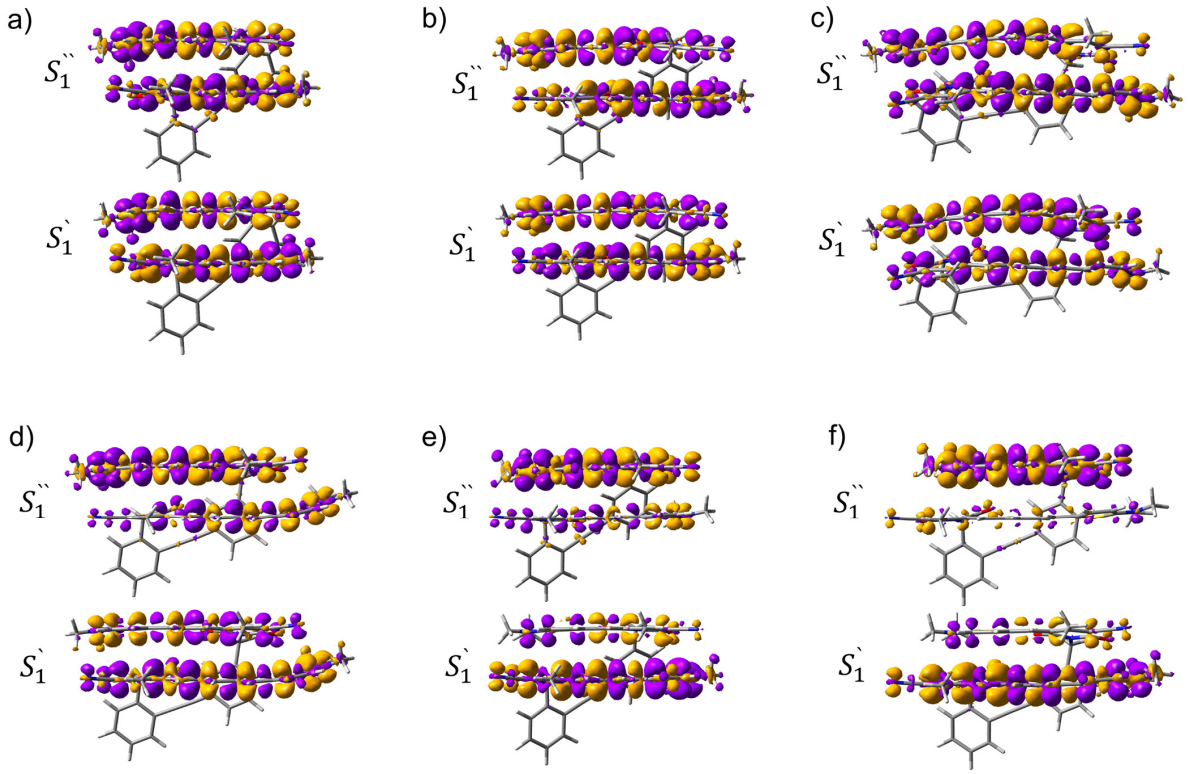

Figure 61 Transition densities (isovalue = 0.0012 a.u.) of the higher ($S_1^{``}$) and lower ($S_1^{`}$) excited state of homo-bis(merocyanines) a) **RR**, b) **BB** and c) **GG** and hetero-bis(merocyanine) dyes d) **BG**, e) **RB** and f) **RG** obtained by TDDFT calculations (ωB97[121]).

The experimentally observed spectral changes upon folding of the herein studied bis(merocyanine) dyes and the quantum chemical calculations (TDDFT) indicate considerable coupling between identical as well as between different chromophores. Therefore, exciton theory was applied to explain the observed absorption properties of the homo- and hetero-dye stacks. The exciton wave function Φ_E of a dimer is described by the linear combination of the localized excitations:[83, 144]

$$\Phi_E = c_a \cdot \varphi_a^* \varphi_b + c_b \cdot \varphi_a \varphi_b^* , \qquad (2)$$

with the ground state wave functions φ_a, φ_b and the excited state wave functions φ_a^*, φ_b^* of chromophore a and b, respectively. The coefficients c_a and c_b that describe the contribution of the individual chromophores to the exciton states of the dimer can be obtained from the normed eigenvectors of the corresponding Hamiltonian matrix (Table 3, for details, see the Appendix, Table A11 and Table A12). The energies of the two exciton states in a hetero-dimer can be calculated according to Equations 3 and 4:[19h]

$$E(S_1') = -0.5\left(\sqrt{(\Delta E_a - \Delta E_b)^2 + 4J^2} - \Delta E_a - \Delta E_b\right); \quad (3)$$

$$E(S_1'') = 0.5\left(\sqrt{(\Delta E_a - \Delta E_b)^2 + 4J^2} + \Delta E_a + \Delta E_b\right); \quad (4)$$

with the transition energies ΔE_a and ΔE_b of the respective monomeric chromophores and the exciton coupling energy J. In case of a homo-dimer ($\Delta E_a = \Delta E_b$) the exciton state energies simplify to

$$E(S_1') = \Delta E_a - J; \quad (5)$$

$$E(S_1'') = \Delta E_a + J. \quad (6)$$

Accordingly, the Davydov splitting, which is defined as the energy difference between the two exciton states, is

$$\Delta E_{DS} = 2J \quad (7)$$

for a homo-dimer and

$$\Delta E_{DS} = 2\sqrt{(\Delta E/2)^2 + J^2} \quad (8)$$

for a hetero-dimer, where ΔE is the difference between the transition energies of the two monomeric chromophores:

$$\Delta E = \Delta E_a - \Delta E_b, \qquad \text{with } \Delta E_a > \Delta E_b. \quad (9)$$

The transition energies of the monomeric chromophores ΔE_a and ΔE_b can be obtained from the absorption maxima of the respective reference dyes in 1,4-dioxane (Figure 55) and the exciton coupling is described in terms of the Coulomb interaction between transition charges (for details, see the Appendix)[124, 145] since the point-dipole approximation is not appropriate owing to the short distance between the interacting chromophores.[146] The calculated values for the exciton coupling energy are in the same order of magnitude for all bis(merocyanine) dyes revealing strong coupling for homo- and hetero-dye stacks (Table 3). However, it has to be noted that the employed model is a simplified picture and that additional effects like polarization[147] and short-range coupling[130c] will also influence the absorption properties of the dye stacks. Nevertheless, the results indicate a strong Coulomb coupling between the chromophores arising from the large transition dipole moments of the chromophores.

Table 3 Energy difference between the excited states (ΔE) of respective monomeric chromophores, exciton coupling energy J and exciton state energies E of homo- (**RR**, **BB** and **GG**) and hetero- (**BG**, **RB** and **RG**) bis(merocyanine) dyes. The coefficients c_a and c_b for the higher (S_1``) and lower exciton state (S_1`) are given as well.

	Homo-dimers			**Hetero-dimers**		
	RR	**BB**	**GG**	**BG**	**RB**	**RG**
ΔE^a / cm^{-1}	0	0	0	1670	3140	4810
J^b / cm^{-1}	1667	1947	1925	1783	1908	1718
$E(S_1``)^c$ / cm^{-1}	20306	17327	15694	16604	19537	19172
$E(S_1`)^c$ / cm^{-1}	16790	13679	11968	12730	14604	13297
$c_a(S_1``)^d$	0.71	0.71	0.71	0.84	0.91	0.95
$c_b(S_1``)^d$	0.71	0.71	0.71	0.54	0.41	0.32
$c_a(S_1`)^d$	0.71	0.71	0.71	–0.54	–0.41	–0.32
$c_b(S_1`)^d$	–0.71	–0.71	–0.71	0.84	0.91	0.95

[a]Calculated by the energy difference between the excited states of the respective chromophores with ΔE_R = 18638 cm^{-1}, ΔE_B = 15503 cm^{-1}, ΔE_G = 13831 cm^{-1}. [b]Calculated by transition charge method. [c]Calculated according to Equations 3-6. [d]Estimated from the normed eigenvectors of the Hamiltonian matrix (see the Appendix, Table A11 and Table A12).

In Figure 62a the exciton state diagram of a merocyanine H-dimer consisting of two chromophores a and b of variable energy difference ΔE between the excited states $S_{1,a}$ and $S_{1,b}$ is displayed to illustrate the exciton coupling between either two identical ($\Delta E = 0$) or different ($\Delta E \neq 0$) chromophores. In a homo-dimer the exciton coupling leads to a splitting of the excited states (Davydov splitting) into two non-degenerated exciton states of higher (S_1``) and lower energy (S_1`) compared to the excited state energy of the monomeric dye. The higher exciton state is described by an in-phase coupling of the transition dipole moments, resulting in a high value for the overall transition dipole moment, and thus the transition to this exciton state is strongly allowed. Therefore, the absorption spectrum of folded bis(merocyanines) **RR** and **BB** and the spectrum of reference **G** dimer (which is used as substitute for the absorption of folded **GG**) show one intense absorption band with a hypsochromic shift (H-band) with regard to the absorption maximum of the respective monomeric reference dyes **R**, **B** and **G** (Figure 56). On the contrary, the out-of-phase coupling of the transition dipole moments in the lower exciton state leads to an annihilation of the overall transition dipole moment in a perfect H-aggregate.

Therefore, transition to the lower exciton state is forbidden and thus, no absorption band is present at lower energies. This is in accordance with the spectra of all homo-dimers that show intense H-bands at 504 nm (**RR**), 604 nm (**BB**) and 668 nm (**G₂**), respectively, and only very weak J-bands arising from a slightly twisted arrangement of the chromophores in the dye stacks (Figure 56). The additionally observed weak absorption band at 541 nm (**RR**) and 644 nm (**BB**) might either result from vibronic progressions or be indicative of the presence of a small amount of unfolded species. Moreover, vibronic coupling might also be responsible for the shoulders at high energies in the absorption spectra of folded **RR** (~ 475 nm) and **BB** (~ 564 nm) and of the spectrum of reference **G₂** (~ 617 nm).

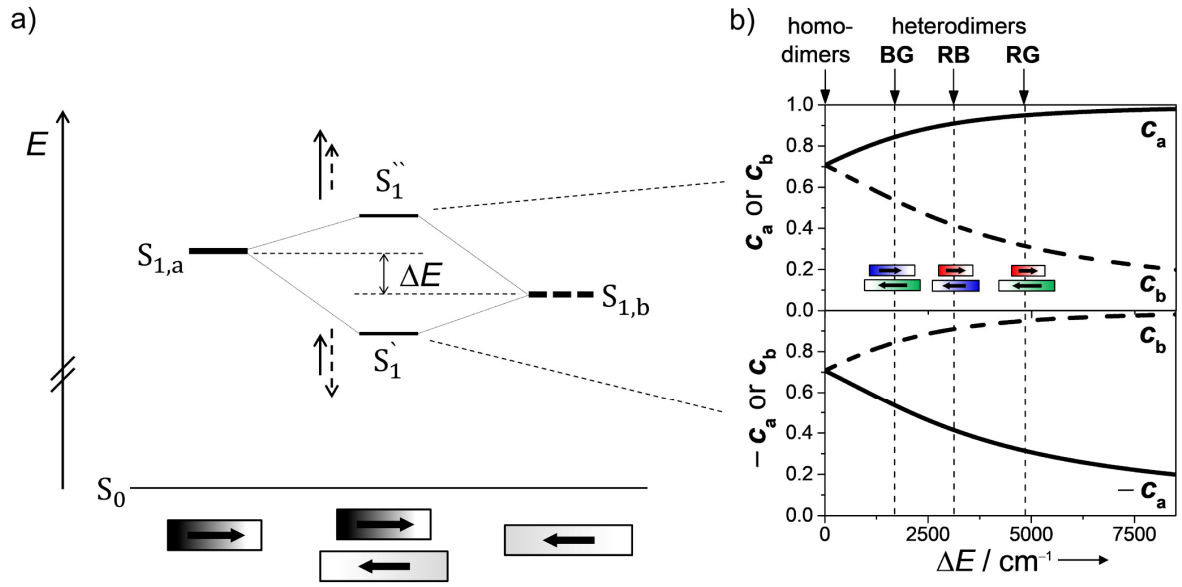

Figure 62 a) Exciton state diagram of a merocyanine H-dimer comprising two chromophores a (solid) and b (dashed) of variable energy difference Δ*E* between the excited states $S_{1,a}$ and $S_{1,b}$ of the individual chromophores. b) Plot of the magnitude of the coefficients c_a and c_b as a function of Δ*E* for the higher (top) and lower exciton state (bottom), assuming a fixed exciton coupling energy of 1800 cm^{-1}.

The results obtained by solvent-dependent UV/vis studies and TDDFT calculations indicate exciton coupling between different types of chromophores, as well. Thus, a splitting of the excited states in the hetero-dimer can be assumed leading to a higher and a lower exciton state. Like in the homo-dimer, transition to the higher exciton state S_1`` is strongly allowed as a result of the in-phase coupling of the transition dipole moments. Whereas in a perfect H-dimer with equal chromophores transition to the lower exciton state is forbidden, it is partially allowed in the hetero-dimer. Even if the transition dipole moments show a perfect parallel orientation the out-of-phase coupling of the transition dipole moments does not result in an overall transition dipole moment of 0 D since the magnitudes of the transition dipole moments of the individual

chromophores are different (Figure 58a-c). Furthermore, whilst the coefficients c_a and c_b in Equation 2 have the same magnitude for a homo-dimer, different values are obtained for the hetero-dimers arising from the energy difference between the chromophores (Table 3, for details, see the Appendix, Table A12). Figure 62b shows how the coefficients c_a and c_b change with increasing energy difference ΔE between the excited states of the interacting chromophores, assuming a fixed coupling energy $J = 1800$ cm^{-1}, which is in the range of the calculated values for the herein investigated merocyanine stacks. For dimers comprising two identical chromophores ($\Delta E = 0$) the magnitude of the coefficients c_a and c_b is identical ($\frac{1}{\sqrt{2}}$), which is in accordance with the TDDFT calculations that reveal an equal distribution of transition densities over both chromophores in the homo-dimers (Figure 61a-c). With increasing energy difference between the excited states of the two coupled chromophores the coefficient c_a, which describes the contribution of the chromophore with higher excited state energy to the exciton state, is approaching one for the higher exciton state and zero for the lower exciton state. The coefficient c_b describing the contribution of the chromophore with lower excited state energy behaves in an opposite manner. It decreases/increases for the higher/lower exciton state upon increasing ΔE. Thus, even if the transition dipole moments of the individual chromophores were identical in a perfect hetero-H-dimer, the overall transition dipole moment for the lower exciton is different from zero. Consequently, the transition is partially allowed leading to a non-negligible J-band in the absorption spectrum, as it is observed in the experimental absorption spectra of the herein investigated hetero-dimers (Figure 60d-f). Since the difference of the magnitudes of c_a and c_b increases with increasing energy difference ΔE, a rise of intensity of the J-band with increasing ΔE should be expected. In fact, this trend can be observed within the series of the present hetero-dimers. Bis(merocyanine) **BG** exhibits the smallest energy difference ΔE_{BG} of 0.21 eV (1670 cm^{-1}) and accordingly, the J-band has the lowest intensity, whereas the J-band of **RG** ($\Delta E_{RG} = 0.60$ eV = 4810 cm^{-1}) exhibits the highest intensity within the series of hetero-dimers. However, one has to notice that in the case of hetero-dimers **BG** and **RG** the J-band is presumably additionally increased due to the increase of the difference between the transition dipole moments of the individual chromophores. The results obtained by TDDFT calculations reveal that with the raise of the energy difference ΔE between the excited states of the monomeric chromophores the transition density of the higher exciton state is increasingly localized on the chromophore with higher excited state energy and in the lower exciton state increasingly on the one with lower excited state energy (Figure 61d-f). Besides, according to

Equation 8, the influence of the exciton coupling energy J on the Davydov splitting decreases with increasing ΔE.[148] Hence, even if strong exciton coupling is present in a hetero-dimer, the spectral changes might be weak if the excited state energy difference ΔE is large. This might be one of the reasons for the long standing perception, that strong exciton coupling only occurs between chromophores of equal excited state energy.[131c, 149]

4.4 Conclusion

A series of new bis(merocyanine) dyes has been synthesized in which either two identical or different dipolar merocyanine chromophores were connected by a diphenylacetylene spacer unit. Detailed UV/vis absorption spectroscopic studies revealed significant spectral changes in solvent mixtures with decreasing polarity, which were attributed to a folding of the molecules into π-stacks composed of two antiparallel merocyanines that exhibit varying excited state energy differences of the chromophores. Only for homo-bis(merocyanine) **GG** a reduced folding tendency was observed since the spacer geometry does not support a perfect antiparallel alignment of the π-extended chromophores. DFT calculations corroborate the folded conformation of the bis(merocyanine) dyes with an antiparallel π-stacked arrangement of the chromophores and simulated absorption spectra obtained by TDDFT calculations are likewise in good agreement with the experimental ones. Quantum chemical calculations revealed strong exciton coupling between the chromophores within the homo- and hetero-π-stacks and accordingly support the notion that the folding-induced spectral changes can be interpreted by exciton theory, not only for homo- but also for hetero-dimers. Hence, the dimers composed of two identical chromophores behave like typical H-aggregates with one intense absorption band at higher energy compared to the absorption of the monomeric constituents, whereas the low energy transition is forbidden. More interestingly, with increasing energy difference ΔE between the excited states of the chromophores in the hetero-dimers, the J-band gains intensity, not only due to the different magnitudes of transition dipole moments of the chromophores but also because of the increased localization of the excitation in the respective exciton state. The present work contributes to a better understanding of the optical properties of hetero-aggregates and shows that strong exciton coupling can also take place between chromophores with significantly different excited state energies.

4.5 Appendix

UV/vis Spectroscopic Studies

Table A9 Absorption maxima λ_{max} and the corresponding extinction coefficients ε_{max} of the reference dyes (**R**, **B** and **G**) and the homo- (**RR**, **BB** and **GG**) and hetero- (**BG**, **RB** and **RG**) bis(merocyanines) in DCM and 1,4-dioxane at 295 K (c = 4 x 10^{-6} M). Since **GG** is only partially folded in 1,4-dioxane, absorption properties of reference **G** dimer (**G_2**) in 1,4-dioxane are included as well.

		λ_{max} / nm (ε_{max} / M^{-1} cm^{-1})	
		DCM	1,4-dioxane
Reference merocyanines	**R**	539 (157100) 507 (39000)[a]	537 (131500) 507 (42500)[a]
	B	655 (229100) 610 (46500)[a]	645 (126700) 602 (65700)[a]
	G	763 (228600) 703 (63200)[a]	722 (73600) 673 (73000)[a]
Homo-bis(merocyanine) dyes	**RR**	538 (170500) 504 (169200)	588 (6900) 541 (29500)[b] 504 (273000) 476 (45500)
	BB	654 (358500) 612 (118300)[a]	730 (6400) 644 (88500)[b] 604 (290100) 564 (42100)
	GG	764 (374900) 706 (126000)[a]	732 (136000)[b] 689 (162800)
	G_2	-	746 (37400)[c] 668 (120700)[c]
Hetero-bis(merocyanine) dyes	**BG**	765 (216800) 656 (250000) 611 (57300)[d**]	815 (26800) 738 (52800)[b] 640 (200500)
	RB	658 (194500) 611 (37300)[d*] 539 (154300) 507 (42100)[d**]	689 (55100) 659 (50000)[b] 532 (157600) 504 (49400)
	RG	766 (215000) 704 (54400)[d*] 540 (152400) 508 (40800)[d**]	767 (76200) 678 (48900)[b] 539 (141300)

[a]Shoulder corresponding to the vibronic progression (0−1 transition) of the main absorption band.
[b]Weak absorption band resulting from vibronic progressions or from a small amount of unfolded species.
[c]Obtained from the calculated (according to the dimerization model) dimer spectrum of reference **G**.
[d]Shoulder in the absorption spectrum corresponding to the 0−1 transition of the chromophore with [*]lower and [**]higher excited state energy.

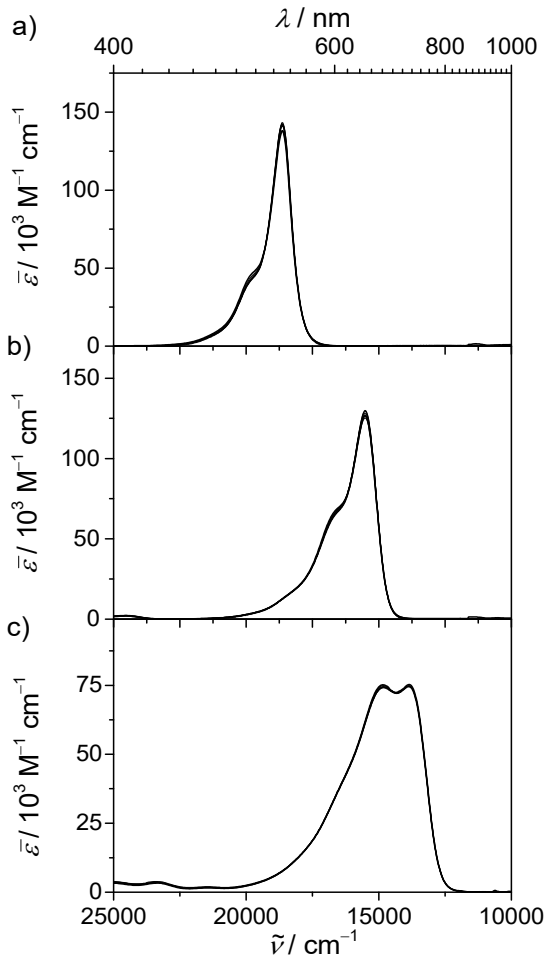

Figure A11 Concentration-dependent UV/vis absorption spectra of reference merocyanines a) **R** (1.9 x 10^{-4} M – 6.0 x 10^{-6} M), b) **B** (2.1 x 10^{-4} M – 6.7 x 10^{-6} M) and c) **G** (1.9 x 10^{-4} M – 7.8 x 10^{-6} M) in 1,4-dioxane at 295 K.

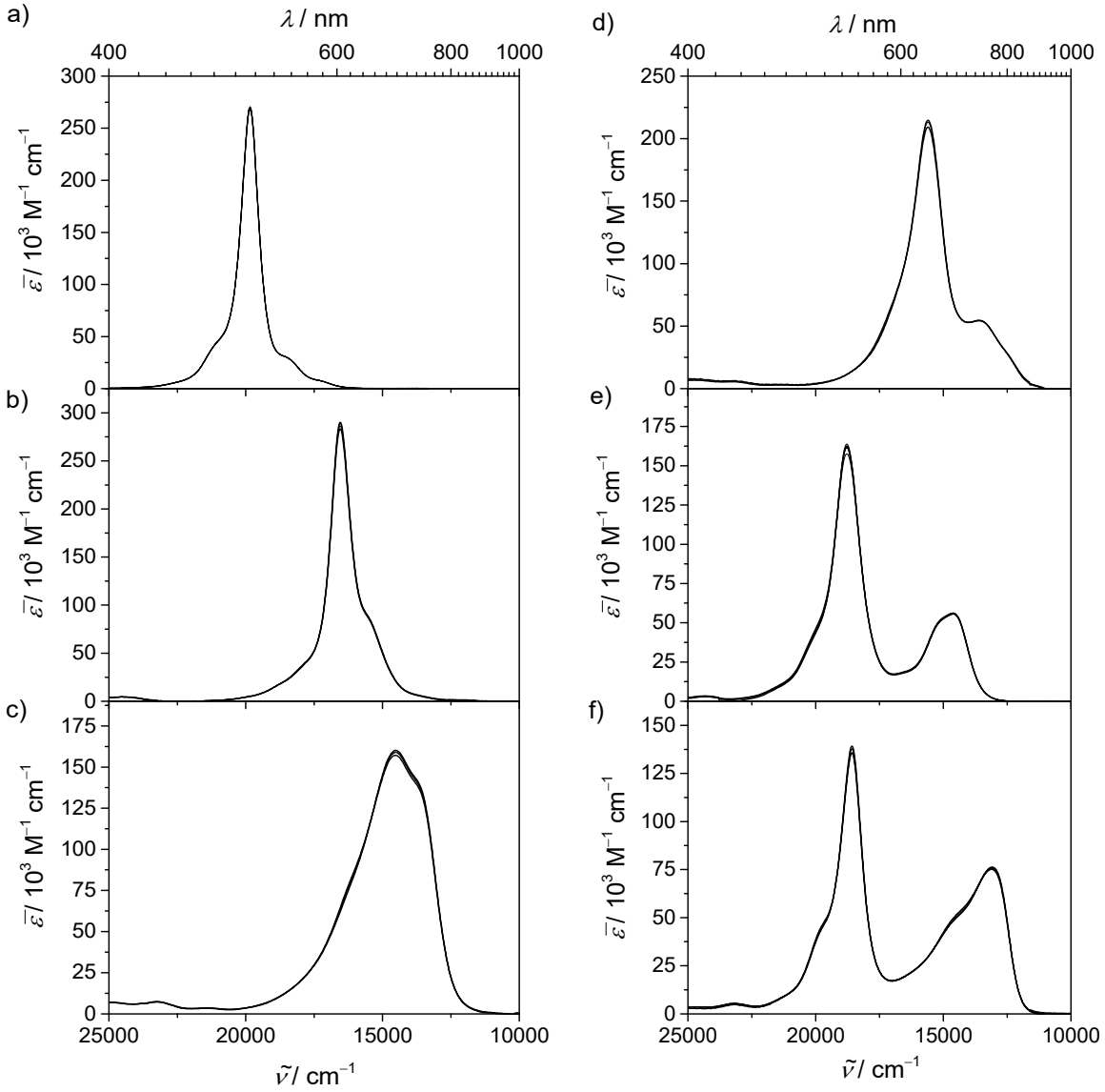

Figure A12 Concentration-dependent UV/vis absorption studies of homo-bis(merocyanine) dyes a) **RR** (9.9 x 10^{-5} M – 9.4 x 10^{-7} M), b) **BB** (2.5 x 10^{-6} M – 7.5 x 10^{-7} M) and c) **GG** (5.3 x 10^{-6} M – 1.9 x 10^{-6} M) and hetero-bis(merocyanine) dyes d) **BG** (4.6 x 10^{-6} M – 1.3 x 10^{-6} M), e) **RB** (4.9 x 10^{-5} M – 1.7 x 10^{-6} M) and f) **RG** (2.6 x 10^{-5} M – 5.9 x 10^{-6} M) in 1,4-dioxane at 295 K.

Only small deviations are observed between the absorption spectra of bis(merocyanine) **GG** and reference merocyanine **G** in 1,4-dioxane (Figure 56c). To elucidate whether this is due to solvatochromism or only partial folding of **GG**, comparison with the absorption spectrum of the reference **G** dimer should provide clarity. Therefore, the aggregation behaviour of reference merocyanine **G** was studied by concentration-dependent UV/vis absorption spectroscopy in 1,4-dioxane (Figure A13a).

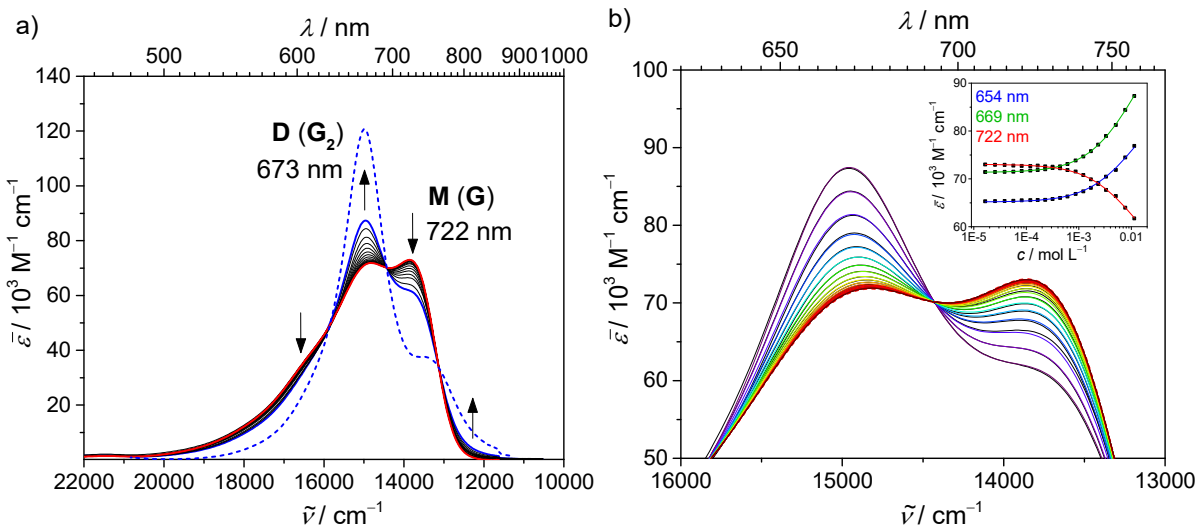

Figure A13 a) Concentration-dependent UV/vis spectra of reference **G** in 1,4-dioxane at 295 K (c = 9.0 x 10^{-3} M – 1.4 x 10^{-5} M) starting at high concentration (solid blue line) and successively diluting the solution (black lines). The spectrum at lowest concentration is depicted in solid red line. Black arrows indicate the decrease in the intensity of the monomer band (M) and the appearance of the dimer band (D) upon increasing concentration. Dashed lines correspond to the calculated spectra of monomer (red) and the dimer (blue) according to the dimerization model. b) Significant area of concentration-dependent UV/vis spectra of **G** (black lines). Colored lines represent the spectra obtained by global fit analysis according to the dimerization model and the inset shows the analysis of the concentration-dependent extinction data at various wavelengths.

At highest dilution (red line) the monomer band is observed with a maximum at 722 nm corresponding to the 0−0 absorption band. In addition, a second pronounced absorption band at 673 nm is present, which can be assigned to the 0−1 absorption band. With increasing concentration the band at 722 nm decreases while concomitantly the band at lower wavelength (673 nm) increases pointing out to the formation of H-type aggregates. Clear isosbestic points are obtained over the whole concentration range indicating a thermodynamic equilibrium between two defined species and the concentration-dependent UV/vis spectral data could be successfully fitted to the dimerization model[18d, 22c] by a global fit analysis (Figure A13b) yielding the calculated absorption spectra of the reference **G** monomer (dashed red line) and the dimer **G_2** (dashed black line, Figure A13a). A dimerization constant K_2^G of 32 M^{-1} is determined, which is in agreement with values reported in literature for similar types of merocyanine dyes.[18d, 117] The calculated monomer spectrum coincides with the experimental one at high dilution. Interestingly, the calculated dimer spectrum reveals a sharp and intense band without considerable vibronic coupling.[9] The shoulder at 746 nm may correspond to a

[9] The dimer spectrum cannot be achieved experimentally since the high absorptivity of the solution limits the spectroscopically detectable concentration range.

weak J-band and suggests a rotational displaced alignment of the two chromophores in the dimer stack. In comparison to the absorption spectrum of bis(merocyanine) **GG** in 1,4-dioxane (Figure 56c) the dimer band of **G** appears at smaller wavelength, which might be attributed to a different arrangement of the chromophores induced by the spacer of **GG**. However, since the H-band of **GG** (at 689 nm) is significantly weaker compared to the dimer band of **G**, it can be concluded that homo-bis(merocyanine) **GG** is only partially folded in the unpolar solvent 1,4-dioxane.

Further evidence for the presence of mainly unfolded species of homo-bis(merocyanine) **GG** in 1,4-dioxane is given by the pronounced tendency of the molecule to aggregate intermolecularly. To investigate this aggregation behaviour concentration-dependent UV/vis absorption studies were performed in 1,4-dioxane (Figure A14a).

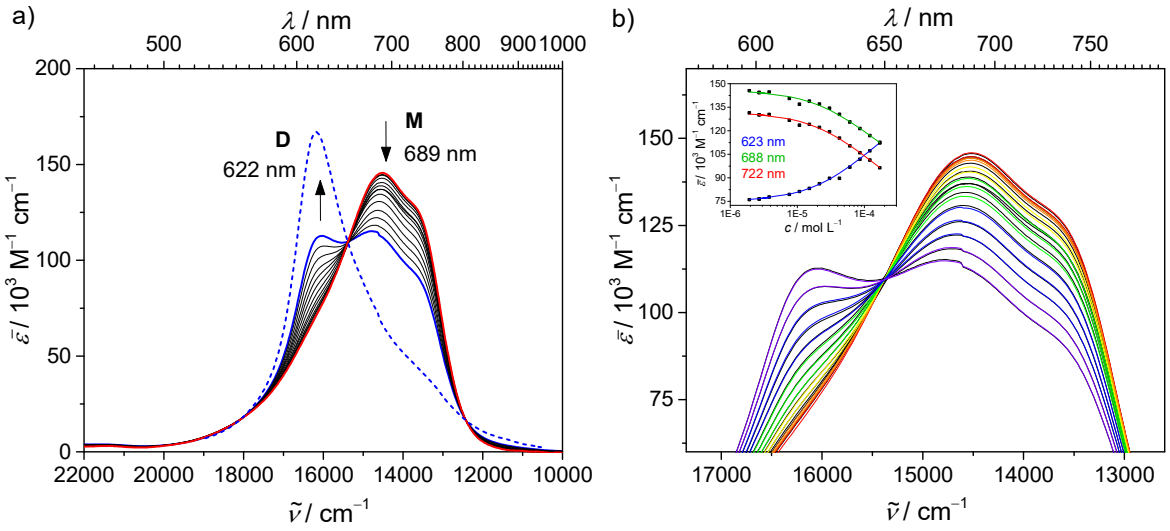

Figure A14 a) Concentration-dependent UV/vis spectra of bis(merocyanine) **GG** in 1,4-dioxane at 295 K (c = 1.7 x 10^{-4} M – 1.9 x 10^{-6} M) starting at high concentration (solid blue line) and successively diluting the solution (black lines). The spectrum at lowest concentration is depicted in solid red line. Black arrows indicate the decrease in the intensity of the monomer band and the appearance of the dimer band upon increasing concentration. Dashed lines correspond to the calculated spectra of monomer (red) and the dimer (blue) according to the dimerization model. b) Significant area of concentration-dependent UV/vis spectra of **GG** (black lines). Colored lines represent the spectra obtained by global fit analysis according to the dimerization model and the inset shows the analysis of the concentration-dependent extinction data at various wavelengths.

At lowest concentration, the absorption spectrum (red line) corresponding to the monomeric species with a maximum at 689 nm is observed. With increasing concentration, this monomer band decreases and a hypsochromically shifted aggregate band appears at 622 nm pointing out to a self-assembly process into H-type aggregates. Well-defined isosbestic points over the whole concentration range reveal a thermodynamic equilibrium between two defined species

and the concentration-dependent spectral data could be successfully fitted with the dimerization model[18d, 22c] by a global fit analysis (Figure A14b) yielding the calculated absorption spectra of the monomer (M, dashed red line) and the dimer (D, dashed blue line, Figure A14a).[10] Compared to the dimerization process of reference **G** a considerably larger value for the dimerization constant $K_2^{\mathbf{GG}}$ of 3.8 x10^3 M^{-1} ($K_2^{\mathbf{G}}$ = 32 M^{-1}) is observed and the aggregate absorption band appears at shorter wavelength (622 nm compared to 673 nm for the dimer band of **G**). Hence, it can be concluded that in the dimer aggregate of **GG** more than two chromophores must interact with each other. Consequently, a tweezer-type formation of dimer complexes with a stack of four antiparallel aligned chromophores comparable to the self-assembly of bis(merocyanine) dyes discussed in Chapter 3 is reasonable. This aggregation motif is only possible if the bis(merocyanine) dye exhibits a spacer unit that keeps the two chromophores at a distinct interplanar distance to prevent intramolecular interactions (see Chapter 3) or if the molecule is mostly in the unfolded conformation, whereas completely folded systems were proven to show folding-induced aggregation into extended H-aggregates.[19g, 90] Hence, the self-assembly behaviour of bis(merocyanine) **GG** further supports the weak folding tendency of **GG** in 1,4-dioxane.

Single-Crystal X-Ray Analysis of Reference Merocyanine G

Single-crystals of reference merocyanine **G** suitable for X-ray structural analysis were grown by slow evaporation of a solution of **G** in chloroform at room temperature.

Single-crystal X-ray diffraction data were collected at 100 K on a Bruker X8APEX-II diffractometer with a CCD area detector and multi-layer mirror monochromated MoK_α radiation. The structure was solved using direct methods, expanded with Fourier techniques and refined with the Shelx software package.[150] All non-hydrogen atoms were refined anisotropically. Hydrogen atoms were included in the structure factor calculation on geometrically idealized positions.

Crystal data for reference merocyanine **G** ($C_{31}H_{35}N_3O_2S$): M_r = 633.05, triclinic space group *P*–1, a = 8.4504(6) Å, b = 9.7732(7) Å, c = 20.3857(15) Å, α = 91.876(3)°, β = 92.162(3)°, γ = 107.909(2)°, V = 1599.1(2) Å^3, Z = 2, ρ_{calcd} = 1.315 g cm^{-3}, μ = 3.467 mm^{-1},

[10] The dimer spectrum cannot be achieved experimentally due to insufficient solubility of the aggregate species.

$F(000) = 664.0$, $F(000') = 668.33$, $T = 100$ K, $R_1 = 0.0491$, $wR^2 = 0.1443$ for all data, 6324 unique reflections and 373 parameters.

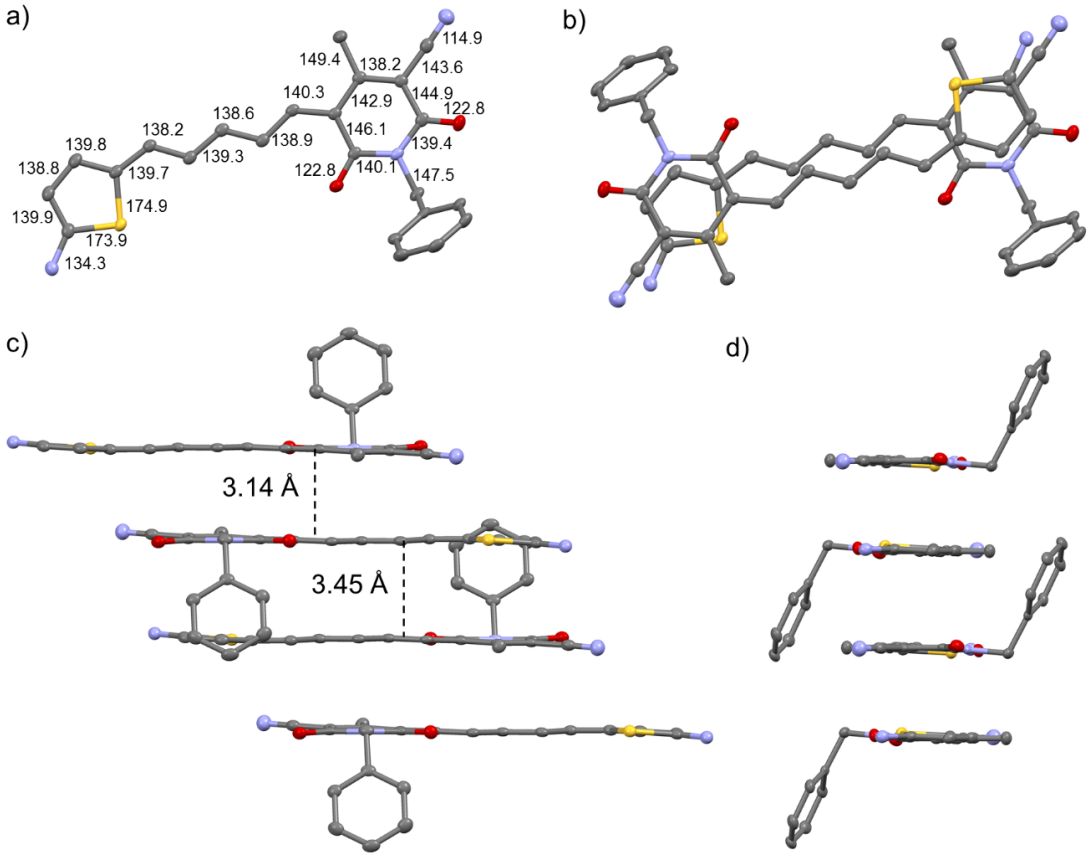

Figure A15 Single-crystal X-ray structure of reference merocyanine **G**. a) Molecular structure with bond length given in pm and b) top view of the dimer synthon with antiparallel aligned chromophores. c,d) The π-stack within the crystal lattice is depicted by different side views. Hydrogen atoms and butyl chains are omitted for clarity; grey C, blue N, red O, yellow S.

Single-crystal X-ray analysis of reference dye **G** revealed chromophores that are almost coplanar with only minor twist angle of 3.13° between the planes of thiophene donor and pyridone acceptor moieties. The solid state packing is composed of dimer units with antiparallel aligned chromophores as main structural motif bearing almost no lateral and longitudinal displacement and therefore, show maximal overlap between the π-surfaces (Figure A15b). Notably, the distance between the molecular plains in these dimers amounts to 3.45 Å (Figure A15c), which is in good accordance with the π-π-distances reported for reference merocyanines **R** and **B**.[82] Furthermore, the dimer units stack into columns with close distance of 3.14 Å between the neighbouring chromophore planes of the respective dimer units and only small lateral displacement facilitates a tightly packed solid state structure.

Computational Details

Geometry-optimizations were performed using the B97D3[139] functional including dispersion correction with def2-SVP[122] as basis set as implemented in the Gaussian 09 program package.[151] Butyl and benzyl groups were replaced by methyl groups. The conductor-like polarizable continuum model (CPCM)[140] was employed to account for solvent effects using 1,4-dioxane as solvent. The structures were geometry-optimized followed by frequency calculations to prove the existence of minima. Small imaginary frequencies <100 cm^{-1} were obtained, which can be considered as artefacts of the calculations.[152] Therefore, the obtained structures (Figure 58) can be seen as real minima.

TDDFT calculations (ωB97[121]/def2-SVP[122]) were performed on the geometry-optimized structures (B97D3[139]/def2-SVP[122]) employing the same solvent model as for the geometry-optimizations. The UV/vis spectra (Figure 60) were simulated with the help of the GaussView 5[128] visualization software package using the results obtained by TDDFT calculations. A half-width at half maximum of 0.11 eV (**RR**), 0.13 eV (**BB**), 0.21 eV (**GG**), 0.17 eV (**BG**), 0.16 eV (**RB**) and 0.17 eV (**RG**) were used for the simulation of the spectra. In addition, the spectra were shifted by 0.41 eV (**RR**), 0.37 eV (**BB**), 0.26 eV (**GG**), 0.28 eV (**BG**), 0.38 eV (**RB**) and 0.35 eV (**RG**) towards lower energies.

Table A10 Bond length (pm) along the polymethine bridge of geometry-optimized structures (B97D3[139]/def2-SVP,[122] using 1,4-dioxane as solvent) of reference merocyanines **R**, **B** and **G**, as well as for chromophore **G** within the folded structures of bis(merocyanine) dyes **RG**, **BG** and **GG**. The bonds are assigned by small letters according to the chemical structures depicted below.

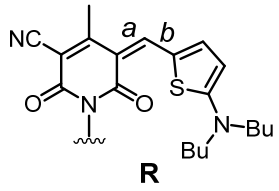

R

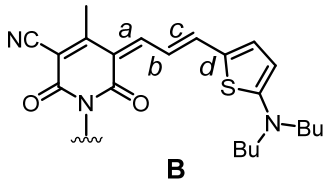

B

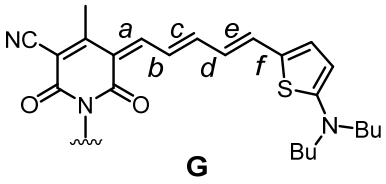

G

bond length / pm	**R**	**B**	**G**	of **G** in the folded structure of bis(merocyanine)			
				RG	**BG**	**GG** (chr. 1)	**GG** (chr. 2)
a	140.7	140.7	140.8	141.2	141.1	141.8	141.4
b	140.7	140.9	140.9	140.1	140.2	139.9	140.1
c	-	139.3	139.5	139.7	139.8	140.0	139.9
d	-	141.1	141.2	140.5	140.4	140.4	140.4
e	-	-	139.0	139.4	139.5	139.5	139.5
f	-	-	141.4	140.6	140.5	140.6	140.5

Determination of the Huang-Rhys factor

The Huang-Rhys factors (*HR*) of monomeric reference dyes **R**, **B** and **G** in DCM and 1,4-dioxane were determined by the ratio between the vibronic 0–1 and 0–0 peak areas. A simplified model was applied assuming that only one effective mode couples to the electronic excitation.[137, 153] Therefore, the experimental absorption spectra were fitted by two Gaussian functions, respectively (Figure A16), with the restriction of equal band widths since the presence of multiple closely-spaced vibrational modes are known to cause a broadening of the higher energy absorption band. From the difference of the resulting peak positions a vibrational frequency of 1200 cm^{-1} is observed, which is in good agreement with the value reported for merocyanine dyes[137] and which is commonly attributed to the vinyl stretching of organic π-conjugated molecules.[130b]

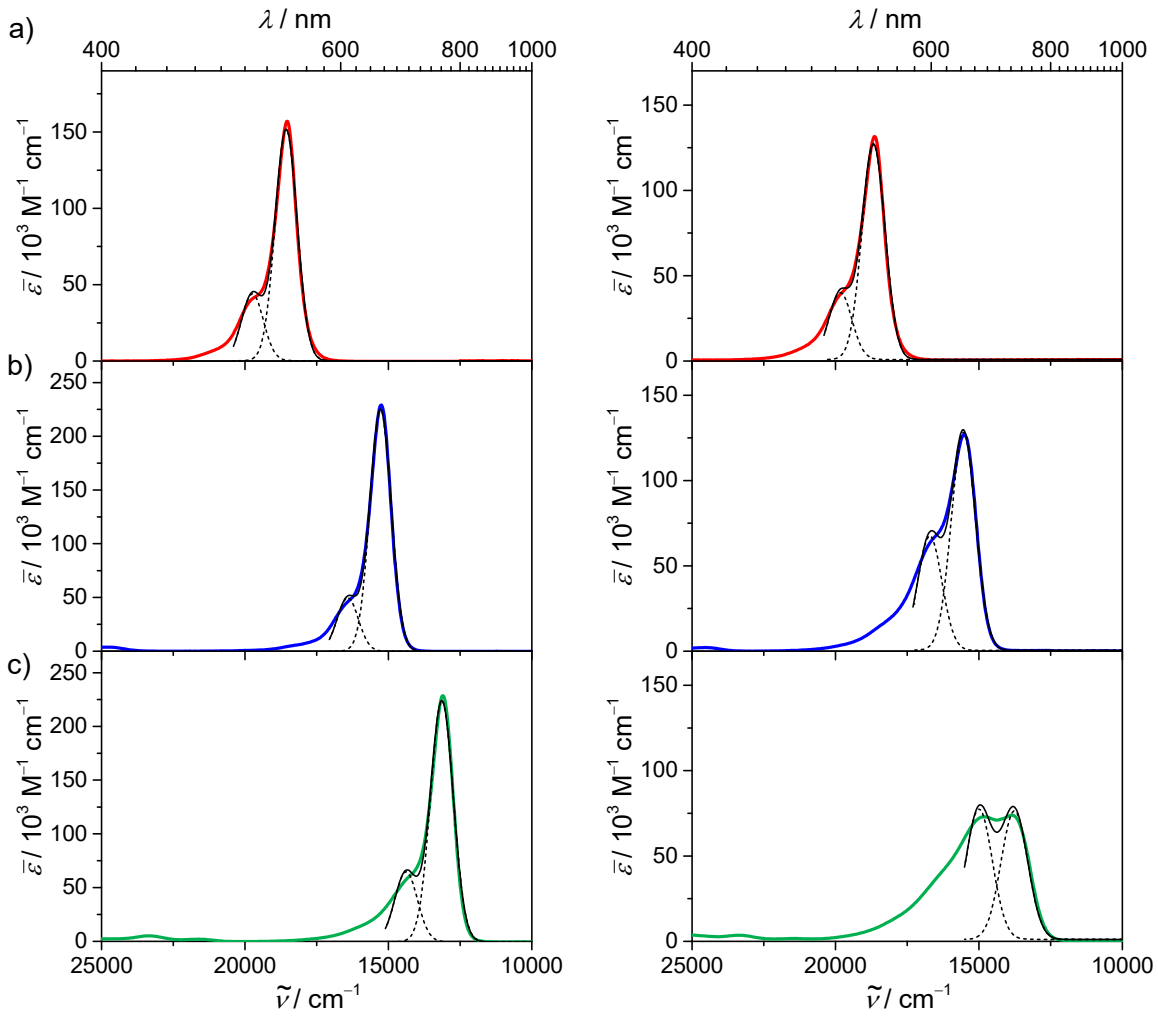

Figure A16 UV/vis absorption spectra of reference merocyanines a) **R**, b) **B** and c) **G** (colored lines) in DCM (left plot) and 1,4-dioxane (right plot) at 295 K (c = 4 x 10^{-6} M). The calculated spectra fitted by two Gaussian functions (dashed black lines) are depicted in solid black lines.

Determination of the exciton coupling energy

The coefficients c_a and c_b describe the contribution of the individual chromophores to the exciton states of the dimer and were obtained from the normed eigenvectors of the corresponding Hamiltonian matrix (Table A11 and Table A12).

Table A11 Hamiltonian matrix for homo-[a] and hetero-[b] bis(merocyanine) dimers.

Homo-dimer	Hetero-dimer
$\begin{pmatrix} 0 & J \\ J & 0 \end{pmatrix}$	$\begin{pmatrix} \frac{\Delta E}{2} & J \\ J & -\frac{\Delta E}{2} \end{pmatrix}$

[a]The excited state energy of the monomeric chromophores was set as zero level.

[b]The arithmetic middle of the excited state energies of the monomeric chromophores was set as zero level.

Table A12 Normed eigenvectors of the Hamiltonian matrix for homo- and hetero-bis(merocyanine) dimers.

	exciton state S_1`	exciton state S_1``
homo-dimers	$c_a = \frac{1}{\sqrt{2}}$ $c_b = -\frac{1}{\sqrt{2}}$	$c_a = \frac{1}{\sqrt{2}}$ $c_b = \frac{1}{\sqrt{2}}$
hetero-dimers	$c_a = \frac{1}{\sqrt{1 + \frac{\left(\sqrt{\left(\frac{\Delta E}{2}\right)^2 + J^2} + \frac{\Delta E}{2}\right)^2}{J^2}}}$ $c_b = -\frac{\left(\sqrt{\left(\frac{\Delta E}{2}\right)^2 + J^2} + \frac{\Delta E}{2}\right)}{J\sqrt{1 + \frac{\left(\sqrt{\left(\frac{\Delta E}{2}\right)^2 + J^2} + \frac{\Delta E}{2}\right)^2}{J^2}}}$	$c_a = \frac{1}{\sqrt{1 + \frac{\left(\sqrt{\left(\frac{\Delta E}{2}\right)^2 + J^2} - \frac{\Delta E}{2}\right)^2}{J^2}}}$ $c_b = -\frac{\left(\sqrt{\left(\frac{\Delta E}{2}\right)^2 + J^2} - \frac{\Delta E}{2}\right)}{J\sqrt{1 + \frac{\left(\sqrt{\left(\frac{\Delta E}{2}\right)^2 + J^2} - \frac{\Delta E}{2}\right)^2}{J^2}}}$

To obtain the exciton coupling energy J between the transition dipole moments of chromophores in a dimer, TDDFT calculations (ωB97[121]/def2-SVP[122]) were performed on the geometry-optimized structures (B97D3[139]/def2-SVP[122]) of reference dyes **R**, **B** and **G** affording the transition densities of the individual chromophores. For the TDDFT calculations, no solvation model was used since the values for the transition dipole moments obtained by employing the conductor-like polarizable continuum model were overestimated. Thus, the values for the transition dipole moments obtained in vacuum (Figure 58a-c) are in good agreement with the experimental ones.[82] The densities were fitted to atomic charges by Mulliken population analysis of the transition densities using the Multiwfn software package[154] to obtain the transition charges of **R**,[20a] **B**[20a] and **G** (Table A13) which were then used to calculate the exciton coupling energy J between the chromophores in the dimer stacks. According to Equation A7, the exciton coupling energy J is defined as the Coulomb interaction between the transition charges of the respective chromophores[124, 145] with the transition charge q_i(a) on atom i of chromophore a, the transition charge q_j(b) on atom j of chromophore b and the position vectors of the respective atoms $\mathbf{r}_i$ and $\mathbf{r}_j$.

$$J = \sum_i \sum_j \frac{q_i(a) \cdot q_j(b)}{|\mathbf{r}_i - \mathbf{r}_j|} \qquad (A7)$$

Table A13 Cartesian coordinates of the geometry-optimized structure of reference dye **G** (B97D3/def-2SVP) and transition charges derived from Mulliken population analysis of the transition density obtained by TDDFT calculations (ωB97/def-2SVP).

	x	*y*	*z*	transition charges
C	–4.550808	–1.097074	0.000030	–0.014404
C	–5.779902	–0.442974	–0.000032	0.047386
C	–5.907167	1.025591	–0.000094	0.013335
N	–4.694698	1.737263	–0.000067	–0.005526
C	–3.412240	1.160247	0.000026	0.011893
C	–3.334125	–0.322963	0.000057	0.043311
C	–2.086604	–0.975631	0.000131	–0.015899
C	–0.785886	–0.432895	0.000115	0.040286
C	–4.502468	–2.604559	0.000049	–0.001814
O	–2.432485	1.908535	–0.000166	0.036052
O	–6.994135	1.600079	–0.000107	0.031324
C	1.674038	–0.774149	0.000133	0.051534
C	0.344551	–1.250149	0.000211	–0.047897
C	4.145224	–1.223088	0.000090	0.037060
S	4.657254	0.476905	0.000020	–0.044463
C	6.355101	0.015456	–0.000400	–0.030321
C	6.506667	–1.389314	–0.000116	0.002277
C	5.274900	–2.061371	0.000037	–0.048443
N	7.325591	0.959567	–0.000970	–0.019506
C	6.968413	2.372383	0.000703	0.017198
C	8.720470	0.532745	0.000047	0.019679
C	2.785153	–1.608504	0.000208	–0.060463
C	–4.747829	3.200743	–0.000152	–0.008851
C	–7.013746	–1.160994	–0.000081	0.005692
N	–8.016913	–1.768952	–0.000136	0.038116
H	–2.123288	–2.072049	0.000212	0.016009
H	–0.669335	0.654333	0.000007	0.008710
H	–5.512374	–3.039621	–0.000070	0.006224
H	–3.966428	–2.982247	–0.889043	0.013199
H	–3.966657	–2.982224	0.889292	0.013198
H	1.822559	0.315654	–0.000036	–0.000310
H	0.199358	–2.342477	0.000337	–0.003025
H	7.477252	–1.888432	–0.000022	–0.022285
H	5.176657	–3.151844	0.000142	–0.028250
H	6.367977	2.630636	–0.893635	–0.021230
H	6.375419	2.630969	0.899953	–0.021318
H	7.882468	2.982862	–0.003310	–0.016587
H	8.951018	–0.070700	0.898531	–0.020198
H	8.950471	–0.075418	–0.895330	–0.020110
H	9.370327	1.419194	–0.002560	–0.018274
H	2.615268	–2.695256	0.000354	–0.018073
H	–4.234882	3.597018	0.891854	0.013166
H	–4.234864	3.596922	–0.892192	0.013174
H	-5.804357	3.497145	–0.000182	0.008422

Chapter 5

—

Summary

Supramolecular chemistry has developed to a vast area of research since non-covalent forces between molecular building blocks provide access to an infinite number of different structural motifs paving the way for the development of new materials with unique functionalities. In particular the controlled self-assembly of organic dye molecules constitutes a smart entry to create innovative materials with immense potential applications. Thus, detailed knowledge about the influence of the supramolecular structure on the material properties plays a key role to optimize device performance on the molecular level. Therefore, the aim of the present work was to create multichromophoric model systems that enable detailed investigations on properties of dye aggregates depending on their size and structure.

Chapter 2 provides an overview on literature known strategies to realize finite-sized supramolecular π-stacks with well-defined number of interacting chromophores. It has been shown that aggregation can be controlled accurately by extrinsic factors such as the utilization of supramolecular templates as well as by the intrinsic design of molecular building blocks. Thus, discrete π-stacks become accessible through the attachment of carefully selected sterically demanding substituents, although it is rather difficult to precisely adjust the steric repulsion. Also the backbone-directed inter- and intramolecular stacking represents a reliable strategy to define the number of stacked chromophore units. In combination with the involvement of highly directional supramolecular forces like dipole-dipole interactions, it proved to be a very promising approach since it is capable of developing discrete one-dimensional structures with high degree of order. In addition, structural characterization of dye aggregates by different analytical techniques has been discussed in this section based on representative examples. Thus, it appears that in most cases results obtained by different

methods adapted to the individual system have to be combined to fully solve the supramolecular structure.

Based on this knowledge, a strategy has been developed to create discrete finite-sized stacks of dipolar merocyanine dyes with well-defined number of interacting chromophores by careful selection of the length and flexibility of the spacer unit of bis(merocyanine) dyes (**Chapter 3**). From previous work it is known that **Bis(MC) 1** bearing two merocyanine chromophores connected by a rigid naphthalenedimethylene spacer self-assembles in solution forming bimolecular complexes with a stack of four antiparallel chromophores (Figure 63). Hence, **Bis(MC) 2** and **Bis(MC) 3** were designed comprising a diphenylacetylene or diphenyl-butadiyne backbone, which provide a larger interplanar distance between the chromophores compared to **Bis(MC) 1**. Furthermore, long alkyl chains were introduced to the backbones, in order to ensure adequate solubility of the aggregates.

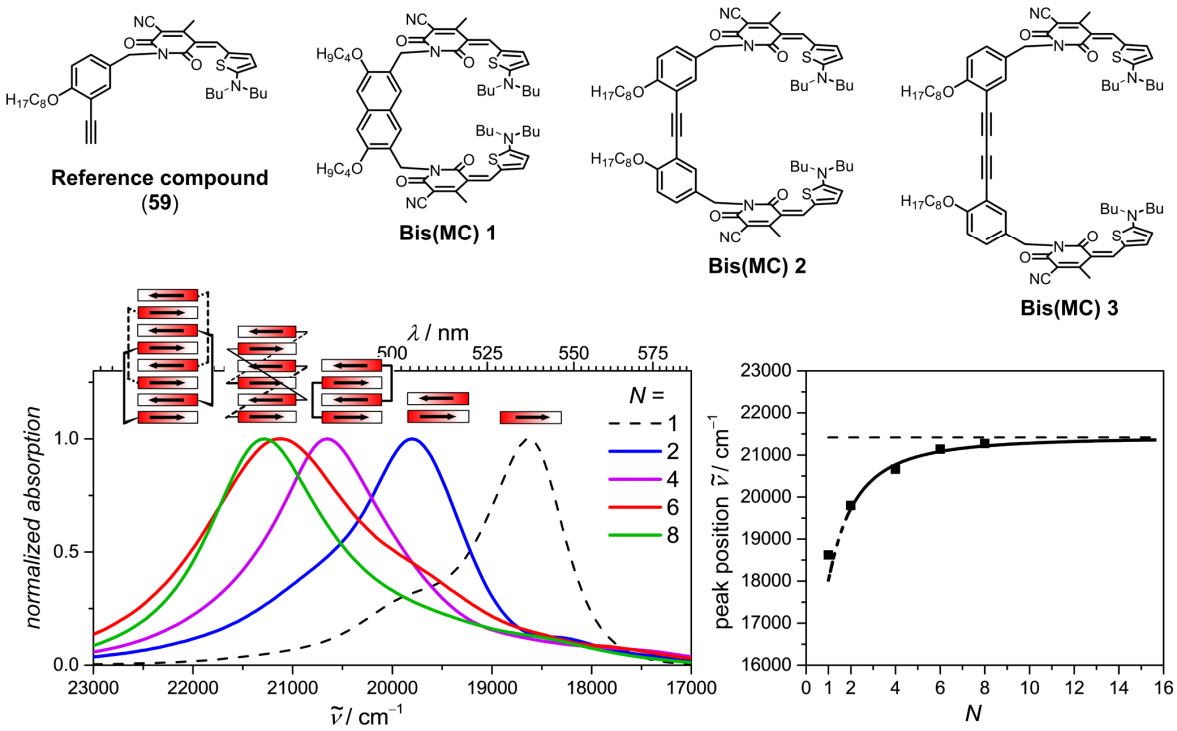

Figure 63 Chemical structures of bis(merocyanine) dyes **Bis(MC) 1**, **Bis(MC) 2** and **Bis(MC) 3** and reference dye **59** and absorption spectra (left plot) of monomer (dotted black line) and dimeric stack (blue line) of the reference dye **59**, tetrachromophoric stack of **Bis(MC) 1** (purple line), hexachromophoric stack of **Bis(MC) 2** (red line) and octachromophoric stack of **Bis(MC) 3** (green line) in THF/MCH mixture (17.5 : 82.5). Peak positions corresponding to the highest exciton state of the respective aggregates with *N* stacking chromophores (right plot).

First of all, synthetic routes to the target compounds and the monochromophoric reference dye **59** are described followed by detailed investigation of the self-assembly behaviour of **Bis(MC) 1**, **Bis(MC) 2** and **Bis(MC) 3** in comparison to the reference merocyanine **59** by

UV/vis absorption studies. For all dyes, spectral changes upon increasing the concentration of a dye solution point out to the formation of H-type aggregates and could be analysed by corresponding global fit routines. Hence, self-assembly of reference dye **59** and of **Bis(MC) 1** into dimers was observed, respectively, which is in accordance with results from earlier work. In contrast, studies on **Bis(MC) 2** indicate the formation of trimeric aggregates comprising a stack of six chromophores and **Bis(MC) 3** shows self-assembly into tetramers with eight stacked merocyanine units. These results are further corroborated by high-resolution mass spectrometry of all bis(merocyanine) aggregate species and by AFM studies that show small spherical nanoparticles, respectively and thus exclude the formation of extended supramolecular polymers. To gain deeper insight into the structure of the merocyanine stacks, **Bis(MC) 3** aggregate was investigated by detailed one- and two-dimensional NMR experiments. The findings are in accordance with a DFTB calculated aggregate model, revealing a centrosymmetric tetramer of **Bis(MC) 3** with a stack of eight antiparallel aligned chromophores. Furthermore, the remarkably sharp and well-resolved proton NMR signals clearly demonstrate the exceptionally high degree of order of this supramolecular structure. Consequently, the series of herein established merocyanine aggregates comprising discrete, highly ordered stacks of two, four, six and eight chromophores constitutes a model system that for the first time allows fundamental studies on aggregate properties depending on the number of interacting dye units. On this basis, optical features of the different aggregate species were compared illustrating an increased hypsochromic shift of the absorption maximum with respect to the monomer absorption (Figure 63), which could be rationalized through exciton theory and quantum chemical calculations. Finally, a relationship between the optical properties and the number of stacked chromophores could be derived, which contributes to a better understanding how the size and structure of supramolecular aggregates affect their electronic properties.

The second part of this work (**Chapter 4**) deals with a systematic investigation of exciton coupling between merocyanine chromophores of different excited state energies. To enable this study, bichromophoric model systems were established by attaching two equal or different merocyanine units in *ortho*- and *meta*-position to a diphenylacetylene spacer unit, which is known to favour an intramolecular folded conformation of the molecules in unpolar solvents with antiparallel stacked chromophores (Figure 64). Thus, homo-bis(merocyanines) **RR**, **BB** and **GG** and hetero-bis(merocyanines) **BG**, **RB** and **RG** comprising various combinations of two of three merocyanine units with different conjugation length were included in this study. The monochromophoric compounds **R**, **B** and **G** serve as reference dyes.

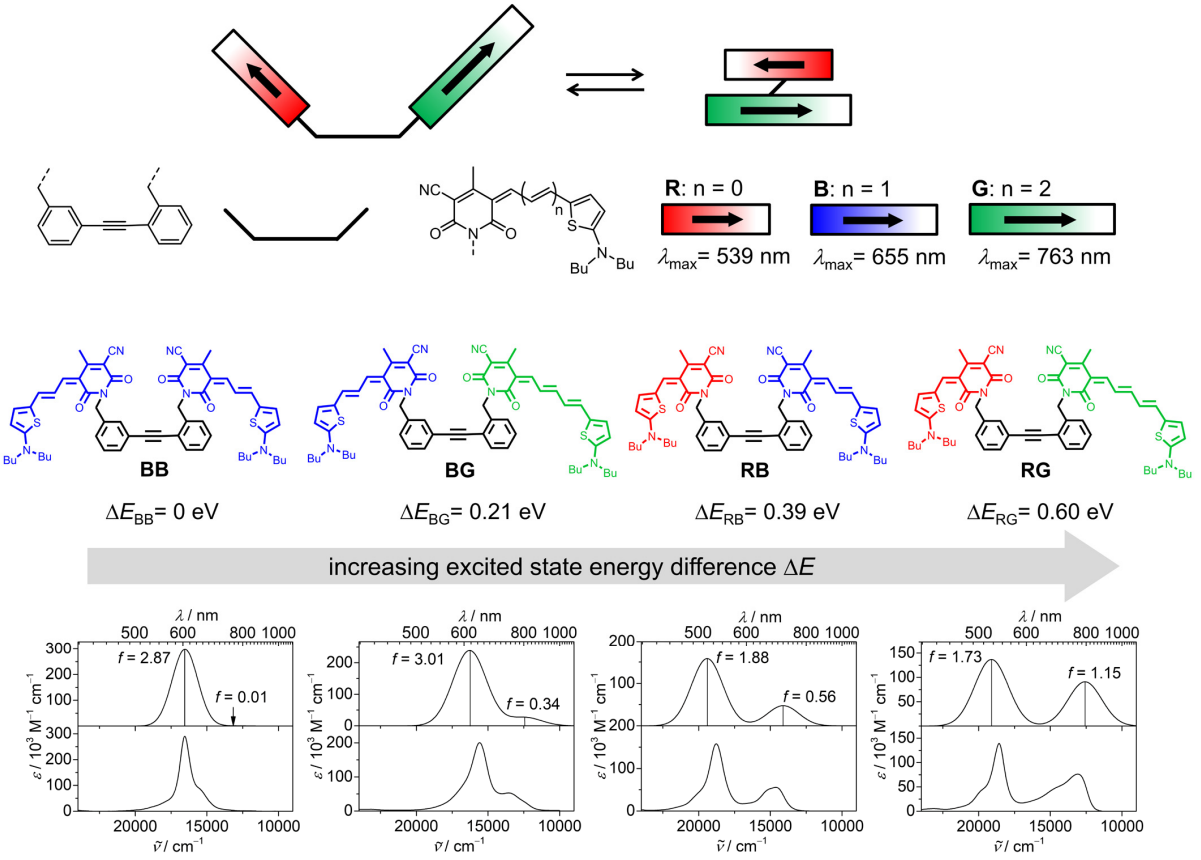

Figure 64 Schematic representation of the folding process of bis(merocyanine) dye **RG** as well as chemical structures of homo-bis(merocyanine) **BB** and hetero-bis(merocyanine) dyes **BG**, **RB** and **RG** comprising variable combinations of two of the three merocyanine chromophores **R** (red), **B** (blue) and **G** (green). Simulated (calculated by TDDFT (ωB97), top) and experimental (1,4-dioxane at 4 x 10^{-6} M, bottom) UV/vis absorption spectra of folded homo-bis(merocyanine) **BB** and hetero-bis(merocyanine) dyes **BG**, **RB** and **RG** (depicted from left to right).

The synthesis of bis(merocyanine) dyes could be achieved by applying different routes for homo- and hetero-systems and the folding behaviour was investigated by UV/vis absorption studies. Solvent-dependent spectral changes of the reference dyes were explained by solvatochromic effects and significant changes in absorption properties of bis(merocyanine) dyes could indeed be attributed to intramolecular folding. Furthermore, geometry-optimization of the folded structures on the DFT level gave insight into the structural arrangement of the chromophores within the foldamers pointing out to an antiparallel π-stacked orientation. In addition, quantum chemical calculations reveal strong exciton coupling between chromophores in homo- and hetero-dye stacks. Hence, model systems have been established that enable exploring optical features not only of dimer aggregates comprising energetically equal dyes but also of hetero-dimers. The simulated absorption spectra (calculated by TDDFT) of all merocyanine dimers are in good agreement with the experimental ones. For homo-dimers, a

hypsochromically shifted absorption band typical for H-type aggregates was observed, which could be explained according to exciton theory by a strongly allowed transition to the higher exciton state, whereas transition to the lower exciton state is entirely forbidden. Interestingly, spectra of hetero-dimers are characterized by one intense H-band at higher energy and a weak J-band at lower energy, which gains intensity with increasing energy difference between the excited states of the chromophores. This partially allowed transition to the lower exciton state was on the one hand attributed to the different magnitudes of transition dipole moments of the chromophores and on the other hand, to the increased localization of the excitation in the respective exciton state, which is in accordance with the transition densities obtained for hetero-dimers by TDDFT-calculations.

In conclusion, the present work demonstrates convenient strategies to achieve supramolecular π-stacks of precisely defined structure based on merocyanine dyes and therefore, illustrates how the structure of dye assemblies can be influenced by the design of the molecular building blocks. Furthermore, the thereby established dye stacks represent valuable model systems that give insights into optical properties of aggregates depending on their structure. Hence, a relationship between molecular design, supramolecular structure and aggregate properties could be deduced providing an important basis for the development of functional materials.

Chapter 6

–

Zusammenfassung

Die supramolekulare Chemie hat sich zu einem wichtigen Forschungsgebiet entwickelt, da die Selbstassemblierung molekularer Bausteine auf Basis nicht-kovalenter Kräfte den Zugang zu einer unendlich großen Anzahl unterschiedlicher Strukturmotive möglich macht und somit den Weg für die Fertigung neuer Materialien mit einzigartigen Funktionalitäten ebnet. Insbesondere die kontrollierte Selbstorganisation organischer Farbstoffmoleküle bietet die Möglichkeit zur Entwicklung innovativer Materialien mit einem enormen Anwendungspotenzial. Grundlegende Kenntnisse über den Einfluss der supramolekularen Struktur auf die Materialeigenschaften spielen somit eine Schlüsselrolle, um die Leistung der Bauteile auf molekularer Ebene zu optimieren. Ziel der vorliegenden Arbeit war es, multichromophore Modellsysteme zu entwickeln, die eine detaillierte Untersuchung der Eigenschaften von Farbstoffaggregaten in Abhängigkeit von ihrer Größe und Struktur ermöglichen.

Kapitel 2 gibt einen Überblick über literaturbekannte Strategien zur Realisierung supramolekularer π-Stapel endlicher Größe mit genau definierter Anzahl an interagierenden Chromophoren. Es wurde gezeigt, dass die Aggregation sowohl durch extrinsische Faktoren wie die Verwendung von Templaten, wie auch durch intrinsische Eigenschaften der molekularen Bausteine kontrolliert werden kann. So ermöglicht die Einführung sorgfältig ausgewählter, sterisch anspruchsvoller Substituenten den Aufbau endlicher π-Stapel, wobei es jedoch schwierig ist, das richtige Verhältnis zwischen sterischer Abschirmung und attraktiver supramolekularer Wechselwirkung zu finden. Darüber hinaus stellt die rückgratunterstützte inter- und intramolekulare Assemblierung eine zuverlässige Strategie dar, um die Anzahl der Chromophore im Stapel genau zu definieren. Insbesondere durch den zusätzlichen Einfluss von gerichteten supramolekularen Kräften wie Dipol-Dipol-Wechselwirkungen erwies sich

dieser Ansatz als vielversprechend für die Realisierung endlicher, eindimensionaler Aggregate mit hochgeordneter Struktur. Des Weiteren wurde in diesem Abschnitt die strukturelle Charakterisierung von Farbstoffaggregaten durch verschiedene analytische Techniken anhand repräsentativer Beispiele diskutiert. Es stellte sich heraus, dass in den meisten Fällen die Aufklärung der supramolekularen Struktur nur durch Kombination von Ergebnissen aus unterschiedlichen Messmethoden, welche individuell an das System angepasst wurden, möglich ist.

Basierend auf diesem Wissen wurde in der vorliegenden Arbeit eine Strategie entwickelt, die durch sorgfältige Auswahl der Länge und Flexibilität der Brückeneinheit von Bis(merocyanin)-Farbstoffen den Aufbau endlicher Stapel bestehend aus dipolaren Merocyaninfarbstoffen mit einer genau definierten Anzahl von wechselwirkenden Chromophoren erlaubt (**Kapitel 3**). Aus früheren Arbeiten ist bereits bekannt, dass **Bis(MC) 1**, welches aus zwei durch eine starre Naphthalindimethylen-Brücke verbundene Merocyanin-Chromophoren besteht, in Lösung bimolekulare Komplexe mit einem Stapel von vier antiparallel angeordneten Chromophoren ausbildet (Abbildung 65). Auf diesen Erkenntnissen aufbauend wurden die Verbindungen **Bis(MC) 2** und **Bis(MC) 3** entworfen, welche ein Diphenylacetylen- oder Diphenylbutadiin-Rückgrat enthalten und somit im Vergleich zu **Bis(MC) 1** einen größeren interplanaren Abstand zwischen den Chromophoren aufweisen. Außerdem wurden lange Alkylketten eingeführt, um ausreichende Löslichkeit der Aggregate in unpolaren Lösungsmitteln zu gewährleisten. Zunächst wurde die Synthese der Zielverbindungen sowie der Referenzverbindung **59** beschrieben, gefolgt von einer detaillierten UV/vis spektroskopischen Untersuchung des Selbstorganisationsverhaltens von **Bis(MC) 1**, **Bis(MC) 2** und **Bis(MC) 3** im Vergleich zum Referenzfarbstoff **59**. Für alle Farbstoffe konnten deutliche spektrale Änderungen bei Erhöhung der Konzentration festgestellt werden, was auf die Bildung von H-artigen Aggregaten hindeutet. Zudem konnten die Daten aus den konzentrationsabhängigen Studien durch die Anpassung an das jeweilige Aggregationsmodell analysiert werden. Folglich wurde für den Referenzfarbstoff **59** sowie für **Bis(MC) 1** ein Dimerisierungsverhalten abgeleitet, was den Ergebnissen früherer Arbeiten entspricht. Im Gegensatz dazu zeigen die Studien von **Bis(MC) 2** die Ausbildung von Trimeraggregaten, welche einen Stapel von sechs Chromophoren umfassen. **Bis(MC) 3** zeigt sogar eine Selbstassemblierung zu Tetrameren mit acht gestapelten Merocyanineinheiten. Diese Ergebnisse werden sowohl durch hochaufgelöste Massenspektren aller Bis(merocyanin)-Aggregatspezies als auch durch AFM-Aufnahmen bestätigt, welche kleine

sphärische Nanopartikel zeigen und somit die Bildung ausgedehnter supramolekularer Polymere ausschließen.

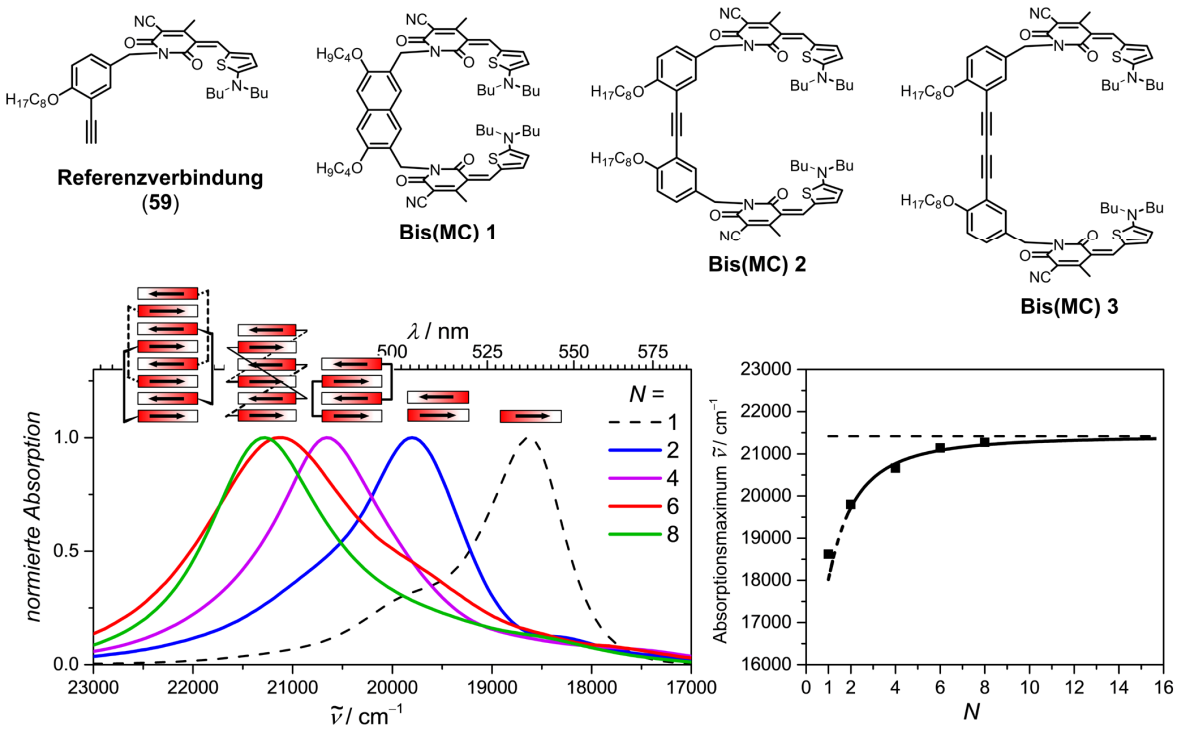

Abbildung 65 Chemische Struktur der Bis(merocyanin)-Farbstoffe **Bis(MC) 1**, **Bis(MC) 2** und **Bis(MC) 3** sowie der Referenzverbindung **59** und Absorptionsspektren (linker Graph) des Monomers (gestrichelte schwarze Linie) und des Dimerstapels (blaue Linie) der Referenzverbindung **59**, des Viererstapels (lilafarbene Linie) von **Bis(MC) 1**, des Sechserstapels (rote Linie) von **Bis(MC) 2** und des Achterstapels (grüne Linie) von **Bis(MC) 3** in einem Lösungsmittelgemisch aus THF/MCH (17.5 : 82.5). Lage der Absorptionsmaxima der jeweiligen Aggregate mit *N* gestapelten Chromophoren (rechter Graph).

Um einen detaillierteren Einblick in die Struktur der Merocyaninaggregate zu erhalten, wurde das **Bis(MC) 3**-Tetramer eingehend mittels ein- und zweidimensionaler NMR-Spektroskopie untersucht. Die Ergebnisse stimmen mit dem berechneten (DFTB) Aggregatmodell überein und zeigen ein zentrosymmetrisches Tetrameraggregat von **Bis(MC) 3**, welches einen Stapel von acht antiparallel ausgerichteten Chromophoren bildet. Darüber hinaus verdeutlichen die bemerkenswert scharfen und gut aufgelösten Protonen-NMR-Signale, dass es sich bei diesem supramolekularen Aggregat um eine außergewöhnlich präzise definierte Struktur handeln muss. Folglich konnten in dieser Arbeit Merocyaninaggregate bestehend aus hochgeordneten Stapeln von zwei, vier, sechs und acht Chromophoren realisiert werden. Die so etablierte Serie stellt ein Modellsystem dar, welches erstmals eine grundlegende Untersuchung der Aggregateigenschaften in Abhängigkeit von der Anzahl der miteinander wechselwirkenden Farbstoffeinheiten ermöglicht. Auf dieser Grundlage zeigte ein Vergleich der optischen Eigenschaften der verschiedenen Aggregatspezies eine zunehmende hypsochrome

Verschiebung des Absorptionsmaximums hinsichtlich der Monomerabsorption (Abbildung 65), was anhand von Exzitonentheorie und quantenchemischen Rechnungen gedeutet werden konnte. Schließlich konnte eine Beziehung zwischen den optischen Eigenschaften und der Anzahl der gestapelten Chromophore abgeleitet werden, was zu einem besseren Verständnis beiträgt, wie die elektronischen Eigenschaften supramolekularer Aggregate durch ihre Größe und Struktur beeinflusst werden.

Der zweite Teil dieser Arbeit (**Kapitel 4**) befasste sich mit der systematischen Untersuchung der Exzitonenkopplung zwischen Merocyaninchromophoren unterschiedlicher Anregungsenergien. Für die Studie wurden Modellsysteme entwickelt, welche zwei gleiche oder verschiedenartige Merocyanineinheiten in *ortho*- und *meta*-Position einer Diphenylacetylen-Brücke enthalten und die in unpolaren Lösungsmitteln eine intramolekular gefaltete Konformation der Moleküle mit antiparallel gestapelten Chromophoren ausbilden (Abbildung 66).

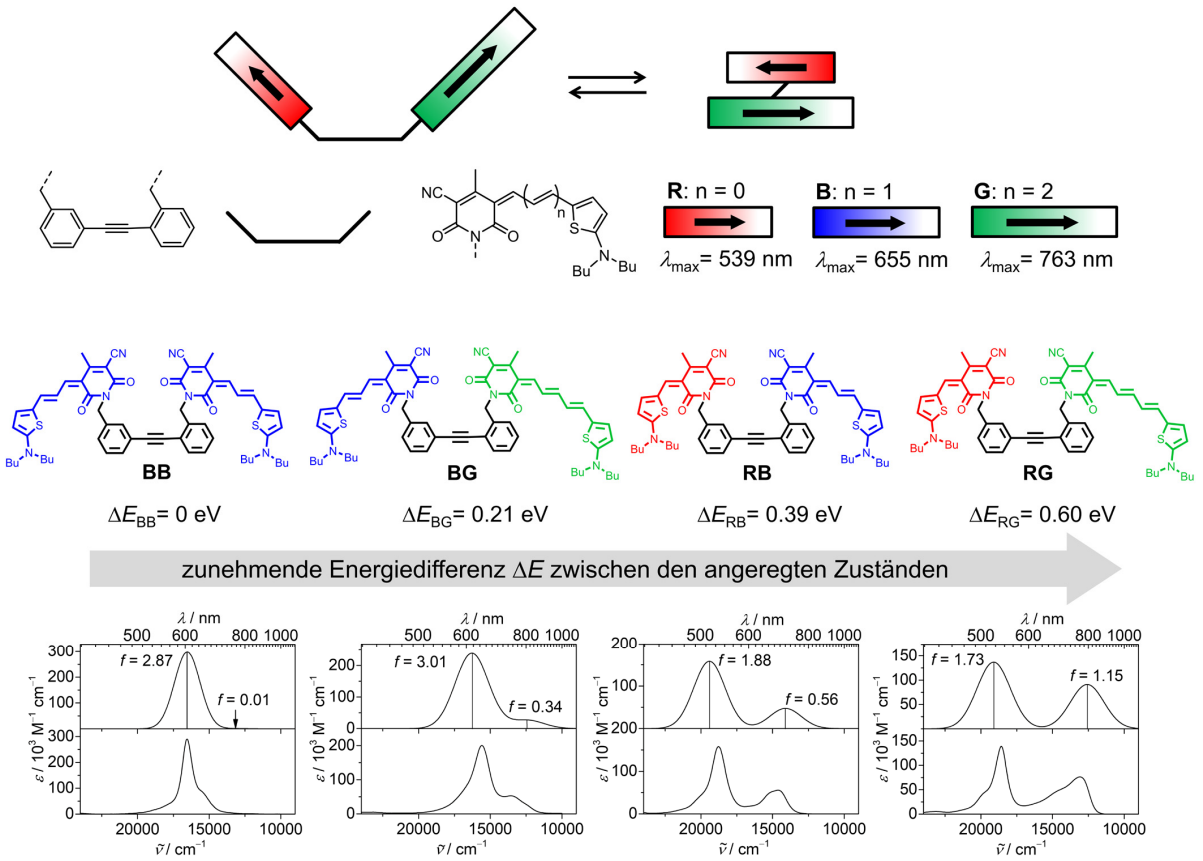

Abbildung 66 Schematische Darstellung des Faltungsprozesses von Bis(merocyanin)-Farbstoff **RG** und chemische Struktur des Homo-Bis(merocyanins) **BB** und der Hetero-Bis(merocyanine) **BG**, **RB** und **RG** mit unterschiedlichen Kombinationen von zwei der drei Merocyaninchromophore **R** (rot), **B** (blau) und **G** (grün). Simulierte (berechnet mittels TDDFT (ωB97), oben) und experimentell erhaltene (1,4-Dioxan bei 4 x 10^{-6} M, unten) UV/vis Absorptionsspektren des gefalteten Homo-Bis(merocyanins) **BB** und der Hetero-Bis(merocyanine) **BG**, **RB** und **RG** (abgebildet von links nach rechts).

So wurden die Homo-Bis(merocyanin)-Verbindungen **RR**, **BB** und **GG** sowie die Hetero-Bis(merocyanin)-Verbindungen **BG**, **RB** und **RG** hergestellt, welche verschiedene Kombinationen von zwei der drei Merocyanineinheiten mit unterschiedlicher Konjugationslänge enthalten. Die einzelnen Farbstoffe **R**, **B** und **G** dienen als Referenzsysteme. Die Synthese der Homo- und Hetero-Bis(merocyanin)-Farbstoffe konnte auf zwei verschiedenen Wegen realisiert werden und das Faltungsverhalten wurde durch UV/vis-Absorptionsstudien untersucht. Lösungsmittelabhängige spektrale Veränderungen der Referenzfarbstoffe konnten durch Solvatochromieeffekte erklärt werden und signifikante Änderungen der Absorptionseigenschaften der Bis(merocyanin)-Farbstoffe in Lösungsmitteln unterschiedlicher Polarität konnten in der Tat auf eine intramolekulare Faltung der Moleküle zurückgeführt werden. Darüber hinaus gewährte die Geometrieoptimierung der gefalteten Strukturen mittels DFT-Rechnungen einen Einblick in die Anordnung der Chromophore in einer antiparallelen Anordnung der π-Flächen im Dimerstapel. Des Weiteren deuten quantenchemische Rechnungen auf eine starke Exzitonenkopplung zwischen den Chromophoren sowohl in den Homo- als auch in den Heterosystemen hin. Somit konnten Modellsysteme etabliert werden, die eine Untersuchung der optischen Eigenschaften von Dimeraggregaten bestehend aus identischen sowie energetisch unterschiedlichen Farbstoffen ermöglichen. Die simulierten Absorptionsspektren (berechnet durch TDDFT) aller Merocyanindimere zeigen eine gute Übereinstimmung mit den experimentellen Spektren. So wurde für die Homodimere eine für H-Aggregate typische hypsochrom verschobene Absorptionsbande beobachtet, die gemäß der Exzitonentheorie mit einem stark erlaubten Übergang in den höheren Exzitonenzustand erklärt werden kann. Der Übergang in den unteren Exzitonenzustand ist hingegen verboten. Interessanterweise zeichnen sich die Spektren der Heterodimere durch eine intensive H-Bande bei höherer Energie und eine schwache J-Bande bei niedrigerer Energie aus, wobei die J-Bande mit zunehmender Energiedifferenz zwischen den angeregten Zuständen der Chromophore an Intensität gewinnt. Dieser teilweise erlaubte Übergang in den unteren Exzitonenzustand konnte einerseits den unterschiedlich großen Übergangsdipolmomenten der Chromophore und andererseits der verstärkten Lokalisierung der Anregung im jeweiligen Exzitonenzustand zugeschrieben werden, was mit den aus TDDFT-Rechnungen erhaltenen Übergangsdichten der Heterodimere übereinstimmt.

Zusammenfassend wurden in der vorliegenden Arbeit zuverlässige Strategien entwickelt, die es ermöglichen, supramolekulare π-Stapel basierend auf Merocyaninfarbstoffen mit exakt definierter Struktur zu erhalten. Es konnte somit aufgezeigt werden, wie die Struktur von Farbstoffaggregaten durch das Design der molekularen Bausteine beeinflusst wird. Darüber

hinaus stellen die so etablierten Farbstoffstapel wertvolle Modellsysteme dar, die Einblicke in die optischen Eigenschaften von Aggregaten in Abhängigkeit von ihrer Struktur geben. Damit konnte eine Beziehung zwischen molekularem Design, supramolekularer Struktur und Aggregateigenschaften abgeleitet werden, welche eine wichtige Grundlage für die Entwicklung funktioneller Materialien bildet.

Chapter 7

–

Experimental Section

7.1 Materials and Methods

UV/vis Spectroscopy

UV/vis absorption spectra were recorded on a Perkin-Elmer Lambda 950, Lambda 35 or JASCO V-760 spectrometer with a scan rate of 120 nm min^{-1} and spectral bandwidth of 1 nm. Conventional quartz cells (Hellma Analytics) of 0.01–10 cm path length were used to cover a suitable concentration range. For concentration-dependent studies, freshly prepared stock solutions in spectroscopic grade solvents (Uvasol) were subsequently diluted to adjust the desired concentration. The temperature was controlled with a PTP-1 Peltier element (Perkin-Elmer) or NCP-706 thermostat (JASCO). The spectra of temperature-dependent measurements were density adjusted. Extinction coefficients were calculated according to the Lambert-Beer law.

NMR-Spectroscopy

NMR spectra were recorded on a Bruker Avance III HD 400 or Avance III HD 600 spectrometer in deuterated solvents at 295 K, unless otherwise stated. The spectra were calibrated to the residual solvent signal as internal standard and the chemical shifts δ are given in ppm. For multiplicities, abbreviations are used as follows: s = singlet, d = doublet, t = triplet, dd = doublet of doublets, td = triplet of doublets, m = multiplet, br = broad. Deuterated solvents were purchased from Sigma Aldrich. NMR spectroscopic studies of **Bis(MC) 3** aggregate were performed in highly deuterated toluene-d_8 (99.96 atom % D) to minimize residual solvent signals.

Mass Spectrometry

High-resolution ESI-TOF mass spectrometry (HRMS) was performed on a Bruker Daltonics micrOTOF focus spectrometer and MALDI -TOF mass spectrometry on a Bruker Daltonics autoflex II LRF spectrometer using *trans*-2-[3-(4-*tert*-butylphenyl)-2-methyl-2-propenylidene]malononitrile (DCTB) as matrix.

Atomic Force Microscopy

AFM experiments were performed with a Bruker AXS MultiMode 8 instrument in the tapping mode under ambient conditions. Silicon cantilevers (Olympus) with a spring constant of 40 N m^{-1} and a resonance frequency of ~300 kHz (10 N m^{-1}/~150 kHz in case of **Bis(MC) 2**) were used. Samples were prepared by spin-coating (4000 rpm) of the respective aggregate solution on *Mica*.

Chromatography

Column chromatography was carried out with commercial glass columns on silica gel (Silica 60, particle size 0.04–0.063 mm, Macherey-Nagel) as stationary phase and thin layer chromatography was conducted on pre-coated silica gel plates 60 with fluorescence indicator UV_{254} (Macherey-Nagel). Solvents were used as received. DCM was distilled before use. Purification of target compounds by preparative high performance liquid chromatography (HPLC) was performed on a JASCO system (PU-2080 PLUS) with a UV/vis detector (UV-2077 PLUS) using a normal-phase column (NUCLEOSIL 100-5 NO_2, Macherey-Nagel) and gel permeation chromatography (GPC) was conducted on a Shimadzu Recycling GPC-system (LC-20AD Prominence pump; SPD-MA20A Prominence diode-array detector) with three preparative columns (Japan Analytical Industries Co., Ltd.). For HPLC and GPC, HPLC grade solvents (methanol, chloroform; stabilized with 0.1% ethanol, Fisher Chemical) were used.

Melting Points

Melting points were determined on an Olympus BX41 optical microscope with heating stage and are uncorrected.

Elemental Analysis

Elemental analyses were conducted on a CHNS 932 analyser (Leco Instruments GmbH).

Chemicals

Bis(triphenylphosphine)palladium(II) dichloride (Carbolution Chemicals)

3-Bromo-4-hydroxybenzonitrile (Alfa Aesar)

Diisopropylamine (Acros Organics)

N,*N*-Diisopropylethylamine (Merck)

(1,3-Dioxolan-2-ylmethyl)tributylphosphonium bromide (TCI)

Lithium aluminum hydride (Merck)

Methyl cyanoacetate (Merck)

Sodium hydride (60% dispersion in mineral oil, Acros Organics)

Tetrabutylammonium fluoride (1M in THF, Alfa Aesar)

Tetrakis(triphenylphosphine)palladium(0) (TCI)

Trimethylsilylacetylene (Carbolution Chemicals)

5-(Dibutylamino)thiophene-2-carbaldehyde (**66a**),[118] (*E*)-3-[5-(dibutylamino)thiophene-2-yl]acrylaldehyde (**66b**),[82] 2-[(3-cyanophenyl)ethynyl]benzonitrile (**72**),[134] hydroxy pyridones **68**,[19h] **70**,[19h] and **75**[82] and merocyanine **69a**[19h] were synthesized following literature procedures.

All merocyanine compounds were isolated by precipitation from DCM solution by the addition of *n*-hexane and subsequent filtration. After washing with *n*-hexane, the dyes were dried in vacuum.

DCM and *n*-hexane were distilled before use. Dry solvents were obtained from a solvent purification system (PURE SOLV MD-5, Innovative Technology Inc.). All other solvents and reagents were obtained from the chemical supply of the University and were used as received without further purification, unless otherwise stated.

7.2 Synthesis

3-Bromo-4-(octyloxy)benzonitrile (61):

3-Bromo-4-hydroxybenzonitrile (**60**) (3.00 g, 15.1 mmol) was dissolved in DMF (150 mL) under a nitrogen atmosphere and potassium carbonate (3.14 g, 22.7 mmol) was added. The suspension was stirred at room temperature for 5 min and then 1-bromooctane (3.95 mL, 4.39 g, 22.7 mmol) was added. After stirring at room temperature for 4 h, distilled water (250 mL) was added and the mixture was extracted with DCM (3 x 100 mL). The combined

organic phases were dried over Na_2SO_4 and the solvent was removed in vacuum. Column chromatography (silica gel, DCM/*n*-hexane 6:4) afforded **61** as a colorless oil.

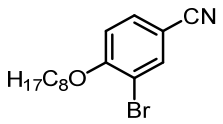

$C_{15}H_{20}BrNO$ (310.24 g mol^{-1})

Yield: 4.49 g (14.5 mmol, 96%), colorless oil.

^{1}H NMR (400 MHz, $CDCl_3$): δ 7.82 (d, ^4J = 2.1 Hz, 1H), 7.56 (dd, ^3J = 8.6 Hz, ^4J = 2.1 Hz, 1H), 6.90 (d, ^3J = 8.6 Hz, 1H), 4.07 (t, ^3J = 6.5 Hz, 2H), 1.90–1.83 (m, 2H), 1.52–1.46 (m, 2H), 1.38–1.26 (m, 8H), 0.89 (t, ^3J = 6.8 Hz, 3H); ^{13}C NMR (101 MHz, $CDCl_3$): δ 159.2, 136.8, 133.1, 118.0, 112.82, 112.80, 105.0, 69.7, 31.9, 29.34, 29.31, 28.9, 26.0, 22.7, 14.2; HRMS (ESI, positive, acetonitrile/chloroform): (*m/z*) $[M+NH_4]^+$, calcd. for $C_{15}H_{24}BrN_2O^+$, 327.1066, found, 327.1066; elemental analysis (calcd., found for $C_{15}H_{20}BrNO$): C (58.07, 58.10), H (6.50, 6.19), N (4.51, 4.57).

4-(Octyloxy)-3-[(trimethylsilyl)ethynyl]benzonitrile (62):

3-Bromo-4-(octyloxy)benzonitrile (**61**) (4.00 g, 12.9 mmol), bis(triphenylphosphine)-palladium(II) dichloride (272 mg, 387 µmol) and copper(I) iodide (73.7 mg, 387 µmol) were suspended in *N*,*N*-diisopropylamine (30 mL) and THF (30 mL) and the mixture was degassed by applying the freeze-pump-thaw method. Trimethylsilylacetylene (3.50 mL, 2.53 g, 25.8 mmol) was added and the mixture was degassed once more. After stirring at 60 °C for 19 h under a nitrogen atmosphere, the solvent was removed in vacuum and the residue was filtrated through a celite pad with DCM. Then the solution was condensed under reduced pressure and the crude product was purified by column chromatography (silica gel, DCM/*n*-hexane 1:1) to give **62** as a yellow oil.

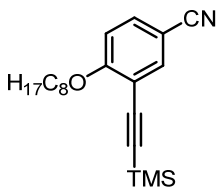

$C_{20}H_{29}NOSi$ (327.54 g mol^{-1})

Yield: 4.22 g (12.9 mmol, 100%), yellow oil.

^{1}H NMR (400 MHz, $CDCl_3$): δ 7.68 (d, ^4J = 2.1 Hz, 1H), 7.53 (dd, ^3J = 8.7 Hz, ^4J = 2.1 Hz, 1H), 6.87 (d, ^3J = 8.7 Hz, 1H), 4.05 (t, ^3J = 6.4 Hz, 2H), 1.88–1.81 (m, 2H), 1.52–1.49 (m, 2H), 1.38–1.29 (m, 8H), 0.89 (t, ^3J = 6.7 Hz, 3H), 0.26 (s, 9H); ^{13}C NMR (101 MHz, $CDCl_3$): δ 163.2, 137.3, 133.9, 118.6, 114.3, 112.1, 103.8, 101.2, 98.7, 69.1, 31.9, 29.45, 29.41, 29.1, 26.0, 22.7, 14.2, –0.04; HRMS (ESI, positive, acetonitrile/chloroform): (*m/z*) $[M+H]^+$, calcd. for $C_{20}H_{30}NOSi^+$, 328.2091, found, 328.2089; elemental analysis (calcd., found for $C_{20}H_{29}NOSi$): C (73.34, 73.19), H (8.92, 8.64), N (4.28, 4.22).

3-Ethynyl-4-(octyloxy)benzonitrile (63):

Tetrabutylammonium fluoride (26.1 mL, 26.1 mmol, 1 M in THF) was added to a solution of 4-(octyloxy)-3-[(trimethylsilyl)ethynyl]benzonitrile (**62**) (4.27 g, 13.1 mmol) in THF (100 mL). After stirring at room temperature for 10 min, distilled water (80 mL) was added and the mixture was extracted with diethyl ether (3 x 50 mL). The combined organic phases were dried over Na_2SO_4 and the solvent was removed in vacuum. Column chromatography (silica gel, DCM/*n*-hexane 1:1) afforded **63** as a pale brown oil.

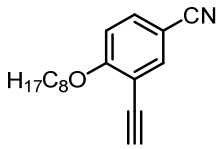

$C_{17}H_{21}NO$ (255.36 g mol^{-1})

Yield: 2.51 g (9.82 mmol, 75%), pale brown oil.

^{1}H NMR (400 MHz, $CDCl_3$): δ 7.72 (d, ^4J = 2.1 Hz, 1H), 7.57 (dd, ^3J = 8.7 Hz, ^4J = 2.1 Hz, 1H), 6.91 (d, ^3J = 8.7 Hz, 1H), 4.08 (t, ^3J = 6.6 Hz, 2H), 3.32 (s, 1H), 1.89–1.82 (m, 2H), 1.52–1.45 (m, 2H), 1.38–1.26 (m, 8H), 0.89 (t, ^3J = 6.7 Hz, 3H); ^{13}C NMR (101 MHz, $CDCl_3$): 163.3, 137.8, 134.3, 118.4, 113.3, 112.2, 103.9, 83.1, 77.8 (overlapped with solvent signal), 69.4, 31.9, 29.35, 29.31, 28.9, 25.9, 22.7, 14.2; HRMS (ESI, positive, acetonitrile/chloroform): (*m/z*) $[M+H]^+$, calcd. for $C_{17}H_{22}NO^+$, 256.1696, found, 256.1698; elemental analysis (calcd., found for $C_{17}H_{21}NO$): C (79.96, 79.89), H (8.29, 8.09), N (5.49, 5.51).

3,3`-(Ethyne-1,2-diyl)bis[4-(octyloxy)benzonitrile] (64):

3-Bromo-4-(octyloxy)benzonitrile (**61**) (680 mg, 2.19 mmol), bis(triphenylphosphine)-palladium(II) dichloride (59.1 mg, 84.2 µmol) and copper(I) iodide (15.9 mg, 84.2 µmol) were suspended in diisopropylamine (30 mL) and THF (65 mL) and the mixture was degassed by applying the freeze-pump-thaw method. A degassed solution of 3-ethynyl-4-

(octyloxy)benzonitrile (**63**) (430 mg, 1.68 µmol) in 5 mL THF was added dropwise at room temperature. After stirring at 50 °C for 41 h under a nitrogen atmosphere, the solvent was removed in vacuum and the residue was filtrated through a celite pad with DCM. Then the solution was condensed under reduced pressure and the crude product was purified by column chromatography (silica gel, DCM/*n*-pentane 2:1) to give **64** as a white solid.

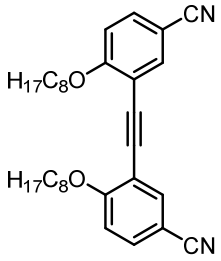

$C_{32}H_{40}N_2O_2$ (484.68 g mol^{-1})

Yield: 590 mg (1.22 mmol, 72%), white solid.

Mp: 93–95 °C; ^{1}H NMR (400 MHz, $CDCl_3$): δ 7.73 (d, ^4J = 2.1 Hz, 2H), 7.58 (dd, ^3J = 8.7 Hz, ^4J = 2.1 Hz, 2H), 6.94 (d, ^3J = 8.7 Hz, 2H), 4.10 (t, ^3J = 6.6 Hz, 4H), 1.92–1.85 (m, 4H), 1.53–1.48 (m, 4H), 1.40–1.25 (m, 16H), 0.86 (t, ^3J = 7.0 Hz, 6H); ^{13}C NMR (101 MHz, $CDCl_3$): 162.7, 137.1, 134.1, 118.5, 114.1, 112.3, 104.0, 89.4, 69.3, 31.8, 29.4, 29.3, 29.0, 26.0, 22.7, 14.2; HRMS (ESI, positive, acetonitrile/chloroform): (*m/z*) [*M*+Na]$^+$, calcd. for $C_{32}H_{40}N_2O_2Na^+$, 507.2982, found, 507.2978; elemental analysis (calcd., found for $C_{32}H_{40}N_2O_2$): C (79.30, 79.04), H (8.32, 8.31), N (5.78, 5.72).

***N,N'*-{[Ethyne-1,2-diylbis(4-(octyloxy)-3,1-phenylene)]bis(methylene)}bis(2-cyanoacetamide) (65):**

Lithium aluminum hydride (93.6 mg, 2.46 mmol) was suspended in dry diethyl ether (15 mL) under a nitrogen atmosphere and the mixture was cooled down to 0 °C. A solution of 3,3'-(ethyne-1,2-diyl)bis[4-(octyloxy)benzonitrile] (**64**) (300 mg, 616 µmol) in dry diethyl ether (40 mL) was then added dropwise and the mixture was stirred at 0 °C for 5 min and for 1 h at room temperature. After addition of distilled water (15 mL), the mixture was extracted with diethyl ether (3 x 30 mL) and the combined organic phases were dried over Na_2SO_4. The solvent was removed under reduced pressure and the resulting yellow oil (345 mg) was stirred with methyl cyanoacetate (190 µL, 2.16 mmol, 214 mg) at room temperature for 18 h. The formed solid was suspended in cold diethyl ether and collected by filtration to give **65** as a beige solid.

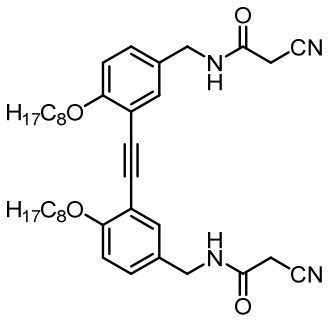

$C_{38}H_{50}N_4O_4$ (626.84 g mol^{-1})

Yield: 196 mg (313 µmol, 51%), beige solid.

Mp: 134–136 °C; ^{1}H NMR (400 MHz, $CDCl_3$): δ 7.41 (d, ^4J = 2.3 Hz, 2H), 7.20 (dd, ^3J = 8.5 Hz, ^4J = 2.3 Hz, 2H), 6.86 (d, ^3J = 8.5 Hz, 2H), 6.33 (br s, 2H), 4.40 (d, ^3J = 5.5 Hz, 4H), 4.05 (t, ^3J = 6.7 Hz, 4H), 3.41 (s, 4H), 1.89–1.82 (m, 4H), 1.53–1.45 (m, 4H), 1.37–1.25 (m, 16H), 0.85 (t, ^3J = 6.9 Hz, 6H); ^{13}C NMR (101 MHz, $CDCl_3$): δ160.7, 159.4, 133.3, 129.5, 128.6, 114.7, 113.8, 112.7, 90.0, 69.1, 43.8, 31.9, 29.5, 29.4, 29.2, 26.1, 26.0, 22.8, 14.2; HRMS (ESI, positive, acetonitrile/chloroform): (*m/z*) $[M+K]^+$, calcd. for $C_{38}H_{50}KN_4O_4^+$, 665.3464, found, 665.3474.

Bis(MC) 2:

Bis(cyanoacetamide) **65** (150 mg, 239 µmol) was suspended in piperidine (6 mL) and ethyl acetoacetate (370 µL, 2.87 mmol, 374 mg) was added to the suspension. The mixture was heated to 100 °C for 30 min and then concentrated HCl was added at room temperature until pH 1 was reached. After addition of distilled water (20 mL), the mixture was extracted with DCM (3 x 30 mL). The combined organic phases were dried over Na_2SO_4 and the solvent was removed under reduced pressure to afford the bis(hydroxypyridone) intermediate as a brown oil, which was subsequently reacted with 5-(dibutylamino)thiophene-2-carbaldehyde (**66a**) (114 mg, 478 µmol) in acetic anhydride (3 mL) at 90 °C for 30 min. After cooling down to room temperature, methanol (20 mL) was added and the resulting solution was concentrated in vacuum. The crude product was purified by column chromatography (silica gel, DCM/MeOH 99.4:0.6) and finally by HPLC (normal-phase, $CHCl_3$/MeOH 95:5) to give **Bis(MC) 2** as a purple solid.

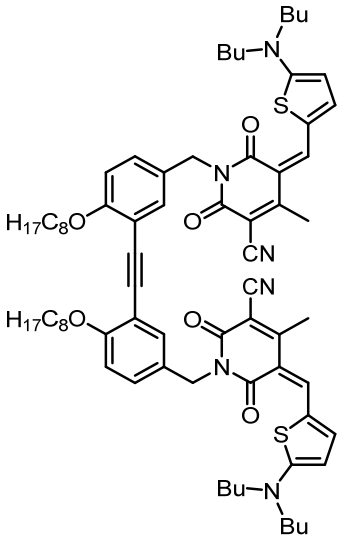

$C_{72}H_{92}N_6O_6S_2$ (1201.68 g mol^{-1})

Yield: 31.0 mg (25.8 µmol, 11%), purple solid.

Mp: 103–104 °C; ^{1}H NMR (600 MHz, $CDCl_3$): δ 7.61 (s, 2H), 7.46 (br, 4H), 7.41 (d, ^3J = 7.9 Hz, 2H), 6.76 (d, ^3J = 8.6 Hz, 2H), 6.30 (d, ^3J = 3.2 Hz, 2H), 5.09 (s, 4H), 3.98 (t, ^3J = 6.7 Hz, 4H), 3.50 (br, 8H), 2.47 (s, 6H), 1.79–1.72 (m, 4H), 1.70–1.67 (m, 8H), 1.42–1.34 (m, 12H), 1.28–1.18 (m, 16H), 0.95 (t, ^3J = 7.3 Hz, 12H), 0.82 (t, ^3J = 7.2 Hz, 6H); ^{13}C NMR (151 MHz, $CDCl_3$): δ 175.9, 163.3, 162.2, 158.9, 158.1, 152.1, 141.9, 134.3, 130.5, 129.9, 124.7, 117.4, 113.4, 112.3, 110.7, 107.2, 94.8, 89.8, 69.1, 42.1, 31.9, 29.5, 29.4, 29.3, 26.0, 22.8, 20.2, 18.9, 14.2, 13.9; HRMS (ESI, positive, acetonitrile/chloroform): (*m/z*) $[M+K]^+$, calcd. for $C_{72}H_{92}KN_6O_6S_2^+$, 1239.6151, found, 1239.6161; UV/vis (DCM, c = 5.2 x 10^{-6} M, 295 K): λ_{max}/nm (ε_{max}/M^{-1} cm^{-1}) = 539 (271000); elemental analysis (calcd., found for $C_{72}H_{92}N_6O_6S_2$): C (71.97, 71.84), H (7.72, 7.82), N (6.99, 6.88).

2-Cyano-*N*-[3-ethynyl-4-(octyloxy)benzyl]acetamide (67):

Lithium aluminum hydride (641 mg, 16.9 mmol) was suspended in dry diethyl ether (50 mL) under a nitrogen atmosphere and the mixture was cooled down to 0 °C. A solution of 3-ethynyl-4-(octyloxy)benzonitrile (**63**) (2.16 g, 8.45 mmol) in dry diethyl ether (100 mL) was then added dropwise and the mixture was stirred at 0 °C for 5 min and for 1 h at room temperature. After addition of distilled water (30 mL), the mixture was extracted with DCM (3 x 50 mL) and the combined organic phases were dried over Na_2SO_4. The solvent was removed under reduced pressure and the resulting yellow oil (2.39 g) was stirred with methyl cyanoacetate (820 µL, 9.30 mmol, 921 mg) at room temperature for 19 h. The formed solid was suspended in cold diethyl ether and collected by filtration to give **67** as a pale grey solid.

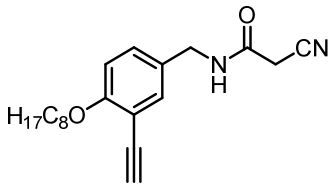

$C_{20}H_{26}N_2O_2$ (326.44 g mol^{-1})

Yield: 1.60 g (4.89 mmol, 63%), pale grey solid.

Mp: 79–80 °C; ^{1}H NMR (400 MHz, $CDCl_3$): δ 7.37 (d, ^4J = 2.4 Hz, 1H), 7.22 (dd, ^3J = 8.5 Hz, ^4J = 2.4 Hz, 1H), 6.85 (d, ^3J = 8.6 Hz, 1H), 6.29 (br s, 1H), 4.38 (d, ^3J = 5.7 Hz, 2H), 4.03 (t, ^3J = 6.6 Hz, 2H), 3.40 (s, 2H), 3.27 (s, 1H), 1.86–1.79 (m, 2H), 1.52–1.44 (m, 2H), 1.38–1.26 (m, 8H), 0.89 (t, ^3J = 6.7 Hz, 3H); ^{13}C NMR (101 MHz, $CDCl_3$): δ 160.7, 160.2, 133.8, 130.1, 128.7, 114.7, 112.5, 112.3, 81.6, 79.6, 69.1, 43.7, 31.9, 29.4, 29.3, 29.1, 26.04, 26.00, 22.8, 14.2; HRMS (ESI, positive, acetonitrile/chloroform): (*m/z*) [*M*+Na]$^+$, calcd. for $C_{20}H_{26}N_2NaO_2^+$, 349.1887, found, 349.1883; elemental analysis (calcd., found for $C_{20}H_{26}N_2O_2$): C (73.59, 73.36), H (8.03, 8.13), N (8.58, 8.50).

(*Z*)-5-{[5-(Dibutylamino)thiophene-2-yl]methylene}-1-[3-ethynyl-4-(octyloxy)benzyl]-4-methyl-2,6-dioxo-1,2,5,6-tetrahydropyridine-3-carbonitrile (59):

Cyanoacetamide **67** (1.05 g, 3.22 mmol) was suspended in piperidine (15 mL) and ethyl acetoacetate (810 µL, 6.45 mmol, 840 mg) was added to the suspension. The mixture was heated to 100 °C for 2 h and then concentrated HCl was added at room temperature until pH 1 was reached. After addition of distilled water (20 mL), the mixture was extracted with DCM (3 x 30 mL) and the combined organic phases were dried over Na_2SO_4. The solvent was removed under reduced pressure to afford the hydroxy pyridone intermediate as a brown oil, which was subsequently reacted with 5-(dibutylamino)thiophene-2-carbaldehyde (**66a**) (1.15 g, 4.80 mmol) in acetic anhydride (35 mL) at 90 °C for 1 h. After cooling down to room temperature, methanol (20 mL) was added and the resulting solution was concentrated in vacuum. The crude product was purified by column chromatography (silica gel, DCM/MeOH 99.5:0.5) and finally by recycling GPC ($CHCl_3$) to give the reference merocyanine dye **59** as a purple solid.

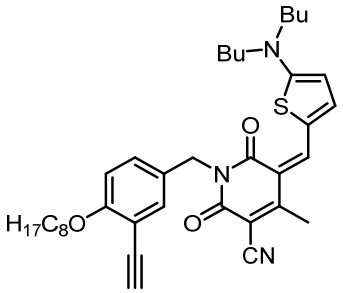

$C_{37}H_{47}N_3O_3S$ (613.86 g mol^{-1})

Yield: 792 mg (1.29 mmol, 40%), purple solid.

Mp: 143–145 °C; ^{1}H NMR (400 MHz, $CDCl_3$): δ 7.66 (d, ^4J = 2.3 Hz, 1H), 7.50 (dd, ^3J = 8.6 Hz, ^4J = 2.3 Hz, 1H), 7.47 (s, 1H), 7.35 (d, ^3J = 5.1 Hz, 1H), 6.77 (d, ^3J = 8.6 Hz, 1H), 6.32 (d, ^3J = 5.1 Hz, 1H), 5.08 (s, 2H), 3.99 (t, ^3J = 6.7 Hz, 2H), 3.55 (t, ^3J = 7.6 Hz, 4H), 3.19 (s, 1H), 2.48 (s, 3H), 1.83–1.71 (m, 6H), 1.49–1.40 (m, 6H), 1.35–1.27 (m, 8H), 1.02 (t, ^3J = 7.4 Hz, 6H), 0.87 (t, ^3J = 6.8 Hz, 3H); ^{13}C NMR (101 MHz, $CDCl_3$): δ175.9, 163.3, 162.2, 159.7, 158.2, 152.1, 142.0, 135.4, 132.0, 130.0, 124.6, 117.3, 111.8, 111.4, 110.7, 107.2, 94.9, 80.8, 80.4, 77.3 (overlapped with solvent signal), 69.0, 42.0, 31.9, 29.49, 29.44, 29.3, 29.1, 26.0, 22.7, 20.2, 19.0, 14.2, 13.9; HRMS (ESI, positive, acetonitrile/ chloroform): (*m/z*) $[M]^+$, calcd. for $C_{37}H_{47}N_3O_3S^+$, 613.3333, found, 613.3340; UV/vis (DCM, c = 5.2 x 10^{-6} M, 295 K): λ_{max}/nm (ε_{max}/M^{-1} cm^{-1}) = 540 (143000); elemental analysis (calcd., found for $C_{37}H_{47}N_3O_3S$): C (72.40, 72.41), H (7.72, 7.83), N (6.85, 7.05), S (5.22, 5.07).

Bis(MC) 3:

A mixture of **59** (52.2 mg, 85.0 µmol), bis(triphenylphosphine)palladium(II) dichloride (29.8 mg, 42.5 µmol) and copper(I) iodide (8.10 mg, 42.5 µmol) in diisopropylamine (4 mL) and THF (15 mL) was stirred at room temperature for 18 h. The suspension was concentrated in vacuum and the residue was filtrated through a celite pad with DCM. The solvent was removed under reduced pressure and the crude product was purified by column chromatography (silica gel, DCM/MeOH 99.5:0.5) to give **Bis(MC) 3** as a purple solid.

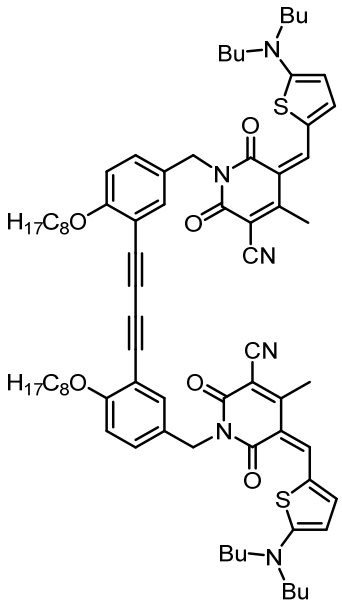

$C_{74}H_{92}N_6O_6S_2$ (1225.71 g mol^{-1})

Yield: 29.2 mg (23.8 µmol, 56%), purple solid.

Mp: 224–225 °C; ^{1}H NMR (400 MHz, $CDCl_3$, 295 K): δ 7.66 (d, ^4J = 1.9 Hz, 2H), 7.50 (dd, ^3J = 8.5 Hz, ^4J = 2.0 Hz, 2H), 7.44 (s, 2H), 7.34 (br, 2H), 6.76 (d, ^3J = 8.6 Hz, 2H), 6.31 (d, ^4J = 3.3 Hz, 2H), 5.07 (s, 4H), 3.98 (t, ^3J = 6.8 Hz, 4H), 3.55 (t, ^3J = 6.9 Hz, 8H), 2.46 (s, 6H), 1.82–1.75 (m, 12H), 1.47–1.40 (m, 12H), 1.31–1.25 (m, 16H), 1.00 (t, ^3J = 7.4 Hz, 12H), 0.83 (t, ^3J = 6.8 Hz, 6H); ^{13}C NMR (101 MHz, $CDCl_3$): δ 176.0, 163.3, 162.3, 160.3, 158.1, 152.2, 141.9, 135.5, 132.0, 130.1, 124.8, 112.0, 111.5, 110.9, 107.1, 94.6, 78.7, 78.0, 69.1, 42.0, 31.9, 29.4, 29.3, 29.1, 26.0, 22.7, 20.2, 18.9, 14.2, 13.9; HRMS (ESI, positive, acetonitrile/chloroform): (*m/z*) $[M]^+$, calcd. for $C_{74}H_{92}N_6O_6S_2^+$, 1224.6514, found, 1224.6534; UV/vis (DCM, c = 4.7 x 10^{-6} M, 295 K): λ_{max}/nm (ε_{max}/M^{-1} cm^{-1}) = 540 (247000); elemental analysis (calcd., found for $C_{74}H_{92}N_6O_6S_2$): C (72.51, 72.52), H (7.57, 7.67), N (6.86, 6.96), S (5.23, 5.00).

(*2E,4E*)-5-[5-(Dibutylamino)thiophene-2-yl]penta-2,4-dienal (66c):[11]

To a solution of (*E*)-3-[5-(dibutylamino)thiophene-2-yl]acrylaldehyde (**66b**) (2.29 g, 8.63 mmol) and (1,3-dioxolan-2-ylmethyl)tributylphosphonium bromide (3.50 g, 9.48 mmol) in 120 mL dry THF was added sodium hydride (60% dispersion in mineral oil; 1.05 g, 26.2 mmol) under a nitrogen atmosphere. After stirring for 20 h at room temperature, the reaction mixture was hydrolysed by acidification with HCl and subsequently extracted with ethyl acetate (3 x 70 mL). The combined organic phases were washed with distilled water

[11] The synthesis of aminothiophene aldehyde **66c** was performed by Lisa Gerbig.[135]

(2 x 100 mL) and brine (2 x 100 mL) and dried over Na_2SO_4. The solvent was removed under reduced pressure and the crude product was purified by column chromatography (silica gel, *n*-hexane/ethyl acetate 7:3) to give **66c** as a deep red oil.

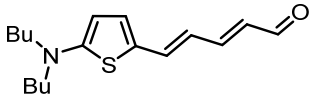

$C_{17}H_{25}NOS$ (291.45 g mol^{-1})

Yield: 2.49 g (8.53 mmol, 98%), deep red oil.

^{1}H NMR (400 MHz, CD_2Cl_2): δ 9.45 (d, ^3J = 8.1 Hz, 1H), 7.17 (ddd, ^3J = 14.8 Hz, ^3J = 11.2 Hz, ^4J = 0.6 Hz, 1H), 7.00 (dd, ^3J = 14.7 Hz, ^4J = 0.6 Hz, 1H), 6.91 (d, ^3J = 4.2 Hz, 1H), 6.31 (dd, ^3J = 14.7 Hz, ^3J = 11.3 Hz, 1H), 6.01 (dd, ^3J = 14.7 Hz, ^3J = 8.2 Hz, 1H), 5.75 (d, ^3J = 4.2 Hz, 1H), 3.29 (t, ^3J = 7.6 Hz, 4H), 1.66–1.59 (m, 4H), 1.40–1.31 (m, 4H), 0.96 (t, ^3J = 7.4 Hz, 6H). ^{13}C NMR (101 MHz, CD_2Cl_2): δ 193.1, 161.5, 153.9, 137.0, 134.2, 127.1, 123.6, 118.4, 102.0, 53.7, 29.5, 20.5, 14.0; HRMS (ESI, positive, acetonitrile/chloroform): (*m/z*) $[M+H]^+$, calcd. for $C_{17}H_{26}NOS^+$, 292.1730, found, 292.1722.

General procedure for the synthesis of merocyanine dyes 69b, 71b and reference merocyanine G:

A suspension of the respective hydroxy pyridone and aminothiophene aldehyde in acetic anhydride was heated for 10–30 min at 90 °C. After cooling down to room temperature, methanol was added and the resulting mixture was concentrated under vacuum. The crude products were purified by column chromatography (silica gel) using DCM/MeOH 99.5:0.5 as eluent and subsequently isolated by precipitation from DCM/*n*-hexane solution.

(*Z*)-5-(*E*)-3-{[5-(Dibutylamino)thiophene-2-yl]allylidene}-1-(3-iodobenzyl)-4-methyl-2,6-dioxo-1,2,5,6-tetrahydropyridine-3-carbonitrile (69b):

Compound **69b** was synthesized according to the general procedure described above by reacting hydroxy pyridone **68** (411 mg, 1.12 mmol) and (*E*)-3-[5-(dibutylamino)thiophene-2-yl]acrylaldehyde (**66b**) (305 mg, 1.13 mmol) in 10 mL acetic anhydride for 30 min yielding a green-blue solid.

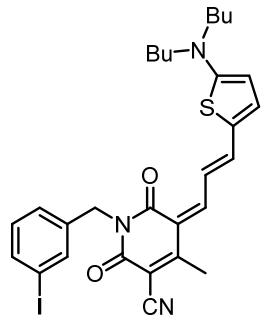

$C_{29}H_{32}IN_3O_2S$ (613.56 g mol^{-1})

Yield: 403 mg (657 µmol, 59%), green-blue solid.

Mp: 227 °C; ^{1}H NMR (400 MHz, $CDCl_3$): δ 7.95 (br, 1H), 7.84 (t, ^4J = 1.6 Hz, 1H), 7.57 (ddd, ^3J = 7.8 Hz, ^4J = 1.8 Hz, ^4J = 1.1 Hz, 1H), 7.46 (ddd, ^3J = 7.7 Hz, ^4J = 1.7 Hz, ^4J = 1.1 Hz, 1H), 7.30 (d, ^3J = 12.4 Hz, 1H), 7.24 (d, ^3J = 13.8 Hz, 1H), 7.14 (br, 1H), 7.03 (t, ^3J = 7.8 Hz, 1H), 6.19 (d, ^3J = 4.7 Hz, 1H), 5.12 (s, 2H), 3.47 (t, ^3J = 7.8 Hz, 4H), 2.46 (s, 3H), 1.75–1.68 (m, 4H), 1.46–1.37 (m, 4H), 1.00 (t, ^3J = 7.4 Hz, 6H). ^{13}C NMR (101 MHz, $CDCl_3$): δ 171.1, 163.5, 162.1, 157.7, 152.0, 149.3, 144.5, 140.4, 137.5, 136.4, 130.2, 128.2, 127.2, 118.9, 117.2, 111.7, 109.9, 95.2, 94.4, 54.8, 42.3, 29.4, 20.3, 19.0, 13.9. HRMS (ESI, positive, acetonitrile/chloroform): (*m/z*) [*M*+H]$^+$, calcd. for $C_{29}H_{33}IN_3O_2S^+$, 614.1333, found, 614.1331; UV/vis (DCM, *c* = 5.3 x 10^{-6} M, 295 K): λ_{max}/nm (ε_{max}/M^{-1} cm^{-1}) = 655 (226100); elemental analysis (calcd., found for $C_{29}H_{32}IN_3O_2S$): C (56.77, 56.83), H (5.26, 5.34), N (6.85, 6.85), S (5.23, 5.07).

(*Z*)-5-(*2E,4E*)-5-{[5-(Dibutylamino)thiophene-2-yl]penta-2,4-diene-1-ylidene}-1-(2-ethynylbenzyl)-4-methyl-2,6-dioxo-1,2,5,6-tetrahydropyridine-3-carbonitrile (71b):

Compound **71b** was synthesized according to the above general procedure by reacting hydroxy pyridone **70** (150 mg, 568 µmol) and (*2E,4E*)-5-[5-(dibutylamino)thiophene-2-yl]penta-2,4-dienal (**66c**) (78.8 mg, 270 µmol) in 4 mL acetic anhydride for 10 min yielding a green-blue solid.

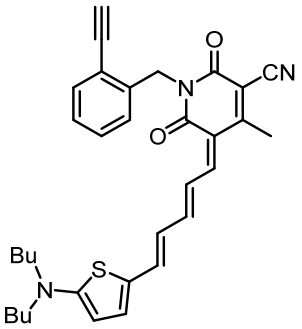

$C_{33}H_{35}N_3O_2S$ (537.72 g mol^{-1})

Yield: 89.4 mg (166 µmol, 62%), green-blue solid.

Mp: 107 °C; ^{1}H NMR (400 MHz, $CDCl_3$): δ 8.03 (br t, ^{3}J = 12.5 Hz, 1H), 7.48 (dd, ^{3}J = 7.6 Hz, ^{4}J = 1.3 Hz, 1H), 7.39 (br d, ^{3}J = 12.8 Hz, 1H), 7.24–7.12 (m, 5H), 6.97 (dd, ^{3}J = 7.8 Hz, ^{4}J = 0.8 Hz, 1H), 6.46 (t, ^{3}J = 12.8 Hz, 1H), 6.05 (d, ^{3}J = 4.7 Hz, 1H), 5.39 (s, 2H), 3.41 (t, ^{3}J = 7.7 Hz, 4H), 3.38 (s, 1H), 2.51 (s, 3H), 1.72–1.64 (m, 4H), 1.43–1.34 (m, 4H), 0.98 (t, ^{3}J = 7.4 Hz, 6H); ^{13}C NMR (101 MHz, $CDCl_3$): δ 167.4, 163.3, 162.0, 159.0, 157.9, 151.5, 141.7, 140.5, 139.8, 132.8, 129.1, 126.5, 125.85, 125.83, 125.4, 121.8, 120.7, 116.9, 113.6, 107.4, 97.0, 82.4, 81.6, 54.3, 41.9, 29.3, 20.2, 19.0, 13.9; HRMS (ESI, positive, acetonitrile/chloroform): (*m/z*) $[M]^+$, calcd. for $C_{33}H_{35}N_3O_2S^+$, 537.2445, found, 537.2443; UV/vis (DCM, c = 5.0 x 10^{-6} M, 295 K): λ_{max}/nm (ε_{max}/M^{-1} cm^{-1}) = 763 (232700); elemental analysis (calcd., found for $C_{33}H_{35}N_3O_2S$): C (73.71, 73.51), H (6.56, 6.80), N (7.81, 7.77), S (5.96, 5.62).

(*Z*)-5-(*2E,4E*)-5-{[5-(Dibutylamino)thiophene-2-yl]penta-2,4-diene-1-ylidene}-1-benzyl-4-methyl-2,6-dioxo-1,2,5,6-tetrahydropyridine-3-carbonitrile (G):

Compound **G** was synthesized according to the general procedure described above by reacting hydroxy pyridone **75** (225 mg, 935 µmol) and (*2E,4E*)-5-[5-(dibutylamino)thiophene-2-yl]penta-2,4-dienal (**66c**) (227 mg, 779 µmol) in 7 mL acetic anhydride for 30 min yielding a green solid.

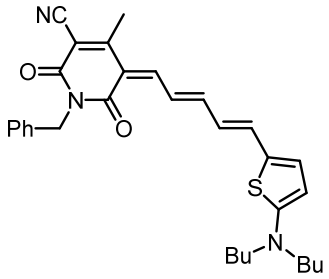

$C_{31}H_{35}N_3O_2S$ (513.70 g mol^{-1})

Yield: 167 mg (326 µmol, 42%), green solid.

Mp: 178 °C; ^{1}H NMR (400 MHz, $CDCl_3$): δ 8.01 (br t, ^{3}J = 11.7 Hz, 1H), 7.51–7.50 (m, 2H), 7.34–7.26 (m, 3H), 7.24–7.20 (m, 1H), 7.15 (t, ^{3}J = 13.1 Hz, 1H), 7.11–7.05 (m, 2H), 6.47 (t, ^{3}J = 13.0 Hz, 1H), 6.02 (d, ^{3}J = 4.6 Hz, 1H), 5.15 (s, 2H), 3.42 (t, ^{3}J = 7.8 Hz, 4H), 2.44 (s, 3H), 1.73–1.65 (m, 4H), 1.45–1.35 (m, 4H), 1.00 (t, ^{3}J = 7.4 Hz, 6H); ^{13}C NMR (101 MHz, $CDCl_3$): δ 167.3, 163.3, 162.0, 158.8, 157.5, 151.3, 141.6, 140.4, 137.8, 129.2, 128.4, 127.3, 126.5, 125.7, 121.8, 116.9, 113.8, 107.4, 97.1, 54.3, 43.1, 29.3, 20.2, 18.9, 13.9; HRMS (ESI, positive, acetonitrile/chloroform): (*m/z*) $[M]^+$, calcd. for $C_{31}H_{35}N_3O_2S^+$, 513.2445, found,

513.2445; UV/vis (DCM, c = 4.0 x 10^{-6} M, 295 K): λ_{max}/nm (ε_{max}/M^{-1} cm^{-1}) = 763 (228600); elemental analysis (calcd., found for $C_{31}H_{35}N_3O_2S$): C (72.48, 72.64), H (6.87, 6.97), N (8.18, 8.40), S (6.24, 6.10).

General procedure for the synthesis of hetero-bis(merocyanine) dyes BG and RG:

Merocyanine dye **71b** and the respective merocyanine **69a**,**b** were suspended in *N*,*N*-diisopropylethylamine and THF or DCM as a solvent and the mixture was degassed by applying the freeze-pump-thaw method. The palladium catalyst and the respective cocatalyst were added at room temperature. After stirring for 1–2 h under a nitrogen atmosphere, the solvent was removed in vacuum. The residue was filtrated through a celite pad with DCM and the solution was condensed under reduced pressure. The crude products were then purified by column chromatography (silica gel, DCM/MeOH 99:1) and recycling GPC ($CHCl_3$) and were subsequently isolated by precipitation from DCM/*n*-hexane solution.

Bis(merocyanine) BG:

Compound **BG** was synthesized according to the general procedure described above by reacting merocyanine **71b** (29.8 mg, 55.4 µmol) and merocyanine **69b** (68.0 mg, 111 µmol) in 15 mL *N*,*N*-diisopropylethylamine and 100 mL DCM. Tetrakis(triphenylphosphine)-palladium(0) (6.40 mg, 5.54 µmol) was used as catalyst and silver(I) oxide (50.0 mg, 216 µmol) as cocatalyst. The reaction mixture was stirred for 2 h at 35 °C yielding a dark green solid.

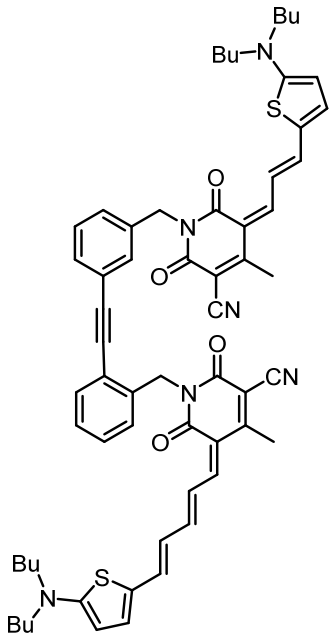

$C_{62}H_{66}N_6O_4S_2$ (1023.37 g mol^{-1})

Yield: 9.80 mg (9.58 µmol, 17%), dark green solid.

Mp: 172 °C; ^{1}H NMR (600 MHz, $CDCl_3$): δ 7.92 (br, 2H), 7.66 (s, 1H), 7.51–7.48 (m, 2H), 7.46 (d, ^{3}J = 7.8 Hz, 1H), 7.29 (t, ^{3}J = 7.8 Hz, 1H), 7.23–7.14 (m, 6H), 7.11 (d, ^{3}J = 4.5 Hz, 1H), 7.05–6.99 (m, 3H), 6.33 (t, ^{3}J = 13.0 Hz, 1H), 6.15 (br, 1H), 6.04 (d, ^{3}J = 4.6 Hz, 1H), 5.38 (s, 2H), 5.18 (s, 2H), 6.46 (t, ^{3}J = 7.9 Hz, 4H), 3.40 (t, ^{3}J = 7.8 Hz, 4H), 2.40 (s, 3H), 2.38 (s, 3H), 1.72–1.65 (m, 8H), 1.42–1.35 (m, 8H), 0.98 (t, ^{3}J = 7.4 Hz, 12H); ^{13}C NMR (151 MHz, $CDCl_3$): δ 171.2, 167.8, 163.5, 163.0, 162.2, 162.1, 158.7, 157.67, 157.63, 151.8, 151.1, 149.1, 144.4, 141.7, 140.8, 139.2, 138.2, 132.4, 131.5, 130.8, 128.9, 128.4, 128.3, 127.2, 126.6, 126.5, 126.3, 125.8, 123.6, 121.8, 121.7, 119.02, 119.00, 117.3, 117.2, 113.4, 111.7, 109.9, 107.8, 96.3, 96.2, 95.1, 94.7, 87.5, 54.9, 54.4, 42.7, 42.4, 29.4, 29.3, 20.3, 20.2, 18.8, 13.9; HRMS (ESI, positive, acetonitrile/chloroform): (*m/z*) $[M]^{+}$, calcd. for $C_{62}H_{66}N_6O_4S_2^{+}$, 1022.4582, found, 1022.4596; UV/vis (DCM, c = 4.0 x 10^{-6} M, 295 K): λ_{max}/nm (ε_{max}/M^{-1} cm^{-1}) = 658 (250000), 766 (216700).

Bis(merocyanine) RG:

Compound **RG** was synthesized according to the general procedure described above by reacting merocyanine **71b** (51.7 mg, 96.1 µmol) and merocyanine **69a** (67.8 mg, 115 µmol) in 8 mL *N*,*N*-diisopropylethylamine and 40 mL THF. Bis(triphenylphosphine)palladium(II) dichloride (6.52 mg, 9.30 µmol) was used as catalyst and copper(I) iodide (1.77 mg, 9.30 µmol) as cocatalyst. The reaction mixture was stirred for 1 h at room temperature yielding a dark violet solid.

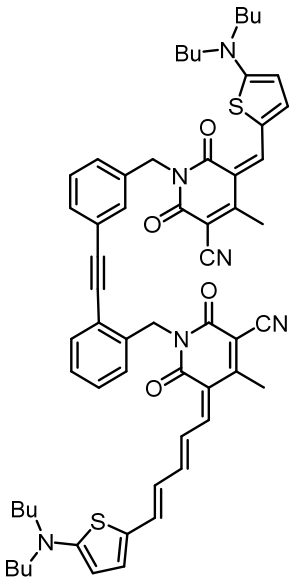

$C_{60}H_{64}N_6O_4S_2$ (997.33 g mol^{-1})

Yield: 14.7 mg (14.7 µmol, 15%), dark violet solid.

Mp: 158–159 °C; ^{1}H NMR (400 MHz, CD_2Cl_2): δ 7.97 (t, ^{3}J = 13.1 Hz, 1H), 7.58–7.51 (m, 4H), 7.46 (dt, ^{3}J = 7.6 Hz, ^{4}J = 1.5 Hz, 1H), 7.40–7.37 (m, 2H), 7.30 (t, ^{3}J = 7.6 Hz, 1H), 7.26–7.20 (m, 5H), 6.95–6.94 (m, 1H), 6.49 (t, ^{3}J = 13.0 Hz, 1H), 6.40 (d, ^{3}J = 5.2 Hz, 1H), 6.13 (d, ^{3}J = 4.9 Hz, 1H), 5.35 (s, 2H), 5.17 (s, 2H), 3.52 (t, ^{3}J = 7.7 Hz, 4H), 3.42 (t, ^{3}J = 7.7 Hz, 4H), 2.49 (s, 3H), 2.48 (s, 3H), 1.72–1.65 (m, 8H), 1.41–1.36 (m, 8H), 0.96 (t, ^{3}J = 7.5 Hz, 12H); ^{13}C NMR (101 MHz, CD_2Cl_2): δ 176.6, 168.9, 163.6, 163.2, 162.6, 162.4, 159.4, 158.7, 158.1, 152.7, 151.2, 142.5, 142.2, 139.8, 138.6, 134.8, 134.7, 132.4, 131.4, 130.9, 130.8, 130.6, 128.7, 128.6, 127.0, 126.7, 125.6, 125.4, 124.9, 123.5, 121.8, 117.7, 117.6, 113.0, 111.5, 108.7, 107.0, 95.8, 95.0, 94.4, 87.3, 54.7 (overlapped with solvent signal), 42.8, 42.2, 29.5, 20.47, 20.44, 19.1, 19.0, 13.92, 13.91, 1.14; HRMS (ESI, positive, acetonitrile/chloroform): (*m/z*) $[M]^+$, calcd. for $C_{60}H_{64}N_6O_4S_2^+$, 996.4425, found, 996.4433; UV/vis (DCM, c = 3.8 x 10^{-6} M, 295 K): λ_{max}/nm (ε_{max}/M^{-1} cm^{-1}) = 540 (152400), 766 (215000).

2-Cyano-*N*-{2-[(3-((2-cyanoacetamido)methyl)phenyl)ethynyl]benzyl}acetamide (73):[133]

Lithium aluminum hydride (664 mg, 17.5 mmol) was suspended in dry diethyl ether (20 mL) under a nitrogen atmosphere and the mixture was cooled down to 0 °C. A solution of 2-[(3-cyanophenyl)ethynyl]benzonitrile (**72**) (1.00 g, 4.38 mmol) in dry diethyl ether (80 mL) was then added dropwise and the mixture was stirred for 5 min at 0 °C and additional 1 h at room temperature. After addition of distilled water (20 mL), the mixture was extracted with diethyl ether (3 x 100 mL) and the combined organic phases were dried over Na_2SO_4. The solvent was removed under reduced pressure and the resulting yellow oil (1.06 g) was stirred with methyl cyanoacetate (1.40 mL, 15.8 mmol, 1.57 g) for 18 h at room temperature. The formed solid was suspended in cold diethyl ether and collected by filtration to give **73** as a grey solid.

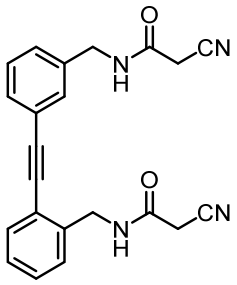

$C_{22}H_{18}N_4O_2$ (370.41 g mol^{-1})

Yield: 1.37 mg (3.70 mmol, 85%), grey solid.

Mp: 154–156 °C; ^{1}H NMR (400 MHz, DMSO-d_6): δ 8.76–8.72 (m, 2H), 7.55 (d, ^{3}J = 7.7 Hz, 1H), 7.49–7.48 (m, 2H), 7.42–7.39 (m, 2H), 7.36–7.32 (m, 3H), 4.52 (d, ^{3}J = 5.7 Hz, 2H), 4.32 (d, ^{3}J = 5.7 Hz, 2H), 3.73 (s, 2H), 3.72 (s, 2H); ^{13}C NMR (101 MHz, DMSO-d_6): δ 162.44, 162.40, 139.8, 139.3, 131.9, 130.2, 130.1, 129.0, 128.9, 128.0, 127.57, 127.50, 122.2, 121.1, 116.26, 116.24, 94.0, 86.9, 42.3, 41.4, 25.4, 25.3; HRMS (ESI, positive, acetonitrile/chloroform): (*m/z*) $[M+H]^+$, calcd. for $C_{22}H_{19}N_4O_2^+$, 371.1503, found, 371.1494.

General procedure for the synthesis of homo-bis(merocyanine) dyes RR, BB and GG:

To a suspension of bis(cyanoacetamide) **73** in 4–6 mL piperidine were added 12 equivalents of ethyl acetoacetate and the mixture was heated for 3 h at 100 °C. After cooling down to room temperature, concentrated HCl was added until pH 1 was reached and the resulting suspension was diluted with distilled water. The formed precipitate was collected by filtration and washed with distilled water and cold diethyl ether. After drying under vacuum, the crude bis(hydroxypyridone) intermediate was reacted with two equivalents of the respective aminothiophene aldehyde **66a-c** in acetic anhydride for 15–45 min at 90 °C. Methanol was then added at room temperature and the resulting solution was concentrated in vacuum. The crude products were purified by column chromatography (silica gel) and subsequently isolated by precipitation from DCM/*n*-hexane solution.

Homo-bis(merocyanine) RR:[133]

Compound **RR** was synthesized according to the general procedure described above using bis(cyanoacetamide) **73** (36.5 mg, 98.6 µmol), ethyl acetoacetate (151 µL, 154 mg, 1.18 mmol) and 2 mL piperidine. The bis(hydroxypyridone) intermediate **74** was reacted with 5-(dibutylamino)thiophene-2-carbaldehyde (**66a**) (47.6 mg, 199 µmol) in 2 mL acetic anhydride for 30 min and the crude product was purified by column chromatography using $CHCl_3$/MeOH 99.8:0.2 as eluent yielding **RR** as a purple solid.

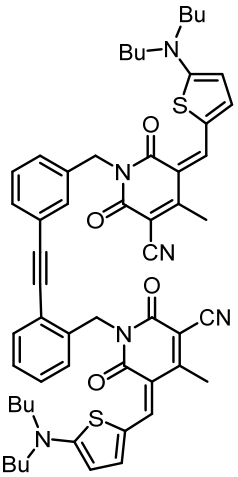

$C_{56}H_{60}N_6O_4S_2$ (945.25 g mol^{-1})

Yield: 19.6 mg (20.7 µmol, 21%), purple solid.

Mp: 202 °C; ^{1}H NMR (600 MHz, DMF-d_7): δ 8.09 (d, ^3J = 5.4 Hz, 1H), 8.05 (d, ^3J = 5.4 Hz, 1H), 7.98 (s, 1H), 7.91 (s, 1H), 7.77 (s, 1H), 7.52 (m, 2H), 7.42–7.38 (m, 2H), 7.31–7.26 (m, 2H), 7.10 (d, ^3J = 7.3 Hz, 1H), 6.87 (d, ^3J = 5.3 Hz, 1H), 6.85 (d, ^3J = 5.3 Hz, 1H), 5.39 (s, 2H), 5.16 (s, 2H), 3.68 (br, 4H), 3.50 (br, 4H, overlapped with solvent signal), 2.57 (s, 3H), 2.46 (s, 3H), 1.79–1.74 (m, 4H), 1.65 (br m, 4H), 1.42–1.37 (m, 4H), 1.29–1.28 (br, 4H), 0.95 (t, ^3J = 7.4 Hz, 6H), 0.88 (br, 6H); ^{13}C NMR (101 MHz, DMF-d_7): δ 177.6, 177.3, 163.4, 163.1, 159.3, 154.37, 154.32, 142.3, 142.2, 140.2, 139.3, 132.0, 131.5, 130.1, 129.0, 128.8, 128.6, 127.1, 126.3, 125.5, 125.4, 123.4, 121.9, 118.1, 117.9, 113.4, 113.1, 106.1, 106.1, 94.8, 92.5, 92.4, 87.7, 42.5, 41.4, 20.08, 20.01, 18.66, 18.62, 13.61; HRMS (ESI, positive, acetonitrile/chloroform): (*m/z*) [*M*+H]$^+$, calcd. for $C_{56}H_{61}N_6O_4S_2^+$, 945.4118, found, 945.4191; UV/vis (DCM, c = 3.7 x 10^{-6} M, 295 K): λ_{max}/nm (ε_{max}/M^{-1} cm^{-1}) = 504 (169200), 538 (170500).

Homo-bis(merocyanine) BB:

Compound **BB** was synthesized according to the general procedure described above using bis(cyanoacetamide) **73** (227 mg, 613 µmol), ethyl acetoacetate (938 µL, 957 mg, 7.35 mmol) and 6 mL piperidine. The bis(hydroxypyridone) intermediate **74** was reacted with (*E*)-3-[5-(dibutylamino)thiophene-2-yl]acrylaldehyde (**66b**) (316 mg, 1.19 mmol) in 12 mL acetic anhydride for 45 min and the crude product was purified by column chromatography using *n*-hexane/ethyl acetate 5:1 as eluent yielding **BB** as a dark blue solid.

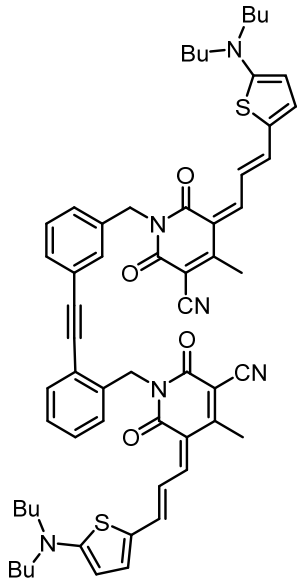

$C_{60}H_{64}N_6O_4S_2$ (997.33 g mol^{-1})

Yield: 110 mg (110 µmol, 18%), dark blue solid.

Mp: 177.0–177.6 °C; ^{1}H NMR (600 MHz, $CDCl_3$): δ 7.87–7.82 (br m, 2H), 7.69 (s, 1H), 7.52–7.49 (m, 3H), 7.30 (t, ^3J = 7.7 Hz, 1H), 7.20–6.96 (m, 9H), 6.16 (m, 2H), 5.34 (s, 2H), 5.15 (s, 2H), 3.47 (t, ^3J = 7.7 Hz, 4H), 3.41 (t, ^3J = 7.7 Hz, 4H), 2.34 (s, 3H), 2.27 (s, 3H), 1.73–1.63 (m, 8H), 1.41–1.34 (m, 8H), 0.97 (t, ^3J = 7.3 Hz, 6H), 0.95 (t, ^3J = 7.4 Hz, 6H); ^{13}C NMR (151 MHz, $CDCl_3$): δ 171.8, 171.2, 163.4, 163.2, 162.26, 162.20, 157.7, 157.4, 151.7, 151.4, 148.9, 148.8, 145.1, 144.5, 139.1, 138.4, 132.4, 131.3, 130.9, 129.2, 128.5, 128.3, 127.5, 127.4, 127.1, 126.5, 125.9, 123.7, 121.6, 119.0, 118.8, 117.58, 117.55, 111.5, 111.3, 111.1, 111.0, 110.2, 94.8, 94.6, 94.0, 87.7, 55.1, 54.9, 42.6, 42.4, 29.3, 20.29, 20.28, 20.25, 18.8, 13.9; HRMS (ESI, positive, acetonitrile/chloroform): (*m/z*) $[M+H]^+$, calcd. for $C_{60}H_{65}N_6O_4S_2^+$, 997.4503, found, 997.4501; UV/vis (DCM, c = 3.9 x 10^{-6} M, 295 K): λ_{max}/nm (ε_{max}/M^{-1} cm^{-1}) = 654 (358500).

Homo-bis(merocyanine) GG:

Compound **GG** was synthesized according to the general procedure described above using bis(cyanoacetamide) **73** (132 mg, 356 µmol), ethyl acetoacetate (546 µL, 557 mg, 4.28 mmol) and 4 mL piperidine. The bis(hydroxypyridone) intermediate **74** was reacted with (*2E,4E*)-5-[5-(dibutylamino)thiophene-2-yl]penta-2,4-dienal (**66c**) (200 mg, 686 µmol) in 10 mL acetic anhydride for 15 min and the crude product was purified by column chromatography using DCM/MeOH 99.4:0.6 as eluent yielding **GG** as a dark violet solid.

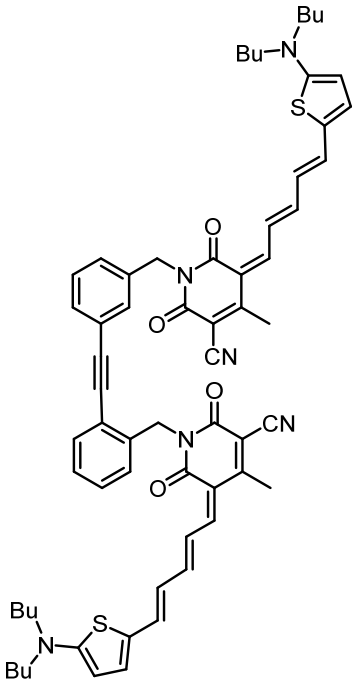

$C_{64}H_{68}N_6O_4S_2$ (1049.41 g mol^{-1})

Yield: 37.4 mg (35.6 µmol, 10%), dark violet solid.

Mp: 165–167 °C; ^{1}H NMR (600 MHz, $CDCl_3$): δ 7.85–7.74 (br m, 2H), 7.68 (s, 1H), 7.57–7.51 (m, 3H), 7.32 (t, ^3J = 7.7 Hz, 1H), 7.22–6.91 (m, 10H), 6.78 (br s, 1H), 6.32–6.24 (m, 2H), 6.03–6.01 (m, 2H), 5.32 (s, 2H), 5.12 (s, 2H), 3.43–3.39 (m, 8H), 2.30 (s, 3H), 2.26 (s, 3H), 1.70–1.65 (m, 8H), 1.41–1.34 (m, 8H), 0.98 (t, ^3J = 7.4 Hz, 6H), 0.97 (t, ^3J = 7.4 Hz, 6H); ^{13}C NMR (151 MHz, $CDCl_3$): δ 169.4, 168.2, 163.1, 163.0, 162.13, 162.11, 159.2, 159.0, 157.4, 157.0, 150.8, 150.1, 142.66, 142.63, 141.99, 141.98, 141.2, 139.2, 138.4, 132.5, 131.9, 131.2, 129.67, 129.66, 128.4, 128.3, 127.2, 126.9, 126.7, 126.6, 125.6, 125.4, 123.5, 121.7, 121.6, 117.5, 117.2, 112.95, 112.94, 112.21, 109.5, 108.4, 95.7, 94.7, 87.7, 54.8, 54.6, 42.7, 42.6, 29.4, 29.3, 20.3, 20.2, 18.9, 13.94, 13.92; HRMS (ESI, positive, acetonitrile/chloroform): (*m/z*) $[M]^+$, calcd. for $C_{64}H_{68}N_6O_4S_2^+$, 1048.4738, found, 1048.4720; UV/vis (DCM, c = 3.7 x 10^{-6} M, 295 K): λ_{max}/nm (ε_{max}/M^{-1} cm^{-1}) = 764 (374900).

References

[1] a) T.-T.-T. Nguyen, M. Baumgarten, A. Rouhanipour, H. J. Räder, I. Lieberwirth, K. Müllen, *J. Am. Chem. Soc.* **2013**, *135*, 4183–4186; b) T. M. Figueira-Duarte, S. C. Simon, M. Wagner, S. I. Druzhinin, K. A. Zachariasse, K. Müllen, *Angew. Chem. Int. Ed.* **2008**, *47*, 10175–10178; c) W.-S. Li, T. Aida, *Chem. Rev.* **2009**, *109*, 6047–6076.

[2] S. Bhosale, A. L. Sisson, P. Talukdar, A. Fürstenberg, N. Banerji, E. Vauthey, G. Bollot, J. Mareda, C. Röger, F. Würthner, N. Sakai, S. Matile, *Science* **2006**, *313*, 84–86.

[3] a) V. Berl, I. Huc, R. G. Khoury, M. J. Krische, J.-M. Lehn, *Nature* **2000**, *407*, 720–723; b) Q. Gan, Y. Ferrand, C. Bao, B. Kauffmann, A. Grélard, H. Jiang, I. Huc, *Science* **2011**, *331*, 1172–1175.

[4] a) M. C. O'Sullivan, J. K. Sprafke, D. V. Kondratuk, C. Rinfray, T. D. W. Claridge, A. Saywell, M. O. Blunt, J. N. O'Shea, P. H. Beton, M. Malfois, H. L. Anderson, *Nature* **2011**, *469*, 72–75; b) F. Zhang, G. Götz, H. D. F. Winkler, C. A. Schalley, P. Bäuerle, *Angew. Chem. Int. Ed.* **2009**, *48*, 6632–6635; c) T. Iwamoto, Y. Watanabe, Y. Sakamoto, T. Suzuki, S. Yamago, *J. Am. Chem. Soc.* **2011**, *133*, 8354–8361; d) M. Mayor, C. Didschies, *Angew. Chem. Int. Ed.* **2003**, *42*, 3176–3179.

[5] a) M. T. Dedeo, D. T. Finley, M. B. Francis, in *Progress in Molecular Biology and Translational Science*, Academic Press, **2011**; b) R. Hull, in *Plant Virology*, 5th ed., Academic Press, Boston, **2014**; c) W.-S. Ryu, *Molecular Virology of Human Pathogenic Viruses*, Academic Press, Boston, **2017**.

[6] a) D.-P. Häder, *Photosynthese*, Thieme, Stuttgart, **1999**; b) G. McDermott, S. M. Prince, A. A. Freer, A. M. Hawthornthwaite-Lawless, M. Z. Papiz, R. J. Cogdell, N. W. Isaacs, *Nature* **1995**, *374*, 517–521; c) T. Pullerits, V. Sundström, *Acc. Chem. Res.* **1996**, *29*, 381–389; d) S. Bahatyrova, R. N. Frese, C. A. Siebert, J. D. Olsen, K. O. van der Werf, R. van Grondelle, R. A. Niederman, P. A. Bullough, C. Otto, C. N. Hunter, *Nature* **2004**, *430*, 1058–1062; e) R. J. Cogdell, A. Gall, J. Köhler, *Q. Rev. Biophys.* **2006**, *39*, 227–324.

[7] J. D. van der Waals, doctoral thesis (On the Continuity of the Gaseous and Liquid States), Universität Leiden, **1873**.

[8] J.-P. Behr, *The Lock-and-Key Principle: The State of the Art – 100 Years On*, John Wiley, Chichester, **1994**.

[9] C. J. Pedersen, *J. Am. Chem. Soc.* **1967**, *89*, 2495–2496.

[10] D. J. Cram, J. M. Cram, *Science* **1974**, *183*, 803–809.

[11] B. Dietrich, J. M. Lehn, J. P. Sauvage, *Tetrahedron Lett.* **1969**, *10*, 2885–2888.

[12] a) V. Balzani, A. Credi, M. Venturi, *Molecular Devices and Machines – A Journey into the Nano World*, 2nd ed., Wiley-VCH, Weinheim, **2008**; b) S. Kassem, T. van Leeuwen, A. S. Lubbe, M. R. Wilson, B. L. Feringa, D. A. Leigh, *Chem. Soc. Rev.* **2017**, *46*, 2592–2621; c) J. D. Badjić, V. Balzani, A. Credi, S. Silvi, J. F. Stoddart, *Science* **2004**, *303*, 1845–1849; d) R. A. van Delden, M. K. J. ter Wiel, M. M. Pollard, J. Vicario, N. Koumura, B. L. Feringa, *Nature* **2005**, *437*, 1337–1340; e) M. C. Jiménez, C. Dietrich-Buchecker, J.-P. Sauvage, *Angew. Chem. Int. Ed.* **2000**, *39*, 3284–3287.

[13] a) J. A. A. W. Elemans, R. van Hameren, R. J. M. Nolte, A. E. Rowan, *Adv. Mater.* **2006**, *18*, 1251–1266; b) S. Yagai, T. Seki, T. Karatsu, A. Kitamura, F. Würthner, *Angew. Chem. Int. Ed.* **2008**, *47*, 3367–3371; c) D. González-Rodríguez, A. P. H. J. Schenning, *Chem. Mater.* **2011**, *23*, 310–325.

[14] S. E. Sheppard, *J. Chem. Soc. Trans.* **1909**, *95*, 15–19.

[15] a) A. S. Davydov, *Sov. Phys. Usp.* **1964**, *7*, 145–178; b) M. Kasha, *Radiat. Res.* **1963**, *20*, 55–70; c) M. Kasha, H. R. Rawls, M. A. E. Bayoumi, *Pure Appl. Chem.* **1965**, *11*, 371–392.

[16] a) T. W. Kelley, P. F. Baude, C. Gerlach, D. E. Ender, D. Muyres, M. A. Haase, D. E. Vogel, S. D. Theiss, *Chem. Mater.* **2004**, *16*, 4413–4422; b) C. Sekine, Y. Tsubata, T. Yamada, M. Kitano, S. Doi, *Sci. Technol. Adv. Mat.* **2014**, *15*, 034203; c) N. Kaur, M. Singh, D. Pathak, T. Wagner, J. M. Nunzi, *Synthetic Met.* **2014**, *190*, 20–26; d) L. Lu, T. Zheng, Q. Wu, A. M. Schneider, D. Zhao, L. Yu, *Chem. Rev.* **2015**, *115*, 12666–12731; e) K. A. Mazzio, C. K. Luscombe, *Chem. Soc. Rev.* **2015**, *44*, 78–90; f) G. J. Hedley, A. Ruseckas, I. D. W. Samuel, *Chem. Rev.* **2017**, *117*, 796–837.

[17] a) A. Liess, A. Lv, A. Arjona-Esteban, D. Bialas, A.-M. Krause, V. Stepanenko, M. Stolte, F. Würthner, *Nano Lett.* **2017**, *17*, 1719–1726; b) A. Arjona-Esteban, J. Krumrain, A. Liess, M. Stolte, L. Huang, D. Schmidt, V. Stepanenko, M. Gsänger, D. Hertel, K. Meerholz, F. Würthner, *J. Am. Chem. Soc.* **2015**, *137*, 13524–13534; c) Y. Zhang, *Phys. Rev. Lett.* **2016**, *116*, 016602.

[18] a) F. Würthner, *Acc. Chem. Res.* **2016**, *49*, 868–876; b) F. Würthner, S. Yao, *Angew. Chem. Int. Ed.* **2000**, *39*, 1978–1981; c) F. Würthner, S. Yao, J. Schilling, R. Wortmann,

M. Redi-Abshiro, E. Mecher, F. Gallego-Gomez, K. Meerholz, *J. Am. Chem. Soc.* **2001**, *123*, 2810–2824; d) F. Würthner, S. Yao, T. Debaerdemaeker, R. Wortmann, *J. Am. Chem. Soc.* **2002**, *124*, 9431–9447.

[19] a) A. Lohr, S. Uemura, F. Würthner, *Angew. Chem. Int. Ed.* **2009**, *48*, 6165–6168; b) F. Würthner, S. Yao, U. Beginn, *Angew. Chem. Int Ed.* **2003**, *42*, 3247–3250; c) S. Yao, U. Beginn, T. Gress, M. Lysetska, F. Würthner, *J. Am. Chem. Soc.* **2004**, *126*, 8336–8348; d) A. Lohr, F. Würthner, *Angew. Chem. Int. Ed.* **2008**, *47*, 1232–1236; e) A. Lohr, F. Würthner, *Chem. Commun.* **2008**, 2227–2229; f) G. Fernández, M. Stolte, V. Stepanenko, F. Würthner, *Chem. Eur. J.* **2013**, *19*, 206–217; g) A. Zitzler-Kunkel, E. Kirchner, D. Bialas, C. Simon, F. Würthner, *Chem. Eur. J.* **2015**, *21*, 14851–14861; h) D. Bialas, E. Kirchner, F. Würthner, *Chem. Commun.* **2016**, *52*, 3777–3780.

[20] a) D. Bialas, A. Zitzler-Kunkel, E. Kirchner, D. Schmidt, F. Würthner, *Nat. Commun.* **2016**, *7*, 12949; b) A. Lohr, M. Grüne, F. Würthner, *Chem. Eur. J.* **2009**, *15*, 3691–3705.

[21] a) G. Scheibe, *Angew. Chem.* **1936**, *49*, 563; b) G. Scheibe, *Angew. Chem.* **1937**, *50*, 212–219; c) E. E. Jelley, *Nature* **1936**, *138*, 1009–1010.

[22] a) L. Brunsveld, B. J. B. Folmer, E. W. Meijer, R. P. Sijbesma, *Chem. Rev.* **2001**, *101*, 4071–4098; b) J. A. A. W. Elemans, A. E. Rowan, R. J. M. Nolte, *J. Mater. Chem.* **2003**, *13*, 2661–2670; c) Z. Chen, A. Lohr, C. R. Saha-Möller, F. Würthner, *Chem. Soc. Rev.* **2009**, *38*, 564–584; d) M. Kastler, W. Pisula, D. Wasserfallen, T. Pakula, K. Müllen, *J. Am. Chem. Soc.* **2005**, *127*, 4286–4296; e) H. Engelkamp, S. Middelbeek, R. J. M. , Nolte, *Science* **1999**, *284*, 785–788.

[23] a) P. M. Saville, E. M. Sevick, *Langmuir* **1998**, *14*, 3137–3139; b) F. Lortie, S. Boileau, L. Bouteiller, C. Chassenieux, F. Lauprêtre, *Macromolecules* **2005**, *38*, 5283–5287.

[24] a) T. Gulder, P. S. Baran, *Nat. Prod. Rep.* **2012**, *29*, 899–934; b) S.-i. Kato, T. Matsumoto, K. Ideta, T. Shimasaki, K. Goto, T. Shinmyozu, *J. Org. Chem.* **2006**, *71*, 4723–4733; c) S. Gabutti, M. Knutzen, M. Neuburger, G. Schull, R. Berndt, M. Mayor, *Chem. Commun.* **2008**, 2370–2372.

[25] a) J. M. Giaimo, J. V. Lockard, L. E. Sinks, A. M. Scott, T. M. Wilson, M. R. Wasielewski, *J. Phys. Chem. A* **2008**, *112*, 2322–2330; b) H. Yoo, J. Yang, A. Yousef, M. R. Wasielewski, D. Kim, *J. Am. Chem. Soc.* **2010**, *132*, 3939–3944.

[26] a) C. A. Schalley, *Analytical Methods in Supramolecular Chemistry*, 2nd ed., Wiley-VCH, Weinheim, **2012**; b) Y. Liu, Z. Wang, X. Zhang, *Chem. Soc. Rev.* **2012**, *41*, 5922–5932; c) P. Hensley, *Structure* **1996**, *4*, 367–373.

[27] a) J. Hentschel, A. M. Kushner, J. Ziller, Z. Guan, *Angew. Chem. Int. Ed.* **2012**, *51*, 10561–10565; b) G. M. L. van Gemert, J. W. Peeters, S. H. M. Söntjens, H. M. Janssen, A. W. Bosman, *Macromol. Chem. Phys.* **2012**, *213*, 234–242; c) M. Nakahata, Y. Takashima, A. Harada, *Macromol. Rapid Commun.* **2016**, *37*, 86–92.

[28] S. Bienz, L. Bigler, T. Fox, *Spektroskopische Methoden in der organischen Chemie*, 9th ed., Georg Thieme, Stuttgart, **2016**.

[29] a) R. B. Martin, *Chem. Rev.* **1996**, *96*, 3043–3064; b) T. F. A. De Greef, M. M. J. Smulders, M. Wolffs, A. P. H. J. Schenning, R. P. Sijbesma, E. W. Meijer, *Chem. Rev.* **2009**, *109*, 5687–5754; c) L. K. S. von Krbek, C. A. Schalley, P. Thordarson, *Chem. Soc. Rev.* **2017**, *46*, 2622–2637; d) N. J. Baxter, M. P. Williamson, T. H. Lilley, E. Haslam, *J. Chem. Soc. Faraday T.* **1996**, *92*, 231–234; e) D. Zhao, J. S. Moore, *Org. Biomol. Chem.* **2003**, *1*, 3471–3491.

[30] a) N. J. Greenfield, *Nat. Protoc.* **2006**, *1*, 2876–2890; b) S. R. Martin, P. M. Bayley, *Absorption and Circular Dichroism Spectroscopy*, Springer New York, Totowa, **2002**.

[31] a) M. W. Freyer, E. A. Lewis, in *Method Cell Biol., Vol. 84*, Academic Press, **2008**, p. 79–113; b) J. A. Thomson, J. E. Ladbury, in *Biocalorimetry 2*, John Wiley & Sons, Ltd, **2005**.

[32] a) T. D. W. Claridge, *High-Resolution NMR Techniques in Organic Chemistry*, 2nd ed., Elsevier, **2009**; b) H. Fribolin, *Basic one- and two-dimensional NMR spectroscopy*, 2rd ed., Wiley-VCH, Weinheim, **1993**; c) K. C. Wong, *J. Chem. Educ.* **2014**, *91*, 1103–1104.

[33] a) F. Ni, H. A. Scheraga, *Acc. Chem. Res.* **1994**, *27*, 257–264; b) M. T. Huggins, F. Billimoria, *J. Chem. Educ.* **2007**, *84*, 471–474.

[34] a) Y. Cohen, L. Avram, L. Frish, *Angew. Chem. Int. Ed.* **2005**, *44*, 520–554; b) L. Avram, Y. Cohen, *Chem. Soc. Rev.* **2015**, *44*, 586–602.

[35] a) S. Podzimek, *Light Scattering, Size Exclusion Chromatography and Asymmetric Flow Field Flow Fractionation*, John Wiley & Sons, Inc., **2011**; b) M. Kerker, *The scattering of light and other electromagnetic radiation*, Academic Press, New York, **1969**.

[36] a) G. Wypych, *Handbook of Solvents*, 2nd ed., ChemTec Publishing, Oxford, **2014**; b) J. Gershberg, F. Fennel, T. H. Rehm, S. Lochbrunner, F. Würthner, *Chem. Sci.* **2016**, *7*, 1729–1737.

[37] A. M. Striegel, W. W. Yau, J. J. Kirkland, D. D. Bly, *Modern Size-Exclusion Liquid Chromatography*, 2nd ed., John Wiley & Sons, Inc., **2009**.

[38] a) C. A. Schalley, A. Springer, *Mass Spectrometry and Gas-Phase Chemistry of Non-Covalent Complexes*, Wiley, Hoboken, NJ, **2009**; b) C. A. Schalley, *Mass Spectrom. Rev.* **2001**, *20*, 253–309; c) J. S. Brodbelt, C. C. Liou, *Pure Appl. Chem.* **1993**, *65*, 409; d) R. Colton, A. D'Agostino, J. C. Traeger, *Mass Spectrom. Rev.* **1995**, *14*, 79–106; e) J. A. Loo, *Mass Spectrom. Rev.* **1997**, *16*, 1–23.

[39] a) V. Rose, J. W. Freeland, S. K. Streiffer, *Scanning Probe Microscopy of Functional Materials: Nanoscale Imaging and Spectroscopy*, 11th ed., Springer, New York, NY, **2011**; b) L. A. Bottomley, *Anal. Chem.* **1998**, *70*, 425–476.

[40] a) E. Yashima, N. Ousaka, D. Taura, K. Shimomura, T. Ikai, K. Maeda, *Chem. Rev.* **2016**, *116*, 13752–13990; b) X. Lin, H. Kurata, D. D. Prabhu, M. Yamauchi, T. Ohba, S. Yagai, *Chem. Commun.* **2017**, *53*, 168–171.

[41] a) W. Clegg, *X-Ray Chrystallography*, 2nd ed., Oxford University Press, **2015**; b) C. Giacovazzo, *Fundamentals of Crystallography*, Oxford University Press, **2002**.

[42] D. H. Busch, *J. Inclus. Phenom. Mol.* **1992**, *12*, 389–395.

[43] a) V. Martí-Centelles, M. D. Pandey, M. I. Burguete, S. V. Luis, *Chem. Rev.* **2015**, *115*, 8736–8834; b) D. V. Kondratuk, L. M. A. Perdigão, A. M. S. Esmail, J. N. O'Shea, P. H. Beton, H. L. Anderson, *Nat. Chem.* **2015**, *7*, 317–322.

[44] a) J. F. Stoddart, L. F. Lindoy, I. M. Atkinson, in *Self Assembly in Supramolecular Systems*, The Royal Society of Chemistry, **2000**, p. 119–184; b) F. M. Raymo, J. F. Stoddart, in *Molecular Catenanes, Rotaxanes and Knots*, Wiley-VCH, **2007**, p. 143–176; c) K. E. Griffiths, J. F. Stoddart, *Pure Appl. Chem.* **2008**, *80*, 485–506; d) J. F. Stoddart, *Chem. Soc. Rev.* **2009**, *38*, 1802–1820.

[45] a) P. R. Ashton, O. A. Matthews, S. Menzer, F. M. Raymo, N. Spencer, J. F. Stoddart, D. J. Williams, *Liebigs Ann./Recueil* **1997**, 2485–2494; b) B. H. Northrop, F. Aricó, N. Tangchiavang, J. D. Badjić, J. F. Stoddart, *Org. Lett.* **2006**, *8*, 3899–3902; c) J. Guo, P. C. Mayers, G. A. Breault, C. A. Hunter, *Nat. Chem.* **2010**, *2*, 218–222.

[46] S. Anderson, H. L. Anderson, in *Templated Organic Synthesis*, Wiley-VCH, **2007**, p. 1–38.

[47] a) J. L. Atwood, J. M. Lehn, *Comprehensive Supramolecular Chemistry: Templating, self-assembly, and self-organization, Vol. 9*, Pergamon, **1999**; b) S. Otto, R. L. E. Furlan, J. K. M. Sanders, *Science* **2002**, *297*, 590–593; c) J.-H. Ryu, H.-J. Kim, Z. Huang, E. Lee, M. Lee, *Angew. Chem. Int. Ed.* **2006**, *45*, 5304–5307; d) S. Furukawa, K. Tahara, F. C. De Schryver, M. Van der Auweraer, Y. Tobe, S. De Feyter, *Angew. Chem. Int. Ed.* **2007**, *46*, 2831–2834; e) N. Lin, A. Langner, S. L. Tait, C. Rajadurai,

M. Ruben, K. Kern, *Chem. Commun.* **2007**, 4860–4862; f) J.-M. Lehn, *Science* **2002**, *295*, 2400–2403.

[48] a) J. M. Berg, J. L. Tymoczko, L. Stryer, *Biochemistry*, 8th ed., W. H. Freeman, New York, **2015**; b) G. Zubay, *Nature* **1958**, *182*, 1290–1292.

[49] a) A. Klug, *Angew. Chem. Int. Ed.* **1983**, *22*, 565–582; b) V. Percec, *J. Macromol. Sci. A* **1996**, *33*, 1479–1496.

[50] P. G. A. Janssen, J. Vandenbergh, J. L. J. van Dongen, E. W. Meijer, A. P. H. J. Schenning, *J. Am. Chem. Soc.* **2007**, *129*, 6078–6079.

[51] a) T. Sugimoto, K. Sada, S. Sakamoto, K. Yamaguchi, S. Shinkai, *Chem. Commun.* **2004**, 1226–1227; b) T. Sugimoto, K. Sada, Y. Tateishi, T. Suzuki, Y. Sei, K. Yamaguchi, S. Shinkai, *Tetrahedron Lett.* **2005**, *46*, 5347–5350.

[52] T. Sugimoto, T. Suzuki, S. Shinkai, K. Sada, *J. Am. Chem. Soc.* **2007**, *129*, 270–271.

[53] J. Stojaković, A. M. Whitis, L. R. MacGillivray, *Angew. Chem. Int. Ed.* **2013**, *52*, 12127–12130.

[54] a) M. E. Belowich, C. Valente, J. F. Stoddart, *Angew. Chem. Int. Ed.* **2010**, *49*, 7208–7212; b) M. E. Belowich, C. Valente, R. A. Smaldone, D. C. Friedman, J. Thiel, L. Cronin, J. F. Stoddart, *J. Am. Chem. Soc.* **2012**, *134*, 5243–5261.

[55] a) J. T. Davis, *Angew. Chem. Int. Ed.* **2004**, *43*, 668–698; b) V. Gubala, D. De Jesús, J. M. Rivera, *Tetrahedron Lett.* **2006**, *47*, 1413–1416.

[56] a) J. T. Davis, S. Tirumala, J. R. Jenssen, E. Radler, D. Fabris, *J. Org. Chem.* **1995**, *60*, 4167–4176; b) G. Gottarelli, S. Masiero, E. Mezzina, S. Pieraccini, J. P. Rabe, P. Samorí, G. P. Spada, *Chem. Eur. J.* **2000**, *6*, 3242–3248.

[57] J. L. Sessler, M. Sathiosatham, K. Doerr, V. Lynch, K. A. Abboud, *Angew. Chem. Int. Ed.* **2000**, *39*, 1300–1303.

[58] a) A. L. Marlow, E. Mezzina, G. P. Spada, S. Masiero, J. T. Davis, G. Gottarelli, *J. Org. Chem.* **1999**, *64*, 5116–5123; b) E. Mezzina, P. Mariani, R. Itri, S. Masiero, S. Pieraccini, G. P. Spada, F. Spinozzi, J. T. Davis, G. Gottarelli, *Chem. Eur. J.* **2001**, *7*, 388–395; c) J. E. Betancourt, J. M. Rivera, *Org. Lett.* **2008**, *10*, 2287–2290; d) M. García-Arriaga, G. Hobley, J. M. Rivera, *J. Am. Chem. Soc.* **2008**, *130*, 10492–10493.

[59] a) V. Gubala, J. E. Betancourt, J. M. Rivera, *Org. Lett.* **2004**, *6*, 4735–4738; b) M. d. C. Rivera-Sánchez, I. Andújar-de-Sanctis, M. García-Arriaga, V. Gubala, G. Hobley, J. M. Rivera, *J. Am. Chem. Soc.* **2009**, *131*, 10403–10405.

[60] D. González-Rodríguez, J. L. J. van Dongen, M. Lutz, A. L. Spek, A. P. H. J. Schenning, E. W. Meijer, *Nat. Chem.* **2009**, *1*, 151–155.

[61] a) I. C. M. Kwan, Y.-M. She, G. Wu, *Chem. Commun.* **2007**, 4286–4288; b) M. Cai, X. Shi, V. Sidorov, D. Fabris, Y.-f. Lam, J. T. Davis, *Tetrahedron* **2002**, *58*, 661–671.

[62] M. Martin-Hidalgo, J. M. Rivera, *Chem. Commun.* **2011**, *47*, 12485–12487.

[63] X. Shi, K. M. Mullaugh, J. C. Fettinger, Y. Jiang, S. A. Hofstadler, J. T. Davis, *J. Am. Chem. Soc.* **2003**, *125*, 10830–10841.

[64] J. E. Betancourt, M. Martín-Hidalgo, V. Gubala, J. M. Rivera, *J. Am. Chem. Soc.* **2009**, *131*, 3186–3188.

[65] a) P. J. Stang, *Chem. Eur. J.* **1998**, *4*, 19–27; b) M. Fujita, *Chem. Soc. Rev.* **1998**, *27*, 417–425.

[66] a) T. S. Koblenz, J. Wassenaar, J. N. H. Reek, *Chem. Soc. Rev.* **2008**, *37*, 247–262; b) M. D. Pluth, R. G. Bergman, K. N. Raymond, *Acc. Chem. Res.* **2009**, *42*, 1650–1659; c) M. Yoshizawa, J. K. Klosterman, M. Fujita, *Angew. Chem. Int. Ed.* **2009**, *48*, 3418–3438.

[67] a) B. Therrien, G. Süss-Fink, P. Govindaswamy, A. K. Renfrew, P. J. Dyson, *Angew. Chem. Int. Ed.* **2008**, *47*, 3773–3776; b) J. E. M. Lewis, E. L. Gavey, S. A. Cameron, J. D. Crowley, *Chem. Sci.* **2012**, *3*, 778–784.

[68] H. Takezawa, T. Murase, G. Resnati, P. Metrangolo, M. Fujita, *J. Am. Chem. Soc.* **2014**, *136*, 1786–1788.

[69] a) P. Mal, B. Breiner, K. Rissanen, J. R. Nitschke, *Science* **2009**, *324*, 1697–1699; b) S. Horiuchi, T. Murase, M. Fujita, *J. Am. Chem. Soc.* **2011**, *133*, 12445–12447.

[70] K. Kumazawa, K. Biradha, T. Kusukawa, T. Okano, M. Fujita, *Angew. Chem. Int. Ed.* **2003**, *42*, 3909–3913.

[71] a) M. Yoshizawa, J. Nakagawa, K. Kumazawa, M. Nagao, M. Kawano, T. Ozeki, M. Fujita, *Angew. Chem. Int. Ed.* **2005**, *44*, 1810–1813; b) K. Ono, M. Yoshizawa, T. Kato, K. Watanabe, M. Fujita, *Angew. Chem. Int. Ed.* **2007**, *46*, 1803–1806; c) S. Mirtschin, A. Slabon-Turski, R. Scopelliti, A. H. Velders, K. Severin, *J. Am. Chem. Soc.* **2010**, *132*, 14004–14005.

[72] T. Murase, K. Otsuka, M. Fujita, *J. Am. Chem. Soc.* **2010**, *132*, 7864–7865.

[73] N. Singh, J.-H. Jo, Y. H. Song, H. Kim, D. Kim, M. S. Lah, K.-W. Chi, *Chem. Commun.* **2015**, *51*, 4492–4495.

[74] a) Y. Yamauchi, M. Yoshizawa, M. Akita, M. Fujita, *J. Am. Chem. Soc.* **2010**, *132*, 960–966; b) Y. Yamauchi, M. Yoshizawa, M. Akita, M. Fujita, *Proc. Natl. Acad. Sci.* **2009**, *106*, 10435–10437.

[75] Y. Yamauchi, M. Yoshizawa, M. Fujita, *J. Am. Chem. Soc.* **2008**, *130*, 5832–5833.

[76] L. Zhang, L. Lin, D. Liu, Y.-J. Lin, Z.-H. Li, G.-X. Jin, *J. Am. Chem. Soc.* **2017**, *139*, 1653–1660.

[77] J. Wu, A. Fechtenkötter, J. Gauss, M. D. Watson, M. Kastler, C. Fechtenkötter, M. Wagner, K. Müllen, *J. Am. Chem. Soc.* **2004**, *126*, 11311–11321.

[78] a) P. D. Frischmann, S. Guieu, R. Tabeshi, M. J. MacLachlan, *J. Am. Chem. Soc.* **2010**, *132*, 7668–7675; b) P. D. Frischmann, B. J. Sahli, S. Guieu, B. O. Patrick, M. J. MacLachlan, *Chem. Eur. J.* **2012**, *18*, 13712–13721; c) X. Wu, R. Liu, B. Sathyamoorthy, K. Yamato, G. Liang, L. Shen, S. Ma, D. K. Sukumaran, T. Szyperski, W. Fang, L. He, X. Chen, B. Gong, *J. Am. Chem. Soc.* **2015**, *137*, 5879–5882.

[79] M. Hutin, J. K. Sprafke, B. Odell, H. L. Anderson, T. D. W. Claridge, *J. Am. Chem. Soc.* **2013**, *135*, 12798–12807.

[80] a) C. Shao, M. Grüne, M. Stolte, F. Würthner, *Chem. Eur. J.* **2012**, *18*, 13665–13677; b) M. M. Safont-Sempere, P. Osswald, K. Radacki, F. Würthner, *Chem. Eur. J.* **2010**, *16*, 7380–7384; c) M. M. Safont-Sempere, P. Osswald, M. Stolte, M. Grüne, M. Renz, M. Kaupp, K. Radacki, H. Braunschweig, F. Würthner, *J. Am. Chem. Soc.* **2011**, *133*, 9580–9591.

[81] N.-T. Lin, A. Vargas Jentzsch, L. Guenee, J.-M. Neudorfl, S. Aziz, A. Berkessel, E. Orentas, N. Sakai, S. Matile, *Chem. Sci.* **2012**, *3*, 1121–1127.

[82] A. Zitzler-Kunkel, M. R. Lenze, N. M. Kronenberg, A.-M. Krause, M. Stolte, K. Meerholz, F. Würthner, *Chem. Mater.* **2014**, *26*, 4856–4866.

[83] E. G. McRae, M. Kasha, *J. Chem. Phys.* **1958**, *28*, 721–722.

[84] B. Alberts, D. Bray, K. Hopkin, A. Johnson, J. Lewis, M. Raff, K. Roberts, P. Walter, *Essential cell biology*, 3 ed., Garland Science, New York, **2010**.

[85] a) J. van Esch, H. Valkenier, S. Hartwig, S. Hecht, in *Foldamers*, Wiley-VCH, **2007**, p. 403–425; b) G. Guichard, I. Huc, *Chem. Commun.* **2011**, *47*, 5933–5941.

[86] a) S. S. Yanari, F. A. Bovey, R. Lumry, *Nature* **1963**, *200*, 242–244; b) F. Hirayama, *J. Chem. Phys.* **1965**, *42*, 3163–3171.

[87] W. Klöpffer, *Chem. Phys. Lett.* **1969**, *4*, 193–194.

[88] S. N. Semerak, C. W. Frank, *Spectroscopy: NMR, Fluorescence, FT-IR*, Springer, Berlin, Heidelberg, **1984**.

[89] F. C. De Schryver, P. Collart, J. Vandendriessche, R. Goedeweeck, A. M. Swinnen, M. Van der Auweraer, *Acc. Chem. Res.* **1987**, *20*, 159–166.

[90] A. Zitzler-Kunkel, M. R. Lenze, K. Meerholz, F. Würthner, *Chem. Sci.* **2013**, *4*, 2071–2075.

[91] L. Lu, R. J. Lachicotte, T. L. Penner, J. Perlstein, D. G. Whitten, *J. Am. Chem. Soc.* **1999**, *121*, 8146–8156.

[92] C. Hippius, I. H. M. van Stokkum, E. Zangrando, R. M. Williams, M. Wykes, D. Beljonne, F. Würthner, *J. Phys. Chem. C* **2008**, *112*, 14626–14638.

[93] E. E. Neuteboom, S. C. J. Meskers, E. W. Meijer, R. A. J. Janssen, *Macromol. Chem. Phys.* **2004**, *205*, 217–222.

[94] a) W. Wang, L.-S. Li, G. Helms, H.-H. Zhou, A. D. Q. Li, *J. Am. Chem. Soc.* **2003**, *125*, 1120–1121; b) J. J. Han, A. D. Shaller, W. Wang, A. D. Q. Li, *J. Am. Chem. Soc.* **2008**, *130*, 6974–6982.

[95] M. C. Traub, K. H. DuBay, S. E. Ingle, X. Zhu, K. N. Plunkett, D. R. Reichman, D. A. Vanden Bout, *J. Phys. Chem. Lett.* **2013**, *4*, 2520–2524.

[96] a) V. Berl, I. Huc, R. G. Khoury, J.-M. Lehn, *Chem. Eur. J.* **2001**, *7*, 2798–2809; b) J. Garric, J.-M. Léger, I. Huc, *Angew. Chem. Int. Ed.* **2005**, *44*, 1954–1958; c) Y. Ferrand, A. M. Kendhale, J. Garric, B. Kauffmann, I. Huc, *Angew. Chem. Int. Ed.* **2010**, *49*, 1778–1781; d) N. Delsuc, S. Massip, J.-M. Léger, B. Kauffmann, I. Huc, *J. Am. Chem. Soc.* **2011**, *133*, 3165–3172; e) M. Kudo, V. Maurizot, B. Kauffmann, A. Tanatani, I. Huc, *J. Am. Chem. Soc.* **2013**, *135*, 9628–9631; f) X. Li, T. Qi, K. Srinivas, S. Massip, V. Maurizot, I. Huc, *Org. Lett.* **2016**, *18*, 1044–1047; g) Q. Gan, X. Wang, B. Kauffmann, F. Rosu, Y. Ferrand, I. Huc, *Nat. Nanotechnol.* **2017**, *12*, 447–452.

[97] a) L. Sebaoun, V. Maurizot, T. Granier, B. Kauffmann, I. Huc, *J. Am. Chem. Soc.* **2014**, *136*, 2168–2174; b) L. Sebaoun, B. Kauffmann, T. Delclos, V. Maurizot, I. Huc, *Org. Lett.* **2014**, *16*, 2326–2329.

[98] R. Scott Lokey, B. L. Iverson, *Nature* **1995**, *375*, 303–305.

[99] a) S. Ghosh, S. Ramakrishnan, *Macromolecules* **2005**, *38*, 676–686; b) S. Ghosh, S. Ramakrishnan, *Angew. Chem. Int. Ed.* **2005**, *44*, 5441–5447.

[100] H. Asanuma, K. Shirasuka, T. Takarada, H. Kashida, M. Komiyama, *J. Am. Chem. Soc.* **2003**, *125*, 2217–2223.

[101] Z. Chen, N. D. Urban, Y. Gao, W. Zhang, J. Deng, J. Zhu, X. C. Zeng, B. Gong, *Org. Lett.* **2011**, *13*, 4008–4011.

[102] a) V. Dehm, M. Büchner, J. Seibt, V. Engel, F. Würthner, *Chem. Sci.* **2011**, *2*, 2094–2100; b) J. Hernando, P. A. J. de Witte, E. M. H. P. van Dijk, J. Korterik, R. J. M. Nolte, A. E. Rowan, M. F. García-Parajó, N. F. van Hulst, *Angew. Chem. Int. Ed.* **2004**, *43*, 4045–4049.

[103] P. A. J. de Witte, M. Castriciano, J. J. L. M. Cornelissen, L. Monsù Scolaro, R. J. M. Nolte, A. E. Rowan, *Chem. Eur. J.* **2003**, *9*, 1775–1781.

[104] a) J. Barbaric, H.-A. Wagenknecht, *Org. Biomol. Chem.* **2006**, *4*, 2088–2090; b) E. Mayer-Enthart, H.-A. Wagenknecht, *Angew. Chem. Int. Ed.* **2006**, *45*, 3372–3375; c) E. Mayer-Enthart, C. Wagner, J. Barbaric, H.-A. Wagenknecht, *Tetrahedron* **2007**, *63*, 3434–3439; d) D. Baumstark, H.-A. Wagenknecht, *Chem. Eur. J.* **2008**, *14*, 6640–6645; e) R. Varghese, H.-A. Wagenknecht, *Chem. Commun.* **2009**, 2615–2624; f) D. Ackermann, R. Häner, *Helv. Chim. Acta* **2004**, *87*, 2790–2804; g) V. L. Malinovskii, F. Samain, R. Häner, *Angew. Chem. Int. Ed.* **2007**, *46*, 4464–4467.

[105] B. Fimmel, M. Son, Y. M. Sung, M. Grüne, B. Engels, D. Kim, F. Würthner, *Chem. Eur. J.* **2015**, *21*, 615–630.

[106] P. A. J. De Witte, J. Hernando, E. E. Neuteboom, E. M. H. P. van Dijk, S. C. J. Meskers, R. A. J. Janssen, N. F. van Hulst, R. J. M. Nolte, M. F. García-Parajó, A. E. Rowan, *J. Phys. Chem. B* **2006**, *110*, 7803–7812.

[107] C. W. Chen, H. W. Whitlock, *J. Am. Chem. Soc.* **1978**, *100*, 4921–4922.

[108] S. C. Zimmerman, C. M. VanZyl, G. S. Hamilton, *J. Am. Chem. Soc.* **1989**, *111*, 1373–1381.

[109] a) F.-G. Klärner, J. Benkhoff, R. Boese, U. Burkert, M. Kamieth, U. Naatz, *Angew. Chem. Int. Ed.* **1996**, *35*, 1130–1133; b) F.-G. Klärner, U. Burkert, M. Kamieth, R. Boese, J. Benet-Buchholz, *Chem. Eur. J.* **1999**, *5*, 1700–1707; c) L. J. D'Souz, U. Maitra, *J. Org. Chem.* **1996**, *61*, 9494–9502; d) H. Nemoto, T. Kawano, N. Ueji, M. Bando, M. Kido, I. Suzuki, M. Shibuya, *Org. Lett.* **2000**, *2*, 1015–1017; e) F.-G. Klärner, J. Panitzky, D. Bläser, R. Boese, *Tetrahedron* **2001**, *57*, 3673–3687.

[110] a) A. Wu, A. Chakraborty, J. C. Fettinger, R. A. Flowers Ii, L. Isaacs, *Angew. Chem. Int. Ed.* **2002**, *41*, 4028–4031; b) S. Ghosh, A. Wu, J. C. Fettinger, P. Y. Zavalij, L. Isaacs, *J. Org. Chem.* **2008**, *73*, 5915–5925.

[111] A. E. Rowan, J. A. A. W. Elemans, R. J. M. Nolte, *Acc. Chem. Res.* **1999**, *32*, 995–1006.

[112] B. Legouin, P. Uriac, S. Tomasi, L. Toupet, A. Bondon, P. van de Weghe, *Org. Lett.* **2009**, *11*, 745–748.

[113] B. W. Greenland, M. B. Bird, S. Burattini, R. Cramer, R. K. O'Reilly, J. P. Patterson, W. Hayes, C. J. Cardin, H. M. Colquhoun, *Chem. Commun.* **2013**, *49*, 454–456.

[114] a) M. Barboiu, E. Petit, G. Vaughan, *Chem. Eur. J.* **2004**, *10*, 2263–2270; b) M. Barboiu, A.-M. Stadler, J.-M. Lehn, *Angew. Chem. Int. Ed.* **2016**, *55*, 4130–4154.

[115] a) R. Bhosale, J. Misek, N. Sakai, S. Matile, *Chem. Soc. Rev.* **2010**, *39*, 138–149; b) T. Aida, E. W. Meijer, S. I. Stupp, *Science* **2012**, *335*, 813–817.

[116] a) S. Ogi, V. Stepanenko, K. Sugiyasu, M. Takeuchi, F. Würthner, *J. Am. Chem. Soc.* **2015**, *137*, 3300–3307; b) C. Shao, M. Stolte, F. Würthner, *Angew. Chem. Int. Ed.* **2013**, *125*, 10657–10661.

[117] A. Zitzler-Kunkel, doctoral thesis (Funktionale Merocyaninfarbstoffe: Synthese, molekulare und Selbstorganisationseigenschaften sowie ihre Anwendung in der organischen Photovoltaik), Universität Würzburg, **2014**.

[118] D. Prim, G. Kirsch, J.-F. Nicoud, *Synlett* **1998**, *4*, 383–384.

[119] T. Katoh, Y. Inagaki, R. Okazaki, *J. Am. Chem. Soc.* **1998**, *120*, 3623–3628.

[120] a) B. Odell, M. V. Reddington, A. M. Z. Slawin, N. Spencer, J. F. Stoddart, D. J. Williams, *Angew. Chem. Int. Ed.* **1988**, *27*, 1547–1550; b) E. J. Dale, N. A. Vermeulen, A. A. Thomas, J. C. Barnes, M. Juríček, A. K. Blackburn, N. L. Strutt, A. A. Sarjeant, C. L. Stern, S. E. Denmark, J. F. Stoddart, *J. Am. Chem. Soc.* **2014**, *136*, 10669–10682.

[121] J.-D. Chai, M. Head-Gordon, *Phys. Chem. Chem. Phys.* **2008**, *10*, 6615–6620.

[122] F. Weigend, R. Ahlrichs, *Phys. Chem. Chem. Phys.* **2005**, *7*, 3297–3305.

[123] a) K. Bergmann, C. T. O'Konski, *J. Phys. Chem.* **1963**, *67*, 2169–2177; b) T. Förster, *Naturwissenschaften* **1946**, *33*, 166–175.

[124] J. C. Chang, *J. Chem. Phys.* **1977**, *67*, 3901–3909.

[125] V. May, O. Kühn, *Charge and Energy Transfer Dynamics in Molecular Systems*, 3rd ed., Wiley-VCH, **2011**.

[126] F. Fennel, S. Wolter, Z. Xie, P.-A. Plötz, O. Kühn, F. Würthner, S. Lochbrunner, *J. Am. Chem. Soc.* **2013**, *135*, 18722–18725.

[127] AFD, 2013.01; Scientific Computing and Modelling NV, Amsterdam, **2013**.

[128] R. Dennington, T. Keith, J. Millam, *GaussView, Version 5*, Semichem Inc., **2009**.

[129] a) H. von Berlepsch, C. Böttcher, L. Dähne, *J. Phys. Chem. B* **2000**, *104*, 8792–8799; b) J. L. McHale, *J. Phys. Chem. Lett.* **2012**, *3*, 587–597; c) S. S. Babu, V. K. Praveen, A. Ajayaghosh, *Chem. Rev.* **2014**, *114*, 1973–2129.

[130] a) G. D. Scholes, G. Rumbles, *Nature Mater.* **2006**, *5*, 683–696; b) F. C. Spano, *Acc. Chem. Res.* **2010**, *43*, 429–439; c) N. J. Hestand, F. C. Spano, *Acc. Chem. Res.* **2017**, *50*, 341–350; d) A. J. Wise, Y. Zhang, J. Fan, F. Wudl, A. L. Briseno, M. D. Barnes, *Phys. Chem. Chem. Phys.* **2014**, *16*, 15825–15830.

[131] a) T. Fujii, H. Kashida, H. Asanuma, *Chem. Eur. J.* **2009**, *15*, 10092–10102; b) P. Ensslen, Y. Fritz, H.-A. Wagenknecht, *Org. Biomol. Chem.* **2015**, *13*, 487–492; c) C.

B. Winiger, S. M. Langenegger, G. Calzaferri, R. Häner, *Angew. Chem. Int. Ed.* **2015**, *54*, 3643–3647; d) Y. Xiang, Q. Zhang, Z. Li, H. Chen, *Mater. Sci. Eng. C* **2017**, *70, Part 2*, 1156–1162.

[132] a) M. Klessinger, *Chem. unserer Zeit* **1978**, *12*, 1–11; b) M. Blanchard-Desce, V. Alain, P. V. Bedworth, S. R. Marder, A. Fort, C. Runser, M. Barzoukas, S. Lebus, R. Wortmann, *Chem. Eur. J.* **1997**, *3*, 1091–1104.

[133] E. Kirchner, Master thesis (Synthese und strukturelle Charakterisierung molekularer Pinzetten basierend auf Merocyaninfarbstoffen), Universität Würzburg, **2013**.

[134] T. Ochi, Y. Yamaguchi, T. Wakamiya, Y. Matsubara, Z.-i. Yoshida, *Org. Biomol. Chem.* **2008**, *6*, 1222–1231.

[135] L. Gerbig, Bachelor thesis (Synthese und Charakterisierung π-verlängerter Merocyaninfarbstoffe), Universität Würzburg, **2016**.

[136] F. Würthner, G. Archetti, R. Schmidt, H.-G. Kuball, *Angew. Chem. Int. Ed.* **2008**, *47*, 4529–4532.

[137] A. Capobianco, R. Borrelli, A. Landi, A. Velardo, A. Peluso, *J. Phys. Chem.* **2016**, *120*, 5581–5589.

[138] a) F. Würthner, R. Wortmann, R. Matschiner, K. Lukaszuk, K. Meerholz, Y. DeNardin, R. Bittner, C. Bräuchle, R. Sens, *Angew. Chem. Int. Ed.* **1997**, *36*, 2765–2768; b) M. Harmata, C. L. Barnes, S. R. Karra, S. Elahmad, *J. Am. Chem. Soc.* **1994**, *116*, 8392–8393.

[139] S. Grimme, J. Antony, S. Ehrlich, H. Krieg, *J. Chem. Phys.* **2010**, *132*, 154104.

[140] M. Cossi, N. Rega, G. Scalmani, V. Barone, *J. Comput. Chem.* **2003**, *24*, 669–681.

[141] a) S. R. Marder, J. W. Perry, *Science* **1994**, *263*, 1706–1707; b) F. Meyers, S. R. Marder, B. M. Pierce, J. L. Brédas, *J. Am. Chem. Soc.* **1994**, *116*, 10703–10714; c) R. L. Gieseking, C. Risko, J. L. Brédas, *J. Phys. Chem. Lett.* **2015**, *6*, 2158–2162.

[142] a) J. Franck, E. G. Dymond, *T. Farad. Soc.* **1926**, *21*, 536–542; b) E. U. Condon, *Selected Scientific Papers of E.U. Condon*, Springer, New York, NY, **1991**; c) C. N. Stedwell, N. C. Polfer, in *Laser Photodissociation and Spectroscopy of Mass-separated Biomolecular Ions*, Springer International Publishing, Cham, **2013**, p. 1–20.

[143] a) W. Liptay, in *Dipole Moments and Polarizabilities of Molecules in Excited Electronic States, Vol. 1*, Academic Press: New York, **1974**, p. 129–229; b) R. Wortmann, K. Elich, S. Lebus, W. Liptay, P. Borowicz, A. Grabowska, *J. Phys. Chem.* **1992**, *96*, 9724–9730; c) G. U. Bublitz, S. G. Boxer, *Annu. Rev. Phys. Chem.* **1997**, *48*, 213–242; d) J. J. Wolff, R. Wortmann, *Adv. Phys. Org. Chem.* **1999**, *32*, 121–217.

[144] S. F. Völker, A. Schmiedel, M. Holzapfel, K. Renziehausen, V. Engel, C. Lambert, *J. Phys. Chem. C* **2014**, *118*, 17467–17482.

[145] K. A. Kistler, F. C. Spano, S. Matsika, *J. Phys. Chem. B* **2013**, *117*, 2032–2044.

[146] D. Beljonne, J. Cornil, R. Silbey, P. Millié, J. L. Brédas, *J. Chem. Phys.* **2000**, *112*, 4749–4758.

[147] S. Sanyal, A. Painelli, S. K. Pati, F. Terenziani, C. Sissa, *Phys. Chem. Chem. Phys.* **2016**, *18*, 28198–28208.

[148] C. Lambert, T. Scherpf, H. Ceymann, A. Schmiedel, M. Holzapfel, *J. Am. Chem. Soc.* **2015**, *137*, 3547–3557.

[149] H. Kashida, N. Higashiyama, T. Kato, H. Asanuma, *Bioorg. Med. Chem.* **2013**, *21*, 6191–6197.

[150] G. Sheldrick, *Acta Crystallogr. A* **2008**, *64*, 112–122.

[151] Gaussian 09, Revision D.01, M. J. Frisch, G. W. Trucks, H. B. Schlegel, G. E. Scuseria, M. A. Robb, J. R. Cheeseman, G. Scalmani, V. Barone, G. A. Petersson, H. Nakatsuji, X. Li, M. Caricato, A. Marenich, J. Bloino, B. G. Janesko, R. Gomperts, B. Mennucci, H. P. Hratchian, J. V. Ortiz, A. F. Izmaylov, J. L. Sonnenberg, D. Williams-Young, F. Ding, F. Lipparini, F. Egidi, J. Goings, B. Peng, A. Petrone, T. Henderson, D. Ranasinghe, V. G. Zakrzewski, J. Gao, N. Rega, G. Zheng, W. Liang, M. Hada, M. Ehara, K. Toyota, R. Fukuda, J. Hasegawa, M. Ishida, T. Nakajima, Y. Honda, O. Kitao, H. Nakai, T. Vreven, K. Throssell, J. J. A. Montgomery, J. E. Peralta, F. Ogliaro, M. Bearpark, J. J. Heyd, E. Brothers, K. N. Kudin, V. N. Staroverov, T. Keith, R. Kobayashi, J. Normand, K. Raghavachari, A. Rendell, J. C. Burant, S. S. Iyengar, J. Tomasi, M. Cossi, J. M. Millam, M. Klene, C. Adamo, R. Cammi, J. W. Ochterski, R. L. Martin, K. Morokuma, O. Farkas, J. B. Foresman, D. J. Fox, Gaussian, Inc., Wallingford CT, **2016**.

[152] E. A. Cobar, R. Z. Khaliullin, R. G. Bergman, M. Head-Gordon, *Proc. Natl. Acad. Sci.* **2007**, *104*, 6963–6968.

[153] K. A. Kistler, C. M. Pochas, H. Yamagata, S. Matsika, F. C. Spano, *J. Phys. Chem. B* **2012**, *116*, 77–86.

[154] T. Lu, F. Chen, *J. Comput. Chem.* **2012**, *33*, 580–592.

Danksagung

Mein besonderer Dank gilt meinem Doktorvater, Herrn Prof. Dr. Frank Würthner, für das Überlassen des sehr interessanten Forschungsthemas und für die hervorragenden Arbeitsbedingungen in seiner Gruppe, welche die Grundlage für den erfolgreichen Abschluss dieser Arbeit bildeten. Weiterhin danke ich ihm herzlich für seine immerwährende Unterstützung, die zahlreichen Ratschläge sowie für die wissenschaftlichen Freiheiten und das damit verbundene Vertrauen mir gegenüber.

Danken möchte ich außerdem Herrn Dr. David Bialas, Herrn Dr. Matthias Stolte, Herrn Dr. Chantu Saha-Möller und Frau Dr. Franziska Fennel für die vielen Diskussionen, die wesentlich zum Gelingen dieser Arbeit beigetragen haben.

Weiterhin danke ich Herrn Dr. Matthias Grüne für seine Zeit und Geduld bei der Einarbeitung in die NMR-Spektroskopie, für sein mir entgegen gebrachtes Vertrauen und dafür, dass er mir mit seinem fachlichen Wissen jederzeit mit Rat und Tat zur Seite stand. Frau Juliane Adelmann, Frau Patricia Altenberger und Frau Elfriede Ruckdeschel danke ich dafür, dass ich bei Fragen und Problemen beim Aufsetzen der Messungen immer auf ihre Hilfe zählen konnte.

Herrn Dr. David Bialas danke ich für die hervorragende Zusammenarbeit und die Durchführung der quantenmechanischen Rechnungen.

Des Weiteren möchte ich mich bei Frau Dr. Franziska Fennel für die Ausarbeitung und Implementierung der Aggregationsmodelle sowie für die Hilfe bei der Interpretation von UV/vis-spektroskopischen Daten bedanken.

Herrn Dr. David Schmidt danke ich für die die Durchführung der Röntgenstrukturanalyse und Herrn Dr. Vladimir Stepanenko für die AFM Messungen. Weiterhin danke ich Herrn Dr. Matthias Büchner, Frau Juliane Adelmann und Frau Antje Heckmann für die Aufnahme und Analyse der Massenspektren.

Für das Korrekturlesen dieser Arbeit danke ich Herrn Dr. David Bialas, Herrn Dr. Andreas Liess, Frau Sabine Seifert und Herrn Reinhard Hecht. Besonderer Dank gilt auch Herrn Dr. Chantu Saha-Möller und Herrn Dr. David Bialas für die gründliche Überarbeitung von Manuskripten.

Für die Unterstützung bei der Synthesearbeit bedanke ich mich bei Julius Albert, Ann-Kathrin Lenz und Anja Hofmann sowie bei den Bachelorstudenten Manuel Weh, Annika Bothe, Lisa Gerbig und bei allen Praktikumsstudenten.

Des Weiteren möchte ich mich bei Herrn Dr. André Zitzler-Kunkel und Herrn Dr. Sabin Suraru für die hilfreichen praktischen Tipps sowie für die unzähligen wissenschaftlichen Diskussionen zu Beginn meiner Doktorarbeit bedanken.

Frau Christiana Toussaint und Frau Eleonore Klaus danke ich für die Unterstützung bei organisatorischen Angelegenheiten und für die Vorbereitung von Reisen zu Workshops und Konferenzen.

Bei Herrn Joachim Bialas bedanke ich mich ganz herzlich für seine unentbehrliche Hilfe im Laboralltag und dafür, dass er mich mit seiner guten Laune immer zum Lachen gebracht hat.

Mein Dank gilt außerdem dem gesamten Arbeitskreis Würthner für die familiäre Arbeitsatmosphäre, die gute Zusammenarbeit im Labor und die lustigen Abende bei den Stammtischen.

Zuletzt möchte ich mich von ganzem Herzen bei meiner Familie bedanken, die mich immer bedingungslos unterstützt und für Abwechslung vom Arbeitsalltag gesorgt hat. Thomas danke ich außerdem für seine grenzenlose Geduld und für sein Verständnis.